Non-Invasive Characterization of Brain Tissue Electrical Properties with MRI

Stefano Mandija

Colophon
Cover: A human brain electrical conductivity map is produced through the mixture of salt and water.
Cover design and layout: S. Mandija.

Non-Invasive Characterization of Brain Tissue Electrical Properties with MRI
PhD thesis, Utrecht University, the Netherlands

S.Mandija@umcutrecht.nl

ISBN/EAN: 978-90-393-6904-3
Printed by: PrintSupport4U

Non-Invasive Characterization of Brain Tissue Electrical Properties with MRI

Non-Invasieve Karakterisering van Elektrische Eigenschappen van de Hersenen met MRI

(met een samenvatting in het Nederlands)

Proefschrift

ter verkrijging van de graad van doctor aan de Universiteit Utrecht
op gezag van de rector magnificus, prof. dr. G.J. van der Zwaan,
ingevolge het besluit van het college voor promoties in het openbaar
te verdedigen op dinsdag 23 januari 2018 des ochtends te 10.30 uur

door

Stefano Mandija

geboren op 27 september 1988
te Camposampiero, Padova (PD), Italië

Promotor: Prof. dr. P.R. Luijten

Copromotoren: Dr. ir. C.A.T. van den Berg

Dr. S.F.W. Neggers

Publication of this thesis was financially supported by:

Philips Healthcare

Brain Science Tools

ChipSoft

Contents

"Non chi comincia, ma quel che persevera."

Nave Scuola Amerigo Vespucci, 1978
Marina Militare Italiana

Chapter 1

General Introduction

The study of the electrical properties of tissues, namely conductivity and permittivity, has already been of great interest for more than a century and it is still an active area of research. Tissue electrical properties determine the pathways of current flow through our body. They are of fundamental importance in understanding the interactions and the effects of electromagnetic fields on our body. For biological tissues, these properties are determined by the molecular composition, cellular structure, amount of intra- and extra-cellular fluids, mobility and concentration of ions, temperature and many other factors. Consequently, tissue electrical properties reflect structural, functional and pathological conditions of tissues. Therefore, measurements of tissue electrical properties could provide valuable information for radiofrequency patient safety in Magnetic Resonance Imaging (MRI), guidance of neuronal stimulation in neuroscience, and could be used as a new endogenous biomarker for example in oncology.

Reported literature values mostly pertain to *ex-vivo* measurements performed with dielectric probes. These measurements can only provide approximated reference values since tissue electrical properties start changing immediately after tissue excision or death. To accurately measure tissue electrical properties, *in-vivo* measurements are highly desired. *In-vivo* measurements should be performed non-invasively and should carry the minimum risk and discomfort for patients. Therefore, direct *in-vivo* measurements using dielectric probes are not possible, except for a few accessible tissues.

With the advent of imaging techniques such as MRI, we are now able to non-invasively assess information such as tissue structure and physiological processes *in-vivo*. MRI is an electromagnetic-based imaging modality. Therefore, since tissue electrical properties modulate the interactions between biological tissues and externally applied electromagnetic fields, MRI has been considered a great candidate to study these properties *in-vivo*. These are the motivations that spurred the research presented in this thesis.

1.1 Tissue electrical properties (EPs)

In presence of time-varying magnetic fields, electric fields and electric currents are induced into conductive materials such as the human tissues. Examples of time-varying magnetic fields are the radiofrequency (RF) field and the gradient fields in MRI, or the transient magnetic field produced by Transcranial Magnetic Stimulators (TMS) (Fig. 1.1). The interaction between these electromagnetic fields and human tissues is a function of the electromagnetic properties of tissues: the magnetic permeability (μ), the relative permittivity (ε_r), and the conductivity (σ) (1).

Transcranial Magnetic Stimulator

3 Tesla MRI System Philips Ingenia

Figure 1.1: TMS system (left) and MRI system (right).

The magnetic permeability describes the degree of magnetization that a material obtains as a response to an applied magnetic field. For human tissues, the relative magnetic permeability varies in the range of 10 ppm. Therefore, it is often approximated with the magnetic permeability in vacuum ($\mu_0 = 4\pi \times 10^{-7}$ H/m). The relative permittivity describes the degree of electrical polarization of a material in presence of an external electric field. In physical terms, the relative permittivity of a material is a measure of the capability of its charges to be stored or its dipoles to rotate in response to an applied electric field. The conductivity (reciprocal of the electric resistance) describes the ability of a material to conduct an electric current, i.e. it is a measure of the capability of its charges (ions) to be transported throughout its volume.

Dielectric probe measurements have shown a significant change of these properties as a function of frequency (Fig. 1.2, A, and Tab. 1.1) (2–5). Tissue permittivity and conductivity show a frequency dependent behavior, which is called dispersion (2,6,7), and vary greatly between different tissues (8,9).

The curves shown in Fig. 1.2, A, are obtained from literature data of the complex relative permittivity ($\hat{\varepsilon}$) for brain tissues, which was measured experimentally (2,10):

$$\hat{\varepsilon}(\omega) = \varepsilon'(\omega) - i\varepsilon''(\omega) \qquad [1.1]$$

with:

$$\varepsilon'(\omega) = \varepsilon_r(\omega) \quad [1.2]$$

$$\varepsilon''(\omega) = \frac{\sigma(\omega)}{\omega\varepsilon_0} \ . \quad [1.3]$$

The parameter ε_0 is the permittivity in vacuum (8.8542×10^{-12}), and ω is the angular frequency ($\omega = 2\pi f$, f: frequency). In eq. [1.2], $\varepsilon_r(\omega)$ is the relative permittivity (Fig. 1.2, A, dashed lines), which modulates the displacement current ($\boldsymbol{J}_D = \varepsilon_0\varepsilon_r(\partial\boldsymbol{E}/\partial t)$, with **E**: electric field). In eq. [1.3], $\sigma(\omega)$ is the conductivity (Fig. 1.2, A, solid lines), which modulates the conduction current ($\boldsymbol{J}_C = \sigma\boldsymbol{E}$). At frequencies where TMS works (1-10 kHz), displacement currents are negligible, as the ratio between eqs. [1.2] and [1.3] is much lower than 1 (Fig. 1.2, B). Instead, at frequencies where MRI works (hundreds of MHz), displacement currents are not negligible anymore, and in combination with conduction currents determine the wave propagation.

Dispersions can be understood in terms of dipoles orientation and charges (ions) movement. At low frequencies, dipoles can follow the change of an applied electric field, whereas charges travel long distances over which a big likelihood of charge-trapping at interfaces exists. The relative permittivity is high and the conductivity is low. As the frequency increases, dipoles are less able to follow the changes in the applied electric field, and the corresponding polarization disappears. Instead, charges travel shorter distances, and therefore the likelihood of charge-trapping at interfaces is reduced. Thus, with increasing frequencies, the permittivity decreases while the conductivity increases, as trapping effects become less important.

In heterogeneous tissues such as biological tissues, three main dispersion bands can be observed: the α-dispersion band (hertz – tens of kilohertz), the β-dispersion band (tens of kilohertz – tens of megahertz), and the γ-dispersion band (gigahertz) (7,11).

The α-dispersion band is very apparent for the permittivity, which reaches very high values, but less noticeable for the conductivity. This reflects the trapping of charges at interfaces and is not related to dipole orientation. At these frequencies, tissue conductivity is dominated by the ionic diffusion process in the extracellular space. Thus, the low frequency tissue conductivity is strongly modulated by the volume fraction of the extracellular space (11,12).

The β-dispersion band is apparent in both permittivity and conductivity. In this dispersion band, polarization of cells membranes occurs. Cells membranes act as a barrier to the ions flow between the intra- and the extra-cellular space. Hence, conductivity measurements in this frequency range would give important information not only on tissue composition but also on tissue micro-structure (10), as they are still related to ionic diffusion.

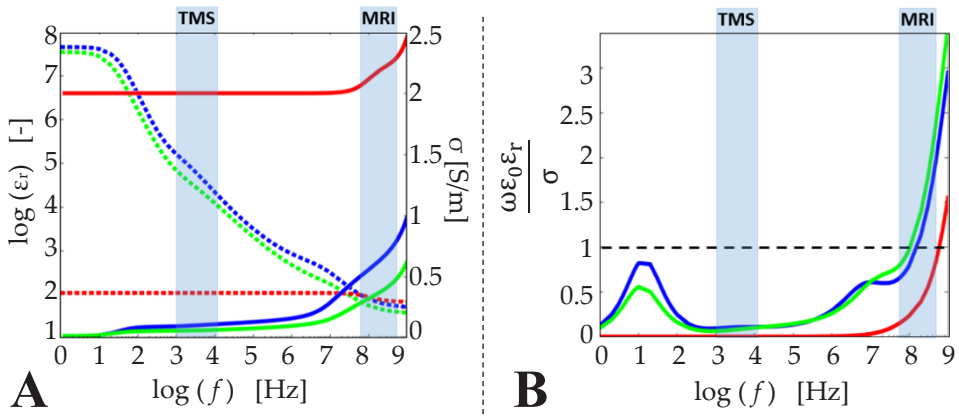

Figure 1.2: Relative permittivity (dashed lines) and conductivity (solid lines) values as a function of the frequency for gray matter (GM, blue), white matter (WM, green), and cerebrospinal fluid (CSF, red). These values were taken from https://www.itis.ethz.ch.

		Low Frequency (LF)		High Frequency (RF)		
		1 kHz	10 kHz	64 MHz	128 MHz	298 MHz
conductivity σ [S/m]	gray matter	9.8×10^{-2}	1.2×10^{-1}	0.51	0.59	0.69
	white matter	6.2×10^{-2}	6.9×10^{-2}	0.29	0.34	0.41
	cerebrospinal fluid	2.0×10^{0}	2.0×10^{0}	2.07	2.14	2.22
	brain (average)	1.2×10^{-1}	1.3×10^{-1}	0.40	0.46	0.55
relative permittivity ε_r [-]	gray matter	1.6×10^{5}	2.2×10^{4}	97	74	60
	white matter	6.9×10^{4}	1.2×10^{4}	68	53	44
	cerebrospinal fluid	1.1×10^{2}	1.1×10^{2}	97	84	73
	brain (average)	1.6×10^{5}	2.2×10^{4}	82	63	52

Table 1.1: Conductivity and relative permittivity values of brain tissues at low frequencies (LF) and at RF frequencies (corresponding to the Larmor frequency respectively of 1.5, 3, and 7T MRI scanners). These values were taken from https://www.itis.ethz.ch.

At microwave frequencies, tissues exhibit the γ-dispersion, which is noticeable especially for the tissue conductivity. In this frequency range, conductivity is modulated mostly by the polarization of water molecules (8).

In addition to these major dispersions, other smaller dispersions occur due to the charging of membranes, the rotational relaxation of bound water or tissue proteins, and other effects (4,7,10). Interesting for MRI applications, the δ-dispersion band can be observed at megahertz frequencies (tens of MHz – hundreds MHz). In this frequency range, cell membranes have negligible impedance, thus currents can pass through the intra/extra-cellular space. Therefore, conductivity measurements at hundreds MHz would not give any information on the underlying tissue structure, but only information on tissue composition.

Tissue EPs values reported in literature mostly pertain to *ex-vivo* measurements performed with dielectric probes (Tab. 1.1). Among reported studies, large variability in the reported values is observed, especially at low frequencies. This variability arises from the fact that tissue EPs change shortly after tissue excision.

Additionally, probe measurements are highly sensitive to systematic errors, such as electrode polarization and lead inductance, in addition to random errors, such as system drift, and environmental changes (temperature and humidity). Thus, these values should be used as a general reference (7). To avoid these errors, measurements of tissue EPs should be performed in *in-vivo*, non-invasively and by carrying the minimum risk and discomfort. This makes probe measurements not suitable for *in-vivo* tissue EPs characterization.

1.2 Experimental characterization of LF tissue electrical properties

In this thesis, "low frequency" (LF) is considered the frequency range where TMS works, i.e. 1 – 10 kHz. In this frequency range, the human body is electrically very heterogeneous (Tab. 1.1) (11,12). Measurements of tissue EPs in this frequency range can provide important information on tissue structure and composition. However at these frequencies, tissue EPs change immediately after tissue excision or death due to variations in the tissue structure and composition, as a consequence of cellular swelling and membrane breakdown, temperature, and humidity (13). In light of these observations, direct *in-vivo* measurements of tissue EPs are highly desired.

For this purpose, two major methodologies have been proposed. Both methodologies aim to measure low frequency tissue conductivity, which modulates how currents flow inside tissues (in the extra-cellular space in this frequency range). However, they significantly differ in the way these currents are introduced inside tissues.

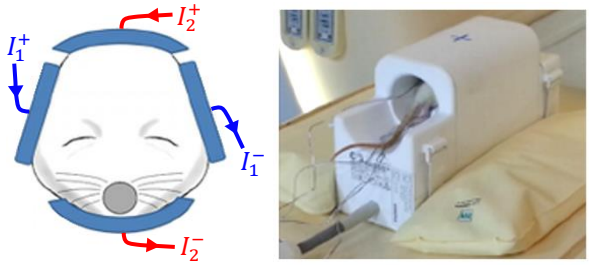

Figure 1.3: MR-EIT setup.

Picture adapted from (83).

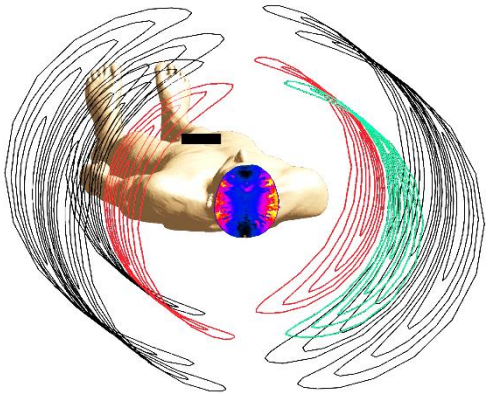

Figure 1.4: Electric field induced in tissues using the x-gradient coil in MRI.

The simulation was performed in Sim4Life (ZMT AG, Zurich, CH), and the values are normalized to the maximum value.

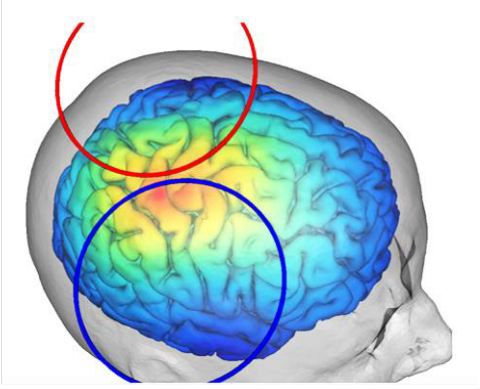

Figure 1.5: Electric field induced in tissues using a TMS coil (the peak is under the TMS coil).

The simulation was performed in SCIRun (http://www.scirun.org), and the values are normalized to the maximum value.

Currents can be directly injected using skin-surface electrodes (current injection methods, see 1.2.1), or can be inductively induced using time-varying magnetic fields (current induction methods, see 1.2.2).

1.2.1 Current injection methods

Since the 1980s, a lot of effort has been made to reconstruct cross-sectional images of conductivity distributions *in-vivo*. The first approach, know as Electrical Impedance Tomography (EIT), aims to reconstruct tissue conductivity by directly injecting currents in tissues, and then measuring the induced voltage using skin-surface electrodes (14,15). However, this technique has not reached the clinical applicability since it presents several methodological limitations in terms of practical feasibility and ill-posedness of the inverse reconstruction problem. In particular, this method is not sensitive to changes in local conductivity distributions in regions away from the body surface.

By exploiting this technique and taking advantage of MRI systems to access deep regions in the body, MR-EIT (Fig. 1.3) allows reconstructions of low frequency tissue conductivity (16–21). MR-EIT is based on the key idea that the injected currents in tissues are modulated by the LF EPs of tissues, and thus the magnetic field originating from these currents according to Biot-Savart's law intrinsically carries information on the underlying tissue EPs. Consequently, MR-EIT aims to measure the small induced modulations in the MR static magnetic field (B_0) originating from these injected currents through phase mapping. From these measurements, conductivity maps can be reconstructed. This technique appears quite appealing. However, in order to achieve enough signal-to-noise ratio (SNR) strong currents (~10 mA) need to be injected for long time intervals (10 ms). These levels of currents can cause pain sensation at the skin-electrode interface. Guidelines on the maximum level of current that can be injected in the human body for imaging purposes are currently missing. The International Electrotechnical Commission defines only the limits for auxiliary, therapeutic, and diagnostic currents (IEC 60601-1/2) (22). Whether these guidelines should apply also for imaging currents still needs to be discussed. For *in-vivo* studies, the maximum current amplitude used is defined as the 90% of the current amplitude that gives pain sensation (20). It is understandable that this methodology has problems related to patient comfort and safety.

1.2.2 Current induction methods

To avoid direct current injection resulting in pain sensation and susceptibility artifacts near the electrodes, currents can be inductively induced in tissue using incident time-varying magnetic fields. An incident, primary time-varying magnetic

field generates eddy currents inside conductive tissues according to the Faraday's law of induction. In turn, these eddy currents create a secondary, induced magnetic field according to the Biot-Savart's law. As in MR-EIT, this secondary magnetic field can be measured using standard MRI systems. Of course, a way to create this time-varying incident magnetic field is needed.

In MRI experiments, LF time-varying magnetic fields are created from the ramping up/down of the MR imaging gradients. These incident time-varying magnetic fields induce electric fields in tissues (Fig. 1.4). Due to the conductive nature of the human tissues, these electric fields result in eddy currents, which are known to cause peripheral nerve stimulation (PNS) (23–25) in case of strong and fast switching of gradients. By exploiting this idea, one could in principle use only an MRI system. First LF eddy currents are inductively induced in tissues by applying time varying gradient fields. Then, as for MR-EIT, the accumulated phase due to the secondary induced magnetic field arising from these induced LF eddy currents is measured (26,27). Subsequently, from these measurements EPs reconstructions can be performed by adopting MR-EIT algorithms. This is a very appealing methodology since it does not require any additional hardware and it does not cause pain sensation.

To map the expected small phase changes, high signal-to-noise ratio (SNR) is needed. The effect of induced tissue eddy currents can be augmented by using TMS devices instead of MRI gradient systems. In TMS, a time-varying incident magnetic field is created by a time-varying current running in an external TMS coil. As for MRI gradient systems, these incident magnetic fields induce electric fields (Fig. 1.5) and therefore LF eddy currents in tissues (28). However, TMS devices allow much stronger current induction than MR gradient systems. In fact, while standard MR gradients allow slew rates of 20 T/s at 10 cm from the gradients isocenter, a TMS device can generate slew rates up to 20000 T/s (29–31). This would results in stronger induced currents and, consequently, stronger induced secondary magnetic field, where information on tissue EPs is imprinted.

1.2.3 Subject-specific LF tissue electrical properties: applications

Being able to measure LF tissue EPs would be important for several applications.

Low frequency EPs values are desired in source localization imaging techniques such as ECG/MCG for the heart, and EEG/MEG for the brain (32). These techniques aim to map the distribution of the current produced by excitable tissues like nerves and muscles through an inversion problem, which requires knowledge of the distribution of the tissues EPs.

Neuronal stimulation techniques such as Deep Brain Stimulation, Transcranial Direct Current Stimulation and Transcranial Magnetic Stimulation, which work at low frequencies (Hz – kHz), would also extremely benefit from subject-specific measurements of LF EPs. Having accurate phase measurements (from which LF tissue EPs could be reconstructed) in combination with detailed subject-specific anatomical maps would be important to accurately characterize via electromagnetic simulation the deployed electric field in the brain, which can cause neuronal activation (33–36). This could in principle be used for guidance of subject-specific dosimetry (intensity of the applied electromagnetic field).

Furthermore, since LF EPs reflect tissue structure and composition, they might be used as a new endogenous biomarker, for example to diagnose ischemia, hemorrhages, inflammation processes and tumors (37,38), where the breakdown of cellular membranes would lead to different tissue structures. In particular, strong changes in LF conductivity, associated to differences in tissue structures, might allow classification of tumor stages.

1.3 Experimental characterization of HF tissue electrical properties

In this thesis, "high frequency" (HF) is considered the frequency range where MRI works (radiofrequencies, RF: 10^7 – 10^9 MHz). Making use of standard MRI systems, electric fields (Fig. 1.6) and thus currents at RF frequencies can be induced in tissues by applying time-harmonic RF fields. RF fields are used in MRI to flip the spins from their orientation along the main magnetic field direction (B_0). The effective transmit field component is known as the B_1^+ field:

$$B_1^+ = (B_x + iB_y)/2 \qquad [1.4]$$

positive, circularly polarized component of the magnetic flux density ($\boldsymbol{B}$), corresponding to the RF transmit field (39,40).

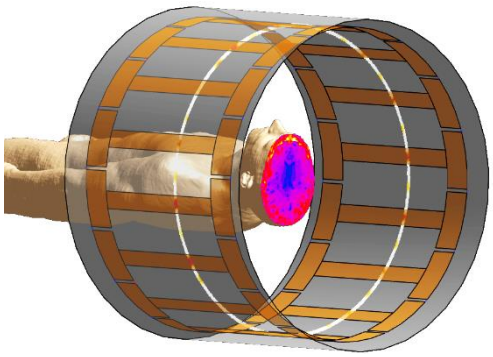

Figure 1.6: Electric field induced in tissues using an MRI body coil in transmit, quadrature mode, 3T.

The simulation was performed in Sim4Life (ZMT, Zurich, CH).

The values are normalized to the maximum value.

Currently, several techniques are available to measure the B_1^+ field, for example the actual flip angle method (AFI) (41), Bloch-Siegert (42), and dual refocusing echo acquisition mode (DREAM) (43).

Analogously to low frequencies, the interaction between these RF fields and tissues is also modulated by the EPs of tissues. However, at RF frequencies EPs of tissues are mainly correlated to the ionic and water content. Therefore, contrarily to LF EPs, at RF frequencies biological tissues appear mainly isotropic, and thus the information on the underlying micro-structure comes less (6,10,44).

Given that we can measure the B_1^+ field and that information on the EPs of tissues is imprinted in this field, in principle we could be able to reconstruct tissue EPs from B_1^+ field measurements. However, to solve this inverse problem, we need a model that links the measured B_1^+ field to the underlying tissue EPs.

1.3.1 MR-Electric Property Tomography (MR-EPT): the forward model

Based on the idea that the effective MR transmit B_1^+ field is modulated by the EPs of tissues at the Larmor frequency ($\omega = \omega_L$), MR-Electrical Property Tomography (MR-EPT) aims to reconstruct tissues EPs directly from measurements of the B_1^+ field (45–48). By combining Ampere's law and Faraday's law, the full Helmholtz equation can be derived in terms of the time-harmonically varying magnetic flux density ($\boldsymbol{B}e^{+i\omega t}$) (39):

$$-\nabla^2\boldsymbol{B}(\boldsymbol{r}) = \frac{\nabla\varepsilon_c(\boldsymbol{r})}{\varepsilon_c(\boldsymbol{r})} \times [\nabla \times \boldsymbol{B}(\boldsymbol{r})] + \omega^2\mu_0\varepsilon_c(\boldsymbol{r})\boldsymbol{B}(\boldsymbol{r}) \qquad [1.5]$$

with the complex permittivity $\varepsilon_c(\boldsymbol{r}) = \varepsilon_0\hat{\varepsilon}(\boldsymbol{r}) = \varepsilon_r(\boldsymbol{r})\varepsilon_0 - \frac{i\sigma(\boldsymbol{r})}{\omega}$, and assuming negligible magnetic permeability variations ($\mu_r = 1$). By assuming piece-wise constant EPs ($\nabla\varepsilon_c = 0$), the simpler homogeneous Helmholtz equation is obtained, in terms of the transmit B_1^+ field:

$$\nabla^2 B_1^+(\boldsymbol{r}) + \gamma^2(\boldsymbol{r})B_1^+(\boldsymbol{r}) = 0 \qquad [1.6]$$

with the complex wave number $\gamma^2(\boldsymbol{r}) \equiv \omega^2\mu_0\varepsilon_c(\boldsymbol{r})$ and $B_1^+ = |B_1^+|e^{i\varphi^+}$ ($|B_1^+|$: magnitude, and φ^+: transmit phase). Based on eq. [1.6], EPs of tissues are reconstructed in MR-EPT according to:

$$\varepsilon_r(\boldsymbol{r}) = \frac{-1}{\mu_0\varepsilon_0\omega^2} Re\left(\frac{\nabla^2 B_1^+(\boldsymbol{r})}{B_1^+(\boldsymbol{r})}\right) \qquad [1.7]$$

$$\sigma(\boldsymbol{r}) = \frac{1}{\mu_0\omega} Im\left(\frac{\nabla^2 B_1^+(\boldsymbol{r})}{B_1^+(\boldsymbol{r})}\right) . \qquad [1.8]$$

By separating the real and the imaginary part, eq. [1.6] can be rewritten as:

$$\gamma^2(\boldsymbol{r}) = -\left[\left(\frac{\nabla^2|B_1^+|}{|B_1^+|} - |\nabla\varphi^+|^2\right) + i(2\nabla(ln|B_1^+|)\cdot\nabla\varphi^+ + \nabla^2\varphi^+)\right]. \qquad [1.9]$$

It has been shown that for low field strengths (1.5 T – 3 T) and small objects such as the human head $\frac{\nabla^2|B_1^+|}{|B_1^+|} \gg |\nabla\varphi^+|^2$ and $2\nabla(ln|B_1^+|)\cdot\nabla\varphi^+ \ll \nabla^2\varphi^+$ (48). Therefore, to a leading order, eqs. [1.7] and [1.8] can be expressed as (48,49):

$$\varepsilon_r(\boldsymbol{r}) = -\frac{\nabla^2|B_1^+(\boldsymbol{r})|}{\mu_0\varepsilon_0\omega^2|B_1^+|} \quad [1.10]$$

$$\sigma(\boldsymbol{r}) = \frac{\nabla^2\varphi^+(\boldsymbol{r})}{\mu_0\omega} \quad . \quad [1.11]$$

Equations [1.10] and [1.11] show that the permittivity can be reconstructed from the curvature (i.e. the Laplacian) of the magnitude of the B_1^+ field, while the conductivity is reflected by the curvature of the phase of the B_1^+ field ($\varphi^+(\boldsymbol{r})$).

1.3.2 Inaccuracies of MR-EPT experiments

Standard MR-EPT reconstructions adopt the previously presented homogeneous Helmholtz model (eq. [1.6]). EPs reconstructions are therefore performed from MRI measurements using eqs. [1.7 – 1.11], where the derivative operations are computed by convolving the acquired MRI images with finite difference schemes in the form of kernels.

However, these equations are valid for idealistic cases. For *in-vivo* MRI experiments, several assumptions need to be made (39,40). It is understandable that these assumptions might lead to reconstruction errors. Therefore, it is fundamental to investigate what is the impact of these errors on the reconstructed EPs values.

Firstly, the homogeneous Helmholtz model assumes piece-wise constant EPs within the adopted derivative kernels. This assumption might not be valid for *in-vivo* situations where EPs may vary within homogeneous tissues. To overcome the piece-wise constant assumption, more advanced reconstruction frameworks such as gradient-based EPT and convection-reaction-diffusion EPT suggested to include gradients in the EPs (50–52). Still, for all these frameworks, the adopted Helmholtz based models are not valid at tissue boundaries where EPs change. This leads to local physical errors (53,54).

Secondly, MR-EPT requires measurements of the complex B_1^+ field. While it possible to measure the magnitude of the B_1^+ field using MRI systems (41,55), measurements of the transmit B_1^+ phase (φ^+) are not feasible. It has been demonstrated that for a birdcage coil operated in quadrature mode (leading to circularly polarized field), and a symmetrical, cylindrical object placed in the center of the coil, the transmit phase can be approximated with half the transceive phase ($\varphi^{\pm}$) (49). Alternatively, to overcome this assumption, multi-transmit systems might be used (55).

Thirdly, Helmholtz-based methods require the computation of spatial derivatives on voxelized data (measured complex B_1^+ field). This operation plays a central role in EPs reconstructions. In standard MR-EPT reconstructions, spatial derivatives are computed using approximated finite difference schemes (49). Alternatively, derivatives could also be analytically computed after fitting a polynomial to the measured field around the point of consideration (56,57). These methods of computing spatial derivatives can be seen more easily as a convolution of the measured B_1^+ field with different kernels K. Since small derivative kernels are highly sensitive to noise (58,59), large derivative kernels (more noise-robust) are often adopted (Fig. 1.7). However, at tissue boundaries, large kernels would include voxels belonging to different tissue types. This results in more spatially extended numerical boundary errors compared to small derivative kernels (severe over/under-estimation of the reconstructed EPs values).

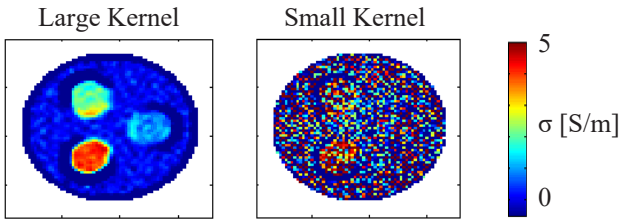

Figure 1.7: Impact of numerical errors as a function of the kernel size for conductivity reconstructions. The use of a large FD kernel introduces severe boundary errors (large under-shooting). The spatial extension of the boundary error is reduced if the small kernel is used. However, small kernels are less noise robust. In fact, severe noise amplification can be observed. Conductivity reconstructions were performed from MRI measurements at 3T (Ingenia, Philips Healthcare, Best, The Netherlands).

1.3.3 Alternative approaches

The MR-EPT methods described above can be considered as "direct methods", i.e. EPs of tissues are reconstructed by computing spatial derivatives of the measured B_1^+ field in the image domain. Therefore, these direct methods run "backwards", as they go from the measured B_1^+ field to the underlying tissue EPs. However, Helmholtz-based methods employ spatial derivatives directly to the measured B_1^+ field. As shown in Fig. 1.7, this operation introduces severe boundary errors and noise amplification in the reconstructed EPs maps. To avoid the computation of spatial derivatives of measured MRI data, "inverse methods" running forward can be used (60–63). Among these approaches, Contrast Source Inversion (CSI) EPT has shown good results especially at tissue boundaries (60).

In parallel, a different reconstruction approach, namely water-EPT (wEPT), which is not derived from electromagnetic (EM) theory, has been recently suggested (64). As said, at RF frequencies EPs are mostly modulated by the ionic content and the water content (5,6,44,65,66). Based on the empirically established correlation between water content and EPs, wEPT aims to reconstruct tissue EPs directly from tissue water content measurements. This reconstruction approach employs two fixed correlations: water-content maps are first reconstructed from T1-weighted maps, then EPs maps are derived from water-content maps. In this way, wEPT is free from the piece-wise constant assumption, phase assumptions, and numerical errors introduced by the differentiation needed in MR-EPT (boundary errors and noise amplification).

1.3.4 Subject-specific HF tissue electrical properties: applications

MR-EPT was initially intended to provide subject-specific tissue EPs maps for RF safety assessment (47,67,68). The interaction between the transmit RF field used in MRI and the human body can cause foci of absorbed energy inside the body. As a consequence, local tissue heating is induced. Currently, patient safety is ensured by the IEC limits (IEC 60601-2-33, third edition) based on the amount of the absorbed energy (Specific Absorption Rate, SAR, W/Kg):

$$SAR = \frac{\sigma|\boldsymbol{E}|^2}{2\rho}. \qquad [1.12]$$

As shown in Eq. [1.12], SAR depends on the tissue electric conductivity, density (ρ), and the total electric field magnitude ($\boldsymbol{E}$). Therefore, we need subject-specific tissue EPs maps to correctly assess subject-specific RF safety, as inter-subject EPs variations would result in different local SAR foci.

Measurements of tissue EPs might also be used as a new biomarker, for example in oncology. In healthy tissues, the intra-cellular sodium concentration (Na^+_{intra}) is about ten times lower than the extra-cellular sodium concentration (Na^+_{extra}) (69–71). This gradient in concentrations is maintained by the sodium-potassium pumps. However in case of tumors, the ionic homeostasis is compromised due to the failure of the sodium-potassium pumps (lack on nutrients, ATP). This results in a considerable increase in the concentration of Na^+_{intra}, while Na^+_{extra} is constantly buffered. Consequently, the total sodium concentration (TSC) will increase (70,72–78). This contributes to a local increase in the tissue conductivity, which can in principle be measured using MR-EPT (79–82).

1.4 Thesis outline

In the next chapter (Chapter 2), the feasibility of measuring EPs at low frequencies (kHz) by means of switching MRI gradients is experimentally investigated. This would be really appealing since no additional hardware is required. For this methodology to work, it is essential that the phase contribution arising from the induced magnetic field due to the LF eddy currents can be measured and distinguished from the other MR phase contributions. This requires measurements with two opposite MR gradient polarities, and very high SNR. Additionally, the impact of small geometrical distortions inherent to this methodology is investigated.

Knowledge of subject-specific low frequency EPs values would be important to guide dosimetry (machine output strength) of Transcranial Magnetic Stimulation treatments. By including subject-specific tissue EPs and structure (brain gyrification) in EM simulations, subject-specific estimations of the deployed electric field in the brain can be obtained. However, validated EM coil models and correct assessment of the incident TMS magnetic field are fundamental to correctly estimate the strength of the induced electric field in the brain, which is ultimately responsible for neuronal activation.

Therefore, in chapter 3, a new methodology is presented to quantitatively map the incident TMS magnetic field with an MR scanner in the region where brain stimulation commonly occurs. This is demonstrated by means of MRI measurements and EM simulations of the incident TMS magnetic field. These measurements will allow validation of TMS coil models used in simulations, guidance of TMS coil positioning and quality assessment of concurrent TMS-MRI studies.

In chapter 4, the feasibility of measuring with an MR scanner the induced magnetic field arising from TMS induced tissue eddy currents is then investigated. By using a TMS device instead of MR gradient systems (chapter 2), much stronger eddy currents can in principle be induced in tissues, resulting in stronger induced magnetic fields. Therefore, lower SNR would be required in the MR measurements. For this purpose, the TMS-MRI setup introduced in chapter 3 was adopted to inductively induce LF eddy currents in a phantom with similar EPs of the human brain CSF. In this chapter, the strength of the induced magnetic arising from the TMS induced eddy currents in tissues is characterized by means of EM simulations on phantoms and realistic human brain models, as well as the required phase accuracy needed to detect these induced magnetic fields in MRI measurements.

Chapters 5 and 6 focuses on high frequency (128 MHz) tissue EPs, as they are expected to differ from low frequency values. High frequency EPs are currently measured using Helmholtz-based MR-EPT approaches. However, experimental assumptions limit the accuracy of these approaches. Although the error introduced

by the MR-EPT assumptions on the reconstructed EPs values has been already investigated, the predicted error levels do not reflect the experimental observations.

Therefore, in chapter 5, another source of error affecting MR-EPT reconstructions is investigated, i.e. the numerical error arising from the computation of spatial derivatives on noisy B_1^+ data using FD kernels, which has been previously overlooked. A quantitative analysis of this numerical error is presented using first an analytical model of a 2D plane wave impinging on a dielectric half-space. Then, the impact of this error on conductivity reconstructions is evaluated by means of EM simulations and MR measurements on a phantom and an *in-vivo* human brain as a function of: kernel size, image resolution and SNR. Furthermore, it is investigated whether mitigation strategies such as Gibbs ringing correction and Gaussian apodization for noise reduction could increase the reconstruction accuracy.

In Chapter 6, *in-vivo* EPs reconstructions using MR-EPT and, alternatively, water content-EPs (wEPT) are presented and compared. The inter/intra-subject reconstruction accuracy and precision is assessed for both techniques. Furthermore, the validity of the adopted model in wEPT is investigated. Finally, the pro and cons of wEPT compared to standard MR-EPT are discussed.

1.5 References

1. Adey WR. Tissue interactions with non-ionizing electromagnetic fields. Physiol. Rev. 1981;61: 435–514.
2. Gabriel C, Gabriel S, Corthout E. The dielectric properties of biological tissues: I. Literature survey. Phys. Med. Biol. 1996;41:2231–2249. doi: 10.1088/0031-9155/41/11/001.
3. Gabriel S, Lau RW, Gabriel C. The dielectric properties of biological tissues: II. Measurements in the frequency range 10 Hz to 20 GHz. Phys. Med. Biol. 1996;41:2251–2269. doi: dx.doi.org/ 10.1088/0031-9155/41/11/002.
4. Gabriel S, Lau RW, Gabriel C. The dielectric properties of biological tissues: III. Parametric models for the dielectric spectrum of tissues. Phys. Med. Biol. 1996;41:2271–2293.
5. Pethig R. Dielectric Properties of Biological Materials: Biophysical and Medical Applications. IEEE Trans. Electr. Insul. 1984;EI-19:453–474. doi: 10.1109/TEI.1984.298769.
6. Foster KR, Schepps JL, Stoy RD, Schwan HP. Dielectric properties of brain tissue between 0.01 and 10 GHz. Phys. Med. Biol. 1979;24:1177–1187. doi: 10.1088/0031-9155/24/6/008.
7. Foster K. The Biomedical Engineering Handbook: Second Edition - Dielectric properties of tissues. 1999.
8. Gabriel C. Compilation of the dielectric properties of body tissues at RF and microwave frequencies. Phys. Dep. - Armstrong Lab. 1996.
9. Geddes LA, Baker LE. The specific resistance of biological material - A compendium of data for the biomedical engineer and physiologist. Med. Biol. Eng. 1967;5:271–293.
10. Miklavcic D, Pavselj N, Hart FX. Electric properties of tissues. Wiley Encycl. Biomed. Eng. 2006;209:1–12. doi: 10.1.1.65.7364.
11. Kuang W, Nelson S. Low-frequency Dielectric Properties of Biological Tissues: A Review with Some New Insights. Trans. ASAE 1998;41:173–184. doi: 10.13031/2013.17142.
12. Gabriel C, Peyman A, Grant EH. Electrical conductivity of tissue at frequencies below 1 MHz. Phys. Med. Biol. 2009;54:4863–4878. doi: 10.1088/0031-9155/54/16/002.
13. Halter RJ, Zhou T, Meaney PM, et al. The correlation of in vivo and ex vivo tissue dielectric properties to validate electromagnetic breast imaging: initial clinical experience. Physiol. Meas. 2009;30:121–123. doi: 10.1088/0967-3334/30/6/S08.The.
14. Barber DC, Brown BH. Applied potential tomography. J. Phys. E Sci. Instrum. 1984;17:723–733.
15. Metherall P, Barber DC, Smallwood RH, Brown BH. Three-dimensional electrical impedance tomography. Nature 1996;380:509–512. doi: 10.1038/380509a0.
16. Ider YZ, Onart S. Algebraic reconstruction for 3D magnetic resonance-electrical impedance tomography (MREIT) using one component of magnetic flux density. Physiol. Meas. 2004;25:281–294. doi: 10.1088/0967-3334/25/1/032.
17. Seo JK, Kwon O, Woo EJ. Magnetic resonance electrical impedance tomography (MREIT): conductivity and current density imaging. J. Phys. Conf. Ser. 2005;12:140–155. doi: 10.1088/1742-6596/12/1/014.
18. Muftuler LT, Hamamura MJ, Birgul O, Nalcioglu O. In vivo MRI electrical impedance tomography (MREIT) of tumors. Proc. 14th Sci. Meet. Int. Soc. Magn. Reson. Med. Seattle, Washington, USA 2006:332.
19. Gao N, Zhu S, He B. Estimation of electrical conductivity distribution within the human head from magnetic flux density measurement. Phys. Med. Biol. 2005;50:2675–2687. doi: 10.1088/0031-9155/50/11/016.

20. Woo EJ, Seo JK. Magnetic resonance electrical impedance tomography (MREIT) for high-resolution conductivity imaging. Physiol. Meas. 2008;29:R1–R26. doi: 10.1088/0967-3334/ 29/10/ R01.

21. Seo JK, Woo EJ. Magnetic Resonance Electrical Impedance Tomography (MREIT). Soc. Ind. Appl. Mat. 2011;53:40–68.

22. Arpinar VE, Hamamura MJ, Degirmenci E, Muftuler LT. MREIT experiments with 200 μA injected currents: a feasibility study using two reconstruction algorithms, SMM and harmonic B(Z). Phys. Med. Biol. 2012;57:4245–4261. doi: 10.1088/0031-9155/57/13/4245.

23. Bencsik M, Bowtell R, Bowley RM. Using the vector potential in evaluating the likelihood of peripheral nerve stimulation due to switched magnetic field gradients. Magn. Reson. Med. 2003;50:405–410. doi: 10.1002/mrm.10520.

24. Chronik BA, Ramachandran M. Simple anatomical measurements do not correlate significantly to individual peripheral nerve stimulation thresholds as measured in MRI gradient coils. J. Magn. Reson. Imaging 2003;17:716–721. doi: 10.1002/jmri.10300.

25. Weinberg IN, Stepanov PY, Fricke ST, et al. Increasing the oscillation frequency of strong magnetic fields above 101 kHz significantly raises peripheral nerve excitation thresholds. Med. Phys. 2012; 39:2578–2583.

26. van Lier ALHMW, van den Berg CAT, Katscher U. Measuring electrical conductivity at low frequency using the eddy currents induced by the imaging gradients. Proc. 20th Sci. Meet. Int. Soc. Magn. Reson. Med. Melbourne, Victoria, Aust. 2012:3467.

27. van Lier ALHMW, van den Berg CAT, Katscher U. MR Electrical Properties Tomography. Patent 2014:20140239951.

28. Ozparlak L, Ider YZ. Induced current magnetic resonance-electrical impedance tomography. Physiol. Meas. 2005;26:S289–S305. doi: 10.1088/0967-3334/26/2/027.

29. De Geeter N, Crevecoeur G, Dupré L, Van Hecke W, Leemans A. A DTI-based model for TMS using the independent impedance method with frequency-dependent tissue parameters. Phys. Med. Biol. 2012;57:2169–2188. doi: 10.1088/0031-9155/57/8/2169.

30. Ilmoniemi RJ, Kičić D. Methodology for combined TMS and EEG. Brain Topogr. 2010;22:233–248. doi: 10.1007/s10548-009-0123-4.

31. Wood AW, Karipidis K. Non-ionizing Radiation Protection: Summary of Research and Policy Options. Wiley; 2017.

32. Plonsey R, Barr RC. Bioelectricity: A Quantitative Approach. Springer Science & Business Media; 2007.

33. Nieminen JO, Koponen LM, Ilmoniemi RJ. Experimental characterization of the electric field distribution induced by TMS devices. Brain Stimul. 2015;8:582–589. doi: 10.1016/j.brs. 2015.01. 004.

34. Janssen AM, Oostendorp TF, Stegeman DF. The effect of local anatomy on the electric field induced by TMS: evaluation at 14 different target sites. Med. Biol. Eng. Comput. 2014;52: 873–883. doi: 10.1007/s11517-014-1190-6.

35. Opitz A, Windhoff M, Heidemann RM, Turner R, Thielscher A. How the brain tissue shapes the electric field induced by transcranial magnetic stimulation. Neuroimage 2011;58:849–859. doi: 10.1016/j.neuroimage.2011.06.069.

36. Thielscher A, Opitz A, Windhoff M. Impact of the gyral geometry on the electric field induced by TMS. Neuroimage 2011;54:234–243. doi: 10.1016/j.neuroimage.2010.07.061.

37. Haltiwanger S. The electrical properties of cancer cells. www.royalrife.com/ haltiwanger1

38. Surowiec AJ, Stuchly SS, Barr JR, Swarup A. Dielectric Properties of Breast Carcinoma and the Surrounding Tissues. IEEE Trans. Biomed. Eng. 1988;35:257–263. doi: 10.1109/10.1374.

39. Katscher U, Kim DH, Seo JK. Recent progress and future challenges in MR electric properties tomography. Comput. Math. Methods Med. 2013:ID 546562. doi: 10.1155/2013/546562.

40. Katscher U, van den Berg C a. T. Electric properties tomography: Biochemical, physical and technical background, evaluation and clinical applications. NMR Biomed. 2017:early view. doi: 10.1002/nbm.3729.

41. Yarnykh VL. Actual flip-angle imaging in the pulsed steady state: A method for rapid three-dimensional mapping of the transmitted radiofrequency field. Magn. Reson. Med. 2007;57:192–200. doi: 10.1002/mrm.21120.

42. Sacolick LI, Wiesinger F, Hancu I, Vogel MW. B1 mapping by Bloch-Siegert shift. Magn. Reson. Med. 2010;63:1315–1322. doi: 10.1002/mrm.22357.

43. Nehrke K, Bornert P. DREAM - A novel approach for robust, ultrafast, multislice B1 mapping. Magn. Reson. Med. 2012;68:1517–1526. doi: 10.1002/mrm.24158.

44. Schepps JL, Foster KR. The Uhf and microwave dielectric properties of normal and tumor tissues variation in dielectric properties with tissue water content. Phys. Med. Biol. 1980;25: 1149–1159.

45. Haacke EM, Petropoulos LS, Nilges EW, Wu DH. Extraction of conductivity and permittivity using magnetic resonance imaging. Phys. Med. Biol. 1991;38:723–734.

46. Wen H. Non-invasive quantitative mapping of conductivity and dielectric distributions using RF wave propagation effects in high-field MRI. Proc. SPIE 5030, Medical Imaging: Physics of Medical Imaging. International Society for Optics and Photonics; 2003. pp. 471–477. doi: 10.1117/12.480000.

47. Katscher U, Voigt T, Findeklee C, Vernickel P, Nehrke K, Dössel O. Determination of Electric Conductivity and Local SAR Via B1 Mapping. IEEE Trans. Med. Imaging 2009;28:1365–1374.

48. Voigt T, Katscher U, Doessel O. Quantitative conductivity and permittivity imaging of the human brain using electric properties tomography. Magn. Reson. Med. 2011;66:456–466. doi: 10.1002/ mrm.22832.

49. van Lier ALHMW, Brunner DO, Pruessmann KP, Klomp DWJ, Luijten PR, Lagendijk JJW, Van Den Berg CAT. B1+ phase mapping at 7 T and its application for in vivo electrical conductivity mapping. Magn. Reson. Med. 2012;67:552–561. doi: 10.1002/mrm.22995.

50. Liu J, Zhang X, Schmitter S, Van de Moortele P-F, He B. Gradient-based electrical properties tomography (gEPT): A robust method for mapping electrical properties of biological tissues in vivo using magnetic resonance imaging. Magn. Reson. Med. 2015;74:634–646. doi: 10.1002/mrm. 25434.

51. Gurler N, Ider YZ. Gradient-Based Electrical Conductivity Imaging Using MR Phase. Magn. Reson. Med. 2016;00:00–00. doi: 10.1002/mrm.26097.

52. Hafalir FS, Oran OF, Gurler N, Ider YZ. Convection-reaction equation based magnetic resonance electrical properties tomography (cr-MREPT). IEEE Trans. Med. Imaging 2014;33:777–793. doi: 10.1109/TMI.2013.2296715.

53. Seo JK, Kim M-O, Lee J, Choi N, Woo EJ, Kim HJ, Kwon OI, Kim DH. Error analysis of non-constant admittivity for MR-based electric property imaging. IEEE Trans. Med. Imaging 2012;31:430–437. doi: 10.1109/TMI.2011.2171000.

54. Duan S, Xu C, Deng G, Wang J, Liu F, Xin SX. Quantitative analysis of the reconstruction errors of the currently popular algorithm of magnetic resonance electrical property tomography at the interfaces of adjacent tissues. NMR Biomed. 2016:744–750. doi: 10.1002/nbm.3522.

55. Zhang X, De Moortele PF Van, Schmitter S, He B. Complex B1 mapping and electrical properties imaging of the human brain using a 16-channel transceiver coil at 7T. Magn. Reson. Med. 2013;69:1285–1296. doi: 10.1002/mrm.24358.

56. Savitzky A, Golay MJE. Smoothing and Differentiation of Data by Simplified Least Squares Procedures. Anal. Chem. 1964;36:1627–1639.

57. Steinier J, Termonia Y, Deltour J. Comments on Smoothing and Differentiation of Data by Simplified Least Square Procedure. Anal. Chem. 1972;44:1906–1909. doi: 10.1021/ac60319a045.

58. Lee S, Bulumulla S, Hancu I. Theoretical Investigation of Random Noise-Limited Signal-to-Noise Ratio in MR-Based Electrical Properties Tomography. IEEE Trans. Med. Imaging 2015;34:2220–2232.

59. Mandija S, Sbrizzi A, van Lier ALHMW, Luijten PR, van den Berg CAT. Artifacts affecting derivatives of B1 maps for EPT reconstructions. Proc. 24th Sci. Meet. Int. Soc. Magn. Reson. Med. Singapore 2016:2989.

60. Balidemaj E, Van Den Berg CAT, Trinks J, Van Lier ALHMW, Nederveen AJ, Stalpers LJ a, Crezee H, Remis RF. CSI-EPT: A Contrast Source Inversion Approach for Improved MRI-Based Electric Properties Tomography. IEEE Trans. Med. Imaging 2015; 34:1788–1796. doi: 10.1109/ TMI.2015.2404944.

61. Ropella KM, Noll DC. A regularized, model-based approach to phase-based conductivity mapping using MRI. Magn. Reson. Med. 2016;00:00:00. doi: 10.1002/mrm.26590.

62. Borsic A, Perreard I, Mahara A, Halter RJ. An inverse problems approach to MR-EPT image reconstruction. IEEE Trans. Med. Imaging 2016;35:244–256. doi: 10.1109/TMI.2015.2466082.

63. Serralles JE, Polimeridis A, Vaidya MV, Haemer G, White JK, Sodickson DK, Lattanzi R. Global Maxwell Tomography: A novel technique for electrical properties mapping without symmetry assumption or edge artifacts. Proc. 24th Sci. Meet. Int. Soc. Magn. Reson. Med. Singapore 2016:2993.

64. Michel E, Hernandez D, Lee SY. Electrical conductivity and permittivity maps of brain tissues derived from water content based on T 1 -weighted acquisition. Magn. Reson. Med. 2016; early view. doi: 10.1002/mrm.26193.

65. Schwan HP, Foster KR. Microwave dielectric properties of tissue. Some comments on the rotational mobility of tissue water. Biophys. J. 1977;17:193–197. doi: 10.1016/S0006-3495(77)85637-3.

66. Farace P, Pontalti R, Cristoforetti L, Antolini R, Scarpa M. An automated method for mapping human tissue permittivities by MRI in hyperthermia treatment planning. Phys. Med. Biol. 1997; 2159:2159–2174. doi: 10.1088/0031-9155/42/11/011.

67. Zhang X, Schmitter S, Moortele V de P, Liu J, He B. From Complex B1 Mapping to Local SAR Estimation for Human Brain MR Imaging Using Multi-Channel Transceiver Coil at 7T. IEEE Trans. Med. Imaging 2013;32:1058–1067. doi: 10.1109/TMI.2013.2251653.

68. Voigt T, Doessel O, Katscher U. Imaging conductivity and local SAR of the human brain. Proc. 17th Sci. Meet. Int. Soc. Magn. Reson. Med. Honolulu, Hawaii, USA 2009:4513.

69. Madelin G, Regatte RR. Biomedical Applications of Sodium MRI In-Vivo. J. Magn. Reson. Imaging 2013;38:511–529. doi: 10.1016/j.micinf.2011.07.011.

70. Nagy IZ, Lustyik G, Nagy VZ, Zarándi B, Freddari C. Intracellular Na+:K+ ratios in human cancer cells as revealed by energy dispersive x-ray microanalysis. Cell Biol. 1981;769–777.

71. Fraser SP, Diss JKJ, Chioni A-M, et al. Human Cancer Biology Voltage-Gated Sodium Channel Expression and Potentiation of Human Breast Cancer Metastasis. Am. Assoc. Cancer Res. 2005:5381–5389.

72. Schepkin VD, Lee KC, Kuszpit K, Muthuswami M, Timothy D, Chenevert TL, Rehemtulla A, Ross BD. Proton and sodium MRI assessment of emerging tumor chemotherapeutic resistance. NMR Biomed. 2006;19:1035–1042. doi: 10.1002/nbm.1074.

73. Camero IL, Smith NKR, Pool TB, Sparks RL. Intracellular Concentration of Sodium and Other Elements as Related to Mitogenesis and Oncogenesis in Vivo. Cancer Res. 1980;1493–1500.

74. Thulborn K, Lui E, Guntin J, Jamil S, Sun Z, Claiborne TC, Atkinson IC. Quantitative sodium MRI of the human brain at 9.4 T provides assessment of tissue sodium concentration and cell volume fraction during normal aging. NMR Biomed. 2015. doi: 10. 1002/nbm.3312.

75. Ouwerkerk R, Bleich KB, Gillen JS, Pomper MG, Bottomley PA. Tissue sodium concentration in human brain tumors as measured with 23Na MR imaging. Radiology 2003;227:529–537. doi: 10.1148/radiol.2272020483.

76. Schepkin VD, Chenevert TL, Kuszpit K, Lee KC, Meyer CR, Johnson TD, Rehemtulla A, Ross BD. Sodium and proton diffusion MRI as biomarkers for early therapeutic response in subcutaneous tumors. Magn. Reson. Imaging 2006;24:273–278.

77. Thulborn KR, Lu A, Atkinson IC, Damen F, Villano J. Quantitative Sodium MR Imaging and Sodium Bioscales for the Management of Brain Tumors. Neuroimaging Clin. N. Am. 2009;19:615–624. doi: 10.1016/j.micinf.2011.07.011.

78. Vitvitsky VM, Garg SK, Keep RF, Albin RL, Banerjee R. Na + and K + ion imbalances in Alzheimer's disease. Biochim. Biophys. Acta - Mol. Basis Dis. 2012;1822:1671–1681. doi: 10.1016/j.bbadis.2012.07.004.

79. van Lier ALHMW, Hoogduin JM, Polders DL, Boer VO, Hendrikse J, Robe PA, et al. Electrical conductivity imaging of brain tumours. Proc. 19th Annu. Meet. ISMRM. Montréal, Québec, Canada 2011;19:4464.

80. Shin J, Kim MJ, Lee J, Nam Y, Kim M, Choi N, Kim S, Kim D-H. Initial study on in-vivo conductivity mapping of breast cancer using MRI. J. Magn. Reson. Imaging 2014:371–378. doi: 10.1002/jmri.24803.

81. Katscher U, Djamshidi K, Voigt T, Ivancevic M, Abe H, Newstead G, Keupp J. Estimation of breast tumor conductivity using parabolic phase fitting. Proc. 20th Sci. Meet. Int. Soc. Magn. Reson. Med. Melbourne, Victoria, Aust. 2012:2335.

82. Katscher U, Abe H, Ivancevic MK, Keupp J. Investigating breast tumor malignancy with electric conductivity measurements. Proc. 23nd Sci. Meet. Int. Soc. Magn. Reson. Med. Toronto, Canada 2015:3306.

83. Oh TI, Kim HB, Jeong WC, Sajib SZK, Kyung EJ, Kim HJ, Kwon OI, Woo EJ. Sub-millimeter resolution electrical conductivity images of brain tissues using magnetic resonance-based electrical impedance tomography. Appl. Phys. Lett. 2015;107. doi: 10.1063/1.4926920.

Chapter 2

A geometrical shift results in erroneous appearance of low frequency tissue eddy current induced phase maps

Magnetic Resonance in Medicine 2016;76(3):905-12.
doi: 10.1002/mrm.25981.

Stefano Mandija

Astrid L.H.M.W. van Lier

Petar I. Petrov

Sebastian F.W. Neggers

Ulrich Katscher

Peter R. Luijten

Cornelis A.T. van den Berg

Abstract

Knowledge on low frequency (LF) tissue conductivity is relevant for various biomedical purposes. To obtain this information, LF phase maps arising from time-varying imaging gradients have been demonstrated to create a LF conductivity contrast. Essential in this methodology is the subtraction of phase images acquired with opposite gradient polarities to separate LF and RF phase effects. Here we demonstrate how sensitive these subtractions are with respect to geometrical distortions. The effect of geometrical distortions on LF phase maps is mathematically defined. After quantifying typical geometrical distortions, their effects on LF phase maps are evaluated using conductive phantoms. For validation, electromagnetic simulations of LF phase maps were performed. Even sub-voxel distortions of 10% of the voxel size, measured for a typical LF MR sequence, cause leakage of RF phase into LF phase of several milli-radians, leading to a misleading pattern of LF phase maps. This leakage is mathematically confirmed, while simulations indicate that the expected LF phase should be in order of micro-radians. The conductivity scaling of LF phase maps is attributable to the RF phase leakage, thus dependent on the RF conductivity. In fact, simulations show that the LF phase is not measurable.

2.1 Introduction

Although MRI is an electro-magnetic (EM) imaging modality, image contrast is predominantly based on differences in magnetic conditions on a microscopic or macroscopic scale. MR-Electrical Properties Tomography (EPT) falls in this sense in a completely new category (1). With EPT it is possible to reconstruct electrical properties contrast images at Larmor frequency (2–12), useful for clinical diagnosis (13,14) and radiofrequency (RF) patient safety (15–18). Instead, at low frequencies (LF, 100 Hz – 1 kHz), where other methods like transcranial magnetic stimulations (TMS) and electrocorticography operate (19–25), knowledge on the relation between electrical conduction and tissue composition is limited. Sparse data show that in this frequency range the human body is electrically very heterogeneous (26–28), hence a better knowledge is important.

MR-Electrical Impedance Tomography (MR-EIT) (29–35) is an MR-based method that allows LF tissue conductivity mapping by combining MR-Current Density Imaging (36–39) and Electrical Impedance Tomography (40–42). However, the reduction of the injected current down to a non-painful level, while maintaining sufficient spatial resolution and signal to noise ratio (SNR), remains a problem.

To avoid direct current injection resulting in pain sensation, a new technique was recently introduced (43–45). This technique uses the MR scanner to measure the accumulated phase induced by LF eddy currents in samples ($\Phi_{LF}(\mathbf{r})$), as in MR-EIT. However, on the contrary to MR-EIT, in this technique currents are inductively generated by the ramp up and down of magnetic gradients, therefore external electrodes are not required anymore. Several studies claimed that Φ_{LF} is measurable with standard MR scanners and correlate with the LF samples conductivity (45–49). However, those experimental findings are in sharp contrast to EM simulations, which indicate that Φ_{LF} should have a very small range (order of μrads), thus hardly measurable (50,51). All experimental studies employing this technique are based on the subtraction of phase images acquired with opposite gradient polarities to separate phase contributions arising from RF transmit fields (Φ_{RF}) and eddy current gradient related fields. Since MR images are prone to geometrical distortions, great care has to be taken when phase images are spatially combined.

In this work we show how crucial correct geometrical registrations between phase images are to correctly reconstruct Φ_{LF} maps by comparing measurements and EM simulations. We also show that even minor sub-voxel mis-registrations lead to imperfect separation of the RF phase, used in EPT, and LF phase. In this case, Φ_{RF}, related to RF conductivity, appears in Φ_{LF} images completely overwhelming their pattern (51). We hypothesize that this effect can be the explanation behind the reported scaling between LF conductivity and LF phase maps reported in various studies.

2.2 Theory

The measured accumulated phases for positive (Φ^{+}_{acc}) and negative (Φ^{-}_{acc}) readout gradient polarities, including only the relevant contributions for this study, can be defined as:

$$\Phi^{+}_{acc}(\mathbf{r}) = \Phi_{RF}(\mathbf{r}) + \Phi_{LF\_TOTAL}(\mathbf{r}) \quad [2.1]$$

$$\Phi^{-}_{acc}(\mathbf{r}) = \Phi_{RF}(\mathbf{r}) - \Phi_{LF\_TOTAL}(\mathbf{r}) \quad [2.2]$$

where Φ_{LF_TOTAL} ($\Phi_{LF\_TOTAL}(\mathbf{r}) = \gamma \int_0^{TE} (\Delta B_{eddy\_phantom}(\mathbf{r},t) + \Delta B_{eddy\_system}(\mathbf{r},t))\, dt$ with **r**: x, y, and z, γ: gyromagnetic ratio, and TE: echo time) includes the phase contribution of both LF-system induced eddy currents (Φ_{eddy_system}) and LF-phantom induced eddy currents (Φ_{LF}, equal to zero if the sample has zero conductivity). From these equations, Φ_{RF} and Φ_{LF} maps can be reconstructed (6,45,49).

For a cylindrical phantom in a birdcage coil in quadrature transmit and reverse quadrature receive mode the RF phase (representing the B_1^+ phase according to the transceive phase assumption) is (1,6):

$$\Phi_{RF}(\mathbf{r}) = \frac{\Phi^{+}_{acc}(\mathbf{r}) + \Phi^{-}_{acc}(\mathbf{r})}{2}. \quad [2.3]$$

For a homogeneous sample, parabolic functions can be adopted to fit along the three spatial directions the transmit phase ($\Phi^{+}(\mathbf{r}) = \Phi_{RF}(\mathbf{r})/2$) (52). Applying the same formulation as in EPT (4,6), but performing analytical differentiation of $\Phi^{+}(\mathbf{r})$, the RF-conductivity is reconstructed:

$$\sigma_{RF} \approx \frac{\nabla^2 \cdot \Phi^{+}_{x,y,z}}{\mu_0 \omega} \quad [2.4]$$

where μ_0 is the free-space magnetic permeability, and ω the Larmor frequency.

The exclusive contribution of phantom eddy current can be calculated using:

$$\Phi_{LF}(\mathbf{r}) = \Phi_{LF\_TOTAL}(\mathbf{r}) - \Phi_{eddy\_system}(\mathbf{r}) \quad [2.5.1]$$

$$= \left(\frac{\Phi^{+}_{acc}(\mathbf{r}) - \Phi^{-}_{acc}(\mathbf{r})}{2}\right)_{\sigma \neq 0} - \left(\frac{\Phi^{+}_{acc}(\mathbf{r}) - \Phi^{-}_{acc}(\mathbf{r})}{2}\right)_{\sigma = 0}. \quad [2.5.2]$$

In eq. [2.5.2], the subtractions in parentheses cancel the contribution of Φ_{RF}, while the second term in parentheses, related to an additional measurement with a non-conductive phantom of the same geometry, compensates for Φ_{eddy_system}. In all measurements, i.e. with different readout directions and phantom conductivities, it is vital that phases of identical physical locations are combined, otherwise, the separation of Φ_{RF} and Φ_{LF} through eqs. [2.3] and [2.5.2] will be imperfect. While a carefully designed setup can guarantee identical positioning of different phantoms, geometrical shifts in the readout direction arising from imaging imperfections are more difficult to avoid. For our application, we consider only the readout direction

"x" where geometrical distortions ($\Delta x(\mathbf{r})$) might occur. By ignoring the phase contribution due to system eddy currents in the LF-accumulated phase formulation, since it can be compensated as shown in eq. [2.5.2], the acquired phase maps in the presence of a geometrical distortion Δx in the same direction of the readout can be modelled as:

$$\Phi^{+}_{acc}(x-\Delta x,y,z) = \Phi_{RF}(x-\Delta x,y,z) + \Phi_{LF}(x-\Delta x,y,z) \quad [2.6.1]$$

$$= \Phi_{RF}(\mathbf{r}) - \Delta x\frac{\partial\Phi_{RF}(\mathbf{r})}{\partial x} + 0(\Delta x^2) + \Phi_{LF}(\mathbf{r}) - \Delta x\frac{\partial\Phi_{LF}(\mathbf{r})}{\partial x} + 0(\Delta x^2) \quad [2.6.2]$$

where a first order Taylor expansion was applied in eq. [2.6.2], and where signs change for $\Phi^{-}_{acc}(x+\Delta x,y,z)$, except for the RF phase. Substituting eq. [2.6.2] in eq. [2.5.2] we can observe that $\Delta x(\partial\Phi_{RF}(\mathbf{r})/\partial x)$ leads to a leakage term of Φ_{RF} (Φ_{RF_leak}) into Φ_{LF} if geometrical corrections are not performed.

In our case, for a homogeneous cylindrical phantom Φ_{RF} can be approximated with a parabolic function ($\Phi_{RF}(x,y=0,z=0)\approx a_x x^2+b_x x+c_x$) (52). Substituting this function into eq. [2.6] yields:

$$\Phi^{SHIFT}_{RF}(\mathbf{r}) \approx \Phi_{RF}(\mathbf{r}) + 0(\Delta x^2) \quad [2.7]$$

$$\Phi^{SHIFT}_{LF}(\mathbf{r}) \approx \Phi_{LF}(\mathbf{r}) - \Delta x\frac{\partial\Phi_{LF}(\mathbf{r})}{\partial x} + 0(\Delta x^2) - \Delta x(2a_x x + b_x)\,. \quad [2.8]$$

We observe that in the case of a geometrical shift Δx, the reconstructed Φ^{SHIFT}_{LF} is contaminated by a term related to Φ_{LF}, and two terms, that originate from the RF phase $\left(\Delta x(2a_x x - b_x)\right)$, defined as the RF phase leakage (Φ_{RF_leak}) that occurs due to a geometrical distortion. In case of a constant geometrical shift, Φ_{RF_leak} has a linear spatial dependence that scales with the shift amplitude and the RF conductivity.

2.3 Methods

2.3.1 Phantoms

For measurements, the ACR phantom (53), typically used to assess image quality, was used to evaluate geometrical distortions that can occur for typical sequences performed to measure LF phase. For this purpose, we used the regular grid placed at the center of the phantom. In addition, three cylindrical agar phantoms were built (diameter = 9.6 cm, length = 20 cm): one non-conductive to compensate for Φ_{eddy_system}, and two conductive (0.8 S/m and 1.6 S/m, 4.5 gr/L and 9.2 gr/L of NaCl respectively, at 23°C and 128 MHz, Agar 2%) (54). These values were confirmed by dielectric probe measurements (85070E, Agilent Technologies, Santa Clara, CA, USA). Due to the sturdy gel nature of the phantoms and a dedicated holder, flow induced by mechanical vibrations and spatial misalignments between measurements performed with different phantoms could be ignored.

For EM simulations, two cylinders were created using GMSH (55), a 3D finite element generator, with the same geometry and properties of the agar phantoms (49).

2.3.2 Simulations

To characterize the range of Φ_{LF}, EM simulations were performed for the two conductive agar phantoms, and for two different incident linear readout gradient strength along the x-direction ($\mathbf{G}_{inc}$), as in the measurements. The incident readout slew rate $\frac{\partial \mathbf{A}_{inc}}{\partial t}$ (57), computed from the vector potential defined on each node of the 3D mesh (49,58–62), was used as input in the EM simulations. By assuming a quasi-static approximation (63,64), the electric field ($\mathbf{E}_{ind}$) induced during the ramp up of $\mathbf{G}_{inc}$ was calculated using:

$$\mathbf{E}_{ind} = -\frac{\partial \mathbf{A}_{inc}}{\partial t} - \nabla V \qquad [2.9]$$

where the scalar potential (V) was derived by minimizing the dissipated power over the conductive volume (57,65).

Once $\mathbf{E}_{ind}$ was computed, the induced phantom eddy current density $\mathbf{J}_{ind}$ was calculated using Ohm's law, and its induced magnetic field $\mathbf{B}_{ind}$ was estimated applying Biot-Savart's law. Finally, Φ_{LF} (accumulated during the ramp up time of the readout gradient: T_{ramp}) could be computed using the z-component of $\mathbf{B}_{ind}$, the only component affecting MR phase images (66):

$$\phi_{LF\_simulated}(\mathbf{r}) = \gamma \int_{T_{ramp}} B_{ind,z}(\mathbf{r}) dt \,. \qquad [2.10]$$

2.3.3 MRI Measurements

In the first experiment, the scaling of the RF-conductivity and the impact of geometrical distortions on Φ_{RF} and Φ_{RF_leak} maps was investigated. Using the agar phantoms, a spin echo sequence was performed on a 3T MR scanner (Achieva, Philips Healthcare, Best, The Netherlands, TR/TE = 1000/4.5 ms, isotropic voxel 2.5 mm, px/BW = 0.42/1029 px/Hz, G_x = 9.67 mT/m, slew rate = 62.4 T/m/s) with a transmit/receive birdcage head coil operated in quadrature and reverse quadrature mode for transmit and receive, respectively. From Φ^{+}_{acc} and Φ^{-}_{acc} maps, Φ_{RF} maps were first reconstructed using equation [2.3]. Then, to investigate the impact of different geometrical distortions, Φ_{RF} maps were reconstructed after applying different sub-voxel shifts (50%, 25%, and 10% of the voxel size) in the readout direction on Φ^{+}_{acc} and Φ^{-}_{acc} maps, and conductivity maps were therefore reconstructed.

Finally, Φ_{RF_leak} maps were computed to evaluate their impact on Φ_{LF} maps. Thanks to the homogeneous agar phantoms properties, we could perform spatial interpolation to increase the resolution without introducing artificial sub-voxel structures.

In the second experiment, we acquired a B_0 map to quantify geometrical distortions that occur while performing typical LF-EPT measurements. Then, we used the regular grid in the center of the ACR phantom to measure geometrical shifts that can arise from system-eddy currents induced by the switching of dedicated gradients (G_d = 30mT/m) placed symmetrically around the 180° pulse on the readout axis, as employed in similar MR-sequences (47,48). For this purpose, we executed the same sequence three times for each readout direction: one without G_d as a reference, and two with G_d but opposite polarities to induce opposite effects: TR/TE = 1000/18 ms, isotropic voxel 2.5 mm, px/BW = 4/106 px/Hz.

After quantifying geometrical distortions for typical LF-phase measurements, we used Φ^{+}_{acc} and Φ^{-}_{acc} maps, acquired in experiment 1, to evaluate their impact on Φ_{LF} maps.

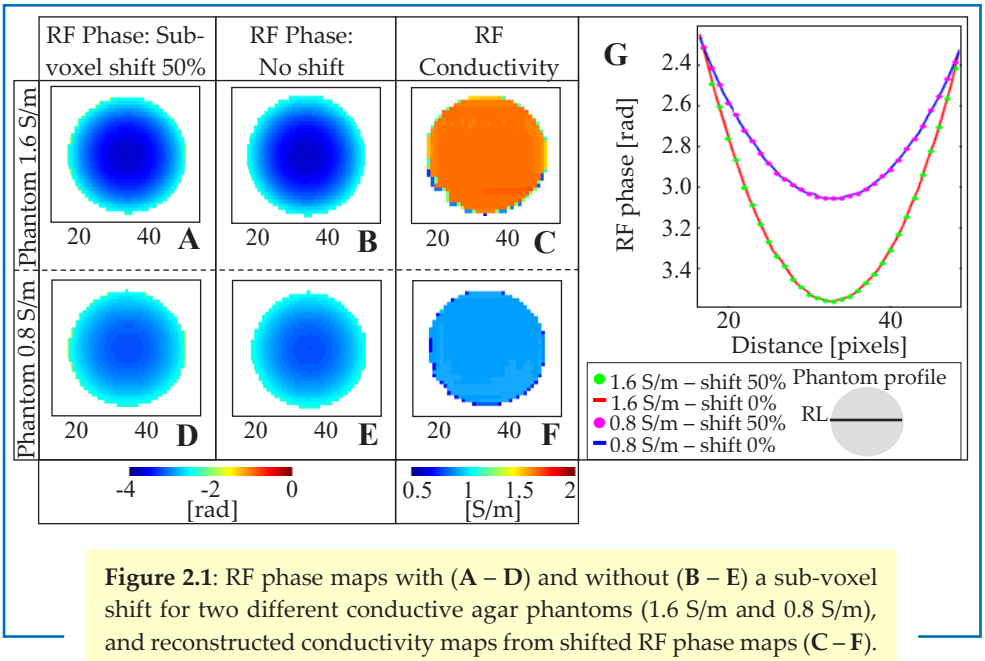

Figure 2.1: RF phase maps with (**A** – **D**) and without (**B** – **E**) a sub-voxel shift for two different conductive agar phantoms (1.6 S/m and 0.8 S/m), and reconstructed conductivity maps from shifted RF phase maps (**C** – **F**). Comparisons between the RF phase profiles (**G**) show the same parabolic shapes scaled with the conductivity of the phantoms.

In the third experiment, the scaling between conductivity and Φ_{LF} maps was investigated. We compared the Φ_{LF} maps reconstructed using eq. [2.5.2] with and without sub-voxel shifts, therefore mimicking geometrical distortions that can arise for the specific px/BW used in experiment 1, with the previously computed Φ_{RF_leak} maps. To distinguish conductivity related patterns from noise dominated patterns, the noise level in the phase images was also calculated (56).

In the fourth experiment, using the phantom with conductivity 1.6 S/m, we investigated the effect of different $\mathbf{G}_{inc}$ on Φ_{LF} maps, anticipating that increasing slew rates would induce increasing phantom eddy current strengths and therefore different Φ_{LF}, as it follows from Faraday's induction law ($\nabla \times \mathbf{E} = -\partial \mathbf{B}/\partial t$). The increase in the slew rate was achieved by keeping the rising time constant T_{ramp} = 0.155 ms while changing the gradient strength ($\mathbf{G}_{inc}$ = 29.18 mT/m and 8.78 mT/m respectively).

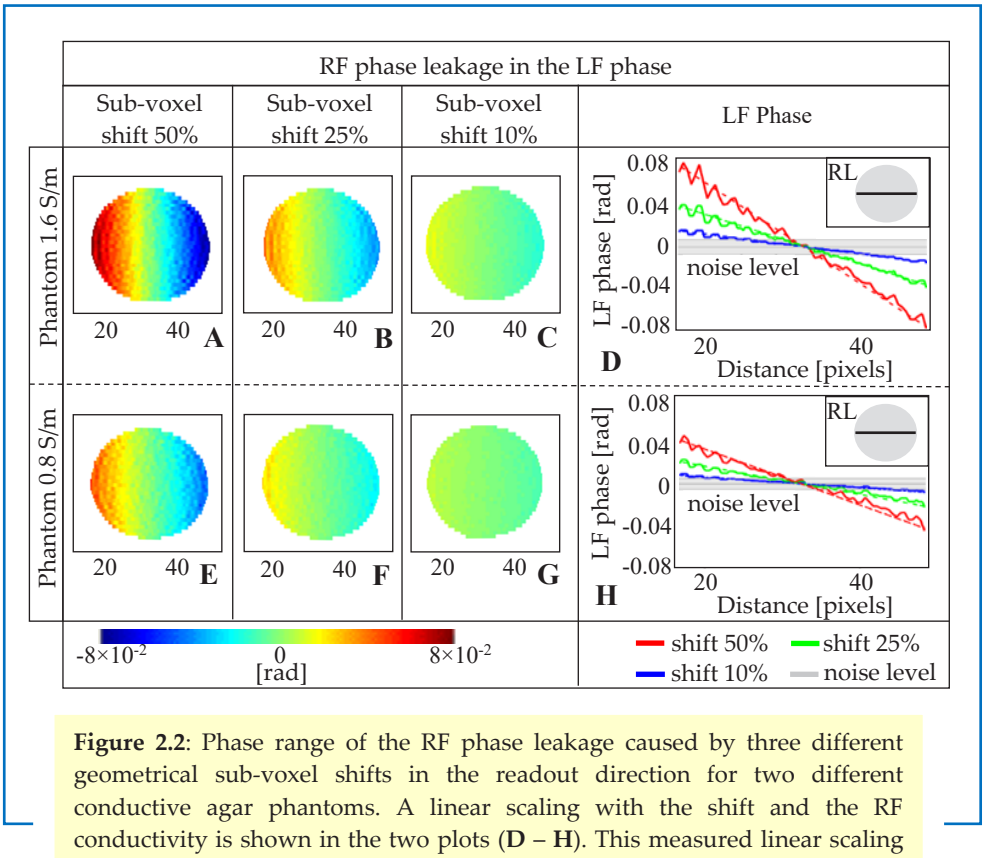

Figure 2.2: Phase range of the RF phase leakage caused by three different geometrical sub-voxel shifts in the readout direction for two different conductive agar phantoms. A linear scaling with the shift and the RF conductivity is shown in the two plots (**D** – **H**). This measured linear scaling (solid lines) coincides with the scaling described in eq. [2.8] (corresponding to RF phase added for different sub-voxel shifts, dotted lines).

2.4 Results

Fig. 2.1 shows that for two different conductive phantoms Φ_{RF} maps are not affected by small sub-voxel shifts. In fact, Φ_{RF} maps correctly scale with the RF-conductivity (Fig. 2.1, G), and conductivity maps reconstructed from RF-phase maps affected by small geometrical distortions reflect theoretical values (Fig. 2.1 C, and F). This demonstrates that EPT is robust for small geometrical distortions.

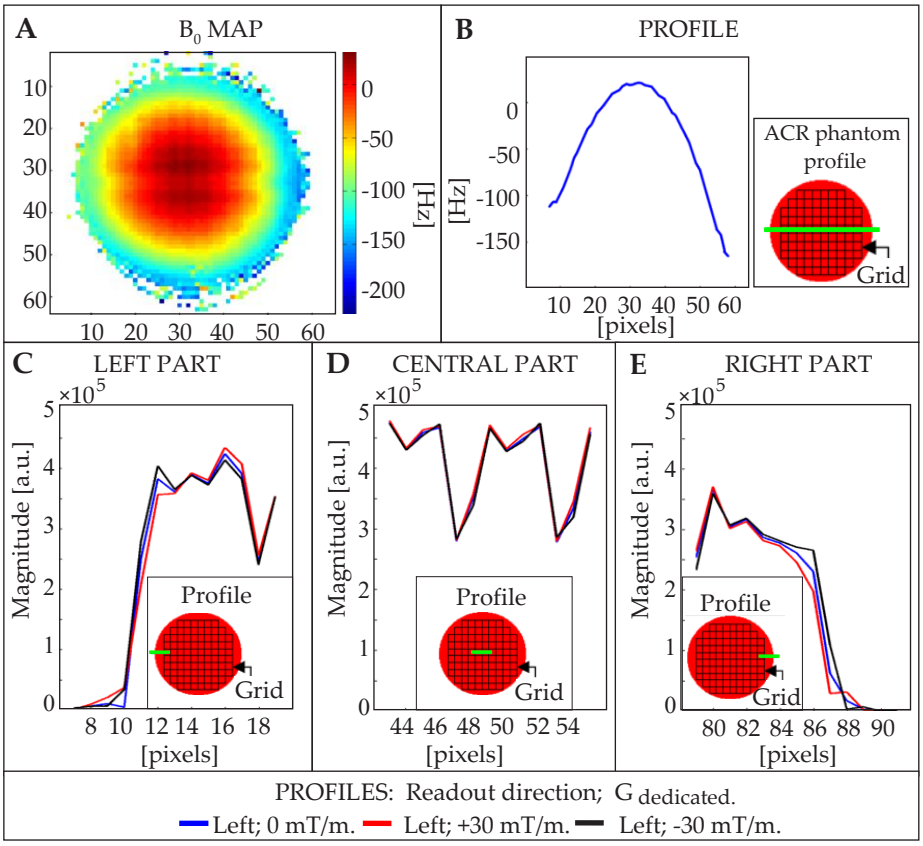

Figure 2.3: B_0 map used to evaluate geometrical distortions induced by B_0 inhomogeneities (**A** – **B**). Additional shift in the readout caused by eddy currents induced by additional dedicated gradients (G_d = 30 mT/m; slew rate = 193.5 T/m/s) placed symmetrically prior and after the 180° RF pulse; for visual purposes only the profiles obtained from images acquired with negative readout polarity (readout direction: left) are shown, (**C**, **D**, and **E**).

Starting from these Φ_{RF} maps, the impact of Φ_{RF_leak} computed using different sub-voxel shifts in the readout direction on Φ_{LF} is shown in Fig. 2.2. As expected from eq. [2.8], Φ_{RF_leak} maps show an increasing linear pattern for increasing shifts, since for a homogeneous phantom the parabolic RF phase leads to a linear RF phase leakage into the LF phase. As shown in the plots D and H, this pattern linearly scales with the shift strength (Δx) and the RF-conductivity parameter (a_x).

To quantify geometrical distortions for typical LF-EPT measurements, the ACR phantom was used. In Fig. 2.3, A and B, a B_0 map and a profile on the readout direction are reported, showing an offset of almost 200 Hz at the periphery of the phantom. In addition, if dedicated gradients are used (Fig. 2.3, C, D, and E), an additional shift of approximately half pixel is observed, especially at the periphery of the phantom (left-right parts) where typically the effects of system eddy currents are the strongest.

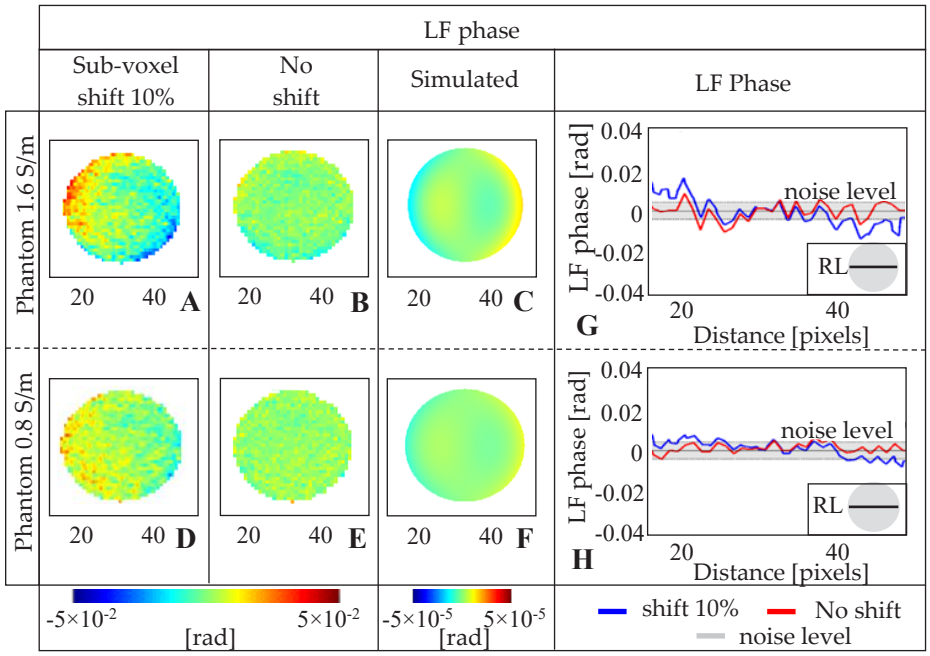

Figure 2.4: LF phase maps with shift (**A** – **D**), without shift (**B** – **E**), and simulated (**C** – **F**) for two different conductive phantoms. Comparisons between the LF phase profiles (**G** and **H**) show scaling with the RF conductivity due to the predominant impact of the RF phase leakage on the LF phase, especially at the edges of the phantoms on the readout direction. LF phase profiles without geometrical distortions are below noise level. This is confirmed by simulations where the phase range is four orders of magnitude lower.

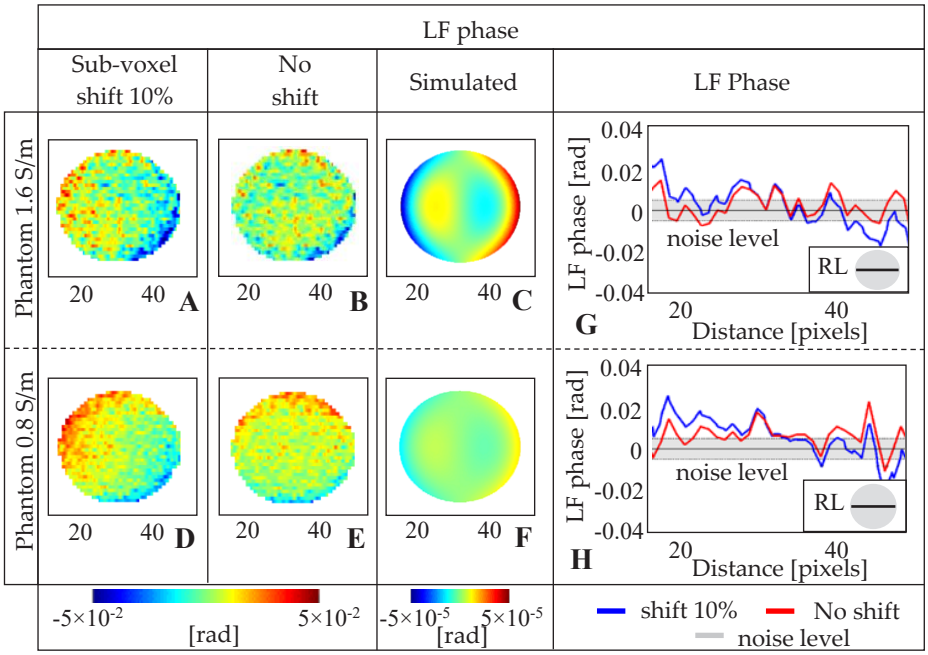

Figure 2.5: LF phase maps with shift (**A** – **D**), without shift (**B** – **E**), and simulated (**C** – **F**) for two different conductive phantoms. Comparisons between the LF phase profiles (**G** and **H**) show scaling with the RF conductivity due to the predominant impact of the RF phase leakage on the LF phase, especially at the edges of the phantoms on the readout direction. LF phase profiles without geometrical distortions are below noise level. This is confirmed by simulations where the phase range is four orders of magnitude lower.

For visual purposes, only the profiles obtained from images acquired with negative readout polarity are shown, while the same effect was also observed for the positive readout polarity. These presented sub-voxel shifts, occurring along the readout direction, may be considered as a pitfall of this technique since they are difficult to characterize and correct.

In the light of these results, in Fig. 2.4 Φ_{LF} maps computed with and without a geometrical distortion of 10% of the voxel size are shown, therefore mimicking the shift caused by an offset of 200 Hz as observed in the previous experiment. A linear scaling with the conductivity is visible in the Φ_{LF} maps computed from phase maps shifted by 10% of the voxel size (Fig. 2.4 A, D, G, and H). However, our simulations indicate that Φ_{LF} should be four orders of magnitude lower than the measured one (Fig. 2.4 C, and F). In fact, if phase images are not affected by geometrical shifts, Φ_{LF} maps are dominated by noise (Fig. 2.4 B, E, G and H).

Since the linear scaling with the conductivity in the shifted Φ_{LF} maps matches the scaling predicted in eq. [2.8] and reported in Fig. 2.2, it can be concluded that the Φ_{RF_leak} caused by geometrical distortions ($\Delta x(\mathbf{r})$) overwhelms the LF phase pattern. Therefore, the observed conductivity scaling depends on RF conductivity.

The predominant contribution of Φ_{RF_leak} in shifted Φ_{LF} maps is confirmed in Fig. 2.5. From Faraday's induction law, Φ_{LF} maps, proportional to the conductivity and the electric field in the phantoms, linearly scale with $\mathbf{G}_{inc}$, as shown in simulations (Fig. 2.5 C, and F). Instead, from measurements, it is clear that, without any geometrical distortions, the pattern of Φ_{LF} is obscured by noise (Fig. 2.5 B, and E), while Φ_{LF} maps computed from phase images affected by geometrical shifts (Fig. 2.5 A, and D) show the same pattern caused by the same Φ_{RF_leak} contribution.

2.5 Discussion

Various groups have proposed to infer electrical conductivity information by inducing LF-eddy currents using the ramp up/down of MR-gradients (43,49). In all these studies subtractions of phase images acquired with opposite readout polarities are performed to decouple the RF phase from the gradient eddy current related phase. In this work we show that these subtractions have to be done carefully, since they are sensitive to geometrical distortions.

As demonstrated using the ACR phantom, a spatial dependent shift e.g. caused by B_0 inhomogeneities (67), and MR-system eddy currents (68) can affect image acquisition. Here we demonstrate that non-corrected geometrical shifts lead to Φ_{RF} leakage into Φ_{LF}. Even sub-voxel shifts in the readout direction of 10% of the voxel size can cause a Φ_{RF_leak} in the order of milli-radians, still four order of magnitude higher than the Φ_{LF} expected from simulations.

Although geometrical distortions are known to be spatially dependent, for this application a constant shift equal to the maximum measured distortions at the phantom edges was a good approximation since at the center of the phantoms, where distortions were smaller, the measured LF-phase was already below the noise level. These findings suggest that it is the Φ_{RF} leakage, that for a homogeneous phantom scales with the RF conductivity and the shift strength, that dominates Φ_{LF} maps resulting in an erroneous appearance of Φ_{LF} proportional to LF conductivity. Instead, in absence of geometrical distortions, the pattern of Φ_{LF} is obscured by noise since Φ_{LF}, as shown in simulations, is too small to be measured. This also explains the measured absence of scaling with different readout gradient strength, as instead it would have been expected from simulations, since the RF phase, from which Φ_{RF_leak} derives, does not depend on the incident gradient slew rate.

To increase the span of Φ_{LF} due to eddy currents in samples, stronger current induction is needed. This may be achieved by moving the sample far away from the gradients isocenter resulting in higher dB/dt levels, while paying attention to stronger eddy current related shifts that, as shown here, must be corrected. However, it is questionable if technical and/or physiological limits will allow gradient strengths sufficient for correct detection of Φ_{LF}.

Instead, as shown in this work, reconstruction of RF tissue conductivity using EPT is hardly influenced by small geometrical distortions. This RF phase leakage can be seen as a finite difference of RF phase taken during acquisition along the readout direction. Therefore, in light of this observation, a potential exploitation of this artifact may be a reduction of the large differentiation kernels used in MR-EPT to reconstruct RF-conductivity by acquiring two phase images with opposite readout directions and an intentionally set frequency-offset. As demonstrated, the subtractions will result in a finite difference approximation of the first order derivative of Φ_{RF} along the readout. A second order derivative is also possible by including an additional phase image without frequency-offset.

2.6 Conclusions

Combinations of phase maps obtained with different gradient polarities should be done carefully since MR images are prone to geometrical shifts leading to RF phase falsely attributed to LF phase. The scaling of the non-corrected Φ_{LF} maps with the conductivity is not caused by different strength of LF induced tissue eddy currents, but is shown to be attributable to the leakage of Φ_{RF}, thus dependent on the RF conductivity. Our results indicate that even a sub-voxel shift can cause significant Φ_{RF} leakage that completely obscures Φ_{LF}, while its impact on the RF phase is much smaller. Therefore, reconstructions of the RF conductivity through EPT are hardly affected.

2.7 References

1. Katscher U, Voigt T, Findeklee C, Vernickel P, Nehrke K, Doessel O. Determination of electrical conductivity and local SAR via B_1 mapping. IEEE Trans. Med. Imaging 2009; 28: 1365–1374.
2. Wen H. Noninvasive quantitative mapping of conductivity and dielectric distributions using RF wave propagation effects in high-field MRI. Proc. SPIE 5030, Medical Imaging: Physics of Medical Imaging. International Society for Optics and Photonics; 2003. pp. 471–477. doi: 10.1117/12.480000.
3. Bulumulla S, Yeo TB, Zhu Y. Direct calculation of tissue electrical parameters from B1 maps. Proc. 17th Sci. Meet. Int. Soc. Magn. Reson. Med. Honolulu, Hawaii, USA 2009; Honolulu:3043.
4. Voigt T, Katscher U, Doessel O. Quantitative conductivity and permittivity imaging of the human brain using electric properties tomography. Magn. Reson. Med. 2011;66:456–466. doi: 10.1002/mrm.22832.
5. Sodickson DK, Alon L, Deniz CM, et al. Local Maxwell Tomography using transmit-receive coil arrays for contact-free mapping of tissue electrical properties and determination of absolute RF phase. Proc. 20th Sci. Meet. Int. Soc. Magn. Reson. Med. Melbourne, Victoria, Aust. 2012;20:387.
6. Van Lier ALHMW, Brunner DO, Pruessmann KP, Klomp DWJ, Luijten PR, Lagendijk JJW, Van Den Berg CAT. B1+ phase mapping at 7 T and its application for in vivo electrical conductivity mapping. Magn. Reson. Med. 2012;67:552–561. doi: 10.1002/mrm.22995.
7. Seo JK, Kim M-O, Lee J, Choi N, Woo EJ, Kim HJ, Kwon OI, Kim D-H. Error analysis of nonconstant admittivity for MR-based electric property imaging. IEEE Trans. Med. Imaging 2012;31:430–437. doi: 10.1109/TMI.2011.2171000.
8. Hafalir FS, Oran OF, Gurler N, Ider YZ. Magnetic resonance electrical properties tomography (MREPT) based on the solution of the convenction-reaction equation. Proc. 21st Sci. Meet. Int. Soc. Magn. Reson. Med. Salt Lake City, Utah, USA 2013:4187.
9. Katscher U, Kim DH, Seo JK. Recent progress and future challenges in MR electric properties tomography. Comput. Math. Methods Med. 2013:ID 546562. doi: 10.1155/2013/546562.
10. Van Lier ALHMW, Raaijmakers A, Voigt T, Lagendijk JJW, Katscher U, Van Den Berg CAT. Electric properties tomography in the human brain at 1.5, 3, and 7 T: a comparison study. Magn. Reson. Med. 2014;71:354–363. doi: 10.1002/mrm.24637.
11. Oran OF, Gurler N, Ider YZ. A simple point-wise formula for double excitation MREPT suitable for reconstructing boundaries. Proc. 22nd Sci. Meet. Int. Soc. Magn. Reson. Med. Milano, Italy 2014;22:3250.
12. Balidemaj E, Trinks J, Remis RF, Crezee H, van Lier ALHMW, Nederveen AJ, van den Berg CAT. Experimental electric field and dielectric tissue property mapping using a regularized CSI-EPT reconstruction method. Proc. 22nd Sci. Meet. Int. Soc. Magn. Reson. Med. Milano, Italy 2014;22:3252.
13. Shin J, Kim MJ, Lee J, Nam Y, Kim M, Choi N, Kim S, Kim D-H. Initial study on in-vivo conductivity mapping of breast cancer using MRI. J. Magn. Reson. Imaging 2014. doi: 10.1002/jmri.24803.
14. Tha KK, Stehning C, Suzuki Y, Katscher U, Keupp J, Kazumata K, Terasaka S, Cauteren M Van, Kudo K, Hiroki S. Noninvasive Evaluation of Electrical Conductivity of the Normal

Brain and Brain Tumors. Proc. 22nd Sci. Meet. Int. Soc. Magn. Reson. Med. Milano, Italy 2014;3:1885.

15. Voigt T, Doessel O, Katscher U. Imaging conductivity and local SAR of the human brain. Proc. 17th Sci. Meet. Int. Soc. Magn. Reson. Med. Honolulu, Hawaii, USA 2009:4513.

16. Balidemaj E, Trinks J, Van Den Berg CAT, Nederveen AJ, van Lier ALHMW, Stalpers LJ, Crezee J, Remis RF. CSI-EPT: A novel contrast source approach to MRI based electric properties tomography and patient-specific SAR. In: International Conference on Electromagnetics in Advanced Applications (ICEAA). IEEE; 2013. pp. 668–671. doi: 10.110 9/ICEAA.2013.6632328.

17. Buchenau S, Haas M, Splitthoff DN, Hennig J, Zaitsev M. Iterative separation of transmit and receive phase contributions and B_1^+ based estimation of the specific absorption rate for transmit arrays. Magn. Reson. Mater. Physics, Biol. Med. 2013;26:463–476. doi: 10.1007 /s10334-013-0367-6.

18. Zhang X, Schmitter S, Moortele V de P, Liu J, He B. From Complex B1 Mapping to Local SAR Estimation for Human Brain MR Imaging Using Multi-Channel Transceiver Coil at 7T. IEEE Trans. Med. Imaging 2013;32:1058–1067. doi: 10.1109/TMI.2013.2251653.

19. Hallett M. Transcranial magnetic stimulation and the human brain. Nature 2000;406:147–150. doi: 10.1038/35018000.

20. Thielscher A, Kammer T. Linking physics with physiology in TMS: a sphere field model to determine the cortical stimulation site in TMS. Neuroimage 2002;17:1117–1130. doi: 10.1006/nimg.2002.1282.

21. Miranda PC, Hallett M, Basser PJ. The Electric Field Induced in the Brain by Magnetic Stimulation : A 3-D Finite-Element Analysis of the Effect of Tissue Heterogeneity and Anisotropy. IEEE Trans. Biomed. Eng. 2003;50:1074–1085.

22. Ridding MC, Rothwell JC. Is there a future for therapeutic use of transcranial magnetic stimulation? Nat. Rev. Neurosci. 2007;8:559–67. doi: 10.1038/nrn2169.

23. Pell GS, Roth Y, Zangen A. Modulation of cortical excitability induced by repetitive transcranial magnetic stimulation: Influence of timing and geometrical parameters and underlying mechanisms. Prog. Neurobiol. 2011;93:59–98. doi: 10.1016/j.pneurobio.2010.10. 003.

24. Harvey BM, Vansteensel MJ, Ferrier CH, et al. NeuroImage Frequency specific spatial interactions in human electrocorticography: V1 alpha oscillations reflect surround suppression. Neuroimage 2013;65:424–432.

25. Mandija S, Petrov P, Neggers B, de Weijer A, Luijten PR, Van Den Berg CAT. MR guidance of TMS for a patient specific treatment plan: MR-based TMS field measurements and electromagnetic simulations. Proc. 23nd Sci. Meet. Int. Soc. Magn. Reson. Med. Toronto, Canada 2015:931.

26. Pethig R. Dielectric Properties of Biological Materials: Biophysical and Medical Applications. IEEE Trans. Electr. Insul. 1984;EI-19:453–474. doi: 10.1109/TEI.1984.298769.

27. Gabriel S, Lau RW, Gabriel C. The dielectric properties of biological tissues: II. Measurements in the frequency range 10 Hz to 20 GHz. Phys. Med. Biol. 1996;41:2251–2269.

28. Gabriel C, Peyman A, Grant EH. Electrical conductivity of tissue at frequencies below 1 MHz. Phys. Med. Biol. 2009;54:4863–4878. doi: 10.1088/0031-9155/54/16/002.

29. Oh SH, Lee B Il, Woo EJ, Lee SY, Cho MH, Kwon O, Seo JK. Conductivity and current density image reconstruction using harmonic B_z algorithm in magnetic resonance electrical impedance tomography. Phys. Med. Biol. 2003;48:3101–3116.

30. Seo JK, Yoon JR, Woo EJ, Kwon O. Reconstruction of conductivity and current density images using only one component of magnetic field measurements. IEEE Trans. Biomed. Eng. 2003;50:1121–1124. doi: 10.1109/TBME.2003.816080.

31. Oh SH, Lee BI, Lee SY, Woo EJ, Cho MH, Kwon O, Seo JK. Magnetic resonance electrical impedance tomography at 3 tesla field strength. Magn. Reson. Med. 2004;51:1292–1296.

32. Ider YZ, Onart S. Algebraic reconstruction for 3D magnetic resonance-electrical impedance tomography (MREIT) using one component of magnetic flux density. Physiol. Meas. 2004;25:281–294. doi: 10.1088/0967-3334/25/1/032.

33. Muftuler LT, Hamamura MJ, Birgul O, Nalcioglu O. *In-vivo* MRI electrical impedance tomography (MREIT) of tumors. Proc. 14th Sci. Meet. Int. Soc. Magn. Reson. Med. Seattle, Washington, USA 2006:332.

34. Zhang X, Yan D, Zhu S, He B. Non-invasive Imaging of Head-Brain Conductivity Profiles Using Magnetic Resonance Electrical Impedance Imaging. IEEE Eng. Med. Biol. Mag. 2008;27:78–83. doi: 10.1109/MEMB.2008.923953.

35. Woo EJ, Seo JK. Magnetic resonance electrical impedance tomography (MREIT) for high-resolution conductivity imaging. Physiol. Meas. 2008;29:R1–R26. doi: 10.1088/0967-3334/29/10/R01.

36. Barber DC, Brown BH. Applied potential tomography. J. Phys. E Sci. Instrum. 1984;17:723–733.

37. Joy MLG, Scott GC, Henkelman RM. In-vivo detection of applied electric currents by magnetic resonance imaging. Magn. Reson. Imaging 1989;7:89–94.

38. Scott GC, Joy MLG, Armstrong RL, Henkelman RM. Measurement of non uniform current density by magnetic resonance. IEEE Trans. Med. Imaging 1991;10:362–374.

39. Scott GC, Joy MLG, Armstrong RL, Henkelman RM. Sensitivity of magnetic-resonance current-density imaging. J. Magn. Reson. 1992;97:235–254. doi: 10.1016/0022-2364(92)90310-4.

40. Webster JG. Electrical Impedance Tomography. Adam Hilger, Bristol, UK 1990.

41. Metherall P, Barber DC, Smallwood RH, Brown BH. Three-dimensional electrical impedance tomography. Nature 1996;380:509–512. doi: 10.1038/380509a0.

42. Boone K, Barber D, Brown B. Imaging with electricity: Report of the European Concerted Action on Impedance Tomography. J. Med. Eng. Technol. 1997;21:201–232.

43. Ozparlak L, Ider YZ. Induced current magnetic resonance-electrical impedance tomography. Physiol. Meas. 2005;26:S289–S305. doi: 10.1088/0967-3334/26/2/027.

44. De Geeter N, Crevecoeur G, Dupré L. Low-parametric induced current - Magnetic Resonance Electrical Impedance Tomography for quantitative conductivity estimation of brain tissues using a priori information: A simulation study. Eng. Med. Biol. Soc. (EMBC), 2010 Annu. Int. Conf. IEEE 2010:5669–5672. doi: 10.1109/IEMBS.2010.5627896.

45. Van Lier ALHMW, van den Berg CAT, Katscher U. Measuring electrical conductivity at low frequency using the eddy currents induced by the imaging gradients. Proc. 20th Sci. Meet. Int. Soc. Magn. Reson. Med. Melbourne, Victoria, Aust. 2012:3467.

46. Oran OF, Hafalir FS, Gurler N, Ider YZ. Convection-Reaction Equation Based Low-Frequency Conductivity Imaging Using Readout Gradient Induced Eddy Currents. Proc. 21st Sci. Meet. Int. Soc. Magn. Reson. Med. Salt Lake City, Utah, USA 2013:4188.

47. Su J, Zheng B, Li SFY, Huang SY. The effects of a time-varying gradient fields on phase maps - theory and experiments. 3rd Int. Work. MRI Phase Contrast Quant. Susceptibility Mapping, Duke Univ. Durham, NC, USA 2014.

48. Liu C, Li W, Argyridis I. Imaging electric conductivity and conductivity anisotropy via eddy currents induced by pulsed field gradients. Proc. 22nd Sci. Meet. Int. Soc. Magn. Reson. Med. Milano, Italy 2014:638.

49. Mandija S, van Lier ALHMW, Thielscher A, Antunes A, Neggers B, Luijten PR, Van Den Berg CAT. Characterizing electrical interactions of tissues with time varying gradient fields: Simulations and measurements. Proc. 22nd Sci. Meet. Int. Soc. Magn. Reson. Med. Milano, Italy 2014:639.

50. Gibbs E, Liu C. Simulating Conductivity Mapping by Gradient Induced Eddy-Currents. 3rd Int. Work. MRI Phase Contrast Quant. Susceptibility Mapping, Duke Univ. Durham, NC, USA 2014.

51. Mandija S, van Lier ALHMW, Petrov P, Neggers B, Luijten PR, Van Den Berg CAT. Geometrical shift results in erroneous appearance of low frequency tissue eddy current induced phase maps: Theory, simulations and measurements. Proc. 23nd Sci. Meet. Int. Soc. Magn. Reson. Med. Toronto, Canada 2015:3289.

52. Katscher U, Djamshidi K, Voigt T, Ivancevic M, Abe H, Newstead G, Keupp J. Estimation of breast tumor conductivity using parabolic phase fitting. Proc. 19th Sci. Meet. Int. Soc. Magn. Reson. Med. Montréal, Québec, Canada 2011:2335.

53. Large Phantom Test Guidance for the ACR MRI Accreditation Program. Am. Coll. Radiol. 2005:6780.

54. Stogryn A. Equations for Calculating the Dielectric constant of saline water. IEEE Trans. Microw. Theory Tech. 1971;19:733–736.

55. Geuzaine C, Remacle JF. Gmsh: a three-dimensional finite element mesh generator with built-in pre- and post-processing facilities. Int. J. Numer. Methods Eng. 2009;79:1309–1331.

56. Haacke EM, Brown RW, Thompson MR, Venkatesan R. Magnetic Resonance Imaging - Physycal Principles and Sequence Design.; 1999 p. 340.

57. Thielscher A, Opitz A, Windhoff M. Impact of the gyral geometry on the electric field induced by transcranial magnetic stimulation. Neuroimage 2011;54:234–243. doi: 10.1016/j.neuroimage.2010.07.061.

58. Cheng DK. Field and Wave Electromagnetics. 2nd ed. Addison Wesley; 1989.

59. Bernstein MA, Zhou XJ, Polzin JA, King KF, Ganin A, Pelc NJ, Glover GH. Concomitant gradient terms in phase contrast MR: Analysis and correction. Magn. Reson. Med. 1998; 39:300–308.

60. Bowtell R, Bowley RM. Analytic calculations of the E-fields induced by time-varying magnetic fields generated by cylindrical gradient coils. Magn. Reson. Med. 2000;44:782–790.

61. Bencsik M, Bowtell R, Bowley RM. Using the vector potential in evaluating the likelihood of peripheral nerve stimulation due to switched magnetic field gradients. Magn. Reson. Med. 2003;50:405–410. doi: 10.1002/mrm.10520.

62. Bencsik M, Bowtell R, Bowley RM. Electric fields induced in the human body by time-varying magnetic field gradients in MRI: numerical calculations and correlation analysis. Phys. Med. Biol. 2007;52:2337–2353. doi: 10.1088/0031-9155/52/9/001.

63. Heller L, van Hulsteyn DB. Brain stimulation using electromagnetic sources: theoretical aspects. Biophys. J. 1992;63:129–138. doi: 10.1016/S0006-3495(92)81587-4.

64. Wagner TA, Zahn M, Grodzinsky AJ, Pascual-Leone A. Three-dimensional head model simulation of transcranial magnetic stimulation. IEEE Trans. Biomed. Eng. 2004;51:1586–1598. doi: 10.1109/TBME.2004.827925.

65. Wang W, Eisenberg SR. A three-dimensional finite element method for computing magnetically induced currents in tissues. IEEE Trans. Magn. 1994;30:5015–5023.

66. Bernstein MA, King KF, Zhou XJ. Handbook of MRI – Pulse Sequence. Elsevier; 2004.

67. Chang H, Fitzpatrick JM. A technique for accurate magnetic resonance imaging in the presence of field inhomogeneities. IEEE Trans. Med. Imaging 1992;11:319–329. doi: 10.1109/42.158935.

68. Le Bihan D, Poupon C, Amadon A, Lethimonnier F. Artifacts and pitfalls in diffusion MRI. J. Magn. Reson. Imaging 2006;24:478–488. doi: 10.1002/jmri.20683.

Chapter 3

MR-based measurements and simulations of the magnetic field created by a realistic TMS coil and stimulator

NMR in Biomedicine 2016;29(11):1590-1600.
doi: 10.1002/nbm.3618.

Stefano Mandija

Petar I. Petrov

Sebastian F.W. Neggers

Peter R. Luijten

Cornelis A.T. van den Berg

Abstract

Transcranial Magnetic Stimulation (TMS) is an emerging technique that allows non-invasive neurostimulation. However, correct validation of electromagnetic models of typical TMS coils and correct assessment of the incident TMS field (B_{TMS}) produced by standard TMS stimulators is still lacking. Such a validation can be performed by mapping B_{TMS} produced by a realistic TMS setup. In this study, we show that MRI can provide precise quantification of the magnetic field produced by a realistic TMS coil and a clinically used TMS stimulator in the region where neurostimulation occurs. Measurements of the phase accumulation created by TMS pulses applied during a tailored MR sequence were performed in a phantom. Dedicated hardware was developed to synchronize a typical, clinically used, TMS setup with a 3T-MR scanner. For comparison purposes, electromagnetic simulations of B_{TMS} were performed. MR-based measurements allow mapping and quantification of B_{TMS} starting from 2.5 cm from the TMS coil. For closer regions, the intra-voxel dephasing induced by B_{TMS} prohibits TMS field measurements. For 1% TMS output the maximum measured value was ~0.1 mT. Simulations reflect quantitatively experimental data. These measurements can be used to validate electromagnetic models of TMS coils, guidance of TMS coil positioning, dosimetry and quality assessment of concurrent TMS-MRI studies without the need of crude methods such as motor threshold for stimulation dose determination.

3.1 Introduction

During the last decade, the interest in medicine and neuroscience to non-invasively stimulate the brain in order to diagnose and treat neurological disorders has grown rapidly. This is in response to the risk of permanent brain damage involved with currently employed invasive techniques such as Deep Brain Stimulation or Cortical Stimulation (1-4). In this context, non-invasive brain stimulation techniques have the theoretical appeal of being able to specifically and selectively manipulate brain functions by directly interfering with the intrinsic electrical activity of neurons (5,6). Currently, investigations based on non-invasive brain stimulation are often performed using Transcranial Magnetic Stimulation (TMS) (7,8).

Introduced in 1985, TMS uses Faraday's electromagnetic (EM) induction principle to elicit brain stimulation in focal brain regions (9,10). A strong current runs through a TMS coil creating a time-varying magnetic field that can be as strong as the static magnetic field of a clinical MR scanner (B_0), but lasts only for a very short period of time (~0.5 ms) (11-13). By penetrating the scalp and the skull, this incident magnetic field induces ionic electrical currents in the area beneath the TMS coil resulting in a focal neuronal activation (14). At present, this technique is largely used as a diagnostic and therapeutic tool in a multitude of conditions affecting the brain such as major depression (15,16), multiple sclerosis (17), stroke (18,19), and epilepsy (20).

However, the application of TMS is plagued by various practical problems: an accurate and consistent positioning of a TMS coil with respect to a predefined brain area (21-23), and a correct evaluation of the TMS dose (24-27). Even when a brain area is well targeted using fMRI neuronavigation systems, knowledge on how the incident TMS magnetic field and the induced electric field are deployed and where the maximal currents are evoked is still limited and not controlled in sufficient detail (12,13,27). Various groups are working on electromagnetic modeling techniques to predict the induced TMS electric field in the human brain based on segmented MRI scans (4,11,14,24,26). For these simulations, having validated electromagnetic models of typical TMS coils and correct assessment of the incident TMS magnetic field would be fundamental for correct neurostimulation predictions. Such a validation can be performed by mapping the incident TMS magnetic field.

Few groups have already shown that it is possible to map the magnetic field produced by idealized TMS coils with an MR scanner (28-30). In these studies, different simplifications were adopted to avoid problems related to the discharging of a real TMS stimulator in an MR scanner: DC batteries were used instead of real TMS stimulators (thus resulting in a different current waveform) and the adopted current values were lower than the ones achievable by setting the output strength of a real TMS stimulator to minimum (23,28,29,31).

Additionally, the adopted TMS coils were different from standard TMS coils, which have a complex geometry consisting of multiple stacked windings, resulting in different magnetic field patterns (28-30). Therefore, these studies represent a valuable proof of concept of the possibility to perform direct MR-based measurements of external magnetic field sources, but the proposed results cannot be directly translated to a realistic TMS-MRI experiment. This raised and left open the main question about the actual possibility to map the TMS field produced by a real TMS setup (stimulator and coil) using an MR scanner.

To correctly map the TMS magnetic field using a realistic TMS setup, different issues need to be addressed. Firstly, it is necessary to use a realistic TMS coil, since it can electromagnetically couple with the MR system (e.g. the cryostat) or with radiofrequency (RF) receive coils in a different way than simple loop coils, with relevant consequences for actual TMS dosimetry (32,33). Secondly, the use of a realistic stimulator, which gives different current strengths and waveforms than the one produced by simple DC batteries (13), is one of the key challenges. In fact, realistic stimulators generate much stronger and highly non-uniform magnetic field than simple DC batteries. Thirdly, it is crucial to precisely synchronize TMS pulses with the MR sequence to avoid imaging distortions. These distortions will occur if TMS pulses are delivered while MR gradients are active (34). Fourthly, precautions need to be taken to avoid image distortions related to current leakage into the TMS coil during recharging of the TMS capacitors (35).

Based on these proof of concept studies, in this study we demonstrate that MRI can quantitatively map the incident TMS magnetic field produced by a realistic TMS setup (stimulator and coil) in the region where brain stimulation commonly occurs (2.5 cm from the coating of the TMS coil) (23). To correctly perform experimental measurements, we apply proposed solutions to the aforementioned issues related to the discharging of a realistic TMS stimulator through a realistic TMS coil in an MR scanner. In addition, we propose a setup to control and correctly synchronise the discharge of a clinically used TMS stimulator while performing an MR experiment, and we present a tailored TMS-MR sequence for actual MR measurements. Finally, thanks to the use of a realistic TMS setup (stimulator and coil), we are able to present the effects of possible artefacts (intra-voxel dephasing) that can affect MR measurements of the TMS magnetic field. Therefore, we also provide guidelines to correctly perform these measurements. For validation purposes and to support our results, simulations are also performed and compared to all the measurements.

3.2 Methods

In this section, we first illustrate the new integrated TMS-MRI setup. Then, we describe the tailored MR sequence, the synchronization protocol adopted in the measurements, and the experiments performed. Finally, we describe the simulation pipeline used for comparison with experimental results.

3.2.1 TMS-MRI setup

The integrated TMS-MRI setup consisted of six different components (Fig. 3.1).

The control box (Fig. 3.1, B) was built in-house to synchronize the TMS stimulator and the MR scanner. It contained a programmable board (PSoC4 CY8CKIT-049, Cypress Semiconductor, San Jose, CA) which received the TTL (transistor-transistor-logic) pulses generated by the MR scanner as input, sending two different control signals (CS) as outputs: the first control signal (Fig. 3.1, CS1) was used to trigger the TMS pulse, while the second signal (Fig. 3.1, CS2) was used to control the relay inside the relay box. This synchronization required precision up to microseconds to detect the TTL pulses and to correctly apply the necessary time delay needed to safely discharge the TMS stimulator prior to the MR readout gradient. On the front side, a switcher button was placed to reset the programmable board prior to each experiment, and four different LEDs were included to visually evaluate the functioning of the board.

The safety box (Fig. 3.1, C), also built in-house, prevented the TMS stimulator from being triggered if the relay in the relay box was in an open position, as later discussed.

The TMS stimulator (Magstim Rapid2, Fig. 3.1, D), placed in the MR control room with all the other boxes, was connected to the TMS coil located in the MR scanner through a filter box. For this specific stimulator, the peak voltage and current of the deployed bipolar TMS pulse at 100% machine output were 5500 A and 1650 V, respectively.

The relay box (Fig. 3.1, E) was used to shield the MR room from the RF noise present in the control room by keeping the relay in an open position, therefore maintaining the Faraday's cage intact in case of no TMS stimulation. In addition, having the relay in an open position while TMS pulses were not discharged ensured that no leakage currents flowed into the TMS coil during recharging of the capacitors in the TMS stimulator (35). This relay was in a closed position only for a very short time interval, i.e. when a TMS pulse was discharged (Fig. 3.2).

The MR compatible TMS coil (Fig. 3.1, F) was a standard figure-8 coil (36), the most common type of coil for TMS applications.

For the purpose of magnetic field mapping, since the only difference between this coil and non-MR-compatible coils consists on the external case (made in ceramic instead of plastic) (36), measurements obtained with such a coil can be directly related to non-MR-compatible coils. The coil was attached to a coil holder that allowed flexible coil placement over a wide range of positions. This holder was also used to firmly fix the phantom and the MR elliptical surface coils. One known problem of discharging a TMS coil in a strong static magnetic field, such as the main magnetic field of an MR scanner, is the torque reaction caused by the Lorentz's forces acting on the coil's wings during stimulations (36,37). This effect might be relevant when angles smaller than 50° between the TMS coil and the B_0-field are adopted in combination with high TMS machine outputs, since the two TMS windings will couple differently with the static B_0-field (32,33,37). For this reason, we never exceeded such an inclination during experiments. In addition, twelve markers (small cylinders filled with water: length = 1.5 cm and diameter = 0.5 cm) were placed on the coil to make it visible in MR images, thus allowing correct 3D reconstruction of actual coil positioning with respect to the phantom in simulations.

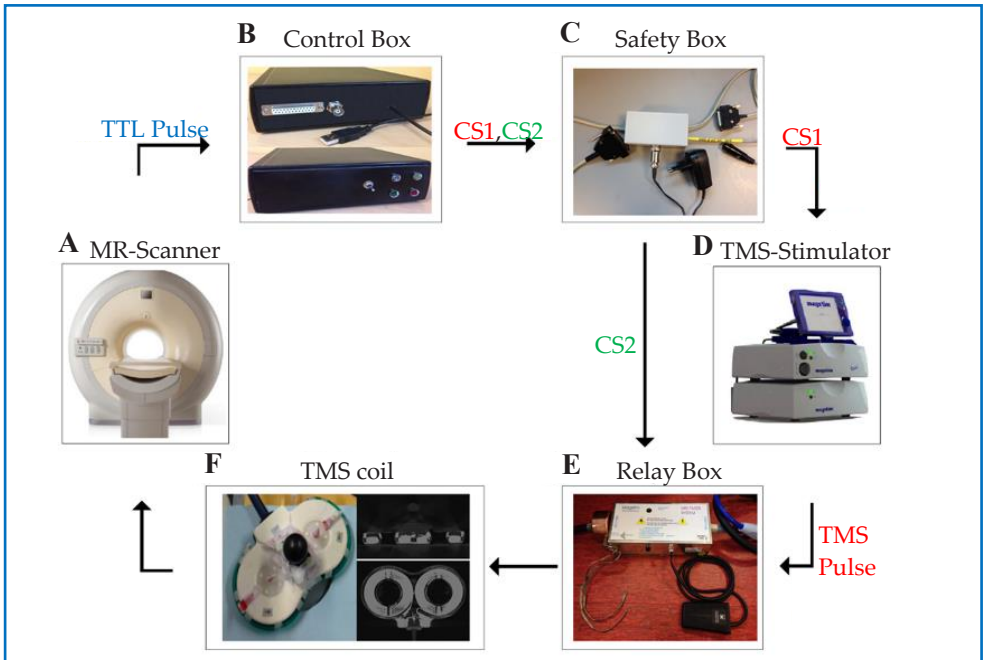

Figure 3.1: The integrated TMS-MRI setup: (**A**) 3T MR scanner (Achieva, Philips, Best, The Netherlands), (**B**) control box, (**C**) safety box, (**D**) TMS stimulator (Magstim Rapid2, Whitland, UK), (**E**) filter box (Magstim Rapid2, Whitland, UK), (**F**) MR compatible TMS coil (Magstim Rapid2, Whitland, UK), x-ray images obtained using a C-arm (BV29, Philips, Best, The Netherlands).

Finally, measurements were performed on a cylindrical agar phantom: diameter = 12.5 cm, length = 20 cm (mimicking the size of a medium human brain), Agar = 20 gr/L, NaCl = 9.2 gr/L, giving a conductivity value of 1.6 S/m (38) (confirmed by dielectric probe measurements: 85070E, Agilent Technologies, Santa Clara, CA), which reflects the conductivity of the cerebrospinal fluid (CSF) in the kHz range (39).

3.2.2 MRI Measurements

As shown in Fig. 3.2, the TMS stimulator was synchronized with the MR sequence in order to measure only the phase accumulation induced by the incident TMS magnetic field. During the 90° RF excitation pulse a TTL 5 V signal, sent by the MR scanner, was detected by the programmable board that controlled the opening and closing of the relay placed in the filter box and the delivery of TMS pulses. Oscilloscope measurements were performed (RTM2034, R&S, Munich, Germany) in order to calculate the exact TMS pulse duration and the exact time necessary for our specific relay to close and open. Based on these measurements, the echo time (TE) was chosen to be 20 milliseconds to safely apply the TMS pulse when MR gradient systems were not active. The relatively long TE could be considered as a disadvantage in terms of signal loss. However, a compromise with the characteristic of the relay was made. In fact, since the relay needed approximately 16 ms to close and 2 ms to open, and the TMS pulse lasted for about 0.5 ms, a TE of 20 ms was a reasonable and justified choice to safely discharge the TMS stimulator prior to the MR readout gradient.

All the performed measurements were obtained with a single echo Spin Echo sequence in a 3T MR scanner (Achieva, Philips Healthcare, Best, The Netherlands) with the body coil in transmit and two sized elliptical surface coils (flex-M and flex-L) for signal reception. To isolate the contribution of the TMS magnetic field, two sets of measurements were needed for each experiment: a first set with TMS pulses applied before each readout, and a second set without TMS pulses (reference set) (Fig. 3.3). The measured phase contribution ($\Phi_{acc}(\vec{r})$: $\Phi_{acc}^{TMS\neq0}(\vec{r})$, and $\Phi_{acc}^{TMS=0}(\vec{r})$, respectively) is:

$$\Phi_{acc}(\vec{r}) = \Phi_{RF}(\vec{r}) + \gamma \int_0^{TE} \Delta B_{0,eddy\_current}(\vec{r},t)dt + \gamma \int_{T_{TMS\_pulse}} \Delta B_{TMS,z}(\vec{r},t)dt \quad [3.1]$$

where $\Phi_{RF}(\vec{r})$ is the phase contribution related to the transmit RF pulse and RF receive phase, $\gamma \int_0^{TE} \Delta B_{0,eddy\_current}(\vec{r},t)dt$ is the contribution related to eddy currents, and $\gamma \int_{T_{TMS\_pulse}} \Delta B_{TMS,z}(\vec{r},t)dt$ is the contribution related to the longitudinal component of the TMS magnetic field induced by the TMS pulse applied before the readout gradient, with γ = gyromagnetic constant, and $\vec{r}$ = x, y, and z.

By subtracting these two sets after phase unwrapping, the z-component of the TMS magnetic field (the only one measurable during an MR experiment) can be reconstructed:

$$\Delta B_{TMS,z}(\vec{r}) = \frac{\Phi_{acc}^{TMS\neq 0}(\vec{r}) - \Phi_{acc}^{TMS=0}(\vec{r})}{\gamma \int_{T_{TMS\_pulse}} A(t)dt} \quad [3.2]$$

with A(t): the real TMS current waveform (A) derived from additional oscilloscope measurements and normalized at 1% machine output.

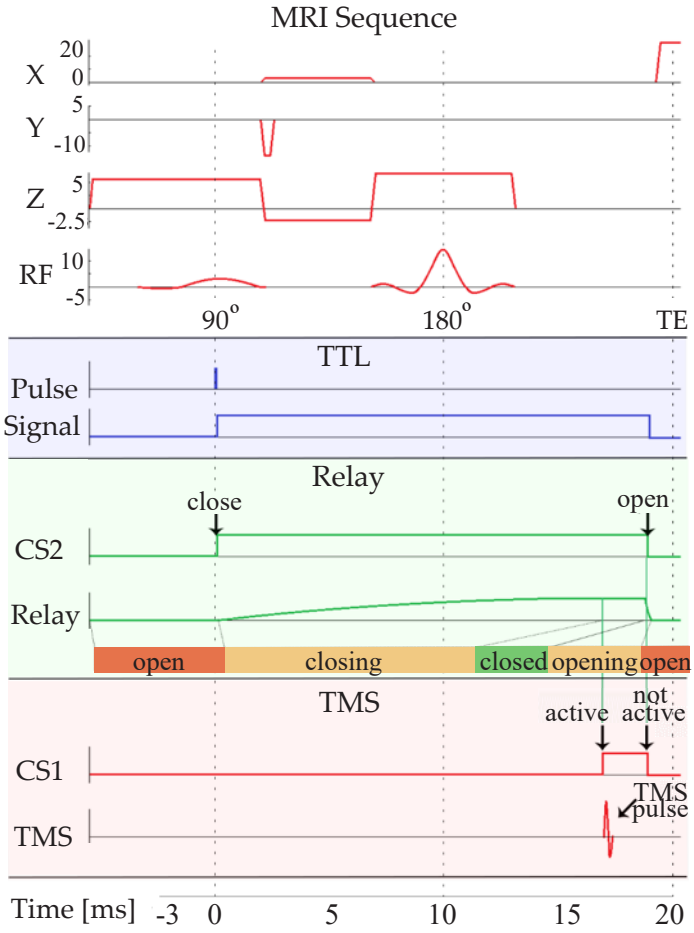

Figure 3.2: The TMS-MRI synchronized sequence. From top to bottom: frequency encoding, phase encoding and slice selection gradient sequences, RF pulse sequence, TTL pulse, TTL signal, relay control signal (CS2 in Fig. 3.1), relay time response (closing and opening), TMS control signal (CS1 in Fig. 3.1), TMS bipolar pulse.

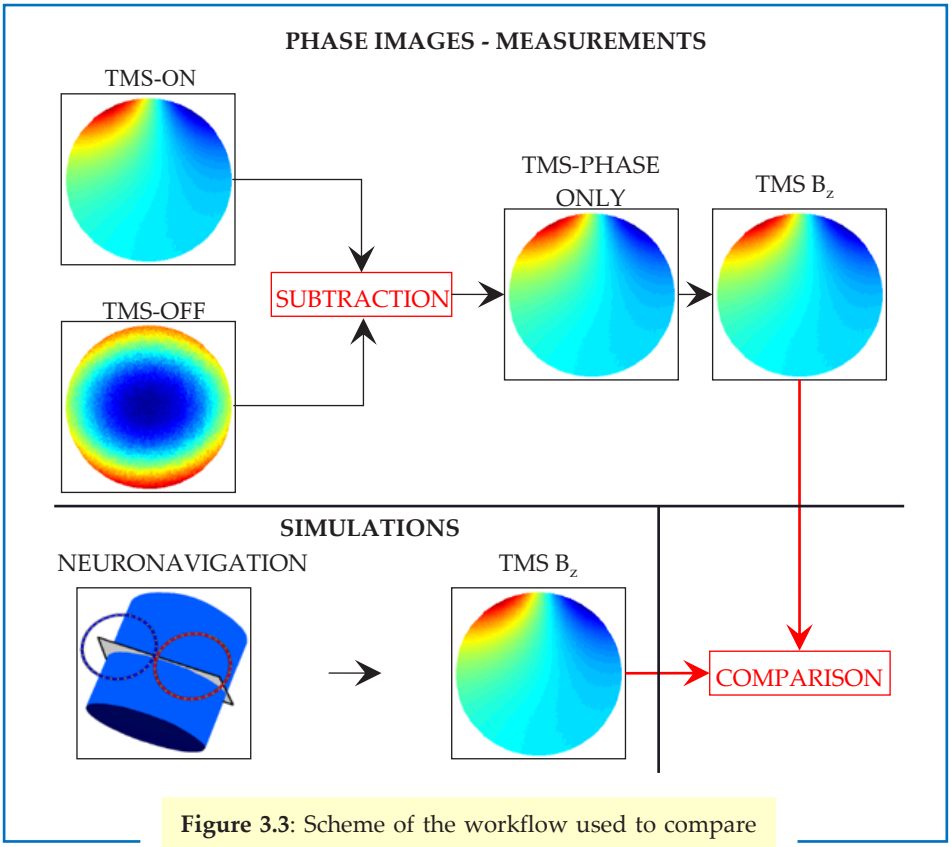

Figure 3.3: Scheme of the workflow used to compare measurements and simulations.

3.2.3 Experiments

EXPERIMENTS 1 – 2

To evaluate the effect of the signal loss induced by the intra-voxel dephasing produced by the additional TMS magnetic field applied prior to the readout gradient, two experiments were performed: for both experiments TR/TE = 1000/20 ms, field of view (FOV) = 160×160×2 mm^3, while the acquired resolution (RES) was 2.5×2.5×2 mm^3, and 1×1×2 mm^3, respectively. For these experiments, the TMS coil was placed horizontally and perpendicularly to the B_0 field, at a distance of 3 cm from the phantom, and the pulse was set to 1% machine output (Fig. 3.4, A).

EXPERIMENT 3

The minimum distance from the TMS coil that allows TMS field measurements without signal loss was characterized. We used the same setup and sequence of the second experiment. The TMS coil was placed at 2 cm from the phantom (Fig. 3.5, A).

EXPERIMENT 4

To evaluate whether the measured TMS induced phase accumulation reflects correctly the TMS machine output strength, three different TMS outputs were tested: 1%, 2%, and 4%. For this experiment, the coil was placed in the same position as the first two experiments. Oscilloscope measurements were also performed to independently test the linear scaling of the TMS field with the stimulator output, and the possible interactions between the TMS magnetic field and the static B_0 field that may affect TMS dosimetry. First, measurements of the voltage induced in a pickup coil placed in the scanner bore instead of the phantom were performed using an oscilloscope and setting the TMS output to 1%, 2%, and 4%, thus reflecting experimental conditions (Fig. 3.6, A). Additional measurements at 25%, 50%, and 75% TMS output were also performed (Fig. 3.6, B), therefore including the range of standard TMS administration outputs.

EXPERIMENTS 5 – 6

Finally, to evaluate the effect of different coil orientations on the measured TMS induced phase accumulation, two experiments were performed while setting the TMS stimulator outputs to 1% for consistency with previous measurements. In the fifth experiment, the plane of the TMS coil was placed horizontally at an angle of 55° with respect to the B_0-field and at a distance of 3 cm from the phantom (Fig. 3.8, E). In the sixth experiment, the TMS coil was placed vertically and perpendicularly to the B_0-field at a distance of 3 cm (Fig. 3.8, I). For each experiment, a T_2 weighted turbo spin echo map was additionally acquired using the body coil to map the TMS coil markers with respect to the phantom: TR / TE = 11760 / 80 ms, FOV = 240×240×210 mm^3, and RES = 1.5×1.5×3 mm^3. These maps were needed in simulations.

3.2.4 Simulations

For comparison purposes the relative position between the phantom and the TMS coil for each MR experiment. All the markers placed on the TMS coil were digitized in 3D with a special, simulations were performed for each experiment in SCIRun (40). Using the acquired T_2 maps and a neural-navigator system (Brain Science Tool BV, The Netherlands) it was possible to correctly replicate tracker, and marked in the T_2 scan (36). A point-based registration algorithm (22) computed the exact location of the TMS coil in the recorded image, and hence with respect to the phantom in the image. This was a crucial step since a non-correct positioning of the TMS coil with respect to the phantom would have resulted in an erroneous calculation of the TMS magnetic field, thus a non-correct comparison with MR experiments (Fig. 3.3).

The simulated coil consisted of two single loops reflecting shape and dimensions of the TMS coil used in the measurements (coil radius = 4.4 cm, distance between coil wings = 0.2 cm) (11-13). Once the TMS coil was correctly placed with respect to the phantom, the incident TMS magnetic field was computed by applying the discretized piece-wise Biot-Savart's law in the same region where measurements were performed. Additionally, simulations were compared to the analytical solution to ensure that the error introduced by the discretization of the TMS coil was negligible (lower than 1% at 1 cm from the center of each loop).

In an MR experiment, the phase accumulation created by the time-varying TMS magnetic field is proportional to the area underneath the TMS current waveform, eq. [3.2] (30). The same phase accumulation can be obtained using the time averaged value of the TMS current waveform (DC current). Therefore, by using independent oscilloscope measurements (Fig. 3.6, A), we were able to first approximate the realistic bipolar current running into the TMS coil with the corresponding DC current value. Then, by using these DC current values obtained from realistic TMS waveforms, it was possible to simulate the corresponding net TMS magnetic field proportional to the net phase accumulation measured in an MR experiment for the same TMS pulse strength and shape. For a machine output of 1%, 2%, and 4%, the DC current values were respectively 3.576, 4.98, and 8.51 A. By following this procedure, simulations were independent from MR measurements, thus allowing correct unbiased comparison.

Finally, to evaluate the difference between the measured and the simulated z-component of the incident TMS field, relative error maps (RE) were computed for each experiment:

$$\mathrm{RE}(\vec{r}) = 100 \times \frac{\Delta B_{TMS,z}^{measured}(\vec{r}) - \Delta B_{TMS,z}^{simulated}(\vec{r})}{\Delta B_{TMS,z}^{simulated}(\vec{r})}. \qquad [3.3]$$

3.3 Results

In the first two experiments we evaluate the impact of a TMS pulse of 1% machine output applied before the readout gradient of a Spin Echo sequence (Fig. 3.4, A). Initial results show a considerable signal loss in the region closest to the phantom (Fig. 3.4, B and C), due to intra-voxel dephasing induced by the strong gradients in the incident TMS magnetic field. This intra-voxel dephasing consists of a phase range per voxel bigger than 2π, thus resulting in a non-measurable signal (Fig. 3.4, B). To reduce this effect, a phase map with a smaller voxel size was acquired, and the reconstructed map of the z-component of the TMS magnetic field was computed (Fig. 3.4, D and E). For these maps, no distortions or signal loss are observed, thus demonstrating that direct measurements of the TMS magnetic field are possible on a clinical MR scanner.

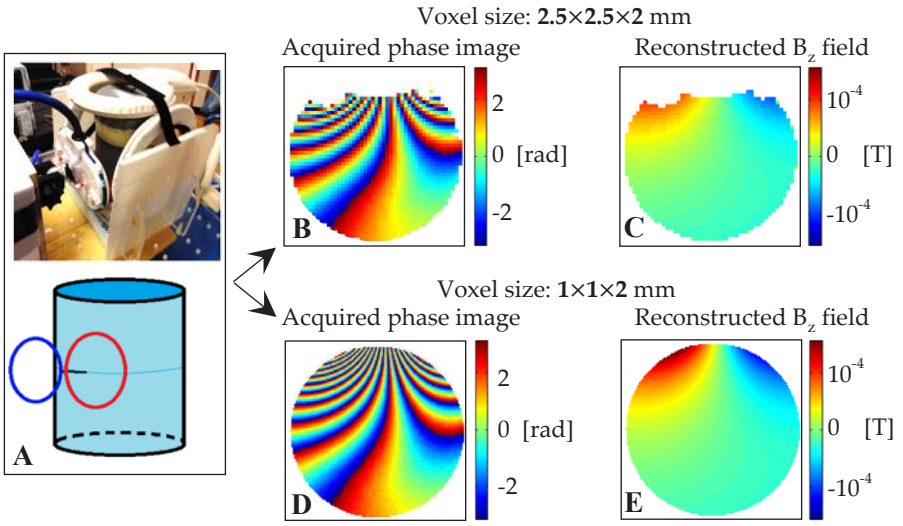

Figure 3.4: (**A**) TMS-MRI setup, (**B**, **C**) the acquired phase map and the reconstructed z-component of the TMS magnetic field (voxel size: 2.5×2.5×2 mm^3), (**D**, **E**) the acquired phase map and the reconstructed z-component of the TMS magnetic field (voxel size: 1×1×2 mm^3).

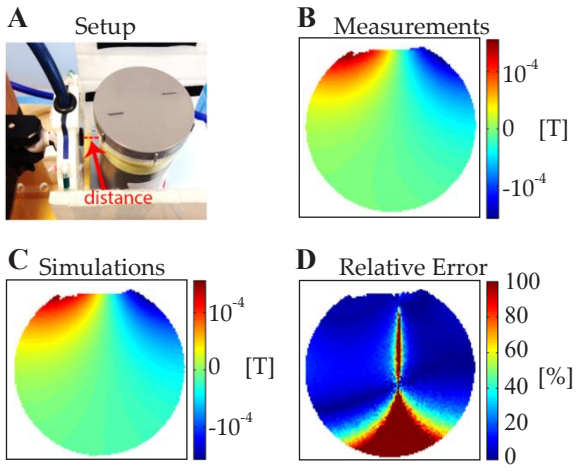

Figure 3.5: (**A**) TMS-MRI setup, (**B**) the measured z-component of the TMS magnetic field, (**C**) the simulated z-component of the TMS magnetic field, (**D**) the relative error.

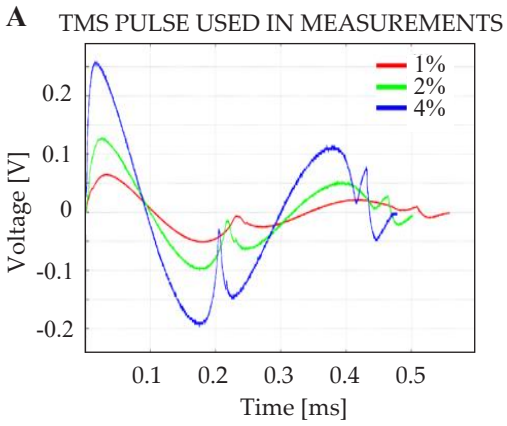

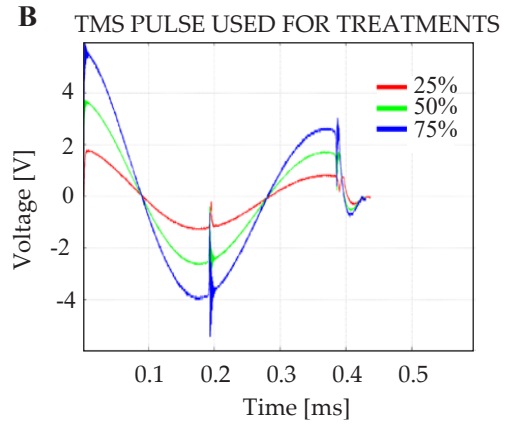

Figure 3.6: Oscilloscope measurements of the TMS current waveform for: (**A**) 1%, 2%, and 4% machine outputs, used for our TMS-MRI experiments, (**B**) 25%, 50%, and 75% machine outputs, commonly used for treatment.

Since neurostimulation typically occurs starting from 2 cm away from the coating of the TMS coil (4), in the third experiment we characterize the minimum distance from the TMS coil that allows TMS field measurements non-affected by intra-voxel dephasing, without the need of an ultra-high resolution acquisition (< 1 mm) leading to impractically long scan times. In Fig. 3.5, A and B, we show the setup and the reconstructed z-component of the TMS magnetic field for a coil placed 2 cm from the phantom. Signal loss is observed in the first 5 mm, indicating that measurements of the TMS magnetic field are possible starting from 2.5 cm away from the coil for the employed resolution. In addition, simulations are also computed (Fig. 3.5, C), and comparison with measurements is performed (Fig. 3.5, D).

Since the spatial region where TMS applications typically evoke meaningful neuronal effects in the brain is between 2 and 6 cm from the TMS coil (23), we can limit the evaluation of the relative error between measurements and simulation only to this relevant zone. From the relative error map, it is clear that in this region the relative error is lower than 10%, thus proving a good quantitative match between measurements and simulations, with the exception of a small line at the center where the error is more than 50%. This high error region is a logical consequence of the division operation (eq. [3.3]), which has at the denominator the simulated TMS magnetic field (nearly zero, perpendicularly to the center of a TMS coil, as expected from theory). As it can be understood, small deviations in the real construction of the TMS coil from the simulated one can also contribute to increase the discrepancy between measurements and simulations in this region. However, since the extension of this region is only few voxels, it can be ignored for our purposes. The low relative error in the remaining region of interest allows us to conclude that it can be possible to calibrate TMS coil simulation based on MR measurement.

In the fourth experiment, we evaluate the scaling of the magnetic field with the TMS machine output. First, oscilloscope measurements are performed to evaluate the non-linearity that occurs for low TMS outputs (Fig. 3.6, A) with respect to usual treatments outputs (Fig. 3.6, B). As shown in Fig. 3.6, A, for low TMS outputs the strength of the TMS pulse does not scale linearly with the machine output, while the pulse duration decreases with the increase of the TMS pulse strength. This non-linear effect is instead not present in the range of higher TMS outputs typically used in clinical treatments (Fig. 3.6, B). These calibration measurements are vital to correctly compute the DC current values used to simulate the magnetic field produced by low TMS outputs, since they do not scale linearly.

In Fig. 3.7, comparisons between measurements (Fig. 3.7, A, E, and I) and simulations (Fig. 3.7, B, F, and J) are performed for 1%, 2%, and 4% TMS outputs. A region of interest (ROI) of 4 cm inside the phantom (red boxes) is considered for this comparison. This will lead to a total distance from the TMS coil of 7 cm, therefore including the region of interest for common TMS applications. To compare the decay of the measured and simulated magnetic fields, profiles depicted in the ROI region are shown in Fig. 3.7 C, G, and K. These profiles show a good match especially in the region closest to the coil where neurostimulation occurs. This is clear from the computed relative error maps (Fig. 3.7 D, H, and L). Excluding the central region containing high error as previously discussed, the mean error in the ROI is less than 10%, therefore providing good agreement between measurements and simulations.

In the last two experiments, two different orientations of the TMS coil are analyzed with respect to the position evaluated until now (Fig 3.8, A, E, and I) to prove the capability of MR systems to correctly measure the TMS magnetic field while assuming different coil orientations.

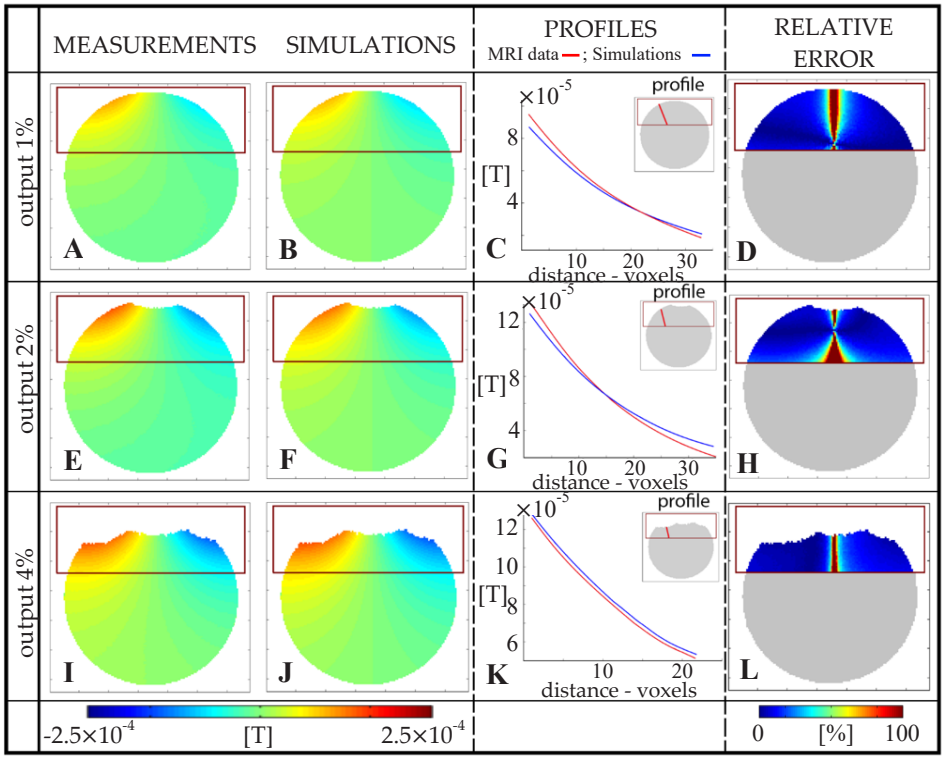

Figure 3.7: Measured z-component of the TMS magnetic field for 1%, 2%, and 4% machine outputs (**A, E,** and **I**). Simulated z-component of the TMS magnetic field for 1%, 2%, and 4% machine outputs (**B, F,** and **J**). Comparison between the measured and simulated z-component of the TMS magnetic field computed along the depicted profiles (**C, G,** and **K**). Relative error maps (**D, H,** and **L**).

For each orientation, measurements and simulations show clearly a specific pattern of the TMS magnetic fields (Fig. 3.8 B, C, F, G, J, and K). By considering a ROI of 2 cm, therefore limiting the comparison between measurements and simulations to the region of interest for TMS applications, it is clear from the relative error maps that the mean error in these regions is less than 15% (without considering the small region in the center with high RE). While this region is observed in the cases where the TMS coil is placed horizontally (Fig 3.8, D, and H), for the case where the coil is placed vertically this region is not visible (Fig 3.8, L). This is because the slice where measurements and simulations were performed was not exactly at the center of the coil, but slightly shifted towards the upper coil wing, thus not on the plane perpendicular to the center of the TMS coil where the z-component of the TMS magnetic field is theoretically zero in simulations.

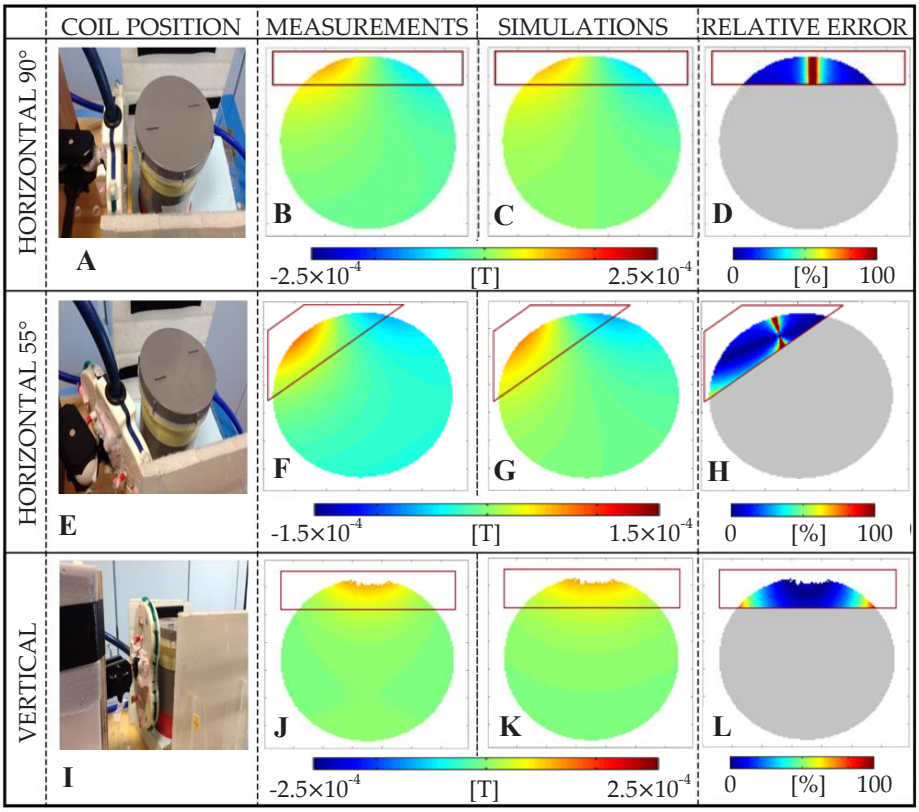

Figure 3.8: Three different coil orientations used for the three different experiments (**A, E,** and **I**). Measurements of the z-component of the TMS magnetic field for the three experiments (**B, F,** and **J**). Simulations of the z-component of the TMS magnetic field for the three experiments (**C, G,** and **K**). Relative error maps for the three experiments (**D, H,** and **L**).

3.4 Discussion

In this study, it is demonstrated that MR-based measurements of the TMS magnetic field produced by a realistic figure-8 TMS coil and a clinical TMS stimulator are feasible. A detailed TMS-MR-compatible setup is described to address technical challenges introduced by the use of a realistic TMS coil and stimulator. In addition, a tailored MR sequence and a synchronization protocol to safely discharge a TMS pulse while performing an MR experiment are described.

Previous studies showed already that it is possible to map the magnetic field produced by loop coils with an MR scanner (23,28-31). Since multiple simplifications in the setup were adopted (use of DC batteries, different current waveform, lower current strengths, different coil shapes), in these proof of concept studies issues related to the discharging of a real TMS stimulator in an MR environment were circumvented.

In this study, a real TMS setup (coil and stimulator) was used to perform direct measurements of the TMS field with an MR scanner. To handle all the issues discussed above, additional hardware was built. From our results, we conclude that measurements of a realistic TMS magnetic field without loss of information are possible up to 2.5 cm from the TMS coil for 1% machine output. Measurements are still feasible up to 4% TMS machine output, but are not applicable to TMS outputs used for standard applications (40-70%). This limitation arises from the fact that increasing output strengths or reducing the distance between the TMS coil and the imaging area will result in increasing intra-voxel dephasing, and thus signal loss. This effect can be potentially overcome by increasing the image resolution, so that the phase range per voxel will be lower than $[-\pi\ \pi)$. However, a higher resolution will result in increasing in the scan time and lower signal-to-noise ratio.

In addition, as shown in this paper, TMS coil models used to predict electromagnetic field distributions and neuronal activation can be validated using this field mapping technique and a real TMS current waveform. As indicated, this validation has to be performed at low TMS machine output values (1-4%) which we believe is not a fundamental limitation. An in-plane resolution of 1 mm and a distance from the TMS coil of 2.5 cm is sufficient, as neurostimulation occurs usually around 2-4 cm away from the scalp (first few centimeters of cortex) (4,23). By using a lookup table obtained from oscilloscope measurements to correctly compensate for the non-linear effect at low field strength, as observed in this study, it is possible to infer the strength of the TMS magnetic field in the typical range of 40-70% machine output. Therefore, a simple linear scaling of unrealistically low DC current values, even compared to 1% TMS machine output, and not derived from realistic TMS current waveforms, is not applicable for real TMS applications and simulations. Moreover, as it is shown in this study, the pattern of the z-component of the incident TMS magnetic field is unique for each coil position. For this reason, a TMS coil model can be validated based only on measurements of the z-component of the incident field, the only component measurable with an MR scanner.

It is also noteworthy to underline that, with these measurements, it is in principle possible to map the total TMS magnetic field. However, this total magnetic field is nearly equal to the incident TMS magnetic field, as secondary induced magnetic fields arising from the induced tissue eddy currents are very small (nT) in this frequency range (41,42).

If one could measure the secondary induced magnetic field variations arising from the induced tissue eddy currents, then *in-vivo* measurements would be valuable, since they will differ from phantom measurements. However, the phase contribution arising from the tissue induced eddy currents is below the MR phase accuracy (~0.01 rads for the adopted sequence), thus not measurable (41,42). Therefore, it will be unlikely that information about the TMS induced electric field or eddy currents (directly connected to neuro-stimulation) can be inferred by using this technique. The proposed measurement technique will exclusively depend on the coil geometry and current strength running into it, which characterize the incident TMS magnetic field. For this reason, since the induced TMS magnetic field can not be measured, *in-vivo* experiments would not add any value to measurements of the incident TMS magnetic field for TMS coil validations. This is because the incident magnetic field would be the same for phantom and *in-vivo* measurements.

For comparison with our experimental findings, simulations were performed using a single loop figure-8 coil model, as suggested in several studies (11,12). We observed that the mean of the relative error in the region of interest for TMS applications is less than 10%. However, this might not be precise enough to accurately predict cortical current flow. We believe that the discrepancy between measurements and simulations can be reduced if more complex geometries are adopted in simulations. Although the focus of this work is not to design a perfect model of the figure-8 coil, this result highlights the necessity and the importance of validating coil models with magnetic field measurements to correctly evaluate the margins of error in the computations of the electromagnetic fields induced by a single TMS pulse.

In summary, mapping the specific magnetic field induced by a real TMS coil and stimulator will be fundamental for various reasons.

First, it will allow validation of numerical EM-simulations of the real TMS field. This will lead to more confidence in interpreting the results of future studies on (neuronal) modeling of TMS induced effects in the brain purely based on simulations of the TMS induced electric field.

Second, it will allow correct guidance and dosimetry for concurrent TMS-MRI studies without the need of crude methods such as motor threshold (43) for stimulation dose determination.

Third, direct measurements of the TMS field at low machine outputs and at intermittent intervals during TMS applications inside an MRI scanner (21,36) can also provide an independent way to online assess quality of the planned experimental session (32,33). In fact, these measurements reflect the functioning of the TMS machine and coil, which can be altered by hardware malfunctioning or unforeseen coupling of the TMS coil with the surrounding leading to asymmetric

currents in the coil wings and therefore different electromagnetic fields. This will allow not only a better planning of TMS treatments, but also will ensure a better inter-subject reproducibility thus improving confidence and reliability of research findings.

3.5 Conclusions

By using a combined TMS-MRI setup and a tailored MR sequence, it is possible to accurately and directly quantify the incident TMS magnetic field in the region relevant for neurostimulation. With these measurements it is possible to validate electromagnetic models of TMS coils. Correct electromagnetic simulations based on validated coil models will allow more confidence in neuronal stimulation predictions. In addition, well validated TMS coil models in combination with an integrated TMS-MRI setup might spur the development of a fully integrated MR-guidance of concurrent TMS-MRI studies based on MR measurements of the TMS field.

3.6 References

1. Fregni F, Pascual-Leone A. Technology insight: non-invasive brain stimulation in neurology - perspectives on the therapeutic potential of rTMS and tDCS. Nat. Clin. Pract. Neurol. 2007;3:383–393. doi: 10.1038/ncpneuro0530.
2. Rossini PM, Rossi S. Transcranial magnetic stimulation: Diagnostic, therapeutic, and research potential. Neurology 2007;68:484–488. doi: http://dx.doi.org/10.1212/01.wnl. 0000 250268.13789.b2.
3. Rossini PM, Burke D, Chen R, Cohen LG, Daskalakis Z, Di Iorio R.,Di Lazzaro V, et.al. Non-invasive electrical and magnetic stimulation of the brain, spinal cord, roots and peripheral nerves: basic principles and procedures for routine clinical and research application. An updated report from an I.F.C.N. Committee. Clin. Neurophysiol. 2015; 126:1071–1107. doi: 10.1016/j.clinph.2015.02.001.
4. Neggers SFW, Petrov PI, Mandija S, Sommer IEC, van den Berg CAT. Understanding the biophysical effects of transcranial magnetic stimulation on brain tissue: The bridge between brain stimulation and cognition. Prog Brain Res, Comput. Neurostimulation 2015;222:229–259. doi: 10.1016/bs.pbr.2015.06.015.
5. Bestmann S, Feredoes E. Combined neurostimulation and neuroimaging in cognitive neuroscience: Past, present, and future. Ann. N. Y. Acad. Sci. 2013;1296:11–30. doi: 10.1111/ nyas.12110.
6. Bestmann S, de Berker AO, Bonaiuto J. Understanding the behavioral consequences of noninvasive brain stimulation. Prog Brain Res, Comput. Neurostimulation 2015;19:75–100. doi: 10.1016/j.tics.2014.10.003.
7. Hallett M. Transcranial magnetic stimulation and the human brain. Nature 2000;406:147–150. doi: 10.1038/35018000.
8. Ridding MC, Rothwell JC. Is there a future for therapeutic use of transcranial magnetic stimulation? Nat. Rev. Neurosci. 2007;8:559–67. doi: 10.1038/nrn2169.
9. Barker AT, Jalinous R, Freeston IL. Non-invasive magnetic stimulation of human motor cortex. Lancet 1985;1:1106–1107. doi: 10.1016/S0140-6736(85)92413-4.
10. Kobayashi M, Pascual-Leone A. Transcranial magnetic stimulation in neurology. Lancet Neurol. 2003;2:145–156. doi: 10.1016/S1474-4422(03)00321-1.
11. Salinas FS, Lancaster JL, Fox PT. Detailed 3D models of the induced electric field of transcranial magnetic stimulation coils. Phys. Med. Biol. 2007;52:2879–2892. doi: 10.1088/ 0031-9155/52/10/016.
12. De Lucia M, Parker GJM, Embleton K, Newton JM, Walsh V. Diffusion tensor MRI-based estimation of the influence of brain tissue anisotropy on the effects of transcranial magnetic stimulation. Neuroimage 2007;36:1159–1170. doi: 10.1016/j.neuroimage.2007. 03.062.
13. De Geeter N, Crevecoeur G, Dupré L, Van Hecke W, Leemans A. A DTI-based model for TMS using the independent impedance method with frequency-dependent tissue parameters. Phys. Med. Biol. 2012;57:2169–2188. doi: 10.1088/0031-9155/57/8/2169.
14. Opitz A, Windhoff M, Heidemann RM, Turner R, Thielscher A. How the brain tissue shapes the electric field induced by transcranial magnetic stimulation. Neuroimage 2011;58:849–859. doi: 10.1016/j.neuroimage.2011.06.069.
15. Fitzgerald PB, Hoy K, McQueen S, Maller JJ, Herring S, Segrave R, Bailey M, Been G, Kulkarni J, Daskalakis ZJ. A randomized trial of rTMS targeted with MRI based neuro-

navigation in treatment-resistant depression. Neuropsychopharmacology 2009;34:1255–1262. doi: 10.1038/npp.2008.233.

16. O'Reardon JP, Solvason HB, Janicak PG, Sampson S, Isenberg KE, Nahas Z, McDonald WM, Avery D, Fitzgerald PB, Loo Colleen Demitrack MA, George MS, Sackeim HA. Efficacy and Safety of Transcranial Magnetic Stimulation in the Acute Treatment of Major Depression: A Multisite Randomized Controlled Trial. Biol. Psychiatry 2007;62:1208–1216. doi: 10.1016/j.biopsych.2007.01.018.

17. Menon P, Geevasinga N, Yiannikas C, Howells J, Kiernan MC, Vucic S. Sensitivity and specificity of threshold tracking transcranial magnetic stimulation for diagnosis of amyotrophic lateral sclerosis: a prospective study. Lancet Neurol. 2015;14:478–484. doi: 10.1016/S1474-4422(15)00014-9.

18. Lefaucheur J-P. Stroke recovery can be enhanced by using repetitive transcranial magnetic stimulation (rTMS). Clin. Neurophysiol. 2006;36:105–115. doi: 10.1016/j.neucli.2006.08.011.

19. Hummel FC, Cohen LG. Non-invasive brain stimulation: a new strategy to improve neurorehabilitation after stroke? Lancet Neurol. 2006;5:708–712. doi: 10.1016/S1474-4422 (06)70525-7.

20. Tergau F, Naumann U, Paulus W, Steinhoff BJ. Low-frequency repetitive transcranial magnetic stimulation improves intractable epilepsy. Lancet 1999;353:2209. doi: 10.1016/ S0140-6736(99)01301-X.

21. Bohning DE, Denslow S, Bohning PA, Walker JA, George MS. A TMS coil position/holding system for MR image-guided TMS interleaved with fMRI. Clin. Neurophysiol. 2003;114: 2210–2219. doi: 10.1016/S1388-2457(03)00232-3.

22. Neggers SFW, Langerak TR, Schutter DJLG, Mandl RCW, Ramsey NF, Lemmens PJJ, Postma A. A stereotactic method for image-guided transcranial magnetic stimulation validated with fMRI and motor-evoked potentials. Neuroimage 2004;21:1805–1817. doi: 10.1016/j.neuroimage.2003.12.006.

23. Navarro De Lara LI, Windischberger C, Kuehne A, Woletz M, Sieg J, Bestmann S, Weiskopf N, Strasser B, Moser E, Laistler E. A novel coil array for combined TMS/fMRI experiments at 3 T. Magn. Reson. Med. 2015;74:1492–1501. doi: 10.1002/mrm.25535.

24. Komssi S, Kähkönen S, Ilmoniemi RJ. The Effect of Stimulus Intensity on Brain Responses Evoked by Transcranial Magnetic Stimulation. Hum. Brain Mapp. 2004;21:154–164. doi: 10.1002/hbm.10159.

25. Nummenmaa A, Stenroos M, Ilmoniemi RJ, Okada YC, Hämäläinen MS, Raij T. Comparison of spherical and realistically shaped boundary element head models for transcranial magnetic stimulation navigation. Clin. Neurophysiol. 2013;124:1995–2007. doi: 10.1016/j.clinph.2013.04.019.

26. Laakso I, Hirata A, Ugawa Y. Effects of coil orientation on the electric field induced by TMS over the hand motor area. Phys. Med. Biol. 2014;59:203–218. doi: 10.1088/0031-9155/ 59/1/203.

27. Sack AT, Cohen Kadosh R, Schuhmann T, Moerel M, Walsh V, Goebel R. Optimizing functional accuracy of TMS in cognitive studies: a comparison of methods. J. Cogn. Neurosci. 2009;21:207–221. doi: 10.1162/jocn.2009.21126.

28. Bohning DE, Pecheny AP, Epstein CM, Speer AM, Vincent DJ, Dannels W, George MS. Mapping transcranial magnetic stimulation (TMS) fields in vivo with MRI. Neuroreport 1997;8:2535–2538. doi: 10.1097/00001756-199707280-00023.

29. Hernandez-Garcia L, Lee S, Grissom W. An approach to MRI-based dosimetry for transcranial magnetic stimulation. Neuroimage 2007; 36:1171–1178. doi: 10.1016/j.neuroimage.2007.03.064.

30. Hernandez-Garcia L, Bhatia V, Prem-Kumar K, Ulfarsson M. Magnetic resonance imaging of time-varying magnetic fields from therapeutic devices. NMR Biomed. 2013;26:718–724. doi: 10.1002/nbm.2919.

31. Peres ASC, Souza VHO, Maziero D, Araujo DB De, Salmon CEG, Baffa O. Vector magnetic field mapping of a Transcranial Magnetic Stimulation coil using Magnetic Resonance Imaging: *in-vitro* and *in-vivo* experiments. IFMBE Proc. 2009;25:571–574.

32. Yau JM, Jalinous R, Cantarero GL, Desmond JE. Static field influences on transcranial magnetic stimulation: Considerations for TMS in the scanner environment. Brain Stimul. 2014;7:388–393. doi: 10.1016/j.brs.2014.02.007.

33. Peterchev A V. Reduction of TMS strength near MRI scanner could be explained by electromagnetic coupling to MRI magnet. Brain Stimul. 2014;7:909–921. doi: 10.1016/j.brs.2014.09.006.

34. Bestmann S, Baudewig J, Frahm J. On the synchronization of transcranial magnetic stimulation and functional echo-planar imaging. J. Magn. Reson. Imaging 2003;17:309–316. doi: 10.1002/jmri.10260.

35. Weiskopf N, Josephs O, Ruff CC, Blankenburg F, Featherstone E, Thomas A, Bestmann S, Driver J, Deichmann R. Image Artifacts in Concurrent Transcranial Magnetic Stimulation (TMS) and fMRI Caused by Leakage Currents: Modeling and Compensation. J. Magn. Reson. Imaging 2009;29:1211–1217. doi: 10.1002/jmri.21749.

36. de Weijer A, Sommer I, Bakker E, Bloemendaal M, Bakker C, Klomp DWJ, Bestmann S, Neggers B. A setup for administering TMS to medial and lateral cortical areas during whole brain fMRI recording. J. Clin. Neurophysiol. 2014;31:474–487.

37. Crowther LJ, Porzig K, Hadimani RL, Brauer H, Jiles DC. Realistically modeled transcranial magnetic stimulation coils for Lorentz force and stress calculations during MRI. IEEE Trans. Magn. 2013;49:3426–3429. doi: 10.1109/TMAG.2013.2247578.

38. Stogryn A. Equations for Calculating the Dielectric constant of saline water. IEEE Trans. Microw. Theory Tech. 1971;19:733–736.

39. Baumann SB, Wonzy DR, Kelly SK, Meno FM. The electrical conductivity of human cerebrospinal fluid at body temperature. IEEE Trans. Biomed. Eng. 1997;44:220–223.

40. Institute S. SCIRun: A Scientific Computing Problem Solving Environment, Scientific Computing and Imaging Institute (SCI). 2015:http://www.scirun.org.

41. Mandija S, van Lier ALHMW, Katscher U, Petrov PI, Neggers SFW, Luijten PR, van den Berg CAT. A geometrical shift results in erroneous appearance of low frequency tissue eddy current induced phase maps. Magn. Reson. Med. 2015. doi: 10.1002/mrm.25981.

42. Gibbs E, Liu C. Feasibility of Imaging Tissue Electrical Conductivity by Switching Field Gradients with MRI. Tomography 2015:125–135. doi: 10.1530/ERC-14-0411.

43. Schutter DJLG, van Honk J. A standardized motor threshold estimation procedure for transcranial magnetic stimulation research. J. ECT 2006;22:176–178. doi: 10.1097/01.yct.0000235924.60364.27.

Chapter 4

Non-invasive electric current induction for low frequency tissue conductivity reconstruction: Is it feasible with a TMS-MRI setup?

Tomography 2016;2(3):203-214.
doi: 10.18383/j.tom.2016.00232.

Stefano Mandija

Petar I. Petrov

Sebastian F.W. Neggers

Peter R. Luijten

Cornelis A.T. van den Berg

Abstract

Non-invasive quantification of subject-specific low frequency (LF) brain tissue conductivity (σ_{LF}) would be valuable for different fields, e.g. neuroscience. MR-Electrical Impedance Tomography allows measurements of σ_{LF}. However, the required high level of direct current injection leads to undesirable pain sensation. Following the same principles but avoiding pain sensation, we evaluate the feasibility of inductively inducing currents using a TMS device and recording the magnetic field variations arising from the induced tissue eddy-currents using a standard 3T-MR scanner. By means of simulations we characterize: the strength of the incident TMS magnetic field arising from the current running in the TMS coil, the strength of the induced magnetic field arising from the induced currents in tissues by TMS pulses, and the MR phase accuracy required to measure this latter magnetic field containing information about σ_{LF}. Then, by means of TMS-MRI measurements we evaluate the achievable phase accuracy for a typical TMS-MRI setup. From measurements and simulations, we observe that it is crucial to discriminate the incident from the induced magnetic field. From our results, the incident TMS magnetic field range is $\pm 10^{-4}$ T, measurable with standard MR scanners. In contrast, the induced TMS magnetic field is much weaker ($\pm 10^{-8}$ T), leading to an MR phase contribution of ~10^{-4} rad. This phase range is too small to be measured, since the phase accuracy for TMS-MRI experiments is ~10^{-2} rads. Thus, although highly attractive, non-invasive measurements of the induced TMS magnetic field and therefore estimations of σ_{LF} are experimentally not feasible.

4.1 Introduction

Non-invasive mapping of tissue electrical properties (EPs) in the MHz range has recently become feasible with the development of MRI-based Electrical Property Tomography (1–5). However, precise knowledge on tissue electrical conductivity at low frequency (LF: Hz - 100 kHz) and the relation between electrical conduction and tissue composition in this frequency range is still limited. In the kHz range, the human body is electrically very heterogeneous (6–8) as cellular fraction, water-ionic content and cell membranes modulate electrical conductivity. Unfortunately, pathologies change these factors causing differences in tissue conductivity values (σ_{LF}) between healthy and non-healthy subjects (9,10). The ability to measure subject-specific σ_{LF} values of brain tissues is especially desired in neuroscience, since various diagnostic techniques and neurostimulation modalities like Transcranial Magnetic Stimulation (TMS) operate in this frequency range (11–14).

TMS is an emerging technique that allows non-invasive modulation of cortical neurophysiology to diagnose and treat neurological disorders (15–20). Based on the Faraday's induction principle, TMS employs a strong, time-varying magnetic field to inductively induce an electric field in the brain that can cause neuroactivation (21–24). Practically, TMS dosimetry is performed in a highly empirical fashion by using the 'motor threshold' (MT) method (20,23), where the motor cortex serves as reference area. However, since the electric field induced in the brain is modulated by the varying EPs and the gyrification of the cortex (25,26), it is understandable that TMS dose varies for brain regions different from the motor cortex (27–30). Therefore, the MT method is unreliable for most TMS purposes (31–33).

To precisely guide TMS administration and to better understand the behavioral consequences of the deployed TMS electric field, different research groups are focusing their investigations on how stimulation parameters (number of TMS pulses, pulses strength, coil models and orientation) affect the induced TMS electric field by means of Electromagnetic (EM) simulations (34–39). While these valuable studies correctly adopt heterogeneous conductive brain models in the computation of the induced TMS electric field, the adopted conductivity values are simply derived from healthy group averages (40–42). Unfortunately, as argued in other studies (24,30,43–46), healthy group averages of σ_{LF} cannot ensure optimal subject-specific dosimetry since various factors such as ageing (47) and pathologies (10) induce variations in σ_{LF} values. Moreover, having subject-specific brain models would be valuable, since the induced electric field is also modulated by the tissue geometry (32,44,48). While this latter requirement can be satisfied by segmenting MR images acquired before TMS administration, being able to non-invasively and non-painfully determine subject-specific tissue σ_{LF} values is still an unresolved issue.

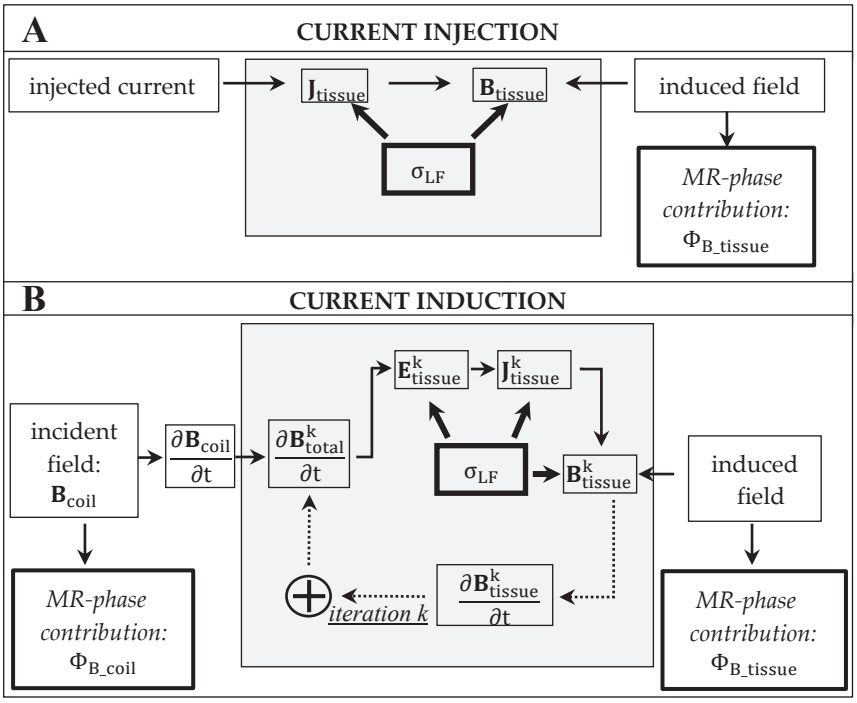

Figure 4.1: (**A**) Current injection: the additional MR phase contribution (Φ_{B_tissue}) contains information on low frequency tissue conductivity. (**B**) Current induction – quasi-static approximation: two additional MR phase contributions. Φ_{B_coil} does not carry any information about σ_{LF}. Instead, Φ_{B_tissue} contains information about σ_{LF}, as for the case of current injection.

Low frequency tissue conductivity can be mapped using MR-Electrical Impedance Tomography (MR-EIT) (49–51). In this technique, strong DC currents (10 mA) are injected into the brain via skin-surface electrodes (Fig. 4.1, A) while the subject is inside an MR scanner. The spatial pattern of these currents is modulated by the underlying tissue σ_{LF} distribution. In turn, these injected currents lead to an induced magnetic field, in which information on σ_{LF} is imprinted. By measuring this induced magnetic field using MR phase measurements, σ_{LF} maps can be reconstructed (52,53). However, strong currents and long injection times (10 ms) are needed to achieve adequate MR phase accuracy in MR-EIT experiments. These requirements result in a sensation of pain that limits the *in-vivo* applicability of MR-EIT.

To map tissue σ_{LF} avoiding direct current injection, it has been suggested to inductively induce currents using time-varying magnetic fields created by external coils (Fig. 4.1, B) (54).

Subsequently, by following this inductive fashion, it has been proposed to directly use the MR gradient coils to induce currents (55–57). In this way, high current density at injection points and thus pain sensation is avoided, making this approach very attractive and applicable to standard clinical MR scanners. However, tissue σ_{LF} reconstructions proved not to be feasible. In fact, it has been shown that the phase contribution arising from the induced magnetic field is too small to be accurately measured with standard MR systems (58,59). Additionally, it has also been shown that subtle, unavoidable imaging distortions hamper measurements of this phase contribution by creating a pseudo-LF conductivity contrast (60).

By following the appealing idea of inductively inducing currents in tissues, in this study we use a TMS setup to induce much stronger currents (Fig. 4.2, A) in combination with an MR scanner used to measure the arising induced magnetic field (Fig. 4.2, B). In fact, while standard MR gradient coils allow slew rates of 20 T/s at 10 cm from the gradients isocenter, a TMS device can generate slew rates up to 20000 T/s. In this way, the reported three orders of magnitude increase needed to measure the induced magnetic field could be theoretically achieved (59).

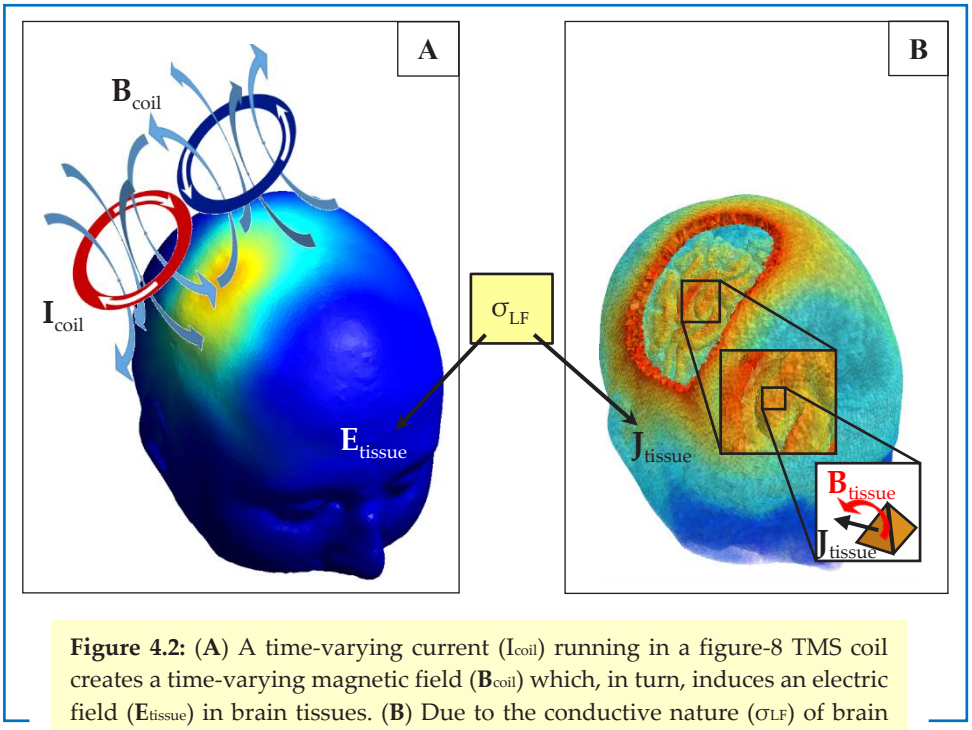

Figure 4.2: (**A**) A time-varying current (I_{coil}) running in a figure-8 TMS coil creates a time-varying magnetic field ($\mathbf{B}_{coil}$) which, in turn, induces an electric field ($\mathbf{E}_{tissue}$) in brain tissues. (**B**) Due to the conductive nature (σ_{LF}) of brain tissues, induced currents ($\mathbf{J}_{tissue}$) arise from $\mathbf{E}_{tissue}$. These induced currents create an induced magnetic field ($\mathbf{B}_{tissue}$). Information on low frequency tissue conductivity σ_{LF} is therefore imprinted only in $\mathbf{B}_{tissue}$ and not in $\mathbf{B}_{coil}$.

We have divided this study in two parts. First, by means of simulations, we characterize the strength of the induced magnetic field carrying information on the induced currents in tissue and thus LF conductivity, versus the incident TMS magnetic field. This was evaluated for different conductive cylindrical models and realistic human brain models. In this way, we characterize the required phase accuracy to detect these induced magnetic fields with MRI. Moreover, we study the impact of different TMS waveforms. Second, MR measurements on phantoms are presented to investigate the achievable phase accuracy for a typical TMS-MRI setup. With this study, we conclude whether inductively inducing currents in tissues by using a TMS-MRI setup is a feasible methodology to perform non-invasive LF tissue conductivity reconstructions.

4.2 Theory

In TMS, the presence of conductive tissues such as the brain underneath the TMS coil leads to correction terms in the computation of the TMS electromagnetic field, which are a function of the tissue conductivity distribution (Fig. 4.1, B). In this kHz range where displacement currents are negligible, these corrections can be modeled by a so called quasi-static approximation (35). For this purpose, Maxwell's equations are expanded in power series in the frequency domain ($\mathbf{E} = \sum_{k=0}^{\infty}(j\omega)^k\mathbf{E}^{[k]}$ and $\mathbf{B} = \sum_{k=0}^{\infty}(j\omega)^k\mathbf{B}^{[k]}$), giving the following relations for a k^{th} order (61):

$$\nabla \times \mathbf{E}^{[k]} = -\frac{\partial \mathbf{B}^{[k-1]}}{\partial t} \quad [4.1]$$

$$\mathbf{J}^{[k]} = \sigma_{LF}\mathbf{E}^{[k]} \quad [4.2]$$

$$\nabla \times \mathbf{B}^{[k]} = \mu_0\mathbf{J}^{[k]} \quad [4.3]$$

where a quasi-static condition is assumed in eq. [4.2] (35,62). For readability purposes, we do not write the spatial dependency ($\mathbf{r}$) of the vector fields explicitly. Additionally, the conductivity σ_{LF} is also a tensor due to tissue anisotropy, but we can consider it as a scalar value for simplicity of derivation. From eq. [4.3], the Biot-Savart's law can be derived:

$$\mathbf{B}^{[k]} = \frac{\mu_0}{4\pi}\int_V \frac{\mathbf{J}^{[k]} \times (\mathbf{r}-\mathbf{r}_0)}{|\mathbf{r}-\mathbf{r}_0|^3} dV_0 \quad . \quad [4.4]$$

In TMS, for k = 0 the zero-order vectors in the brain/object satisfy the static field equations $\nabla \times \mathbf{E}^{[0]} = 0$, $\mathbf{E}^{[0]} = 0$, $\nabla \times \mathbf{B}^{[0]} = 0$, $\nabla \cdot \mathbf{B}^{[0]} = 0$. $\mathbf{B}^{[0]}$ is the incident TMS magnetic field arising from the current running in the TMS coil, thus not carrying any information about tissue conductivity. Throughout the paper, we will refer to this magnetic field as $\mathbf{B}_{coil}$:

$$\mathbf{B}^{[0]} = \mathbf{B}_{coil} \quad [4.5]$$

which gives an MR phase contributions defined as Φ_{B_coil} (63). Higher-order field corrections of order k can be computed by using the vectors of order k-1 as sources (Fig. 4.1, B). For k = 1:

$$\nabla \times \mathbf{E}^{[1]} = -\frac{\partial \mathbf{B}^{[0]}}{\partial t} = -\frac{\partial \mathbf{B}_{coil}}{\partial t} \quad [4.6]$$

$$\mathbf{J}^{[1]} = \sigma_{LF}\mathbf{E}^{[1]} \quad [4.7]$$

$$\nabla \times \mathbf{B}^{[1]} = \mu_0 \mathbf{J}^{[1]} \quad [4.8]$$

$$\mathbf{B}^{[1]} = \frac{\mu_0}{4\pi}\int_V \frac{\mathbf{J}^{[1]} \times (\mathbf{r}-\mathbf{r}_0)}{|\mathbf{r}-\mathbf{r}_0|^3} dV_0 \quad [4.9]$$

where $\mathbf{E}^{[1]}$and $\mathbf{J}^{[1]}$ are respectively the first order electric field and current density induced in a conductive domain such as the brain, and $\mathbf{B}^{[1]}$ is the first order induced magnetic field arising from $\mathbf{J}^{[1]}$. Therefore information on tissue conductivity is imprinted in $\mathbf{B}^{[1]}$.

The total induced electric field in brain tissues, called as $\mathbf{E}_{tissue}$ in this paper, is:

$$\mathbf{E}_{tissue} = \sum_{k=1}^{\infty} \mathbf{E}^{[k]}. \quad [4.10]$$

In principle, $\mathbf{E}_{tissue}$ is a solenoidal electric field induced by the time varying incident TMS magnetic field $\mathbf{B}_{coil}$ (eq. [4.6]). However, due to the non-homogeneous conductivity distribution of brain tissues, charge accumulation occurs at the boundaries between different conductive structures. This leads to a conservative electric field which affects the incident, solenoidal electric field (25,35,48):

$$\mathbf{E}_{tissue} = \mathbf{E}_{solenoidal} + \mathbf{E}_{conservative} \quad [4.11]$$

$\mathbf{E}_{solenoidal}$ is proportional to the incident time-varying vector potential $\mathbf{A}_{coil}$, which depends solely on the TMS coil configuration and level of current running into it ($\mathbf{E}_{solenoidal} = -\frac{\partial \mathbf{A}_{coil}}{\partial t}$). Thus, $\mathbf{E}_{solenoidal}$ is always present, independently from the conductor underneath the TMS coil. Instead, $\mathbf{E}_{conservative}$, which arises from the charge accumulation at tissue boundaries between different conductive tissues ($\mathbf{E}_{conservative} = -\nabla\varphi$, with φ electrical potential), is directly modulated by the underlying tissue geometry and conductivity distribution σ_{LF} (25,35,48). From eq. [4.2], the total induced current density in tissue, called as $\mathbf{J}_{tissue}$, is therefore $\mathbf{J}_{tissue} = \sigma_{LF}\mathbf{E}_{tissue}$.

Analogously to eq. [4.10], the total induced TMS magnetic field, called as $\mathbf{B}_{tissue}$, is:

$$\mathbf{B}_{tissue} = \sum_{k=1}^{\infty} \mathbf{B}^{[k]} \quad [4.12]$$

which gives an MR phase contributions defined as Φ_{B_tissue}. By combining eqs. [4.5] and [4.12], the total TMS magnetic field is therefore defined:

$$\mathbf{B}_{total} = \sum_{k=0}^{\infty} \mathbf{B}^{[k]} = \mathbf{B}^{[0]} + \sum_{k=1}^{\infty} \mathbf{B}^{[k]} = \mathbf{B}_{coil} + \mathbf{B}_{tissue}\,. \quad [4.13]$$

4.3 Methods

4.3.1 Simulations

The aim of EM simulations was to characterize the strength of the incident ($\mathbf{B}_{coil}$) and the induced ($\mathbf{B}_{tissue}$) TMS fields by employing the quasi-static approximation described in the theory section. We then assessed the phase accuracy needed to detect Φ_{B_tissue} in concurrent TMS-MRI experiments. Additionally, we characterized the impact of different conductivity distributions σ_{LF} on $\mathbf{B}_{tissue}$.

Three simulations have been performed in SCIRun (64): two on conductive cylinders and one on a realistic human brain model. For the performed simulations, the TMS coil was modeled using two single-plane spiral wings (65), reflecting the geometry of the TMS coil used in the measurements. These wings were placed at 5 cm from the cylinders to mimic the actual position used in the measurements and in contact with the scalp to mimic the position in realistic TMS treatments.

In the first simulation, we characterized the strength of the z-component of the net (time average over the TMS pulse) incident TMS magnetic field B_{coil_z}, the only one component (parallel to the MR static magnetic field B_0) measurable in an MR experiment. We also characterized the range of the net phase contribution Φ_{B_coil} that would arise from B_{coil_z} in an MR experiment. In an MR experiment, the phase contribution Φ_{B_coil} is proportional to the area underneath the TMS current waveform (63). The same phase contribution can be obtained by using the time average value of the TMS current waveform (appendix A, $\overline{I_{coil}}$) computed from independent oscilloscope measurements. For this simulation, a typical bipolar TMS pulse that lasts for a full period was used (Fig. 4.3, A). The TMS output was set to 1%, leading to a $\overline{I_{coil}}$=3.5 A. By applying the Biot-Savart law, the net B_{coil_z} was computed. This simulation was performed by using a homogeneous conductive cylinder (Fig. 4.4, A) with the same geometry and electric conductivity of the phantom used in the measurements (Fig. 4.4, D). In this way, consistent comparison with measurements could be performed. However, for a bipolar TMS pulse that last for a full period the net induced current in tissue $\overline{\mathbf{J}_{tissue}}$ is zero (appendix A and Fig. 4.3, B) (66). Thus, obviously the induced magnetic field B_{tissue_z} and its related phase contribution Φ_{B_tissue} are zero.

Since information on σ_{LF} is imprinted solely in $\mathbf{B}_{tissue}$, to induce a non-zero net B_{tissue_z} a truncated TMS waveform should be used (appendix A and Fig. 4.3, case 2). Consequently, in the second simulation we used the same waveform adopted in the first simulation but truncated at the first quarter (63): TMS output 1% and $t_1 = 0.1$ ms, leading to $\overline{I_{coil}} = 35$ A and a rate of change of the coil current of 0.55×10^6 A, in line with other studies (36,42). We characterized the strength of the net B_{coil_z} and Φ_{B_coil} for such a truncated TMS pulse.

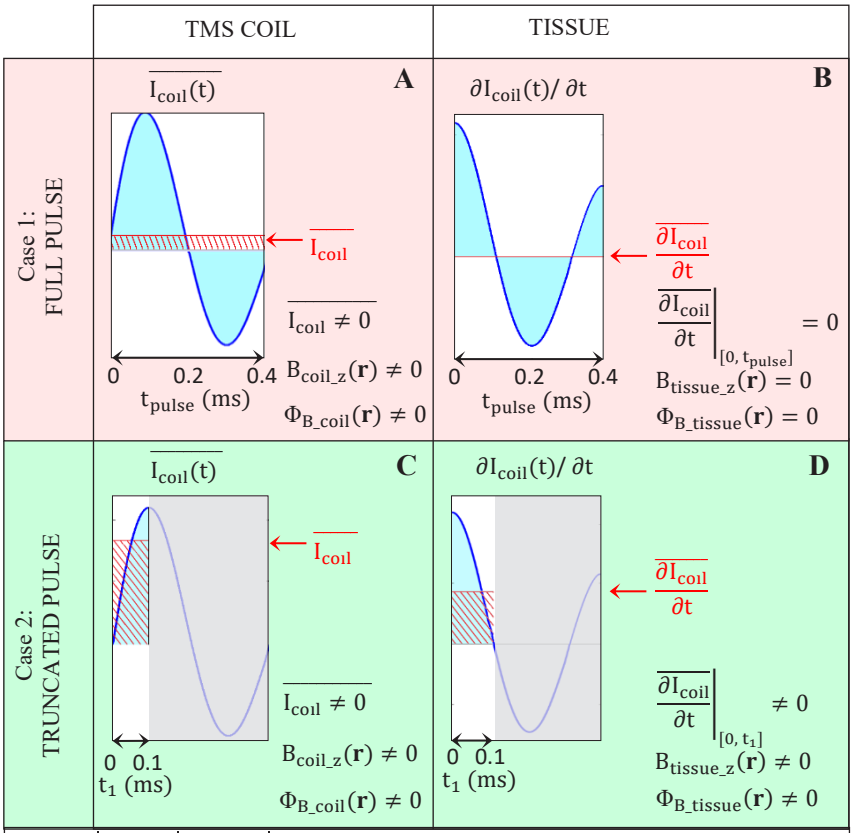

MRI scan	σ	TMS	E: Measured accumulated phase
M1	$\neq 0$	ON	$\Phi_{acc}(\mathbf{r}) = \Phi_{MRI}(\mathbf{r}) + \Phi_{TMS}(\mathbf{r}) = \Phi_{MRI}(\mathbf{r}) + \Phi_{B\_coil}(\mathbf{r}) + \Phi_{B\_tissue}(\mathbf{r})$
M2	$\neq 0$	OFF	$\Phi_{acc}(\mathbf{r}) = \Phi_{MRI}(\mathbf{r})$
M3	$= 0$	ON	$\Phi_{acc}(\mathbf{r}) = \Phi_{MRI}(\mathbf{r}) + \Phi_{TMS}(\mathbf{r}) = \Phi_{MRI}(\mathbf{r}) + \Phi_{B\_coil}(\mathbf{r}); \quad \Phi_{B_{tissue}}(\mathbf{r}) = 0$
M4	$= 0$	OFF	$\Phi_{acc}(\mathbf{r}) = \Phi_{MRI}(\mathbf{r})$

Figure 4.3: Net TMS-coil current, net incident TMS magnetic field and its related phase contribution for a full TMS pulse shape (**A**) and for a truncated TMS pulse shape (**C**). The pulse shape of the current running in the TMS coil was derived from oscilloscope measurements. Net time derivative of the TMS-coil current (proportional to the induced electric field), net induced TMS magnetic field and its related phase contribution for a full TMS pulse shape (**B**) and for a truncated TMS pulse shape (**D**). Four concurrent TMS-MRI measurements (**E**).

Then, the 3D mesh model, the conductivity distribution and the vector potential (computed using the rate of change of the coil current) (35) were given as input to the FEM solver to compute $\mathbf{E}_{tissue}$ and $\mathbf{J}_{tissue}$. From $\mathbf{J}_{tissue}$, the strength of B_{tissue_z} and the range of Φ_{B_tissue} were characterized. By performing this simulation on two different conductive cylinders (one homogeneous and one consisting of two different conducting compartments, Fig. 4.4, A, and B) (67), the impact of different conductive compartments was evaluated.

SIMULATIONS

A HOMOGENEOUS CYLINDER

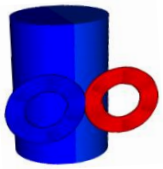

Diameter = 12 cm
Length = 20 cm
σ = 1.6 S/m

B NON-HOMOGENEOUS CYLINDER

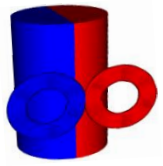

Diameter = 12 cm
Length = 20 cm
σ = 1.6 S/m
σ = 0.8 S/m

C HUMAN BRAIN MODEL

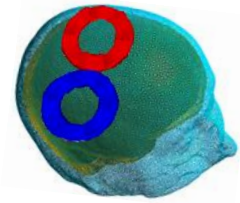

σ [S/m]	GM	WM	CSF	Skull	Skin
Model 1	0.27	0.12	1.65	0.01	0.46
Model 2	0.61	0.29	1.52	0.01	0.46
Model 3	0.1	0.065	2	0.01	0.46

MEASUREMENTS

D

	σ_{RF} [S/m]	Agar [gr/L]	NaCl [gr/L]	T [°C]	f [MHz]	Diameter [cm]	Length [cm]
Conductive phantom	1.6	20	9.2	23	128	12	20
Reference phantom	0	20	0	23	128	12	20

Figure 4.4: Cylindrical models used in simulations: one homogeneous (**A**) and one with two compartments (**B**). The 3D-mesh was performed using GMSH. Realistic human brain model and three sets of tissue conductivity used in simulations (**C**). Geometry and composition of the experimental phantoms (**D**). Conductivity values were confirmed by dielectric probe measurements (85070E Agilent Technology, Santa Clara, CA).

In the third simulation we defined the strength of B_{coil_z} and B_{tissue_z} for realistic, *in-vivo* situations by using a realistic human brain model (68) and the truncated TMS waveform adopted in the second simulation. We therefore explored the feasibility of measuring Φ_{B_tissue} *in-vivo* by characterizing the required phase accuracy for concurrent TMS-MRI experiments. Additionally, we evaluated the impact of different σ_{LF} distributions on $\mathbf{E}_{tissue}$ (relevant quantity for TMS dosimetry) and $\mathbf{B}_{tissue}$. Finally, we characterized the phase accuracy needed to detect subtle variations in $\mathbf{B}_{tissue}$ arising from these variations in σ_{LF}. The phase accuracy determines the feasibility of this technique. The adopted σ_{LF} values reflect the conductivity variations reported in other studies (35,38,42) (Fig. 4.4, C).

4.3.2 MRI Measurements

Concurrent TMS-MRI measurements were conducted in a 3T MR scanner (Achieva, Philips Healthcare, Best, The Netherlands) with elliptical surface MR receive coils (flex-M) and using a standard TMS stimulator (Magstim Rapid2, Whitland, UK) with an MR-compatible figure-8 TMS coil (28,69). By using a typical TMS-MRI setup, the phase accuracy characterized by these measurements is representative.

The MR sequence adopted was a Spin-Echo sequence: TR/TE = 1000/50 ms, FOV = 160×160×2.5 mm^3, resolution = 2.5×2.5×2.5 mm^3, voxel/BW = 0.15/3 kHz, NSA = 2. The TMS device was synchronized with the MR sequence by using as a reference time point the MR-TTL (transistor-transistor logic) signal delivered at every RF excitation. TMS pulses were delivered prior to each readout gradient (69). The surface of the TMS coil was placed at 4.5 cm from the phantoms. For each experiment, four measurements were performed to correctly isolate the phase contributions Φ_{B_coil} and Φ_{B_tissue} (appendix B and Fig. 4.4, D: M1-4). For the measurements with TMS-on, the TMS outputs were 1% and 4%, respectively for the first and the second TMS-MRI experiment. Since a standard TMS stimulator was used, only bipolar pulses that lasted for a full period could be employed (Fig. 4.3, case 1). For these measurements, we prepared two agar phantoms sturdy enough to prevent motion artifacts (60): one conductive (1.6 S/m) and one non-conductive, as a reference to compensate for Φ_{B_coil} (appendix B, Fig. 4.4, D). The two phantoms were placed at the same position in the scanner by using a dedicated phantom holder.

With these experiments, we characterized the phase range of Φ_{TMS}, which in principle includes both the contributions Φ_{B_coil} and Φ_{B_tissue}, by using the conductive phantom (appendix B). We also characterized the phase range of only Φ_{B_coil} by using the non-conductive phantom. This allowed direct comparison with the first simulation. We finally characterized the achievable MR phase accuracy (inverse of the signal-to-noise ratio, SNR) (59) to enable Φ_{B_tissue} measurements in concurrent TMS-MRI experiments for a realistic TMS-MRI setup.

4.4 Results

The impact of a realistic TMS pulse shape that lasts for a full period (Fig. 4.3, case 1) on the TMS related phase contribution Φ_{B_coil} is characterized by using the homogeneous cylinder (Fig. 4.5, A). The results of this first simulation are shown on the same plane where measurements were performed, thus mimicking the experimental setup and allowing direct comparison with the measurements. From simulations, B_{coil_z} is on the order of 10^{-5} T (Fig. 4.5, B) leading to a Φ_{B_coil} in the order of radians (Fig. 4.5, C). This result suggests that Φ_{B_coil}, and thus B_{coil_z}, can be measured in an MR experiment.

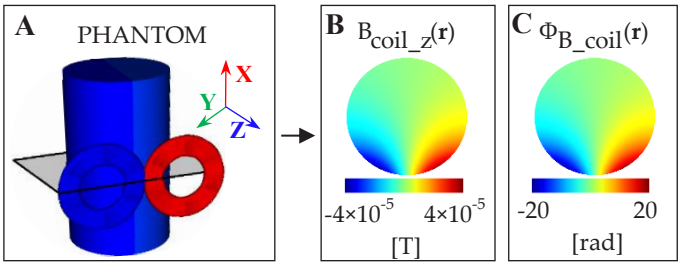

Figure 4.5: Phantom simulation (full TMS waveform): the displayed maps are extracted from 3D simulations on the same plane where measurements were performed. **(A)** Homogeneous cylindrical model. **(B)** Z-component of $\mathbf{B}_{coil}$ and **(C)** Φ_{B_coil} maps, both independent from the sample conductivity.

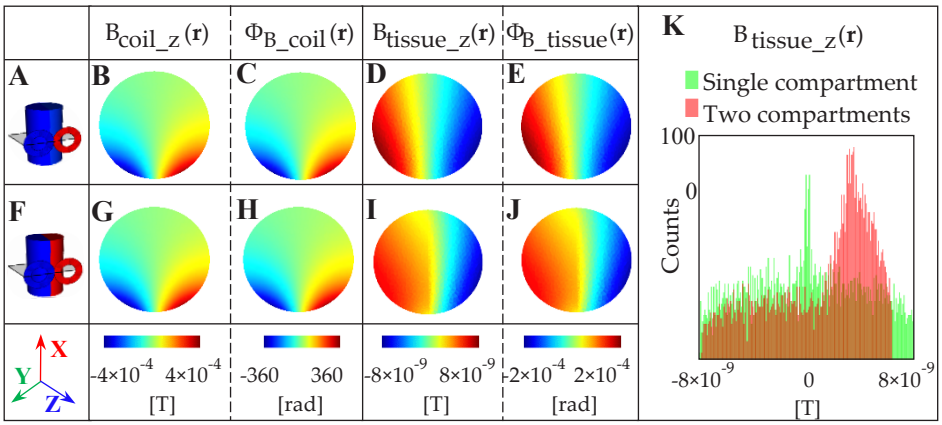

Figure 4.6: Phantom simulations (truncated TMS waveform). **(A)** Homogeneous and **(F)** two-compartment cylindrical models. **(B, G)** Z-component of $\mathbf{B}_{coil}$ and **(C, H)** Φ_{B_coil} maps, independent from the sample conductivity. **(D, I)** Z-component of $\mathbf{B}_{tissue}$ and **(E, J)** Φ_{B_tissue} maps for the two cylindrical models. **(K)** Histograms of $\mathbf{B}_{tissue}$ for the two models. Clearly visible the variation in $\mathbf{B}_{tissue}$ patterns between the two models.

In Fig. 4.6, the results from the second simulations on two conductive cylinders and using the truncated TMS pulse waveform to induce a non-zero B_{tissue_z} (Fig. 4.3, case 2) are shown. We observe that the use of a truncated TMS waveform leads to an increase in B_{coil_z} (10^{-4} T) and, consequently, in Φ_{B_coil} (10^{2} rads) with respect to the use of a full TMS waveform (Fig. 4.5). Additionally, by comparing the results obtained from the two different conductive cylinders, we observe that the incident magnetic field B_{coil_z} (Fig. 4.6, B and G) and its related phase contribution Φ_{B_coil} (Fig. 4.6, C and H) are not affected by the presence of different conductive compartments. This is because the incident magnetic field does not depend on the conductivity of the structure underneath the TMS coil. Instead, as shown by these simulations, the conductivity distribution σ_{LF} modulates the induced magnetic field B_{tissue_z} (Fig. 4.6, D and I) and thus its related phase contribution Φ_{B_tissue} (Fig. 4.6, E and J). The impact of σ_{LF} variations is clearly visible from the discrepancy between the histograms of the two B_{tissue_z} maps (Fig. 4.6, K). However, it is important to note that the induced magnetic field B_{tissue_z} (~10^{-8} T) is about four orders of magnitude lower than incident magnetic field B_{coil_z} (10^{-4} T). As shown in Fig. 4.6, E and J, Φ_{B_tissue} is in the range of ~10^{-4} rads. This result characterizes the phase accuracy needed to measure B_{tissue_z} in concurrent TMS-MRI experiments. Moreover, these results highlight the challenge of correctly disentangling phase contributions arising from B_{coil_z} and B_{tissue_z}, as the latter field is a very small fraction of the former.

In the third simulations, the impact of inter-subject variations of σ_{LF} on $\mathbf{E}_{tissue}$ and B_{tissue_z} and the range of B_{coil_z} and B_{tissue_z} is characterized for a realistic human brain model. For the adopted three brain models, the norm of $\mathbf{E}_{tissue}$ is shown on the gray matter (GM) and white matter (WM) surfaces (Fig. 4.7). Our results are in line with the results presented in (35). By comparing the mean and standard deviation of the top 30% values of $\|\mathbf{E}_{tissue}\|$ for the three models (calculated independently for each brain model in GM and WM), we observe that different σ_{LF} values induce significant variations in $\mathbf{E}_{tissue}$ (Fig. 4.7, bar-plots). This highlights the importance of accurately measuring subject-specific tissue σ_{LF} values to guide TMS dosimetry.

For each brain model (Fig. 4.8, A), B_{tissue_z} and the related phase contribution Φ_{B_tissue} are computed (Fig. 4.8, C). The induced magnetic field B_{tissue_z} (10^{-8} T) is about four orders of magnitude lower than incident magnetic field B_{coil_z} (10^{-4} T) (Fig. 4.8, B), in line with what was previously observed for the cylindrical structure (Fig. 4.6). Additionally B_{tissue_z} maps show slightly different patterns between the three different brain models due to the different conductivity distributions. This is a direct consequence of the previously observed variations in the $\mathbf{E}_{tissue}$ maps. As shown in Fig. 4.8, D, variations in σ_{LF} lead to magnetic field variations in the range of nT. From these results, we conclude that the necessary MR phase accuracy needed to measure Φ_{B_tissue} for *in-vivo* TMS-MRI experiments is about 10^{-4} rads. Still, higher accuracy will be needed to detect variations in tissue conductivity distributions.

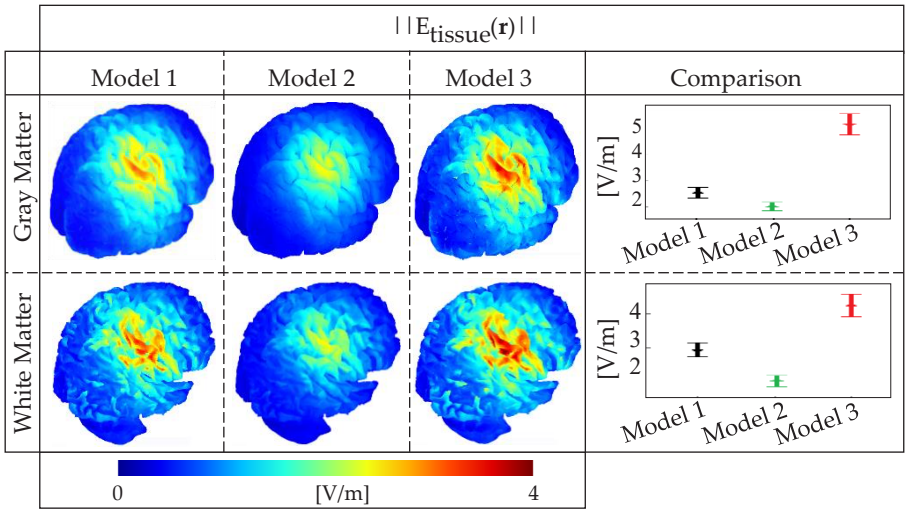

Figure 4.7: Norm of $\mathbf{E}_{tissue}$ in the gray matter (GM - top row) and white matter (WM - bottom row) for the three brain models. Mean and standard deviation of the top 30% values of the norm of $\mathbf{E}_{tissue}$ for each brain model in GM and WM. It is visible how different σ_{LF} distributions lead to significant variations in $\mathbf{E}_{tissue}$.

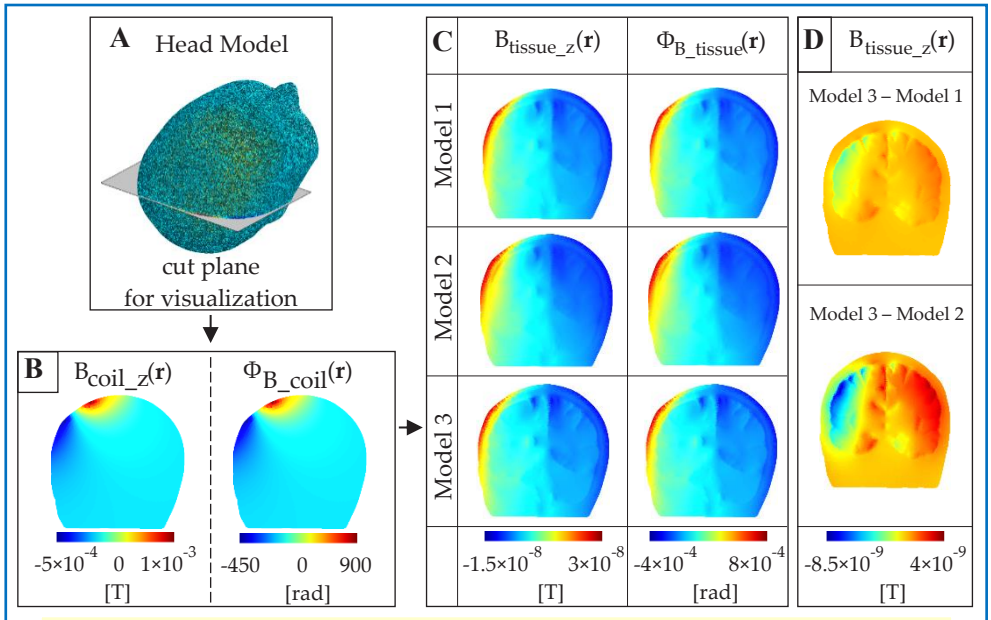

Figure 4.8: (A) Realistic head model. **(B)** Z-component of $\mathbf{B}_{coil}$ and Φ_{B_coil} maps, independent from σ_{LF}. **(C)** For each model, the z-component of $\mathbf{B}_{tissue}$ and Φ_{B_tissue} are computed. **(D)** Variations in the z-component of $\mathbf{B}_{tissue}$ due to different conductivity distributions. These maps were computed by subtracting $\mathbf{B}_{tissue}$ of model 3 and $\mathbf{B}_{tissue}$ of model 1 (upper part), $\mathbf{B}_{tissue}$ of model 2 (bottom part).

In Fig. 4.9 and Fig. 4.10, the results of the two experiments performed by using a realistic TMS-MRI setup and a full TMS waveform are proposed. With these experiments, we assess the attainable MR phase accuracy for concurrent TMS-MRI experiments. In both experiments, two phase maps were acquired for each phantom (one conductive and one non-conductive): one with TMS-on (Fig. 4.9, and 4.10, A, and C) and one with TMS-off (Fig. 4.9, and 4.10, B, and D). The significant impact of different Φ_{RF} (RF phase contribution, ~3 rads, appendix B), which scales with the RF conductivity (MHz), is visible in the measurements with TMS-off. This highlights the importance of correctly compensating for Φ_{RF}.

By subtracting the phase maps measured with TMS-on and TMS-off (appendix B, eq. [4.B2], subtraction inside parentheses), Φ_{TMS} (Fig. 4.9, and 4.10, E) and Φ_{B_coil} (Fig. 4.9, and 4.10, F) are computed for the conductive and the non-conductive phantoms, respectively. As shown in the plots (Fig. 4.9, and 4.10, G), Φ_{TMS} coincides with Φ_{B_coil}. From Φ_{B_coil} maps, the z-component of $\mathbf{B}_{coil}$ is reconstructed (Fig. 4.9, and 4.10, H). The range of the measured Φ_{B_coil} (radians) and B_{coil_z} (10^{-5} T) reflects quantitatively the values previously observed in simulations. Finally, Φ_{B_tissue} maps can be in principle obtained by subtracting Φ_{TMS} and Φ_{B_coil} maps (appendix B, eq. [4.B2], subtraction between parentheses) (Fig. 4.9, and 4.10, I).

For the performed measurements, the actual MR phase accuracy for Φ_{B_tissue} detection is estimated to be in the order of 10^{-2} rad, which is two orders higher than what is required from simulations. Additionally, for the adopted full TMS waveform we should observe that Φ_{B_tissue} is zero, since the net induced $\mathbf{J}_{tissue}$ is zero. Still, in Φ_{B_tissue} maps we can observe a certain pattern in the range of 0.1 rads. This pattern is caused by an imperfect compensation of Φ_{B_coil} while performing the subtraction between Φ_{TMS} and Φ_{B_coil} (relative error ~1%). Therefore, this result highlights that very high precision is required to correctly compensate for Φ_{B_coil}.

Finally, to evaluate whether a stronger net incident TMS magnetic field could be of benefit, we performed a second experiment with a TMS output of 4%. From our measurements (Fig. 4.10), significant image corruption can be observed in the region underneath the TMS coil. This corruption arises from the intra-voxel dephasing created by the stronger incident, highly non-uniform TMS magnetic field $\mathbf{B}_{coil}$.

4.5 Discussion

Being able to measure subject-specific σ_{LF} would be valuable for different fields of research such as oncology and neuroscience (11–14,70). In MR-EIT, *in-vivo* conductivity measurements requires direct injection of eddy currents in tissue and measurements of their impact on the MR phase (49–51). In this study, we explored whether inductive generation of currents by means of an MR compatible TMS setup could be a less painful alternative to MR-EIT.

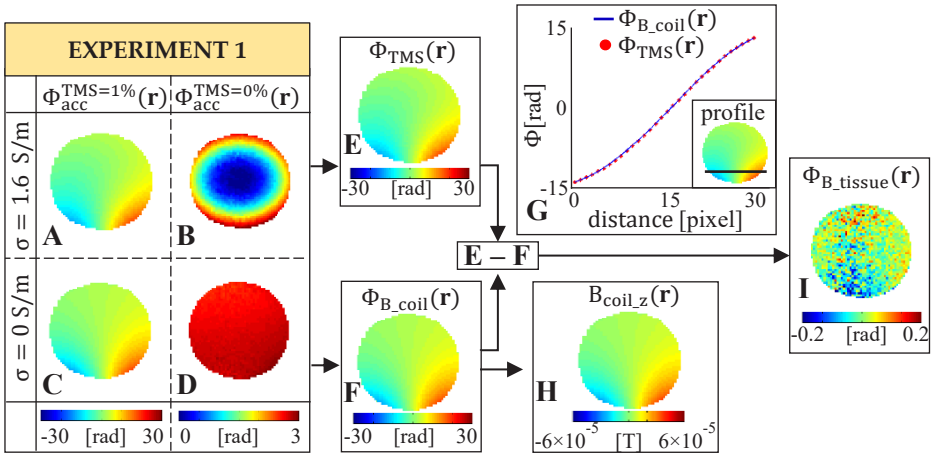

Figure 4.9: Experiment 1: TMS = 1%. Phase maps with TMS-ON for the conductive **(A)** and non-conductive **(C)** phantom. Phase maps with TMS-OFF for the conductive **(B)** and non-conductive **(D)** phantom. **(E)** Reconstructed Φ_{TMS} map for the conductive phantom. **(F)** Reconstructed Φ_{B_coil} map for the reference phantom. **(G)** Comparison between Φ_{TMS} and Φ_{B_coil} profiles. **(H)** Reconstructed B_{coil_z} map. **(I)** Φ_{B_tissue} map (subtraction between Φ_{TMS} and Φ_{B_coil}).

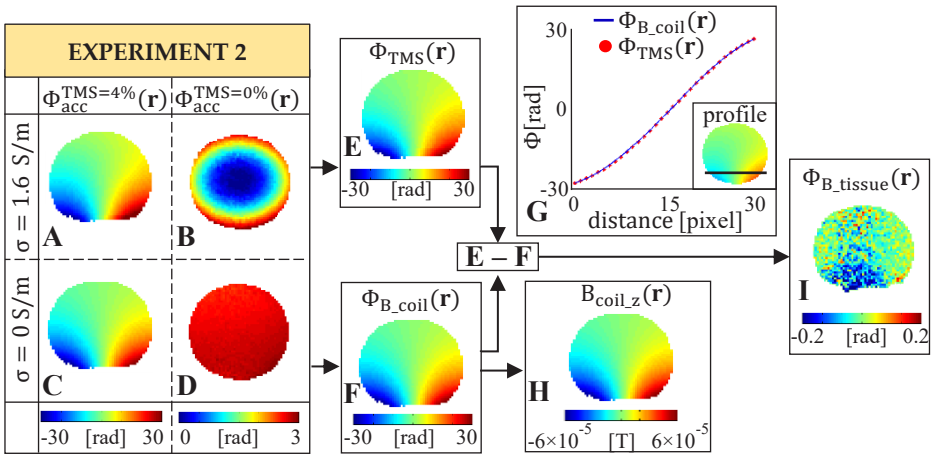

Figure 4.10: Experiment 2: TMS = 4%. Phase maps with TMS-ON for the conductive **(A)** and non-conductive **(C)** phantom. Phase maps with TMS-OFF for the conductive **(B)** and non-conductive **(D)** phantom. **(E)** Reconstructed Φ_{TMS} map for the conductive phantom. **(F)** Reconstructed Φ_{B_coil} map for the reference phantom. **(G)** Comparison between Φ_{TMS} and Φ_{B_coil} profiles. **(H)** Reconstructed B_{coil_z} map. **(I)** Φ_{B_tissue} map (subtraction between Φ_{TMS} and Φ_{B_coil}).

Such a setup is able to generate much stronger time-varying magnetic fields than the time-varying magnetic fields of switched MR gradient coils previously proposed in other studies (58–60). Still, as shown by our analysis, three main challenges hamper measurements of the induced magnetic field arising from inductively induced currents in tissues.

First, for such an inductive technique to work, it is crucial to correctly disentangle the incident magnetic field from the induced magnetic field. This is because, only this latter field contains information on tissue σ_{LF}. For this purpose, subtractions between different phase images are needed (appendix B). The fundamental problem is that the induced magnetic field $\mathbf{B}_{tissue}$ is about 10^{-4} lower that the incident magnetic field $\mathbf{B}_{coil}$. Therefore, very high precision and reproducibility is required to correctly disentangle the phase contribution Φ_{B_tissue} arising from $\mathbf{B}_{tissue}$ from the phase contribution Φ_{B_coil} arising from $\mathbf{B}_{coil}$.

Second, as demonstrated, information on σ_{LF} is only imprinted in $\mathbf{B}_{tissue}$. Therefore, to reconstruct σ_{LF} the net $\mathbf{B}_{tissue}$ has to be non-zero. As discussed in this work, this requirement is satisfied if a truncated TMS pulse is used. However, for standard TMS setups, only TMS pulses that last for a full period can be employed, thus the net $\mathbf{B}_{tissue}$ is zero (appendix A, Fig. 4.3, case 1) (66). Therefore, an additional setup (pulse modulator) should be used to comply with this requirement.

Third, supposing that it would be possible to correctly isolate Φ_{B_tissue} from all the other phase contributions, from our simulations the phase range of Φ_{B_tissue} is in the order of 10^{-4} rads. This phase range is about two orders of magnitude lower than the detectable phase in concurrent TMS-MRI experiments. Additionally, to distinguish variations in the tissue conductivity, even higher phase accuracy would be needed.

In order to bring Φ_{B_tissue} into a measurable phase range, one should increase $\mathbf{B}_{tissue}$ of at least two orders of magnitude. To strengthen $\mathbf{B}_{tissue}$, one can increase the strength of the induced current $\mathbf{J}_{tissue}$ by increasing the TMS pulse frequency and pulse strength.

By increasing the pulse frequency, i.e. reducing the induction time (t_i), stronger $\mathbf{J}_{tissue}$ and therefore $\mathbf{B}_{tissue}$ can be achieved. On the other hand, attention has to be paid not to enter into a different dispersion band. Brain tissues exhibit the beta dispersion centered between 10^5-10^7 Hz. Above this dispersion band (100 MHz), the cell membranes exhibit a negligible impedance, so currents are capable to pass through both the extracellular and intracellular media (71). To avoid conductivity reconstructions in a different frequency dispersion band, thus non-directly translatable to LF tissue conductivity, the TMS-pulse frequency (1-10 kHz) can be increased by an additional factor of 10 (i.e. t_i=0.01 ms). However, in an MRI experiment the measured net Φ_{B_tissue} is proportional to both B_{tissue_z} and the induction time t_i.

Hence, in the computation of Φ_{B_tissue}, the increase in B_{tissue_z} is cancelled by the reduction in the induction time t_i, leading to an unchanged Φ_{B_tissue} range. For this reason, the increase of the TMS-pulse frequency would not be a beneficial solution.

As aforementioned, another strategy to increase the induced $\mathbf{J}_{tissue}$ can be to strengthen the TMS output. $\mathbf{B}_{tissue}$ increases with a stronger TMS output, but $\mathbf{B}_{coil}$ increases as well. Unfortunately, as already observed in Fig. 4.10, this leads to considerable signal dephasing. From our results, a truncated TMS pulse and much stronger TMS outputs should be used to bring Φ_{B_tissue} above the noise level. To comply with such a requirement, one should measure much stronger, highly non-uniform Φ_{B_coil}. Consequently, to avoid signal dephasing, one should therefore reduce considerably the voxel size (range of μm).

This latter observation brings us to a final consideration. A smaller voxel size comes quickly at the cost of SNR loss. Instead, to detect very small magnetic field fluctuations such as the one produced by $\mathbf{B}_{tissue}$, the SNR should be considerably increased. Thus, only the number of scan repetitions (NSA) can be increased. However, in practice, unfeasible scan time would be required to achieve enough SNR for Φ_{B_tissue} measurements.

As discussed, the unsuccessful ability to measure $\mathbf{B}_{tissue}$ by inductively inducing currents in the brain using a combined TMS-MRI setup arises from the physical limitations behind the physics of the induction principle. On the contrary, by injecting currents in tissues (MR-EIT), direct measurements of $\mathbf{B}_{tissue}$, and consequently σ_{LF} reconstructions, are feasible. The first macroscopic difference between the two techniques is that in MR-EIT images subtractions between different conductive phantoms are not needed. This is because currents are directly injected into the brain, thus there is not an incident magnetic field $\mathbf{B}_{coil}$. Secondly, for both techniques, Φ_{B_tissue} is proportional to B_{tissue_z} and to t_i, time of injection/induction. Despite the comparable B_{tissue_z} range ($\pm 10^{-8}$ T), the relevant difference in the time of injection/induction (10 ms in MR-EIT and 0.1 ms in TMS-MRI) leads to a measurable/non-measurable Φ_{B_tissue} in MR-EIT and in TMS-MRI, respectively (72).

These observations define the physical limitations hampering the feasibility of non-invasively measuring subject-specific σ_{LF}. Hence, future studies should focus on alternative methodologies to non-invasively and non-painfully measure $\mathbf{B}_{tissue}$ for subject-specific σ_{LF} reconstructions.

4.6 Conclusions

Low-frequency tissue conductivity σ_{LF} reconstructions can only be performed by measuring the phase contribution arising from the induced magnetic field in which information on σ_{LF} is imprinted.

However, despite stronger currents being inductively induced using a TMS stimulator compared to MR gradient coils, these measurements are not feasible with a standard TMS-MRI setup. This is because the induced magnetic field is very weak, thus very high SNR is required to correctly measure it. If a higher level of current running through the TMS coil is used to strengthen the induced currents in tissues and to increase the induced magnetic field, considerable image dephasing would be observed due to the strong, highly non-uniform incident TMS magnetic field. In the light of our observations, we believe that direct σ_{LF} reconstructions performed by inductively inducing currents in the brain are not feasible even if a TMS-MRI setup is used.

4.7 Appendices

Appendix A

In TMS, a damped sinusoidal current runs in the TMS coil (73):

$$I_{coil}(t) = Ie^{-\alpha t}\sin(\omega_{TMS}t) \quad [4.A1]$$

with α: damping factor, $\omega_{TMS} = 2\pi f_{TMS}$, and $f_{TMS} \approx 5$ kHz. If a TMS pulse that lasts for a full sinusoidal period is used (Fig. 4.3, case 1, pulse duration = t_{pulse}), the time average of the current running in the coil is not zero:

$$\overline{I_{coil}} = \frac{1}{t_{pulse}}\int_0^{t_{pulse}} I_{coil}(t)dt \neq 0\ . \quad [4.A2]$$

Consequently, as suggested in previous studies (63,74), it is possible to measure the net incident TMS magnetic field B_{coil_z} leading to the MR phase contribution Φ_{B_coil} in concurrent TMS-MRI experiments (Fig. 4.3, A). However, to reconstruct the LF conductivity of the imaging sample, the phase contribution Φ_{B_tissue} arising from the LF currents induced in tissues ($\mathbf{J}_{tissue}$) has to be measured. Unfortunately, if a full TMS pulse is used, it follows from eqs. [4.1] and [4.2] that there is no net induced current in tissue (Fig. 4.3, B):

$$\overline{\mathbf{J}_{tissue}(\mathbf{r})} \propto \frac{1}{t_{pulse}}\int_0^{t_{pulse}} \frac{\partial \mathbf{B}_{coil}(\mathbf{r},t)}{\partial t}dt = 0\ . \quad [4.A3]$$

Thus from eq. [4.4], the net B_{tissue_z} and consequently its MR phase contribution Φ_{B_tissue} are zero (66). For this case, direct information on σ_{LF} cannot be achieved. To maximize Φ_{B_tissue}, a TMS pulse shape truncated at the first quarter of a bipolar TMS pulse should be used (Fig. 4.3, case 2, pulse duration = t_1), as in a previous reported study (63). For this second case (Fig. 4.3, C and D):

$$\overline{I_{coil}} = \frac{1}{t_1}\int_0^{t_1} I_{coil}(t)dt \neq 0 \quad [4.A4]$$

$$\overline{\mathbf{J}_{tissue}(\mathbf{r})} \propto \frac{1}{t_1}\int_0^{t_1} \frac{\partial \mathbf{B}_{coil}(\mathbf{r},t)}{\partial t}dt \neq 0\ . \quad [4.A5]$$

Therefore, from eqs. [4.A4] and [4.A5] it follows that both TMS related phase contributions Φ_{B_coil} and Φ_{B_tissue} are not zero. Thus, for this case, direct information on σ_{LF} can in principle be achieved from measurements of Φ_{B_tissue}. Still, it is crucial to correctly disentangle these two phase contributions (see appendix B).

As a final remark, it has to be noted that $\overline{I_{coil}}$ is much stronger for a truncated TMS pulse than a full TMS pulse with the same TMS output strength. This is because, for a truncated TMS pulse only the first half of the positive current lobe is considered, while the negative lobe which reduces the strength of $\overline{I_{coil}}$ is not present.

Appendix B

In a TMS-MRI experiment, if a TMS pulse is delivered between the MRI RF excitation pulse and the MRI readout gradient, the measured phase accumulation Φ_{acc} is composed by two main terms:

$$\Phi_{acc}(\mathbf{r}) = \Phi_{MRI}(\mathbf{r}) + \Phi_{TMS}(\mathbf{r}) \, . \qquad [4.B1]$$

Φ_{MRI} is the intrinsic MR phase contribution. It takes into account the RF phase contribution Φ_{RF}, which depends on the sample conductivity at the RF frequency (MHz), and the system-eddy-currents phase contribution Φ_{system}.

Φ_{TMS} is the total TMS related phase contribution arising from $\mathbf{B}_{total}$. Therefore, from eq. [4.13], it follows that Φ_{TMS} includes both the phase contributions Φ_{B_coil} and Φ_{B_tissue} arising from the incident and the induced TMS magnetic field, respectively. Since information on tissue σ_{LF} is imprinted only in the induced TMS magnetic field $\mathbf{B}_{tissue}$, an additional challenge in concurrent TMS-MRI experiment is to isolate Φ_{B_tissue} from all the other phase contributions. For this purpose four measurements are needed: two on a conductive sample and two on a non-conductive, reference sample, and with TMS on/off for each sample (Fig. 4.3, E: M1-4) (60):

$$\Phi_{B\_tissue}(\mathbf{r}) = (\Phi_{M1}(\mathbf{r}) - \Phi_{M2}(\mathbf{r}))_{\sigma\neq 0} - (\Phi_{M3}(\mathbf{r}) - \Phi_{M4}(\mathbf{r}))_{\sigma=0} \, . \qquad [4.B2]$$

The subtraction between parentheses, related to measurements performed on a conductive sample and on the reference sample, isolates the two TMS related phase contributions Φ_{B_tissue} and Φ_{B_coil}. In principle, the MR related phase contribution Φ_{system}, which does not change for different measurements, is also compensated with this subtraction. Instead, since the RF phase Φ_{RF} scales directly with the RF conductivity of the sample, Φ_{RF} would not be correctly compensated if only the subtraction between different conductive samples is performed. Therefore, to correctly compensate for Φ_{RF} it is necessary to compute the subtractions inside the two parentheses, related to measurements performed on the same phantom and with TMS on and off, respectively.

4.8 References

1. Voigt T, Katscher U, Doessel O. Quantitative conductivity and permittivity imaging of the human brain using electric properties tomography. Magn. Reson. Med. 2011;66:456–466. doi: 10.1002/mrm.22832.
2. Sodickson DK, Alon L, Deniz CM, et al. Local Maxwell Tomography using transmit-receive coil arrays for contact-free mapping of tissue electrical properties and determination of absolute RF phase. Proc. 20th Sci. Meet. Int. Soc. Magn. Reson. Med. Melbourne, Victoria, Aust. 2012;20:387.
3. van Lier ALHMW, Brunner DO, Pruessmann KP, Klomp DWJ, Luijten PR, Lagendijk JJW, Van Den Berg CAT. B1+ phase mapping at 7 T and its application for in-vivo electrical conductivity mapping. Magn. Reson. Med. 2012;67:552–561. doi: 10.1002/mrm.22995.
4. Lee J, Shin J, Kim D. MR-Based Conductivity Imaging Using Multiple Receiver Coils. Magn. Reson. Med. 2015. doi: 10.1002/mrm.25891.
5. Liu J, Zhang X, Schmitter S, Van de Moortele P-F, He B. Gradient-based electrical properties tomography (gEPT): A robust method for mapping electrical properties of biological tissues in-vivo using magnetic resonance imaging. Magn. Reson. Med. 2015; 74:634–646. doi: 10.1002/mrm.25434.
6. Pethig R. Dielectric Properties of Biological Materials: Biophysical and Medical Applications. IEEE Trans. Electr. Insul. 1984;EI-19:453–474. doi: 10.1109/TEI.1984.298769.
7. Gabriel S, Lau RW, Gabriel C. The dielectric properties of biological tissues: II. Measurements in the frequency range 10 Hz to 20 GHz. Phys. Med. Biol. 1996;41:2251–2269. doi: http://dx.doi.org/10.1088/0031-9155/41/11/002.
8. Gabriel C, Peyman A, Grant EH. Electrical conductivity of tissue at frequencies below 1 MHz. Phys. Med. Biol. 2009;54:4863–4878. doi: 10.1088/0031-9155/54/16/002.
9. Gullmar D, Haueisen J, Reichenbach JR. Influence of anisotropic electrical conductivity in white matter tissue on the EEG/MEG forward and inverse solution. A high-resolution whole head simulation study. Neuroimage 2010;51:145–163. doi: 10.1016/j.neuroimage.2010.02.014.
10. Jochmann T, Güllmar D, Haueisen J, Reichenbach JR. Influence of tissue conductivity changes on the EEG signal in the human brain - A simulation study. Z. Med. Phys. 2011:102–112. doi: 10.1016/j.zemedi.2010.07.004.
11. Ilmoniemi RJ, Kičić D. Methodology for combined TMS and EEG. Brain Topogr. 2010;22:233–248. doi: 10.1007/s10548-009-0123-4.
12. Harvey BM, Vansteensel MJ, Ferrier CH, et al. Frequency specific spatial interactions in human electrocorticography: V1 alpha oscillations reflect surround suppression. Neuroimage 2013;65:424–432. doi: doi:10.1016/j.neuroimage.2012.10.020.
13. de Berker AO, Bikson M, Bestmann S. Predicting the behavioral impact of transcranial direct current stimulation: issues and limitations. Front. Hum. Neurosci. 2013;7:613. doi: 10.3389/fnhum.2013.00613.
14. Peters JC, Reithler J, Schuhmann T, de Graaf T, Uludag K, Goebel R, Sack AT. On the feasibility of concurrent human TMS-EEG-fMRI measurements. J. Neurophysiol. 2013: 1214–1227. doi: 10.1152/jn.00071.2012.
15. Hummel FC, Cohen LG. Non-invasive brain stimulation: a new strategy to improve neurorehabilitation after stroke? Lancet Neurol. 2006;5:708–712. doi: 10.1016/S1474-4422(06)70525-7.

16. O'Reardon JP, Solvason HB, Janicak PG, et al. Efficacy and Safety of Transcranial Magnetic Stimulation in the Acute Treatment of Major Depression: A Multisite Randomized Controlled Trial. Biol. Psychiatry 2007;62:1208–1216. doi: 10.1016/j.biopsych.2007.01.018.

17. Rossini PM, Rossi S. Transcranial magnetic stimulation: Diagnostic, therapeutic, and research potential. Neurology 2007;68:484–488. doi: http://dx.doi.org/10.1212/01.wnl.0000250268.13789.b2.

18. Fregni F, Pascual-Leone A. Technology insight: noninvasive brain stimulation in neurology - perspectives on the therapeutic potential of rTMS and tDCS. Nat. Clin. Pract. Neurol. 2007;3:383–393. doi: 10.1038/ncpneuro0530.

19. Pollak TA, Nicholson TR, Edwards MJ, David AS. A systematic review of transcranial magnetic stimulation in the treatment of functional (conversion) neurological symptoms. J. Neurol. Neurosurg. Psychiatry 2014;85:191–197. doi: 10.1136/jnnp-2012-304181.

20. Rossini PM, Burke D, Chen R, et al. Non-invasive electrical and magnetic stimulation of the brain, spinal cord, roots and peripheral nerves: basic principles and procedures for routine clinical and research application. An updated report from an I.F.C.N. Committee. Clin. Neurophysiol. 2015;126:1071–1107. doi: 10.1016/j.clinph.2015.02.001.

21. Kobayashi M, Pascual-Leone A. Transcranial magnetic stimulation in neurology. Lancet Neurol. 2003;2:145–156. doi: 10.1016/S1474-4422(03)00321-1.

22. Siebner HR, Hartwigsen G, Kassuba T, Rothwell JC. How does transcranial magnetic stimulation modify neuronal activity in the brain? Implications for studies of cognition. Cortex 2009:1035–1042. doi: 10.1016/j.cortex.2009.02.007.

23. Schutter DJLG, van Honk J. A standardized motor threshold estimation procedure for transcranial magnetic stimulation research. J. ECT 2006;22:176–178. doi: 10.1097/01.yct.0000235924.60364.27.

24. Bestmann S, de Berker AO, Bonaiuto J. Understanding the behavioural consequences of noninvasive brain stimulation. Prog Brain Res, Comput. Neurostimulation 2015;19:75–100. doi: 10.1016/j.tics.2014.10.003.

25. Roth BJ, Saypol JM, Hallett M, Cohen LG. A theoretical calculation of the electric field induced in the cortex during magnetic stimulation. Electroencephalogr. Clin. Neurophysiol. Potentials Sect. 1991;81:47–56. doi: http://dx.doi.org/10.1016/0168-5597(91)90103-5.

26. Tofts PS, Branston NM. The measurement of electric field, and the influence of surface charge, in magnetic stimulation. Electroencephalogr. Clin. Neurophysiol. 1991;81:238–239. doi: 10.1016/0168-5597(91)90077-B.

27. Komssi S, Kähkönen S, Ilmoniemi RJ. The Effect of Stimulus Intensity on Brain Responses Evoked by Transcranial Magnetic Stimulation. Hum. Brain Mapp. 2004;21:154–164. doi: 10.1002/hbm.10159.

28. de Weijer A, Sommer I, Bakker E, Bloemendaal M, Bakker C, Klomp DWJ, Bestmann S, Neggers B. A setup for administering TMS to medial and lateral cortical areas during whole brain fMRI recording. J. Clin. Neurophysiol. 2014;31:474–487. doi: 10.1097/WNP.0000000000000075.

29. Janssen AM, Oostendorp TF, Stegeman DF. The effect of local anatomy on the electric field induced by TMS: evaluation at 14 different target sites. Med. Biol. Eng. Comput. 2014;52:873–883. doi: 10.1007/s11517-014-1190-6.

30. Wassermann EM. Variation in the response to transcranial magnetic brain stimulation in the general population. Clin. Neurophysiol. 2002;113:1165–1171. doi: 10.1016/S1388-2457 (02)00144-X.

31. Stokes MG, Chambers CD, Gould IC, Henderson TR, Janko NE, Allen NB, Mattingley JB. Simple Metric For Scaling Motor Threshold Based on Scalp-Cortex Distance: Application to Studies Using Transcranial Magnetic Stimulation. J. Neurophysiol. 2005;94:4520–4527. doi: 10.1152/jn.00067.2005.

32. Peterchev A V., Wagner TA, Miranda PC, Nitsche MA, Paulus W, Lisanby SH, Pascual-Leone A, Bikson M. Fundamentals of transcranial electric and magnetic stimulation dose: Definition, selection, and reporting practices. Brain Stimul. 2012;5:435–453. doi: 10.1016/ j.brs.2011.10.001.

33. Neggers SFW, Petrov PI, Mandija S, Sommer IEC, van den Berg CAT. Understanding the biophysical effects of transcranial magnetic stimulation on brain tissue: The bridge between brain stimulation and cognition. Prog Brain Res, Comput. Neurostimulation 2015;222:229–259. doi: 10.1016/bs.pbr.2015.06.015.

34. Sack AT, Cohen Kadosh R, Schuhmann T, Moerel M, Walsh V, Goebel R. Optimizing functional accuracy of TMS in cognitive studies: a comparison of methods. J. Cogn. Neurosci. 2009;21:207–221. doi: 10.1162/jocn.2009.21126.

35. Thielscher A, Opitz A, Windhoff M. Impact of the gyral geometry on the electric field induced by transcranial magnetic stimulation. Neuroimage 2011;54:234–243. doi: 10.1016/ j.neuroimage.2010.07.061.

36. Laakso I, Hirata A, Ugawa Y. Effects of coil orientation on the electric field induced by TMS over the hand motor area. Phys. Med. Biol. 2014;59:203–218. doi: 10.1088/0031-9155/59/1/203.

37. Krieg TD, Salinas FS, Narayana S, Fox PT, Mogul DJ. Computational and experimental analysis of TMS-induced electric field vectors critical to neuronal activation. J. Neural Eng. 2015;12:1–11. doi: 10.1088/1741-2560/12/4/046014.

38. Paffi A, Camera F, Carducci F, Rubino G, Tampieri P, Liberti M, Apollonio F. A Computational Model for Real-Time Calculation of Electric Field due to Transcranial Magnetic Stimulation in Clinics. Int. J. Antennas Propag. 2015:1–12. doi: http://dx.doi.org/ 10.1155/2015/976854.

39. Janssen AM, Oostendorp TF, Stegeman DF. The coil orientation dependency of the electric field induced by TMS for M1 and other brain areas. J. Neuroeng. Rehabil. 2015:12–47. doi: 10.1186/s12984-015-0036-2.

40. Geddes LA, Baker LE. The specific resistance of biological material-A compendium of data for the biomedical engineer and physiologist. Med. Biol. Eng. 1967;5:271–293. doi: 10.1007/ BF02474537.

41. Latikka J, Kuurne T, Eskola H. Conductivity of living intracranial tissues. Phys. Med. Biol. 2001;46:1611–1616. doi: 10.1088/0031-9155/46/6/302.

42. Wagner TA, Zahn M, Grodzinsky AJ, Pascual-Leone A. Three-dimensional head model simulation of transcranial magnetic stimulation. IEEE Trans. Biomed. Eng. 2004;51:1586–1598. doi: 10.1109/TBME.2004.827925.

43. Wagner T, Fregni F, Eden U, Ramos-Estebanez C, Grodzinsky A, Zahn M, Pascual-Leone A. Transcranial magnetic stimulation and stroke: A computer-based human model study. Neuroimage 2006;30:857–870. doi: 10.1016/j.neuroimage.2005.04.046.

44. Opitz A, Windhoff M, Heidemann RM, Turner R, Thielscher A. How the brain tissue shapes the electric field induced by transcranial magnetic stimulation. Neuroimage 2011;58:849–859. doi: 10.1016/j.neuroimage.2011.06.069.

45. Wenger C, Salvador R, Basser PJ, Miranda PC. The electric field distribution in the brain during TTFields therapy and its dependence on tissue dielectric properties and anatomy: a computational study. Phys. Med. Biol. 2015;60:7339–7357. doi: 10.1088/0031-9155/60/18/7339.

46. Opitz A, Fox MD, Craddock RC, Colcombe S, Milham MP. An integrated framework for targeting functional networks via transcranial magnetic stimulation. Neuroimage 2016:86–96. doi: 10.1016/j.neuroimage.2015.11.040.

47. Peyman A, Gabriel C, Grant EH, Vermeeren G, Martens L. Variation of the dielectric properties of tissues with age: the effect on the values of SAR in children when exposed to walkie-talkie devices. Phys. Med. Biol. 2009;54:227–241. doi: 10.1088/0031-9155/55/17/5249.

48. Miranda PC, Hallett M, Basser PJ. The Electric Field Induced in the Brain by Magnetic Stimulation : A 3-D Finite-Element Analysis of the Effect of Tissue Heterogeneity and Anisotropy. IEEE Trans. Biomed. Eng. 2003;50:1074–1085. doi: 10.1109/TBME.2003.816079.

49. Oh SH, Lee BI, Lee SY, Woo EJ, Cho MH, Kwon O, Seo JK. Magnetic resonance electrical impedance tomography at 3 tesla field strength. Magn. Reson. Med. 2004;51:1292–1296. doi: 10.1002/mrm.20091.

50. Zhang X, Yan D, Zhu S, He B. Noninvasive Imaging of Head-Brain Conductivity Profiles Using Magnetic Resonance Electrical Impedance Imaging. IEEE Eng. Med. Biol. Mag. 2008;27:78–83. doi: 10.1109/MEMB.2008.923953.

51. Woo EJ, Seo JK. Magnetic resonance electrical impedance tomography (MREIT) for high-resolution conductivity imaging. Physiol. Meas. 2008;29:R1–R26. doi: 10.1088/0967-3334/29/10/R01.

52. Seo JK, Yoon JR, Woo EJ, Kwon O. Reconstruction of conductivity and current density images using only one component of magnetic field measurements. IEEE Trans. Biomed. Eng. 2003;50:1121–1124. doi: 10.1109/TBME.2003.816080.

53. Ider YZ, Onart S. Algebraic reconstruction for 3D magnetic resonance-electrical impedance tomography (MREIT) using one component of magnetic flux density. Physiol. Meas. 2004;25:281–294. doi: 10.1088/0967-3334/25/1/032.

54. Ozparlak L, Ider YZ. Induced current magnetic resonance–electrical impedance tomography. Physiol. Meas. 2005;26:S289–S305. doi: 10.1088/0967-3334/26/2/027.

55. van Lier ALHMW, van den Berg CAT, Katscher U. Measuring electrical conductivity at low frequency using the eddy currents induced by the imaging gradients. Proc. 20th Sci. Meet. Int. Soc. Magn. Reson. Med. Melbourne, Victoria, Aust. 2012:3467.

56. Liu C, Li W, Argyridis I. Imaging electric conductivity and conductivity anisotropy via eddy currents induced by pulsed field gradients. Proc. 22nd Sci. Meet. Int. Soc. Magn. Reson. Med. Milano, Italy 2014:638.

57. Oran OF, Gurler N, Ider YZ. Feasibility of conductivity imaging based on slice selection and readout gradient induced eddy-currents. Proc. 23nd Sci. Meet. Int. Soc. Magn. Reson. Med. Toronto, Canada 2015:930.

58. Gibbs E, Liu C. Feasibility of Imaging Tissue Electrical Conductivity by Switching Field Gradients with MRI. Tomography 2015:125–135. doi: 10.1530/ERC-14-0411.

59. Oran OF, Ider YZ. Feasibility of Conductivity Imaging Using Subject Eddy Currents Induced by Switching of MRI Gradients. Magn. Reson. Med. 2016. doi: 10.1002/mrm.26283.

60. Mandija S, van Lier ALHMW, Katscher U, Petrov PI, Neggers SFW, Luijten PR, van den Berg CAT. A geometrical shift results in erroneous appearance of low frequency tissue eddy current induced phase maps. Magn. Reson. Med. 2015. doi: 10.1002/mrm.25981.

61. Schavemaker P, Sluis L van der. Electrical Power System Essentials. John Wiley and Sons Inc.; 2008.

62. Laakso I, Hirata A. Fast multigrid-based computation of the induced electric field for transcranial magnetic stimulation. Phys. Med. Biol. 2012;57:7753–7765. doi: 10.1088/0031-9155/57/23/7753.

63. Hernandez-Garcia L, Bhatia V, Prem-Kumar K, Ulfarsson M. Magnetic resonance imaging of time-varying magnetic fields from therapeutic devices. NMR Biomed. 2013. doi: 10.1002/nbm.2919.

64. Institute S. SCIRun: A Scientific Computing Problem Solving Environment, Scientific Computing and Imaging Institute (SCI). 2015:http://www.scirun.org.

65. Petrov PI, Mandija S, van den Berg CAT, Neggers SFW. Impact of TMS coil modeling detail on FEM simulation accuracy of the induced electrical field. Proc. Int. Conf. Basic Clin. Multimodal Imaging 2015, Utrecht, Netherlands.

66. Miniussi C, Paulus W, Rossini PM. Transcranial Brain Stimulation. CRC Press; 2012.

67. Geuzaine C, Remacle JF. Gmsh: a three-dimensional finite element mesh generator with built-in pre- and post-processing facilities. Int. J. Numer. Methods Eng. 2009;79:1309–1331. doi: 10.1002/nme.2579.

68. Windhoff M, Opitz A, Thielscher A. Electric Field Calculations in Brain Stimulation Based on Finite Elements: An Optimized Processing Pipeline for the Generation and Usage of Accurate Individual Head Models. Hum. Brain Mapp. 2013;34:923–935. doi: 10.1002/hbm.21479.

69. Mandija S, Petrov P, Neggers B, de Weijer A, Luijten PR, Van Den Berg CAT. MR guidance of TMS for a patient specific treatment plan: MR based TMS field measurements and electromagnetic simulations. Proc. 23nd Sci. Meet. Int. Soc. Magn. Reson. Med. Toronto, Canada 2015:931.

70. Aminoff MJ, Boller F, Swaab DF. Brain Stimulation: Handbook of Clinical Neurology. (Lozano AM, Hallett M, editors.). Elsevier; 2013.

71. Foster K. The Biomedical Engineering Handbook: Second Edition - Dielectric properties of tissues. 1999.

72. Kim HJ, Jeong WC, Sajib SZK, Kim MO, Kwon OI, Je Woo E, Kim DH. Simultaneous imaging of dual-frequency electrical conductivity using a combination of MREIT and MREPT. Magn. Reson. Med. 2014;71:200–208. doi: 10.1002/mrm.24642.

73. De Geeter N, Crevecoeur G, Dupré L, Van Hecke W, Leemans A. A DTI-based model for TMS using the independent impedance method with frequency-dependent tissue parameters. Phys. Med. Biol. 2012;57:2169–2188. doi: 10.1088/0031-9155/57/8/2169.

74. Navarro De Lara LI, Windischberger C, Kuehne A, Woletz M, Sieg J, Bestmann S, Weiskopf N, Strasser B, Moser E, Laistler E. A novel coil array for combined TMS/fMRI experiments at 3 T. Magn. Reson. Med. 2015;74:1492–1501. doi: 10.1002/mrm.25535.

Chapter 5

Error analysis of Helmholtz-based MR-Electrical Property Tomography

Magnetic Resonance in Medicine 2017; in press.
doi: 10/1002/mrm.27004.

Stefano Mandija

Alessandro Sbrizzi

Ulrich Katscher

Peter R. Luijten

Cornelis A.T. van den Berg

Abstract

MR-Electrical Properties Tomography (MR-EPT) aims to measure tissue electrical properties by computing spatial derivatives of measured B_1^+ data. This computation is very sensitive to spatial fluctuations caused, for example, by noise and Gibbs ringing. In this work, the error arising from the computation of spatial derivatives using finite difference kernels (FD error) has been investigated. In relation to this FD error, it has also been investigated whether mitigation strategies such as Gibbs ringing correction and Gaussian apodization can be beneficial for conductivity reconstructions. Conductivity reconstructions were performed on a phantom and a human brain at 3T by means of simulations and MR-measurements. The accuracy was evaluated as a function of image resolution, FD kernel size, k-space windowing and SNR. The impact of mitigation strategies was also investigated. The adopted small FD kernel is highly sensitive to spatial fluctuations, whereas the large FD kernel is more noise-robust. However, large FD kernels lead to more extended numerical boundary error propagation, which severely hampers the MR-EPT reconstruction accuracy for highly spatially convoluted tissue structures such as the human brain. Mitigation strategies slightly improve the accuracy of conductivity reconstructions. For the adopted derivative kernels and the investigated scenario, MR-EPT conductivity reconstructions show low accuracy: less than 37% of the voxels have a relative error lower than 30%. The numerical error introduced by the computation of spatial derivatives using FD kernels is one of the major causes of limited accuracy in Helmholtz-based MR-EPT reconstructions.

5.1 Introduction

The measurement of electrical properties (EPs) of human tissues such as conductivity (σ) and permittivity (ε) is a challenge that has attracted several researchers in the past decades (1). EPs measurements can be useful for various applications including patient safety (2-4), oncology (5,6) and dosimetry of neurostimulation techniques like Transcranial Magnetic Stimulation (TMS) (7-9). Among related techniques such as Electrical Impedance Tomography (EIT) (10,11), MR-EIT (12-14), and Magneto-Acoustic Tomography (MAT) (15,16), MR-Electrical Properties Tomography (MR-EPT) has recently gained considerable interest.

MR-EPT aims at non-invasive measurements of EPs at RF frequencies (64-300 MHz) using standard MR-scanners (2,17,18). This technique has already been applied in *in-vivo* studies showing EPs reconstructions on patients with brain (19,20), breast (5,21), and cervical (22) cancer. However, the presented results are affected by a large variability in the reconstructed EPs values (23-26). Most of the MR-EPT studies rely on the homogeneous Helmholtz model, which assumes piecewise constant EPs (1,24,25,27-29). According to this model, EPs are reconstructed by computing spatial derivatives directly on measured MRI data (complex transmit RF field, B_1^+) (25,26,28,30-35). For the particular case of conductivity reconstructions, derivatives can be computed on the measured RF phase only, thus avoiding mapping of the B_1^+ magnitude. This is known as the "phase-only approach", leading to approximated conductivity reconstructions (36,37). However, the homogeneous Helmholtz model, which relies on the assumption of piecewise constant EPs, is not valid at tissue boundaries where EPs rapidly change causing discontinuities (38,39). To overcome the piecewise constant EPs assumption, a few studies extended the homogeneous Helmholtz model by including smooth variations in the EPs (gradient-based approaches) (26,34,35,40). In these exploratory studies, EPs are derived using a partial differential equation, which includes the gradient of the EPs.

Both homogeneous and extended Helmholtz-based models aim to reconstruct EPs by computing spatial derivatives directly on measured data. Spatial derivatives of discretized MRI data are computed by convolving the acquired MR images with finite difference (FD) kernels (37,41). At tissue boundaries, large FD kernels include voxels that belong to regions with different EPs, leading to erroneous reconstructions (numerical boundary error) that propagate into homogeneous regions. Additionally, this derivative operation performed using FD kernels is very sensitive to local signal fluctuations which hamper the reconstruction accuracy. These fluctuations arise from the intrinsic noise in MR images and lead to noise amplification in the reconstructed EPs maps (42,43). It is therefore fundamental to achieve high signal-to-noise ratio (SNR) during MR acquisitions (42,43). Alternatively, noise mitigation strategies such as image filters combined with large FD kernels can be used (21,26,35,37,38).

Moreover, since MRI images are reconstructed from a finite number of Fourier samples in k-space, additional fluctuations arise from k-space truncation (Gibbs ringing) (44), whose impact on EPs reconstructions has not been studied yet. We define the FD error as the numerical error introduced by these factors in the computation of spatial derivatives using FD kernels.

The lack of accuracy in MR-EPT reconstructions arising from the invalidity of the homogeneous Helmholtz model (38) and the error caused by applying FD kernels over tissue boundaries (for noiseless cases) (39) has already been investigated. In this manuscript, we focus instead on the numerical FD error, which has always been overlooked. It is crucial to characterize this FD error in order to effectively investigate mitigation strategies or alternative reconstructions methods. For this purpose, we first analytically investigate its impact on MR-EPT conductivity reconstructions. Then we evaluate the impact of noise and Gibbs ringing on the computation of spatial derivatives with respect to the voxel size and the size of FD kernels. We also evaluate the impact of mitigation strategies such as Gibbs ringing correction and Gaussian apodization in k-space. This analysis is performed by means of electromagnetic simulations and MR-measurements for an agar-based phantom and a human brain. In this work we will show that the computation of spatial derivatives using FD kernels is a major source of error, even if mitigation strategies are adopted. This error leads to limited accuracy in Helmholtz-based EPs reconstructions.

5.2 Theory

By combining Ampere's and Faraday's laws, the full Helmholtz equation can be derived (29):

$$-\nabla^2 \boldsymbol{B}(\boldsymbol{r}) = \frac{\nabla \varepsilon_c(\boldsymbol{r})}{\varepsilon_c(\boldsymbol{r})} \times [\nabla \times \boldsymbol{B}(\boldsymbol{r})] + \omega^2 \mu_0 \varepsilon_c(\boldsymbol{r}) \boldsymbol{B}(\boldsymbol{r}) \qquad [5.1]$$

where the complex permittivity $\varepsilon_c(\boldsymbol{r}) = \varepsilon_r(\boldsymbol{r})\varepsilon_0 - \frac{i\sigma(\boldsymbol{r})}{\omega}$ is a function of the conductivity (σ), the relative permittivity (ε_r), the angular frequency (ω), the free space permittivity (ε_0) and permeability (μ_0).

By assuming piecewise constant EPs ($\nabla \varepsilon_c = 0$), the term $(\nabla \varepsilon_c / \varepsilon_c) \times [\nabla \times \boldsymbol{B}(\boldsymbol{r})]$ in eq. [5.1] disappears. This leads to the homogeneous Helmholtz equation, written in terms of the transmit MR field (B_1^+):

$$\nabla^2 B_1^+(\boldsymbol{r}) + \gamma^2(\boldsymbol{r}) B_1^+(\boldsymbol{r}) = 0 \qquad [5.2]$$

with the complex wave number $\gamma^2 \equiv \omega^2 \mu_0 \varepsilon_c$. This equation relates the EPs of an object and the transmit, circularly polarized MR field ($B_1^+(\boldsymbol{r}) = (B_x + iB_y)/2$).

Based on eq. [5.2], EPs are computed in standard MR-EPT as:

$$\varepsilon_r(\boldsymbol{r}) = \frac{-1}{\mu_0 \varepsilon_0 \omega^2} Re\left(\frac{\nabla^2 B_1^+(\boldsymbol{r})}{B_1^+(\boldsymbol{r})}\right) \quad [5.3]$$

$$\sigma(\boldsymbol{r}) = \frac{1}{\mu_0 \omega} Im\left(\frac{\nabla^2 B_1^+(\boldsymbol{r})}{B_1^+(\boldsymbol{r})}\right) \quad [5.4]$$

with $B_1^+(\boldsymbol{r}) \neq 0$. An analysis of the error introduced by using eq. [5.2] instead of [5.1] can be found in literature (38,39).

For conductivity reconstructions, an approximated version of eq. [5.4] can be used (36,37). This solution only requires measurements of the B_1^+ phase ($\varphi^+(\boldsymbol{r})$) leading to the "phase-only" approach:

$$\sigma = \frac{1}{\mu_0 \omega} Im\left(\frac{\nabla^2 e^{i\varphi^+(r)}}{e^{i\varphi^+(r)}}\right) . \quad [5.5]$$

Equation [5.2] is used in MR-EPT as a generalized model, meaning that ε_r and σ are calculated over the whole field of view. However, given the aforementioned invalidity between regions with different EPs, reconstructions of ε_r and σ at boundaries are prone to error. We define the error arising from the invalidity of eq. [5.2] at tissue boundaries as the "model invalidity error". Additionally, due to the discretized nature of the measured B_1^+ field, derivatives on voxelized data are approximated by using various sizes of finite difference (FD) kernels. The computation of spatial derivatives on noisy discretized data using FD kernels leads to an additional error, which we define as the "FD error".

For explanation purposes, we analyze the impact of the FD error for a 1-D Helmholtz equation. We therefore consider a plane wave travelling along the positive z-direction and normally incident to the boundary ($z = z_0$) between two homogeneous, infinite regions with different EPs (Fig. 5.1 A). For a time harmonic field, we have (45):

$$E(z) = \begin{cases} (E^0 e^{-iz\gamma_1} + rE^0 e^{iz\gamma_1})\hat{x} & z < z_0 \quad [5.6a] \\ (tE^0 e^{-iz\gamma_2})\hat{x} & z > z_0 \quad [5.6b] \end{cases}$$

$$B(z) = \begin{cases} \mu_0 \left(\frac{E^0}{\eta_1} e^{-iz\gamma_1} - r\frac{E^0}{\eta_1} e^{iz\gamma_1}\right)\hat{y} & z < z_0 \quad [5.7a] \\ \mu_0 \left(t\frac{E^0}{\eta_2} e^{-iz\gamma_2}\right)\hat{y} & z > z_0 \quad [5.7b] \end{cases}$$

where r and t are respectively the reflection and transmission coefficients for a plane wave (with $t = 1 + r$), $\eta_{1,2}$ are the intrinsic wave impedances of the two regions ($\eta = \sqrt{\frac{i\omega\mu_0}{\sigma + i\omega\varepsilon_r\varepsilon_0}}$), and $\gamma_{1,2}$ depends on the EPs of the two regions (45).

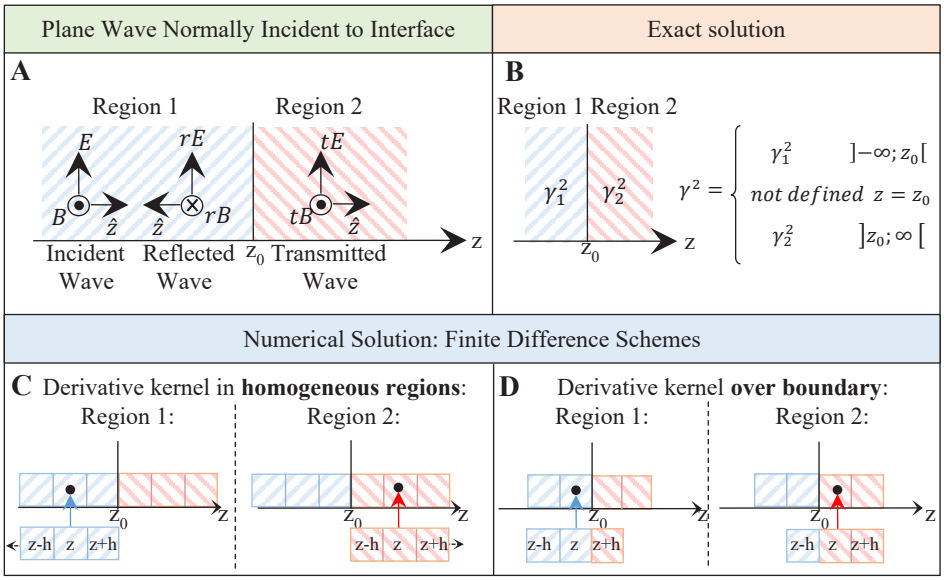

Figure 5.1: A) Plane wave normally incident to an interface. **B**) Solution of Eq. [5.2]. **C**) Derivative scheme on voxelized data in homogeneous regions: 3-points central FD kernel. **D**) Derivative scheme on voxelized data over the boundary between the two different regions.

5.2.1 Model Invalidity Error

To extract EPs for this 1-D scenario, we solve the 1-D Helmholtz equation for γ^2, assuming piecewise constant EPs:

$$\gamma^2 = -\left(\frac{\frac{dB(z)^2}{d^2z}}{B(z)}\right) = \begin{cases} \gamma_1^2 & z < z_0 \quad [5.8a] \\ not\ defined & z = z_0 \quad [5.8b] \\ \gamma_2^2 & z > z_0 \quad . \quad [5.8c] \end{cases}$$

Equations 5.8a and 5.8c show that EPs can theoretically be reconstructed in homogeneous regions using the homogeneous Helmholtz model (Fig. 5.1, B). At boundaries, $dB(z)^2/d^2z$ is instead not defined (eq. [5.8b]). Therefore, reconstructions of ε_r and σ at this location are not possible.

Note that this observation applies to eq. [5.2], but also to eq. [5.1], since the term $\nabla\varepsilon_c$ is not defined at tissue boundaries either.

5.2.2 FD Error

HOMOGENEOUS REGIONS

After voxelization, spatial derivatives are computed by convolving the discretized signal with FD kernels (*K*). This approximation leads to numerical errors. For illustration purposes, we derive the numerical error inside homogeneous regions as a function of the voxel size (h) by applying a 3-points FD kernel ($f''(z) \approx \frac{f(z-h)-2f(z)+f(z+h)}{h^2}$, with f generic function) (Fig. 5.1, C).

For region 1, we find:

$$\left(\frac{\frac{dB(z)^2}{d^2z}}{B(z)}\right) \approx \frac{B(z)*K}{B(z)} \approx \frac{\frac{E^0}{\eta_1}\left(e^{-i(z-h)\gamma_1}-2e^{-iz\gamma_1}+e^{-i(z+h)\gamma_1}\right)}{\frac{E^0}{\eta_1}\left(e^{-iz\gamma_1}-re^{iz\gamma_1}\right)h^2} - \frac{\frac{rE^0}{\eta_1}\left(e^{i(z-h)\gamma_1}-2e^{iz\gamma_1}+e^{i(z+h)\gamma_1}\right)}{\frac{E^0}{\eta_1}\left(e^{-iz\gamma_1}-re^{iz\gamma_1}\right)h^2} \quad [5.9]$$

where z is the coordinate of the central voxel of the derivative kernel after voxelization. This approximation is reliable only when the whole kernel is confined inside a homogeneous region.

The difference between the analytical and the numerical solutions defines the absolute error ($\epsilon(h)$) introduced by the FD approximation in homogeneous regions:

$$\epsilon(h) = \Delta\gamma^2 = -\gamma_1^2 - \frac{e^{-i(z-h)\gamma_1}-2e^{-iz\gamma_1}+e^{-i(z+h)\gamma_1}}{\left(e^{-iz\gamma_1}-re^{iz\gamma_1}\right)h^2} + \frac{r\left(e^{i(z-h)\gamma_1}-2e^{iz\gamma_1}+e^{i(z+h)\gamma_1}\right)}{\left(e^{-iz\gamma_1}-re^{iz\gamma_1}\right)h^2} \quad [5.10]$$

For $h \to 0$, $\epsilon(h)$ is:

$$\lim_{h\to 0}\epsilon(h) = -\gamma_1^2 - \lim_{h\to 0}\left(\frac{-\gamma_1^2 e^{-i(z-h)\gamma_1}-\gamma_1^2 e^{-i(z+h)\gamma_1}+r\gamma_1^2 e^{i(z-h)\gamma_1}+r\gamma_1^2 e^{i(z+h)\gamma_1}}{2\left(e^{-iz\gamma_1}-re^{iz\gamma_1}\right)}\right) = 0 \quad [5.11]$$

after applying the de L'Hopital's theorem twice to evaluate the limit. This shows that, as expected for the noiseless case, the pure numerical error tends to zero for decreasing voxel sizes. Analogous solution can be found for region 2.

However, in reality, the measured $B_1^+(\boldsymbol{r})$ field in an MRI experiment is affected by spatial fluctuations ($\varsigma(\boldsymbol{r})$) arising from several factors such as thermal noise, k-space truncation (window function w) leading to Gibbs ringing, and $B_1^+(\boldsymbol{r})$ reconstruction techniques. The measured $B_1^+(\boldsymbol{r})$ field is therefore:

$$B_{1,meas}^+(\boldsymbol{r}) = B_1^+(\boldsymbol{r}) + \varsigma(\boldsymbol{r}) \quad [5.12]$$

where $B_1^+(\boldsymbol{r})$ is the true value of the B_1^+ field, which is not affected by any perturbations.

Therefore, for the considered plane wave, after including the additional perturbation term $\varsigma(z)$ into eq. [5.10] we obtain the noisy error model:

$$\epsilon_{meas}(h) = \epsilon(h) - \frac{\varsigma(z+h)-2\varsigma(z)+\varsigma(z-h)}{h^2\left(\frac{E^0}{\eta_1}\left(e^{-iz\gamma_1}-re^{iz\gamma_1}\right)+\varsigma(z)\right)} \quad . \quad [5.13]$$

Due to the random nature of the noise, the numerator of eq. [5.13] does not necessarily vanish if the limit of $\epsilon_{meas}(h)$ is evaluated for $h \to 0$. This leads to:

$$\lim_{h\to 0} \epsilon_{meas}(h) = 0 - \lim_{h\to 0} \frac{\varsigma(z+h)-2\varsigma(z)+\varsigma(z-h)}{h^2\left(\frac{E^0}{\eta_1}\left(e^{-iz\gamma_1}-re^{iz\gamma_1}\right)+\varsigma(z)\right)} = \infty \,. \qquad [5.14]$$

Equation [5.14] highlights how susceptible computations of spatial derivatives on noisy voxelized data are even inside homogeneous regions.

INTERFACES

In MR-EPT, FD kernels are applied over the whole field of view. For locations adjacent to the interface z_0, the adopted FD kernel will therefore contain voxels of different regions (Fig. 5.1, D). In the noiseless case, for the region 1, eq. [5.7] leads to:

$$\left(\frac{\frac{dB(z)^2}{d^2z}}{B(z)}\right) \approx \frac{\frac{E^0}{\eta_1}e^{-i(z-h)\gamma_1}-2\frac{E^0}{\eta_1}e^{-iz\gamma_1}+t\frac{E^0}{\eta_2}e^{-i(z+h)\gamma_2}-\frac{rE^0}{\eta_1}\left(e^{i(z-h)\gamma_1}-2e^{iz\gamma_1}\right)}{\frac{E^0}{\eta_1}\left(e^{-iz\gamma_1}-re^{iz\gamma_1}\right)h^2} \,. \qquad [5.15]$$

Without loss of generalization, we define $z_0 = 0$, and $z = -h/2$, the z-coordinate of the central voxel of the derivative scheme. For this case, eq. [5.11] becomes:

$$\lim_{h\to 0} \epsilon(h) = -\gamma_1^2 - \frac{\frac{i\gamma_1}{\eta_1}+\frac{i\gamma_1 r}{\eta_1}-\frac{i\gamma_2 t}{\eta_2}}{\lim\limits_{h\to 0}\frac{2}{\eta_1}\left(e^{-i\frac{h}{2}\gamma_1}-re^{i\frac{h}{2}\gamma_1}\right)h} = \infty \,. \qquad [5.16]$$

Equation [5.16] shows that the numerical error introduced by the use of FD schemes over interfaces increases with the difference in the EPs between regions. Ultimately, contrarily to the homogeneous case, this error corrupts the computation of EPs at interfaces even for noiseless cases for reducing voxel sizes.

5.3 Methods

We first characterized the FD error for conductivity reconstructions using the adopted plane wave model and the 3-points FD kernel. For explanation purposes, we used the EPs of the white matter to characterize the FD error in a homogeneous region according to eqs. [5.11] and [5.14]. To characterize the FD error over a boundary (eq. [5.16]), different tissue combinations were used (Supporting Fig. 5.S1, A) (39).

Afterwards, by means of electromagnetic simulations and MR-measurements, we characterized the FD error in conductivity reconstructions for a phantom and a human brain as a function of the image resolution and the size of FD kernels. We also evaluated whether Gibbs ringing correction and Gaussian apodization in k-space could be of help.

5.3.1 Simulations

FDTD simulations were performed on a cylindrical phantom model and on a human head model (Duke, Virtual Family) with piecewise constant EPs using the software Sim4Life (ZMT AG, Zurich, CH) (Supporting Fig. 5.S1, B and C). To evaluate the impact of discontinuities in EPs on conductivity reconstructions, three different conductive tubes were placed into the cylindrical phantom model. These models were placed inside a birdcage body coil model (Supporting Fig. 5.S1, D) resonant at 128 MHz and driven in quadrature mode, thus mimicking the MR experimental setup. An isotropic grid size of 2x2x2 mm^3 was used for both the phantom and the human brain models. With this setup we simulated the transmit B_1^+ complex field, which is needed for conductivity reconstructions. These simulations allowed us to perform a quantitative comparison between the ground truth and the reconstructed electrical conductivity values. Two phantom simulations and one human head model simulation were performed.

In the first phantom simulation, we initially evaluated the impact of the size of FD kernels for noiseless standard (B_1^+ magnitude included) MR-EPT conductivity reconstructions. Two sizes of FD kernels were considered: a small 3-points FD kernel (K_3: 3×3×3 voxels, *del2* function in Matlab, R2013a, The Mathworks Inc., USA), and a larger, noise-robust FD kernel (K_7: 7×7×5 voxels). The large FD kernel K_7 employs the so-called noise-robust kernel "K_{large}" (reported in the appendix B of reference (37)) to compute the in-plane derivatives (x/y-directions), and it employs the kernel "K_{small}" of reference (37) to compute the derivatives through-planes (z-direction). The simulated complex B_1^+ field was directly used as input for conductivity reconstructions (eq. [5.4]) (convolution of the complex B_1^+ field with FD kernels: standard MR-EPT). Afterwards, we evaluated the impact of image perturbations arising from two factors: k-space truncation (truncation window: w) leading to Gibbs ringing artifact, and, additionally, thermal noise ($\xi(\boldsymbol{r})$). We characterized the accuracy of these reconstructions by defining with $V_{RE<30\%}$ the percentage of voxels with relative error (RE) lower than 30%. To simulate the Gibbs ringing artifact, the simulated B_1^+ field was first oversampled (factor 16) using spline function interpolation in Matlab. Subsequently, the k-space obtained after FFT of the oversampled data was truncated using a boxcar window (w). The size of the truncation window was chosen such that the voxel size of the B_1^+ field reconstructed from the truncated k-space was 2x2x2 mm^3. This truncation in k-space, which is equal to a convolution in image domain with a kernel W ($W = FT^{-1}(w)$), leads to Gibbs ringing in the reconstructed B_1^+ field. Thermal noise was then included by independently adding Gaussian noise to the real and imaginary part of the complex B_1^+ field such that the final SNR (B_1^+ magnitude) was equal to 30.

In the second phantom simulation, we investigated whether Gibbs ringing correction and Gaussian apodization in k-space improve the accuracy of conductivity reconstructions as a function of the voxel size (2×2×2 mm^3 and 4×4×4 mm^3, respectively). Different voxel sizes were achieved by changing the extension of the boxcar truncation window (w) in k-space. To simulate the intrinsic increase in SNR correlated to a larger voxel size, the SNR was 30 and 120, respectively for the 2×2×2 mm^3 and 4×4×4 mm^3 grid sizes. To allow direct comparisons with the MR measurements, phase-only conductivity reconstructions were performed. Gibbs ringing correction was performed using an online-available software (default parameters were used) (44). This correction consists of interpolating the image based on local subvoxel-shifts to sample the ringing pattern at the zero-crossings of the oscillating sinc-function (W, inverse Fourier transform of the boxcar window w). Apodization in k-space was performed using a Gaussian window with a k-space standard deviation (σ_k) leading to a full-width-half-maximum of the corresponding kernel in image domain ($FWHM_i$) of 1 voxel ($FWHM_i = \left(N\sqrt{-2\ln(0.5)}\right)/(\pi\sigma_k)$, where N denotes the number of voxels) (35,46).

For the human head model simulation, standard (B_1^+ magnitude included) MR-EPT conductivity reconstructions were performed (eq. [5.4]). As for the phantom simulations, we evaluated the impact of FD kernel sizes, Gibbs ringing correction and Gaussian apodization. The human head simulation was performed with the SNR obtained in the *in-vivo* MR measurements (SNR ≈ 50, evaluated in a homogeneous region inside the white matter) to allow direct comparisons (47).

Finally, by comparing the conductivity values reconstructed from the human head simulation with the ground-truth values, we evaluated the accuracy of standard MR-EPT conductivity reconstructions in the head as a function of the SNR and the FD kernel size. This evaluation was performed after mitigation strategies were adopted on a whole head section (7 cm thick), and, separately, on the cerebrospinal fluid (CSF), gray matter (GM) and white matter (WM). For completeness and comparison purposes, this evaluation was also performed for phase-only MR-EPT conductivity reconstructions.

5.3.2 MRI Measurements

MR measurements were performed using a 3T scanner (Ingenia, Philips HealthCare, Best, The Netherlands) with the body coil for transmitting, and a 15-channel head coil to receive. A vendor specific algorithm (Philips, Constant Level of Appearance - CLEAR) available on Philips MR scanners was used to convert the receive phase measured with the head coil to the body coil, as if the body coil would have been used both for transmitting and receiving. A phantom MR-experiment and an *in-vivo* MR-experiment were performed.

For the phantom MR-experiment, a cylindrical agar-based phantom with three inner compartments was built, similarly to the phantom used for the simulations. During phantom preparation, agar 2% was added to prevent motion/flow artifacts. Different amounts of NaCl were also added in the inner compartments to obtain different conductivity values (Supporting Fig. 5.S1, E). The impact of Gibbs ringing correction and Gaussian apodization in k-space was evaluated for phase-only conductivity reconstructions, allowing comparison with the second phantom simulation results. For this purpose, two phase maps acquired using two single echo Multi-slice Spin-Echo sequences with opposite readout gradient polarities (to compensate for potential eddy current related artifacts) were combined to compute the RF phase maps used for phase-only conductivity reconstructions: TR/TE = 900/5 ms, in-plane field of view = 256×256 mm^2, voxel size = 2×2×2 mm^3 and 4×4×4 mm^3 for the high and low-resolution experiments, respectively. This sequence was chosen to minimize the impact of B0 distortions, motion, and scan time.

An *in-vivo* MR-experiment was also performed on a healthy 28 year old male volunteer following local ethical protocols. For this *in-vivo* MR-experiment, standard (B_1^+ magnitude included) conductivity reconstructions were performed as a function of: FD kernel sizes, Gibbs ringing correction and Gaussian apodization. This allowed comparison of the simulations results to conductivity reconstructions from *in-vivo* data. Analogously to the phantom MR-measurements, two single echo Spin-Echo sequences were acquired with a voxel size of 2×2×3 mm^3 to map the RF phase, the other parameters were kept unchanged.

To map the B_1^+ magnitude needed for standard MR-EPT reconstructions, a dual TR AFI sequence was performed: TR1/TR2/TE = 50/250/2.5 ms, flip angle = 65°, field of view = 256×256×90 mm^3, and voxel size = 2×2×3 mm^3.

Contrarily to conductivity reconstruction from simulations (3D kernels applied to 3D volumes), conductivity reconstructions from MR measurements were performed on one selected slice by applying the corresponding 2D versions of the previously described 3D kernels. In particular, K_3 (*del2* function) was a 3×3×1 kernel, and K_7 (7×7×1) was the so called "$K_{large,2}$" in the appendix B of reference (37), applied along the x/y-directions.

5.4 Results

5.4.1 Plane Wave Model

In Fig. 5.2 A (noiseless case: red circles, with noise: blue triangles), the FD error inside a homogeneous region (WM) is characterized for a 3-points FD kernel as a function of the voxel size for conductivity reconstructions (eqs. [5.11] and [5.14]). For the noiseless case, the FD error is negligible.

Instead, in the presence of noise, the use of FD schemes leads to severe FD errors for reducing voxel sizes (e.g. voxel size = 2 mm: $\Delta\sigma \approx 2$ S/m, with $\Delta\sigma = \sigma_{theoretical} - \sigma_{reconstructed}$). This applies also for conductivity reconstructions over boundaries between different tissues (Fig. 5.2, B). Additionally, we can observe how the FD error over boundaries increases for increasing contrasts in the EPs between adjacent tissues. For instance, for a voxel size of 2 mm, typical errors obtained are: $\Delta\sigma_{CSF-GM} \approx 12$ S/m, $\Delta\sigma_{GM-WM} \approx 3$ S/m.

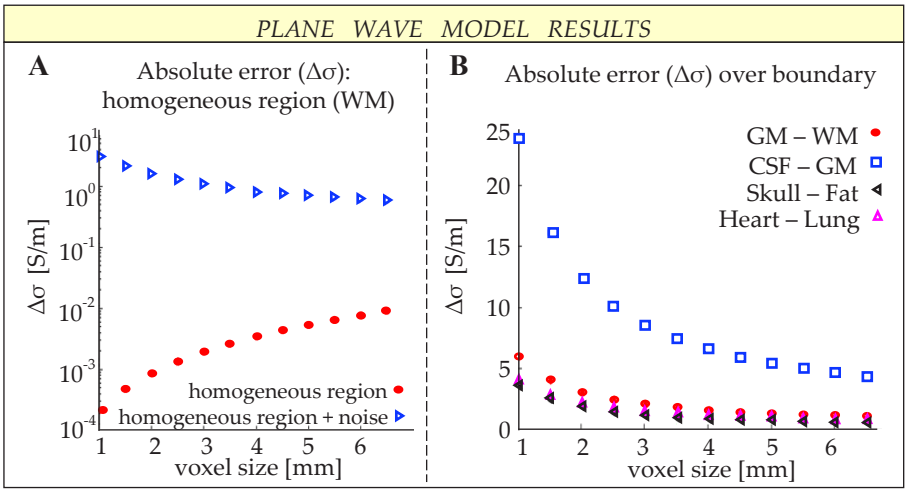

Figure 5.2: A) Absolute errors (logarithm scale) for conductivity reconstructions in a homogeneous region (white matter) **B**) Absolute errors (linear scale) in conductivity reconstructions over a boundary between different tissues (no noise included).

5.4.2 Phantom Simulations

The results of the first phantom simulation are presented in Fig. 5.3 (A: noiseless case, B: Gibbs ringing included, and C: noise included) (profiles are shown in Supporting Fig. 5.S2). For the noiseless case, standard (B_1^+ magnitude included) MR-EPT conductivity reconstructions are accurate inside homogeneous regions: absolute error ($\Delta\sigma$) ≈ 0 S/m, as expected from the plane wave results. We also observe that a smaller FD kernel leads to lower boundary error propagation resulting in a globally higher $V_{RE<30\%}$: 80% for K_3, and 55% for K_7, respectively. However, reconstructions performed using small FD kernels are highly sensitive to spatial fluctuations arising from Gibbs ringing and noise. For realistic conditions, larger FD kernels lead to more accurate reconstructions (Fig. 5.3, C: $V_{RE<30\%} \approx 3\%$ for K_3, and 18% for K_7, respectively). Ultimately, Gibbs ringing leads to structured artifacts that propagate from boundaries, while noise leads to a more speckled artifact pattern.

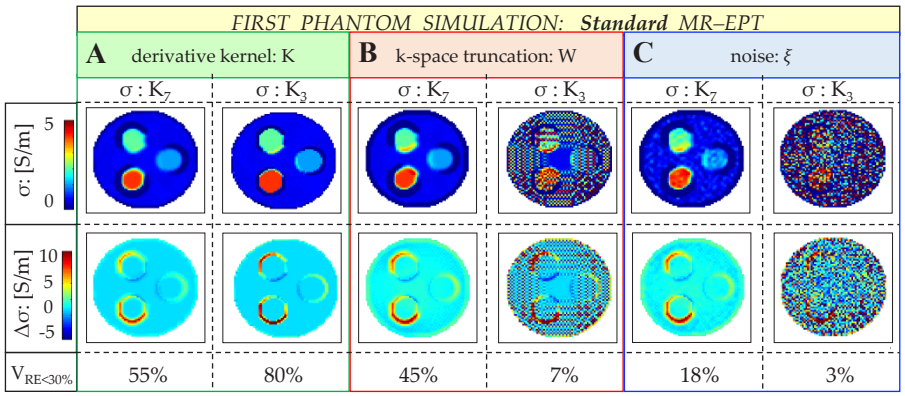

Figure 5.3: First phantom simulation. Standard (B_1^+ magnitude included) MR-EPT. **A**) Impact of two different FD kernel sizes (K_3 and K_7) on conductivity reconstructions. **B**) Impact of spatial fluctuations arising from k-space truncation (W). **C**) Impact of additional spatial fluctuations arising from thermal noise (ξ) (SNR = 30). Absolute error maps are shown in the second row. The reported $V_{RE<30\%}$ values indicate the percentage of voxels with a relative error lower than 30%.

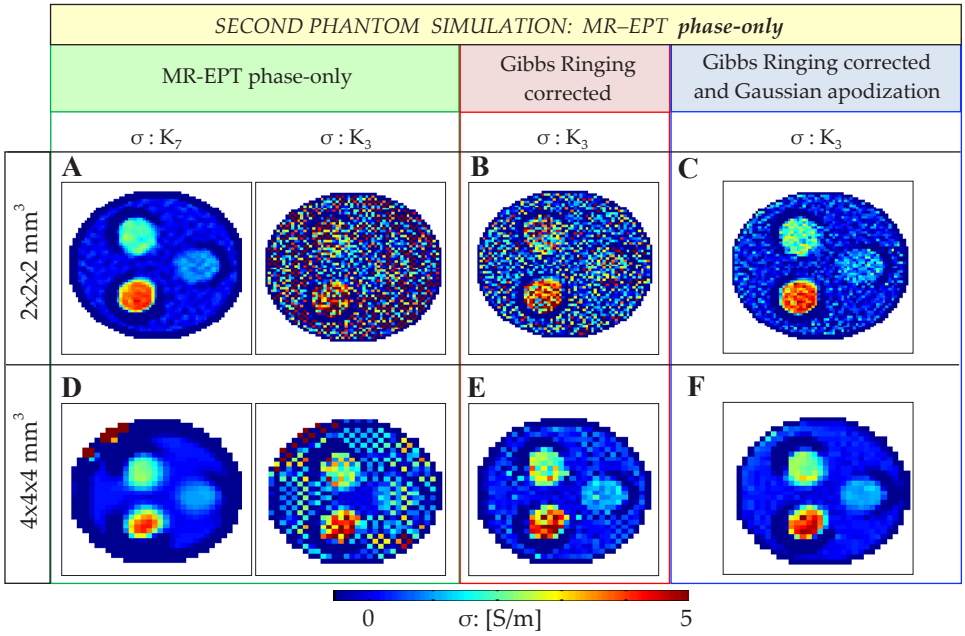

Figure 5.4: Second phantom simulation. Phase-only conductivity reconstructions: Impact of FD kernel size (**A, D**), Gibbs ringing correction (**B, E**) and additional Gaussian apodization (**C, F**) for a voxel size of 2×2×2 mm^3 and 4×4×4 mm^3.

SECOND PHANTOM SIMULATION MR-EPT phase-only	Resolution	$V_{RE<30\%}$	
		K_7	K_3
Phase-only	2×2×2 mm³ (Fig. 5.4, A)	17%	3%
	4×4×4 mm³ (Fig. 5.4, D)	15%	5%
Phase-only + Gibbs Ringing correction	2×2×2 mm³ (Fig. 5.4, B)	17%	5%
	4×4×4 mm³ (Fig. 5.4, E)	15%	14%
Phase-only + Gibbs Ringing correction + Gaussian apodization	2×2×2 mm³ (Fig. 5.4, C)	17%	10%
	4×4×4 mm³ (Fig. 5.4, F)	15%	17%

Table 5.1: Second phantom simulation: $V_{RE<30\%}$ of the phase-only MR-EPT conductivity reconstructions shown in Fig. 5.4 (black). In gray, the $V_{RE<30\%}$ values of the conductivity reconstructions that are not shown in Fig. 5.4, since no improvement was observed.

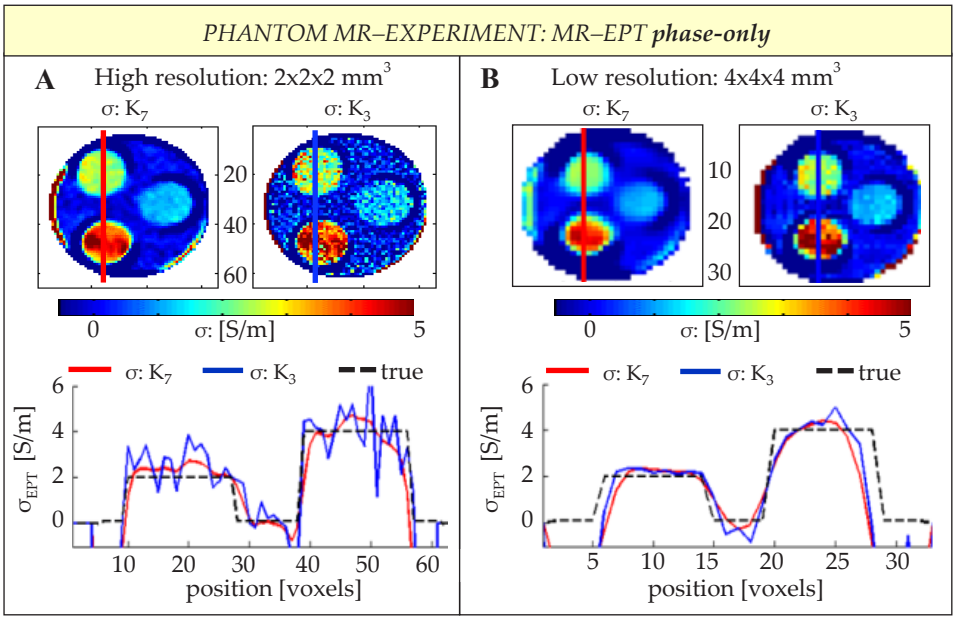

Figure 5.5: Phantom MR-experiment. Phase-only conductivity reconstructions for a voxel size of 2×2×2 mm³ (**A**) and 4×4×4 mm³ (**B**). For both cases, reconstructions were performed after both Gibbs ringing correction and Gaussian apodization.

The results of the second phantom simulation, which evaluate the impact of mitigation strategies as a function of the voxel size for phase-only conductivity reconstructions, are presented in Fig. 5.4 (A, B, and C: voxel size = 2 mm, D, E, and F: voxel size = 4 mm) (profiles are shown in Supporting Fig. 5.S3). The corresponding $V_{RE<30\%}$ values are reported in Tab. 5.1. In the presence of realistic perturbations (noise and Gibbs ringing), phase-only (Fig. 5.4, A – Tab. 5.1) and standard (B_1^+ magnitude included) (Fig. 5.3, C) MR-EPT conductivity reconstructions show comparable $V_{RE<30\%}$ values. If corrections are not applied, K_7 performs globally better than K_3, since it is more robust with respect to noise.

However, the use of a large FD kernel comes at the cost of severe boundary error propagation, especially if it is combined with a large voxel size. For K_7, the reconstruction accuracy does not improve if Gibbs ringing correction and Gaussian apodization are applied (Tab. 5.1, not shown in Fig. 5.4). Instead, some improvement is visible when K_3 is used. For high resolution images (Fig. 5.4, A – C), conductivity reconstructions, which are corrupted by the noise at the high frequencies in k-space, improve only after Gaussian apodization is applied. However, the overall accuracy remains quite low ($V_{RE<30\%} \approx 10\%$). To further reduce the impact of noise, larger voxels may be used (Fig. 5.4, D – F). In an MRI experiment, this would lead to an increase in the SNR. However, this comes at the cost of stronger Gibbs ringing artifact. As shown by our results for low resolution images, the reconstruction accuracy is improved by Gibbs ringing correction. Still, even after applying both Gibbs ringing correction and Gaussian apodization, $V_{RE<30\%}$ is not higher than 20%.

5.4.3 Phantom MRI Measurements

Phase-only conductivity reconstructions from MR-measurements on the phantom are shown in Fig. 5.5 (A: high resolution images, B: low resolution images) after Gibbs ringing correction and Gaussian apodization were performed. These reconstructions confirm the results observed in the second phantom simulation.

The noise is the main cause of FD error for high resolution images, especially if small FD kernels (K_3) are used . This error is reduced if larger kernels (K_7) or larger voxel sizes are adopted. If both large kernels and large voxel sizes are used, conductivity reconstructions are more accurate inside homogeneous regions. However, this comes at the cost of severe boundary error propagation (Fig. 5.5 B, with respect to Fig. 5.5, A), which makes this solution problematic for EPs reconstructions of tissues with high spatial variations such as the human brain.

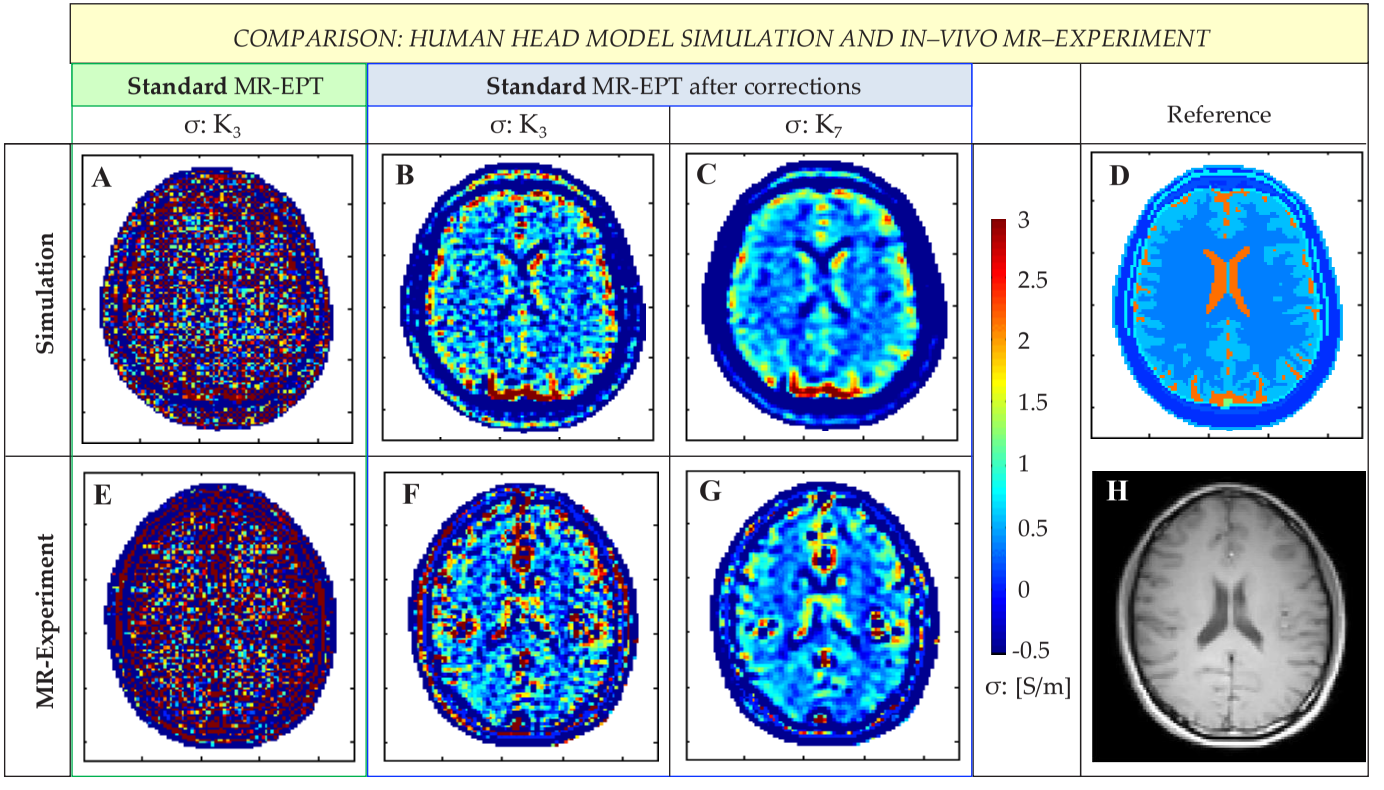

Figure 5.6: Comparison between conductivity reconstructions from the head model simulation and the *in-vivo* MR-experiment. Standard (B_1^+ magnitude included) MR-EPT conductivity reconstructions before (**A** and **E**) and after (**B**, **C**, **F** and **G**) Gibbs ringing correction and Gaussian apodization were applied, for two different FD kernel sizes: K_3 (**A**, **B**, **E** and **F**), and K_7 (**C** and **G**). Ground truth conductivity map for the simulation (**D**). T1-weighted image from the MRI measurements (**H**).

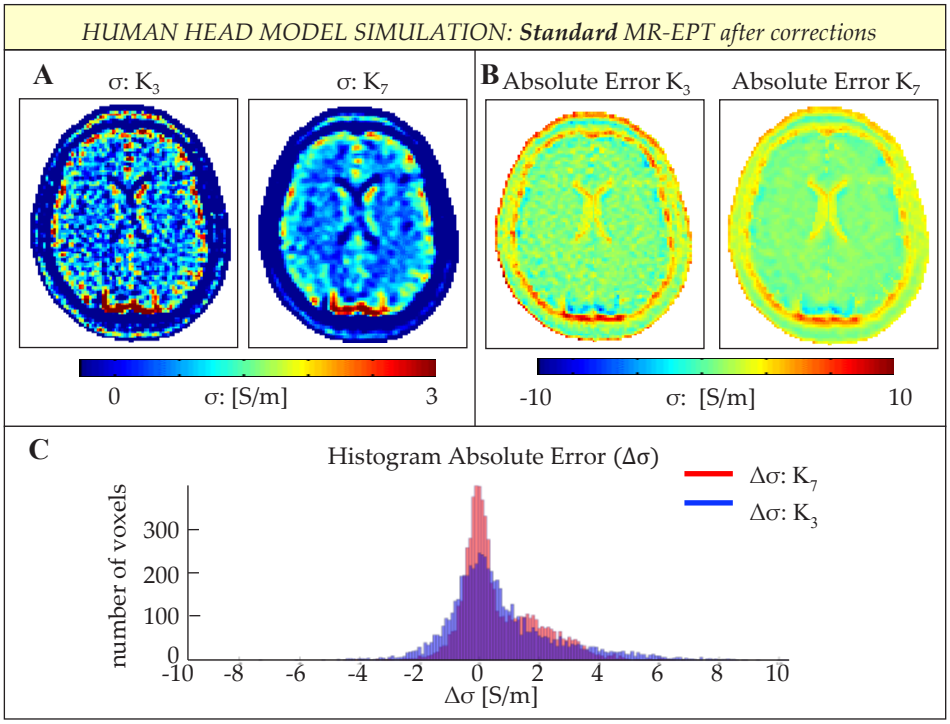

Figure 5.7: Phantom MR-experiment. Standard conductivity reconstructions for a voxel size of 2×2×2 mm^3 (**A**) and 4×4×4 mm^3 (**B**). For both cases, reconstructions were performed after both Gibbs ringing correction and Gaussian apodization.

$V_{RE<30\%}$		SNR infinite		SNR 50		SNR 10	
HUMAN HEAD MODEL SIMULATION		K_7	K_3	K_7	K_3	K_7	K_3
BRAIN SECTION	Phase-only	10%	10%	10%	10%	10%	5%
voxels: 131638	Standard MR-EPT	17%	17%	16%	10%	11%	5%
CSF	Phase-only	22%	18%	21%	17%	21%	14%
voxels: 10043	Standard MR-EPT	20%	18%	20%	17%	19%	14%
GM	Phase-only	13%	11%	13%	11%	12%	6%
voxels: 34038	Standard MR-EPT	16%	13%	16%	12%	14%	6%
WM	Phase-only	14%	15%	14%	9%	12%	5%
voxels: 42584	Standard MR-EPT	31%	37%	30%	16%	16%	5%

Table 5.2: Human head model simulation: $V_{RE<30\%}$ for a whole 3D brain section (thickness: 7 cm), and for the only CSF, GM, and WM regions inside this section. Conductivity reconstructions were performed using standard (B_1^+ magnitude included) MR-EPT and phase-only MR-EPT approaches, two different kernel sizes (K_7 and K_3) and different SNR levels (infinite, 50, and 10), after both Gibbs ringing correction and Gaussian apodization were applied.

5.4.4 *In-Vivo* Conductivity Reconstructions

To evaluate the impact of the presented issues and mitigation strategies for *in-vivo* situations, *in-vivo* standard (B_1^+ magnitude included) MR-EPT conductivity reconstructions from simulations and measurements are compared in Fig. 5.6. Analogously to the phantom results, reconstructions using K_3 are severely corrupted if derivatives are computed by directly convolving the complex B_1^+ field with the FD kernel. After correcting for Gibbs ringing and applying Gaussian apodization, reconstructions performed using K_3 are improved. However, strong variability in the reconstructed values is still observed, even if the larger kernel (K_7) is used.

In Fig. 5.7 and Tab. 5.2, the results of the analysis based on the human head model simulation are presented. From Fig. 5.7, B and C, we can observe that the computed absolute errors are in line with the values predicted using the plane wave model. In particular, we observe that the reconstructed conductivity values are often underestimated (positive $\Delta\sigma$). If K_7 is used, the impact of spatial fluctuations on conductivity reconstructions is reduced inside large homogeneous regions such as the WM. As reported in Tab. 5.2, the accuracy of the reconstructed values is slightly higher than K_3 reconstructions. However, more boundary error propagation is introduced (see for example the ventricles). This limits the reconstruction accuracy for spatially convoluted tissues such as the GM and the CSF, whose conductivity reconstructions are highly affected by the surrounding tissues.

To evaluate the impact of different noise levels for *in-vivo* conductivity reconstructions, a summary of the reconstruction accuracy based on the human head model simulation in a head section, CSF, GM and WM regions is shown for different SNR levels (Tab. 5.2), after Gibbs ringing correction and Gaussian apodization were performed. For completeness, $V_{RE<30\%}$ is reported for conductivity reconstructions using both the complex B_1^+ field (standard MR-EPT) and the phase-only approach. Although the reconstruction performed with K_7 qualitatively show a nice conductivity contrast (Fig. 5.6, C), the global accuracy is generally low and does not substantially improve with increasing SNR levels. Ultimately, even for the WM, which is the largest homogeneous tissue in the brain, $V_{RE<30\%}$ is at most 37%.

5.5 Discussion

In this work, we performed an error analysis on Helmholtz-based MR-EPT reconstructions, which aim to solve the so-called inverse problem, i.e. direct reconstruction of EPs from measured data. These reconstructions are performed by computing spatial derivatives in the image domain of the acquired MR images. Here we focused on the most commonly adopted homogeneous Helmholtz approach, which assumes piecewise constant EPs (24,25,27-29,33,48).

At the same time, our conclusions largely apply for the full Helmholtz-based approaches since they also require computation of spatial derivatives on noisy data.

In particular, we focused on conductivity reconstructions, considering that permittivity reconstructions are much more challenging, as errors in B_1^+ magnitude mapping techniques play an important role. However, we can expect similar conclusions for permittivity reconstructions as they share the same workflow.

Phantom measurements and simulations were first presented to characterize the impact of various factors that affect the computation of spatial derivatives using FD kernels: voxel size, size of FD kernels, k-space truncation, and SNR. Additionally, to evaluate the impact of these factors for *in-vivo* cases, reconstructions from simulations and measurements on a human brain were presented. With this analysis (based on the conductivity reconstructions from the simulations), we showed that one main source of error in Helmholtz-based MR-EPT reconstructions is the computation of spatial derivatives on noisy discretized data using FD kernels. To the best of our knowledge, this work is the first that quantitatively derives the numerical FD error in MR-EPT reconstructions starting from a theoretical model.

In theory, the solution of the homogeneous Helmholtz equation would lead to correct EPs reconstructions inside homogeneous regions (eqs. [5.8a,c]). However, the homogeneous Helmholtz model is invalid at boundaries, where EPs rapidly change. This leads to local errors (model invalidity error) in EPs reconstructions (eq. [5.8b]), as discussed in (38,39).

In practice, as shown by the noiseless phantom simulations, an additional numerical error is introduced when EPs are derived by approximating spatial derivatives using finite difference kernels, which are directly applied to voxelized B_1^+ data, (eqs. [5.9] and [5.15]). For noiseless cases, this approximation leads to accurate results inside homogeneous regions (eq. [5.11], Fig. 5.3, A). Instead, over tissue boundaries, the adopted FD kernels include voxels that belong to different conductive regions, resulting in erroneous reconstructions that propagate inside homogeneous regions. The amplitude of this numerical boundary error depends on the contrast between the compartments (eq. [5.16])

In reality, the acquired images are intrinsically affected by local fluctuations arising, for example, from thermal noise and the limited extension of the truncated k-space (Gibbs ringing). Computation of derivatives on noisy data using FD kernels amplifies the noise level in the reconstructed EPs maps (42) leading to severe errors, which are in the range of the EPs values themselves. This makes EPs reconstructions challenging not only at boundaries, but also inside homogeneous regions (eq. [5.13], Fig. 5.3, A, and C). These additional imperfections result in different optimal choices of FD kernels based on a trade-off between robustness to spatial fluctuations and numerical boundary error propagation.

As shown by our phantom results, a small FD kernel (K_3) leads to spatially limited boundary errors, which would be ideal for convoluted tissue structures such as the human brain. However, small kernels are highly sensitive to local signal fluctuations (mainly noise). To minimize the impact of spatial fluctuations, large FD kernels, such as K_7 or Savitzky-Golay (SG), in combination with Gaussian apodization and large voxel sizes (bigger than 2 mm) are often adopted. In this work, the adopted large kernel K_7 was used to evaluate the impact of large derivative kernels on conductivity reconstructions. We have demonstrated that this solution leads to accurate reconstructions only inside homogeneous regions larger than the FD kernel size (5).

However, the use of noise-robust large FD kernels comes at the cost of more extended numerical boundary errors. In (42), it has been shown that the SG kernel (49) is more optimal for noise reduction inside homogeneous regions. However, the spatial extension of the SG kernel is in the same order as the K_7 kernel employed here. Therefore numerical boundary errors will be similar, or even worse as the SG kernel weighs heavily distant voxels inside the kernel (42). For *in-vivo* applications, this numerical boundary error is a crucial issue which limits the accuracy of the reconstructed EPs (26,37). For example, for convoluted tissues such as the CSF and the GM regions, which have a spatial extension smaller than large derivative kernels, this numerical boundary error is a main source of inaccuracy resulting into an underestimation of the reconstructed conductivity values, as neighboring tissues with lower conductivity values are also included into the derivative kernel. Ultimately for brain tissues, $V_{RE<30\%}$ was lower than 30%, for the investigated scenario (as shown by the head model simulation results).

Finally, Gibbs ringing is always present in MRI experiments. Gibbs ringing consists of additional local fluctuations in image domain arising from the finite nature of the acquired k-space. As observed from our results, its impact on conductivity reconstructions increases with the voxel size. Hence, while increasing voxel sizes allows higher SNR (lower fluctuations arising from noise), at the same time, it leads to stronger Gibbs ringing.

The presented results apply for 3T head setup, as this is most widely available. To increase the SNR and to achieve higher spatial resolutions (lower boundary error propagation by allowing for smaller kernels), MR-EPT reconstructions at higher field strengths such as 7T can be performed (25,32,37). At 7T, the local field curvature (positively correlated to tissue EPs) is also higher, but the approximations for standard MR-EPT are less valid (25), making EPs reconstructions still challenging. Nevertheless, more accurate EPs reconstructions at 7T are feasible if multi-channel transmit/receive head coils are used in combination with advanced algorithms like the gradient-EPT framework (35).

It is noteworthy to realize that other sources of error, which were not analyze in this paper, might further affect the accuracy of *in-vivo* MR-EPT reconstructions. These additional errors might arise from the piecewise constant EPs assumption for *in-vivo* MR-experiments, the transceive phase assumption, non-ideal B_1^+ magnitude mapping techniques, and measured phase components unrelated to RF phase. Furthermore, reconstructions from MR measurements unfortunately had to be performed in a 2D fashion, since the adopted Multi Slice sequence demonstrated random phase offsets between slices on our scanner, which prevented computing spatial derivative through slices correctly. In principle, this might introduce an additional error. However, we verified this by means of the human head model simulations (data not shown), and we observed that this error is minimal (26). Still, the experimental observations are in line with 3D simulations results. Moreover, the performed error analysis mostly relies on the 3D simulation results, as ground truth values were available. Ultimately, the presented simulation results show that the numerical FD error (direct computation of spatial derivatives on noisy MR data) has already a major impact on the final accuracy of MR-EPT reconstructions.

As shown in this work, the low accuracy of Helmholtz-based MR-EPT reconstructions arises from the direct computation of spatial derivatives on noisy MR data. These derivative-based methods can be classified as "direct methods", since they aim to reconstruct tissue EPs directly from the measured B_1^+ field. In order to circumvent derivative operations on noisy measured B_1^+ data, different approaches have been recently proposed (48,50-53). In these approaches, based on an integral formulation, the reconstruction problem has been reformulated into an inverse fashion, i.e. they fit a model of the EPs distribution to the measured B_1^+ field using iterative minimization methods, thus avoiding derivative operations. Preliminary studies have shown good results especially at tissue boundaries. We believe that this inverse type of approaches should be further investigated to avoid the transceive phase assumption, mitigation strategies, trade-offs, and particular setups, which are instead needed for the Helmholtz-based approaches.

5.6 Conclusions

In this work, we showed that the numerical error arising from the computation of spatial derivatives on noisy discretized data using FD kernels is one of the major impediments for MR-EPT. In particular, for *in-vivo* situations, the use of large FD kernels leads to a severe numerical boundary error propagation that corrupts MR-EPT reconstructions.

5.7 Supporting Information

A

Tissue type EPs (frequency:128 MHz)

	σ [S/m]	ε_r [-]
WM	0.34	52
GM	0.58	73
CSF	2.14	84
Skull	0.06	14
Fat	0.04	6
Heart	0.77	84
Lung	0.58	63
Skin	0.54	62

C

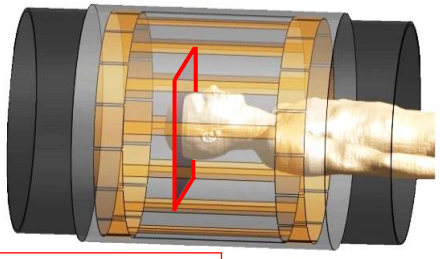

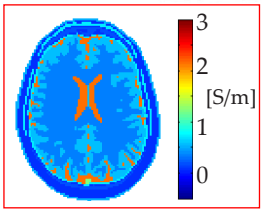

B

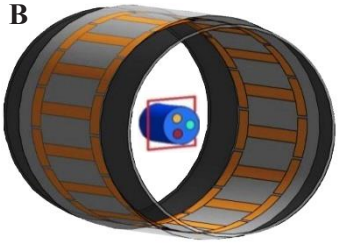

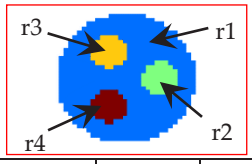

Region	Radius [cm]	σ [S/m]
r1	6.25	0.1
r2	1.5	1
r3	1.5	2
r4	1.5	4

D

High-Pass Birdcage Coil

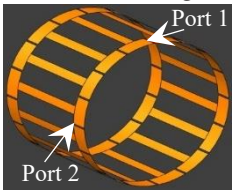

Resonance Frequency = 128 MHz

Length = 58 cm

Diameter= 70.4 cm

E

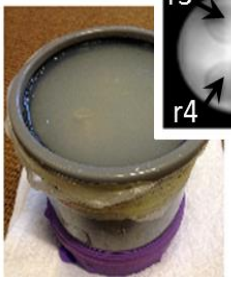

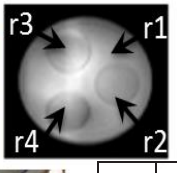

	Radius [cm]	σ [S/m]
r1	6.25	0.1
r2	2	1
r3	2	2
r4	2	4

Supporting Figure 5.S1: Overview of the simulations and measurements setup. **A**) Tissues EPs. **B**) Phantom model inside the birdcage body coil. **C**) Duke model inside the birdcage body coil. **D**) Birdcage coil parameters. **E**) Agar-based phantom used for the MR-experiments.

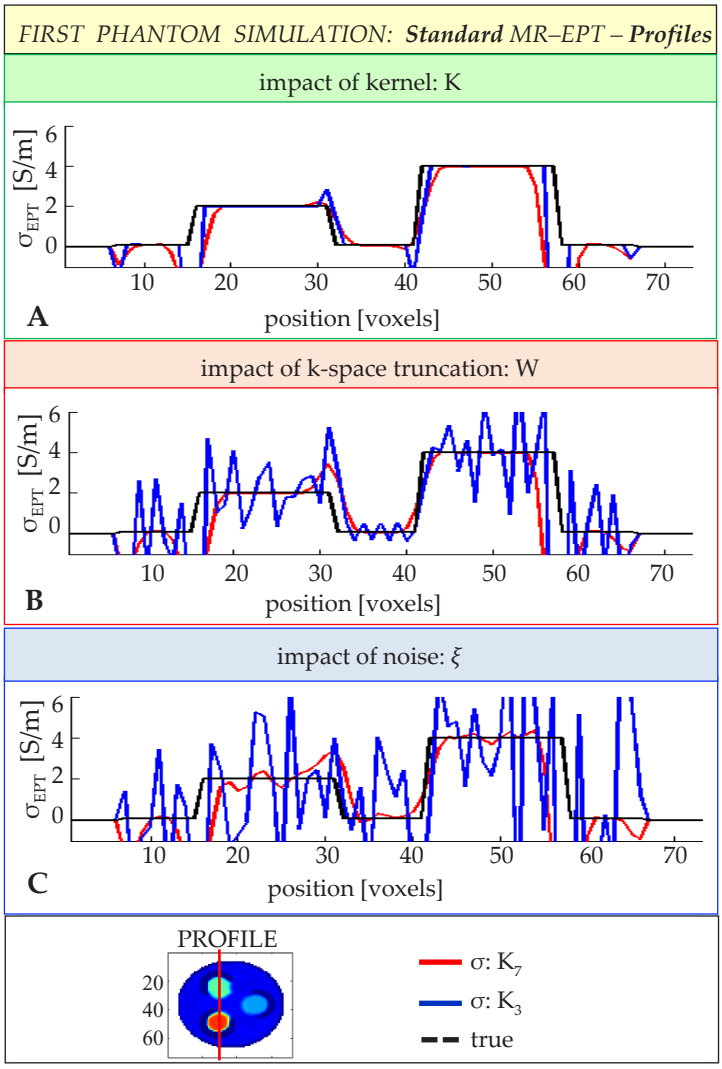

Supporting Figure 5.S2: Profiles of the standard (B_1^+ magnitude included) MR-EPT conductivity reconstructions presented in the first phantom simulation (Fig. 5.3). **A**) Impact of two different FD kernel sizes (K_3 and K_7) on conductivity reconstructions. **B**) Impact of spatial fluctuations arising from k-space truncation (W). **C**) Impact of additional spatial fluctuations arising from thermal noise (ξ) (SNR = 30).

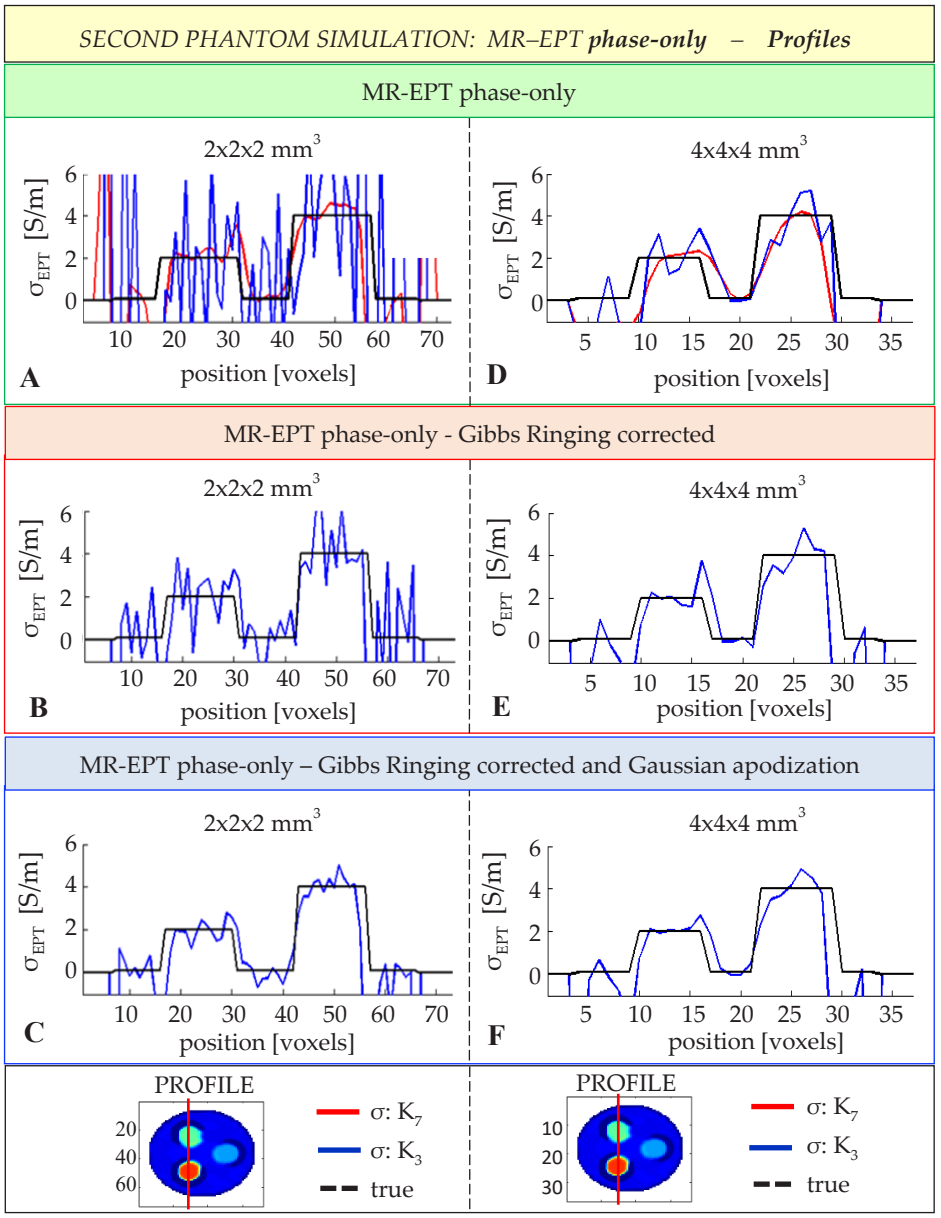

Supporting Figure 5.S3: Profiles of the phase-only conductivity reconstructions presented in the second phantom simulation (Fig. 5.4). Impact of FD kernel size (**A, D**), Gibbs ringing correction (**B, E**) and additional Gaussian apodization (**C, F**) for a voxel size of 2x2x2 mm^3 and 4x4x4 mm^3, respectively.

5.8 References

1. Katscher U, van den Berg C a. T. Electric properties tomography: Biochemical, physical and technical background, evaluation and clinical applications. NMR Biomed. 2017: early view. doi: 10.1002/nbm.3729.
2. Katscher U, Voigt T, Findeklee C, Vernickel P, Nehrke K, Dössel O. Determination of Electric Conductivity and Local SAR Via B1 Mapping. IEEE Trans. Med. Imaging 2009; 28:1365–1374.
3. Zhang X, Schmitter S, Moortele V de P, Liu J, He B. From Complex B1 Mapping to Local SAR Estimation for Human Brain MR Imaging Using Multi-Channel Transceiver Coil at 7T. IEEE Trans. Med. Imaging 2013;32:1058–1067. doi: 10.1109/TMI.2013.2251653.
4. Balidemaj E, Trinks J, Remis RF, Crezee H, van Lier ALHMW, Nederveen AJ, van den Berg CAT. Experimental electric field and dielectric tissue property mapping using a regularized CSI-EPT reconstruction method. Proc. 22nd Sci. Meet. Int. Soc. Magn. Reson. Med. Milano, Italy 2014;22:3252.
5. Shin J, Kim MJ, Lee J, Nam Y, Kim M, Choi N, Kim S, Kim D-H. Initial study on in vivo conductivity mapping of breast cancer using MRI. J. Magn. Reson. Imaging 2014:371–378. doi: 10.1002/jmri.24803.
6. Tha KK, Stehning C, Suzuki Y, Katscher U, Keupp J, Kazumata K, Terasaka S, Cauteren M Van, Kudo K, Hiroki S. Noninvasive Evaluation of Electrical Conductivity of the Normal Brain and Brain Tumors. Proc. 22nd Sci. Meet. Int. Soc. Magn. Reson. Med. Milano, Italy 2014;3:1885.
7. Hallett M. Transcranial magnetic stimulation and the human brain. Nature 2000;406:147–150. doi: 10.1038/35018000.
8. Hummel FC, Cohen LG. Non-invasive brain stimulation: a new strategy to improve neurorehabilitation after stroke? Lancet Neurol. 2006;5:708–712. doi: 10.1016/S1474-4422(06)70525-7.
9. Ridding MC, Rothwell JC. Is there a future for therapeutic use of transcranial magnetic stimulation? Nat. Rev. Neurosci. 2007;8:559–67. doi: 10.1038/nrn2169.
10. Metherall P, Barber DC, Smallwood RH, Brown BH. Three-dimensional electrical impedance tomography. Nature 1996;380:509–512. doi: 10.1038/380509a0.
11. Cheney M, Isaacson D, Newell JC. Electrical impedance tomography. Soc. Ind. Appl. Mat. 1999;41:85–101. doi: 10.1007/s00101-007-1273-y.
12. Oh SH, Lee B Il, Woo EJ, Lee SY, Kim T-S, Kwon O, Seo JK. Electrical conductivity images of biological tissue phantoms in MREIT. Physiol. Meas. 2005;26:S279–S288. doi: 10.1088/0967-3334/26/2/026.
13. Muftuler LT, Hamamura MJ, Birgul O, Nalcioglu O. In vivo MRI electrical impedance tomography (MREIT) of tumors. Proc. 14th Sci. Meet. Int. Soc. Magn. Reson. Med. Seattle, Washington, USA 2006:332.
14. Woo EJ, Seo JK. Magnetic resonance electrical impedance tomography (MREIT) for high-resolution conductivity imaging. Physiol. Meas. 2008;29:R1–R26. doi: 10.1088/0967-3334/29/10/R01.
15. Xu Y, He B. Magnetoacoustic Tomography with Magnetic Induction (MAT-MI). Phys. Med. Biol. 2005:5175–5187. doi: 10.1038/nature13314.A.

16. Li X, Xu Y, He B. Imaging electrical impedance from acoustic measurements by means of magnetoacoustic tomography with magnetic induction (MAT-MI). IEEE Trans. Biomed. Eng. 2007;54:323–330. doi: 10.1109/TBME.2006.883827.

17. Haacke EM, Petropoulos LS, Nilges EW, Wu DH. Extraction of conductivity and permittivity using magnetic resonance imaging. Phys. Med. Biol. 1991;38:723–734.

18. Wen H. Noninvasive quantitative mapping of conductivity and dielectric distributions using RF wave propagation effects in high-field MRI. Proc. SPIE 5030, Medical Imaging: Physics of Medical Imaging. International Society for Optics and Photonics; 2003. pp. 471–477. doi: 10.1117/12.480000.

19. Voigt T, Vaterlein O, Stehning C, Katscher U, Fiehler J. In vivo glioma characterization using MR conductivity imaging. Proc. 19th Sci. Meet. Int. Soc. Magn. Reson. Med. Montréal, Québec, Canada 2011;19:127.

20. Van Lier ALHMW, Hoogduin JM, Polders DL, Boer VO, Hendrikse J, Robe PA, Woerdeman PA, Lagendijk JJW, Luijten PR, van den Berg CAT. Electrical conductivity imaging of brain tumours. Proc. 19th Annu. Meet. ISMRM. Montréal, Québec, Canada 2011;19:4464.

21. Katscher U, Abe H, Ivancevic MK, Keupp J. Investigating breast tumor malignancy with electric conductivity measurements. Proc. 23nd Sci. Meet. Int. Soc. Magn. Reson. Med. Toronto, Canada 2015:3306.

22. Balidemaj E, de Boer P, van Lier a LHMW, Remis RF, Stalpers LJ a, Westerveld GH, Nederveen a J, van den Berg C a T, Crezee J. *In vivo* electric conductivity of cervical cancer patients based on B1+ maps at 3T MRI. Phys. Med. Biol. 2016;61:1596–1607. doi: 10.1088/0031-9155/61/4/1596.

23. Kim D, Choi N, Gho S, Shin J, Liu C. Simultaneous Imaging of In-vivo Conductivity and Susceptibility. Magn. Reson. Med. 2014;71:1144–1150. doi: 10.1002/mrm.24759.

24. Lee J, Shin J, Kim D. MR-Based Conductivity Imaging Using Multiple Receiver Coils. Magn. Reson. Med. 2015. doi: 10.1002/mrm.25891.

25. Van Lier ALHMW, Raaijmakers A, Voigt T, Lagendijk JJW, Katscher U, Van Den Berg CAT. Electric properties tomography in the human brain at 1.5, 3, and 7 T: a comparison study. Magn. Reson. Med. 2014;71:354–363. doi: 10.1002/mrm.24637.

26. Gurler N, Ider YZ. Gradient-Based Electrical Conductivity Imaging Using MR Phase. Magn. Reson. Med. 2016;00:00–00. doi: 10.1002/mrm.26097.

27. Lee SK, Bulumulla S, Wiesinger F, Sacolick L, Sun W, Hancu I. Tissue electrical property mapping from zero echo-time magnetic resonance imaging. IEEE Trans. Med. Imaging 2015;34:541–550. doi: 10.1109/TMI.2014.2361810.

28. Marques JP, Sodickson DK, Ipek O, Collins CM, Gruetter R. Single acquisition electrical property mapping based on relative coil sensitivities: A proof-of-concept demonstration. Magn. Reson. Med. 2015;74:185–195. doi: 10.1002/mrm.25399.

29. Zhang X, Liu J, He B. Magnetic Resonance Based Electrical Properties Tomography: A Review. IEEE Rev Biomed Eng 2014;7:87–96.

30. Bulumulla S, Yeo TB, Zhu Y. Direct calculation of tissue electrical parameters from B1 maps. Proc. 17th Sci. Meet. Int. Soc. Magn. Reson. Med. Honolulu, Hawaii, USA 2009; Honolulu:3043.

31. Sodickson DK, Alon L, Deniz CM, et al. Local Maxwell Tomography using transmit-receive coil arrays for contact-free mapping of tissue electrical properties and

determination of absolute RF phase. Proc. 20th Sci. Meet. Int. Soc. Magn. Reson. Med. Melbourne, Victoria, Aust. 2012;20:387.

32. Zhang X, De Moortele PF Van, Schmitter S, He B. Complex B1 mapping and electrical properties imaging of the human brain using a 16-channel transceiver coil at 7T. Magn. Reson. Med. 2013;69:1285–1296. doi: 10.1002/mrm.24358.

33. Katscher U, Kim DH, Seo JK. Recent progress and future challenges in MR electric properties tomography. Comput. Math. Methods Med. 2013:ID 546562. doi: 10.1155/2013/546562.

34. Hafalir FS, Oran OF, Gurler N, Ider YZ. Convection-reaction equation based magnetic resonance electrical properties tomography (cr-MREPT). IEEE Trans. Med. Imaging 2014;33:777–793. doi: 10.1109/TMI.2013.2296715.

35. Liu J, Zhang X, Schmitter S, Van de Moortele P-F, He B. Gradient-based electrical properties tomography (gEPT): A robust method for mapping electrical properties of biological tissues in vivo using magnetic resonance imaging. Magn. Reson. Med. 2015;74:634–646. doi: 10.1002/mrm.25434.

36. Voigt T, Katscher U, Doessel O. Quantitative conductivity and permittivity imaging of the human brain using electric properties tomography. Magn. Reson. Med. 2011;66:456–466. doi: 10.1002/mrm.22832.

37. Van Lier ALHMW, Brunner DO, Pruessmann KP, Klomp DWJ, Luijten PR, Lagendijk JJW, Van Den Berg CAT. B1+ phase mapping at 7 T and its application for in vivo electrical conductivity mapping. Magn. Reson. Med. 2012;67:552–561. doi: 10.1002/mrm.22995.

38. Seo JK, Kim M-O, Lee J, Choi N, Woo EJ, Kim HJ, Kwon OI, Kim D-H. Error analysis of nonconstant admittivity for MR-based electric property imaging. IEEE Trans. Med. Imaging 2012;31:430–437. doi: 10.1109/TMI.2011.2171000.

39. Duan S, Xu C, Deng G, Wang J, Liu F, Xin SX. Quantitative analysis of the reconstruction errors of the currently popular algorithm of magnetic resonance electrical property tomography at the interfaces of adjacent tissues. NMR Biomed. 2016:744–750. doi: 10.1002/nbm.3522.

40. Li C, Yu W, Huang SY. An MR-Based Viscosity-Type Regularization Method for Electrical Property Tomography. Tomography 2017;3:50-59. doi: 10.18383/j.tom.2016.00283.

41. Lee S. Minimum-noise Laplacian kernel for MR-based electrical properties tomography. Proc. 23nd Sci. Meet. Int. Soc. Magn. Reson. Med. Toronto, Canada 2015:3301.

42. Lee S, Bulumulla S, Hancu I. Theoretical Investigation of Random Noise-Limited Signal-to-Noise Ratio in MR-Based Electrical Properties Tomography. IEEE Trans. Med. Imaging 2015;34:2220–2232.

43. Shin J, Lee J, Kim M, Choi N, Seo JK, Kim D. Quantitative Conductivity Estimation Error due to Statistical Noise in Complex B + Map. Jksmrm 2014;18:303–313.

44. Kellner E, Dhital B, Kiselev VG, Reisert M. Gibbs-ringing artifact removal based on local subvoxel-shifts. Magn. Reson. Med. 2015;76:1574-1581. doi: 10.1002/mrm.26054.

45. Hayt WH, Buck J a. Engineering electromagnetics. 8th Ed. McGraw-Hill; 2011.

46. Strupp JP. FWHM Equations. https://www.cmrr.umn.edu/stimulate/frame/fwhm/node1.html

47. Dietrich O, Raya JG, Reeder SB, Reiser MF, Schoenberg SO. Measurement of signal-to-noise ratios in MR images: Influence of multichannel coils, parallel imaging, and reconstruction filters. J. Magn. Reson. Imaging 2007;26:375–385. doi: 10.1002/jmri.20969.

48. Borsic A, Perreard I, Mahara A, Halter RJ. An inverse problems approach to MR-EPT image reconstruction. IEEE Trans. Med. Imaging 2016;35:244–256. doi: 10.1109/TMI.2015.2466082.

49. Savitzky A, Golay MJE. Smoothing and Differentiation of Data by Simplified Least Squares Procedures. Anal. Chem. 1964;36:1627–1639.

50. Balidemaj E, Van Den Berg CAT, Trinks J, Van Lier ALHMW, Nederveen AJ, Stalpers LJ a, Crezee H, Remis RF. CSI-EPT: A Contrast Source Inversion Approach for Improved MRI-Based Electric Properties Tomography. IEEE Trans. Med. Imaging 2015;34:1788–1796. doi: 10.1109/TMI.2015.2404944.

51. Ropella KM, Noll DC. A regularized, model-based approach to phase-based conductivity mapping using MRI. Magn. Reson. Med. 2016;00:00:00. doi: 10.1002/mrm.26590.

52. Schmidt R, Webb A. A new approach for electrical properties estimation using a global integral equation and improvements using high permittivity materials. J. Magn. Reson. 2016;262:8–14. doi: 10.1016/j.jmr.2015.11.002.

53. Serralles JE, Polimeridis A, Vaidya MV, Haemer G, White JK, Sodickson DK, Lattanzi R. Global Maxwell Tomography: A novel technique for electrical properties mapping without symmetry assumption or edge artifacts. Proc. 24th Sci. Meet. Int. Soc. Magn. Reson. Med. Singapore 2016:2993.

Chapter 6

Helmholtz-based and water content MR-Electrical Properties Tomography: An in-vivo comparison study

In submission in:
Magnetic Resonance in Medicine.

Stefano Mandija

Petar I. Petrov

Jord T. Vink

Sebastian F.W. Neggers

Peter R. Luijten

Cornelis A.T. van den Berg

Abstract

Water content-Electrical Properties Tomography (wEPT) aims to convert water content maps into electrical properties (EPs: conductivity σ, and permittivity ε_r) maps using an empirical model. However, this model is calibrated using literature EPs values, assumed correct, obtained from *ex-vivo* probe measurements. In this study, the validity of the model employed in wEPT is verified for white matter conductivity reconstructions (σ_{WM}) using *in-vivo* MR-Electrical Properties Tomography (MR-EPT) reconstructions as an independent instrument. The accuracy of MR-EPT and wEPT reconstructions at 3T on eight healthy volunteers was assessed with respect to literature values, used to calibrate the wEPT model. Then, the wEPT model was recalibrated using the mean MR-EPT-σ_{WM} value computed among the subjects after WM erosion to avoid boundary errors. Mean wEPT-σ_{WM} values were recomputed and compared with the values previously obtained from the wEPT model calibrated with literature EPs data. Electromagnetic simulations demonstrated that MR-EPT is not accurate on a voxel-to-voxel basis. However, provided sufficient erosion, experimental mean MR-EPT-σ_{WM} values of 8 volunteers agreed with literature. wEPT allows accurate EPs reconstructions with high resolution. wEPT-σ_{WM} values computed using the model calibrated with either the literature-σ_{WM} or MR-EPT-σ_{WM} values are in good agreement. This verifies the validity of the wEPT model calibrated using literature EPs values for the WM region. wEPT allows more accurate and precise EPs reconstructions than MR-EPT. The wEPT model has been verified for σ_{WM}reconstructions in healthy subjects. Care has to be taken for pathological cases, since the wEPT model is calibrated using healthy brain tissues EPs values.

6.1 Introduction

Tissue Electrical Properties (EPs: conductivity σ, and permittivity ε_r), regulate how electromagnetic (EM) fields, such as MR radiofrequency fields (RF: 64-300 MHz) (1–3), interact with the human body. Thus, subject-specific EPs measurements could provide important information to correctly assess the local specific absorption rate (SAR) (1,4). Furthermore, it has also been shown that tumors have different EPs than normal tissues (5,6). Therefore, EPs measurements could in principle be used as a biomarker for diagnostic purposes (6–10).

MR-Electrical Properties Tomography (MR-EPT) is a non-invasive technique that aims to reconstruct RF tissue EPs from measurements of the complex B_1^+ field using clinical MRI scanners (11,12). Standard MR-EPT reconstructions are based on the homogeneous Helmholtz equation (13,14), which assumes piece-wise constant EPs. To avoid this assumption, recent studies suggested employing the full Helmholtz equation, thus including gradients of the EPs inside homogeneous regions. All Helmholtz-based methods require the computation of spatial derivatives on measured data. This operation, performed using finite difference kernels, is highly sensitive to noise (15,16). To reduce the impact of noise, large derivative kernels are often adopted (13,15), at the cost of severe numerical errors at boundaries (17). Currently, these issues considerably hamper the accuracy of MR-EPT reconstructions for highly spatially convoluted tissues such as the human brain.

In parallel, a different MR-based approach named as water content-EPT (wEPT), based on an empirical framework, has been recently proposed (18). wEPT relies on the fact that, at RF frequencies where MRI works, the impedance of cell membranes becomes negligible allowing currents to pass through. Hence at these frequencies, the EPs are predominantly modulated by the tissue ionic concentrations and water content (19,20) according to the Maxwell's mixture theory (21–23). By assuming that the ionic homeostasis maintains constant cellular osmolarity (ionic concentrations) in healthy tissues, tissue EPs can be correlated with the free water content (19,23,24).

The wEPT framework is based on two steps. In the first step, wEPT exploits the known relation between water content and the T_1-T_2 relaxation times (25–30). In particular for brain tissues, water content maps are computed from MR-images based on an empirical relation between water content and the T_1 (27,31). In the second step, water content maps are converted into EPs maps by employing an empirical relation between water content and tissue EPs, calibrated using literature EPs data (18). The validity of this second calibration step can be questioned for *in-vivo* usage for a given human subject. First of all, the adopted literature EPs values pertain to excised tissues, which might differ from *in-vivo* tissues. Secondly, not much is known about inter-subject variation of EPs values. Hence, it is questionable whether this framework can be applied *in-vivo* to each human subject (12).

In this study, we have investigated the validity of the empirical relation adopted in the second step of wEPT using MR-EPT as an independent instrument. For this purpose we have performed a study where *in-vivo* MR-EPT and wEPT measurements on eight healthy subjects were compared. Firstly, we have performed a rigorous electromagnetic simulation study to validate the accuracy of our experimental MR-EPT maps of the spatially convoluted human brain tissues (white matter, WM, gray matter, GM, and the cerebrospinal fluid, CSF). Finally, these findings enabled us to verify the empirical relation employed in the second step of wEPT for WM conductivity reconstructions. This verification was done by recalibrating the wEPT model using the independently computed mean MR-EPT-σ_{WM} value among all the subjects after eroding WM boundary regions.

6.2 Methods

Following local ethical protocols, MRI measurements were performed on eight volunteers (two males, six females, mean age: 21.75 year old, standard deviation: 2.25 years) using a clinical 3T MR-scanner (Achieva, Philips HealthCare, Best, The Netherlands) and a 8-channel transmit/receive head coil. MR-acquisitions and EPs reconstructions using MR-EPT and wEPT were executed as it follows. Two analyses were then performed.

6.2.1 Standard MR-EPT

MR-EPT reconstructions were performed according to (13):

$$\varepsilon_r(\boldsymbol{r}) = \frac{-1}{\mu_0 \varepsilon_0 \omega^2} Re\left(\frac{\nabla^2 B_1^+(\boldsymbol{r})}{B_1^+(\boldsymbol{r})}\right) \quad [6.1]$$

$$\sigma(\boldsymbol{r}) = \frac{1}{\mu_0 \omega} Im\left(\frac{\nabla^2 B_1^+(\boldsymbol{r})}{B_1^+(\boldsymbol{r})}\right) \quad [6.2]$$

with ω: Larmor angular frequency, ε_0/μ_0: free space permittivity/permeability, and $\boldsymbol{r}$: x/y/z-coordinates. As shown in these two equations, the complex B_1^+ field needs to be measured. The B_1^+ magnitude was measured using a dual-TR (AFI) sequence (32): $TR_1/TR_2/TE$ = 50/250/2.5 ms, flip angle = 65°, field of view (FOV) = 240x240x90 mm^3, voxel size = 2.5x2.5x3 mm^3. For the B_1^+ phase, the transceive phase assumption was adopted (13), i.e. the B_1^+ phase was approximated with half of the transceive phase ($\varphi^{\pm}$) (13,14). To map the transceive phase, two phase maps acquired using two single-echo Spin-Echo (SE) sequences with opposite readout gradient polarities were combined ($\varphi^{\pm} = \frac{(\varphi_{\text{spin\_echo\_1}} + \varphi_{\text{spin\_echo\_2}})}{2}$), thus minimizing the impact of potential eddy-currents related artifacts (13,33).

A vendor specific algorithm available on Philips MRI systems (Constant Level of Appearance, CLEAR) was used to divide out the receive phase of the receive coils. For each SE sequence, the adopted sequence parameters were: TR/TE = 800/6 ms, FOV = 240x240x90 mm^3, voxel size = 2.5x2.5x2.5 mm^3, slice gap = 0.5 mm, number-of-signal averaging (NSA) = 2, and signal-to-noise-ratio (SNR) ≈ 70 (34). The total acquisition time for these three sequences was about 25 minutes. Gibbs ringing correction and k-space Gaussian apodization were performed to minimize the impact of high frequency spatial fluctuations in MR-EPT reconstructions as in (17).

6.2.2 Water content EPT

For wEPT reconstructions, the procedure presented in (18) was followed. These reconstructions were based on two steps, each requiring a calibration.

In the first step, the known relation between tissue water content and T_1 was exploited (27,31). As in (18), eq. [6.3] was used to compute water content maps ($W(\boldsymbol{r})$) from image ratio ($I_r(\boldsymbol{r})$) maps (T1-weighted maps) obtained by dividing two T_1-weighted Spin-Echo maps acquired with different TRs (700/3000 ms, respectively):

$$W(\boldsymbol{r}) = w_1 e^{-w_2 I_r(\boldsymbol{r})} . \quad [6.3]$$

The other scan parameters were: TE = 6 ms, FOV = 240x240x90 mm^3, voxel size = 1x1x1.5 mm^3, slice gap = 1.5 mm, NSA = 1, SNR ≈ 30. To allow direct comparison with MR-EPT reconstructions, the same physical volumes were acquired (total acquisition time ~20 minutes).

To verify the values of the model parameters w_1 and w_2 in eq. [6.3] suggested in (18), we first computed w_1 and w_2 for each subject by fitting literature water content values of GM, WM and CSF against the mean I_r values measured for each subject in these three brain regions. To isolate these tissues, brain tissue segmentation was performed with SPM12 (WTCN, UCL, London, UK) for each subject using the volumes acquired with the SE sequence with short-TR. Only the voxels with a probability value (P) > 99% to belong to a certain tissue were considered. Then, the mean w_1 and w_2 values among subjects were computed (w_{1_mean} = 1.527, and w_{2_mean} = 1.484). These values agree with the values in (18), and were therefore adopted to compute water content maps from I_r maps for each subject according to eq. [6.3].

In the second step, EPs maps were derived from $W(\boldsymbol{r})$ maps according to (18):

$$\sigma(\boldsymbol{r}) = c_1 + c_2 e^{c_3 W(\boldsymbol{r})} \quad [6.4]$$

$$\varepsilon_r(\boldsymbol{r}) = p_1 W(\boldsymbol{r})^2 + p_2 W(\boldsymbol{r}) + p_3 \quad [6.5]$$

with $c_1/c_2/c_3$ = 0.286/1.526× 10^{-5}/11.852 , and $p_1/p_2/p_3$=-287/591/-220.

The parameters used in these two empirical relations were derived in (18) from a second calibration procedure consisting in fitting literature water content values against literature EPs values (assumed correct) for the GM, WM, and CSF. We verified the validity of eq. [6.4] for the WM region in our second analysis.

6.2.3 Analyses

In the first analysis, the MR-EPT and wEPT reconstruction accuracy and precision were characterized for the GM, WM, and CSF. We defined the conductivity reconstructions accuracy as: $\Delta\sigma_{\%} = 100 \times \frac{\sigma_{\text{measured}} - \sigma_{\text{literature}}}{\sigma_{\text{literature}}}$, assuming literature values as a reference; and analogously $\Delta\varepsilon_{\%}$ for permittivity reconstructions. We defined the precision as the standard deviation of the reconstructed EPs inside segmented brain regions. For these MR-EPT reconstructions, a 7×7 voxels derivative kernel (K_7^{2D}) was used in-plane (13), thus assuming negligible the contribution from derivatives across slices (35,36) (see supporting information). For each subject, GM, WM, and CSF regions were isolated by segmenting one of the two Spin-Echo volumes used to compute the transceive phase. The voxels with P < 99% were excluded (Fig. 6.1, A, example of MR-EPT-mask). wEPT reconstructions were performed according to eqs. [6.4] and [6.5], whose parameters $c_{1/2/3}$ and $p_{1/2/3}$ were calibrated using literature EPs values. The segmented masks previously used to compute the mean I_r values for each subject were adopted (Fig. 6.1, B, example of wEPT-mask).

In the second analysis, we verified eq. [6.4] for the WM region using independent MR-EPT reconstructions performed with both the derivative kernel K_7^{2D} and a smaller kernel (K_3^{2D}, see supporting information). K_3^{2D} is less noise-robust than K_7^{2D}, but allows less spatial extension of boundary errors. First, the MR-EPT WM masks were eroded by two voxels (Fig. 6.1, C) to allow reliable reconstructions of the mean MR-EPT-σ_{WM}value for each subject. To verify whether this erosion was sufficient to exclude regions affected by boundary errors, we additionally performed MR-EPT reconstructions in the WM from simulated complex B_1^+ fields (see supporting information).

Then, the mean MR-EPT-σ_{WM}value among subjects ($\sigma_{WM-Eroded}^{MREPT}$) was used to recalibrate the parameters $c_{1/2/3}$ in eq. [6.4] of wEPT. The recalibrated $c_1/c_2/c_3$ values were $0.230/3.89\times 10^{-5}/10.935$, respectively. Finally, for each subject, the mean wEPT-σ_{WM} value was recalculated and compared to the previously computed value in the first analysis, where the $c_1/c_2/c_3$ parameters were instead calibrated using literature, *ex-vivo* EPs values. We therefore characterized the error introduced by the use of literature EPs values in the wEPT calibration procedure for wEPT-σ_{WM} reconstructions.

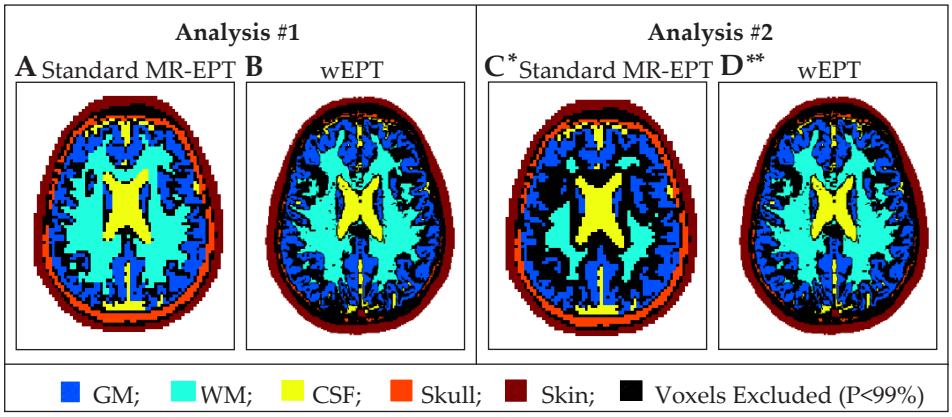

Figure 6.1: Example of the masks used for MR-EPT and wEPT in the two analyses for one slice of one subject. *Noticeable the additional erosion by two voxels for the mask used in MR-EPT in the second analysis (**C**). **The masks used for wEPT were the same for both analyses (**B**, **D**), i.e. no additional erosion was performed for the wEPT masks in the second analysis.

6.3 Results

6.3.1 First analysis

EPs reconstructions performed using MR-EPT and wEPT are shown for all volunteers on one transversal slice (Fig. 6.2). Mean EPs and standard deviations values for the GM, WM, and CSF are reported in Tab. 6.1.

MR-EPT conductivity reconstructions show significant spatial fluctuations. The mean MR-EPT-σ_{WM} value among subjects is 0.4 S/m (~20% overestimation compared to the reference literature value). For the GM and CSF, the mean conductivities are highly underestimated due to severe boundary errors introduced by the spatially convoluted structure of these tissues. The observed standard deviations, comparable to the mean conductivity values, indicate strong intra/inter-subject variability, thus low precision. MR-EPT permittivity reconstructions are instead not feasible.

wEPT EPs reconstructions (Fig. 6.2, second and fourth rows) allow more spatial details in EPs reconstructions (deep gray matter regions are noticeable) than MR-EPT, and fluctuations inside homogeneous regions are much less pronounced. Mean EPs values in the GM, WM, and CSF are in good agreement with literature values ($\Delta\sigma_{\%}$, $\Delta\varepsilon_{\%}$ < 5%). Furthermore, the standard deviation values in wEPT reconstructions are much lower than MR-EPT reconstructions, thus indicating higher precision.

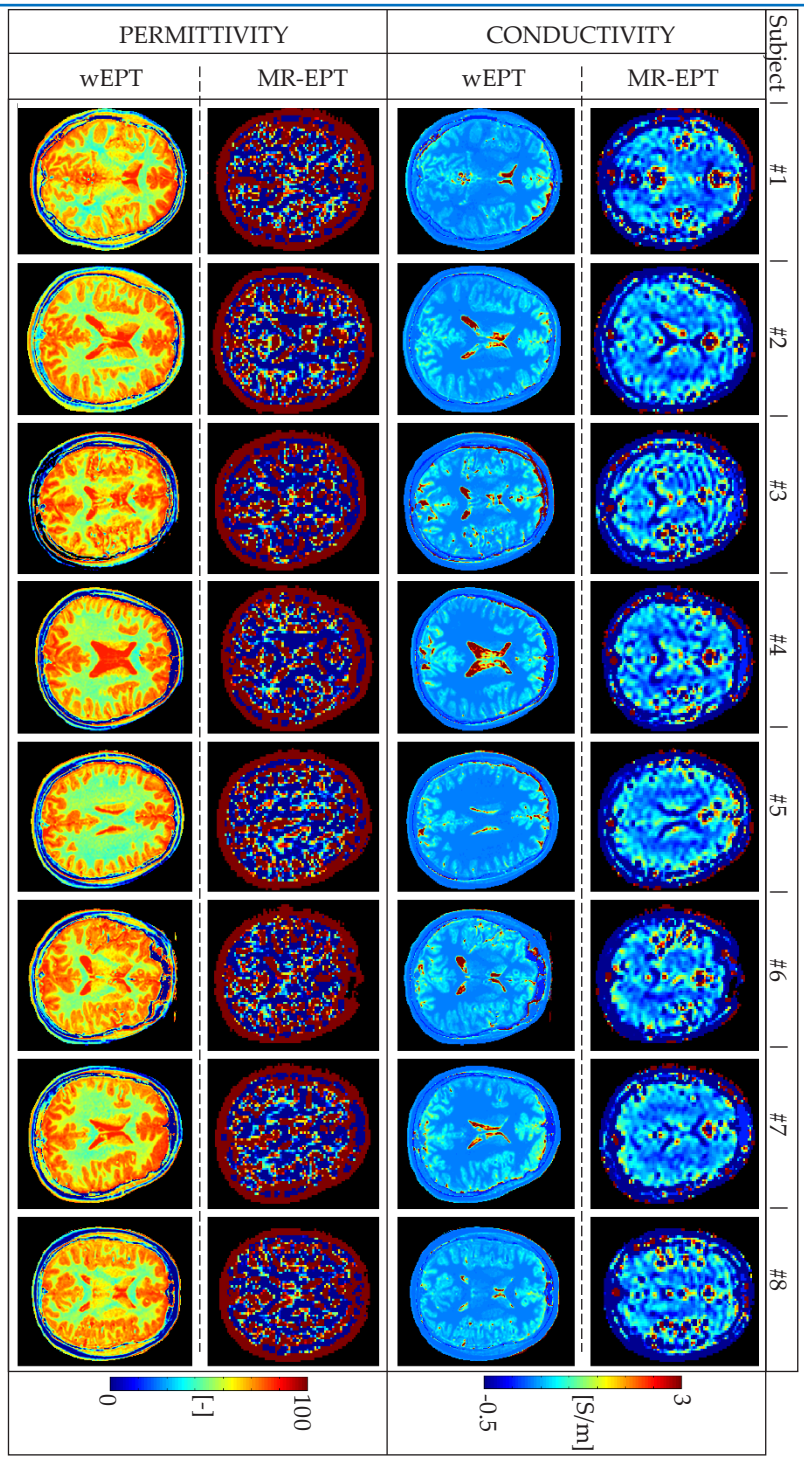

Figure 6.2: Overview of the reconstructed conductivity and permittivity maps using standard MR-EPT and wEPT for all the subjects. For each subject, EPs reconstructions are shown on the same slice to allow direct comparison between techniques. Between subjects, EPs reconstructions are displayed on different slices.

	CONDUCTIVITY: σ [S/m]						*PERMITIVITY*: ε_r [-]		
	GM		**WM**		**CSF**		**GM**	**WM**	**CSF**
Subject	MR-EPT	wEPT	MR-EPT	wEPT	MR-EPT	wEPT	wEPT	wEPT	wEPT
1	0.37 [1.41]	0.62 [0.16]	0.43 [0.45]	0.35 [0.02]	0.29 [2.76]	1.79 [1.52]	72.9 [4.8]	52.3 [5.9]	80.4 [5.8]
2	0.52 [0.81]	0.59 [0.12]	0.38 [0.41]	0.34 [0.02]	0.18 [1.98]	1.65 [1.59]	72.3 [4.1]	51.2 [4.8]	79.3 [7.3]
3	0.41 [1.07]	0.56 [0.14]	0.38 [0.39]	0.34 [0.02]	0.36 [1.93]	2.56 [3.17]	70.5 [7.1]	49.1 [7.6]	79.7 [8.1]
4	0.46 [1.16]	0.60 [0.14]	0.36 [0.39]	0.34 [0.02]	0.39 [2.11]	2.16 [1.99]	72.0 [4.8]	51.2 [4.6]	80.5 [5.8]
5	0.55 [0.81]	0.58 [0.12]	0.41 [0.32]	0.34 [0.02]	0.52 [1.69]	1.95 [1.97]	72.1 [4.1]	50.1 [4.8]	80.1 [5.4]
6	0.55 [0.87]	0.63 [0.14]	0.39 [0.39]	0.35 [0.02]	0.40 [1.92]	2.48 [2.58]	73.6 [4.0]	53.3 [4.1]	81.1 [5.1]
7	0.52 [0.96]	0.68 [0.18]	0.40 [0.33]	0.35 [0.02]	0.68 [2.13]	2.15 [1.80]	74.5 [4.4]	53.0 [5.6]	81.4 [4.6]
8	0.46 [1.00]	0.60 [0.17]	0.42 [0.42]	0.35 [0.02]	0.22 [1.64]	1.51 [1.36]	72.9 [5.1]	52.8 [5.1]	80.0 [5.1]
Mean	0.48 [1.03]	0.61 [0.15]	0.40 [0.39]	0.35 [0.02]	0.38 [2.05]	2.03 [2.08]	72.6 [4.8]	51.6 [5.4]	80.3 [6.0]
Reference	0.59		0.34		2.14		73.5	52.5	84.1

Table 6.1: Summary of the mean conductivity and permittivity values and their standard deviation for each subject and among all subjects for standard MR-EPT reconstructions using K_7^{2D}, and for wEPT reconstructions calibrated with literature EPs values. For standard MR-EPT, permittivity values are not reported since reconstructions do not lead to realistic values.

	WM CONDUCTIVITY :σ_{WM}[S/m]								*WM Water content* [%]	
	MR-EPT				**wEPT**, calibrated with					
Subject	K_7^{2D}		K_3^{2D}		literature-σ_{WM}		$\sigma_{WM-Eroded}^{MREPT}$			
1	0.32	[0.25]	0.32	[1.05]	0.35	[0.02]	0.31	[0.03]	69.7	[0.03]
2	0.32	[0.22]	0.33	[0.86]	0.34	[0.02]	0.31	[0.02]	69.1	[0.02]
3	0.29	[0.26]	0.28	[1.10]	0.34	[0.02]	0.30	[0.03]	68.1	[0.04]
4	0.29	[0.21]	0.29	[0.93]	0.34	[0.02]	0.31	[0.02]	69.0	[0.02]
5	0.31	[0.20]	0.31	[0.93]	0.34	[0.02]	0.30	[0.02]	68.5	[0.02]
6	0.31	[0.22]	0.30	[1.09]	0.35	[0.02]	0.32	[0.02]	70.2	[0.02]
7	0.31	[0.19]	0.30	[0.89]	0.35	[0.02]	0.32	[0.03]	70.1	[0.03]
8	0.32	[0.26]	0.33	[1.15]	0.35	[0.02]	0.31	[0.02]	69.9	[0.02]
Mean	0.31	[0.23]	0.31	[1.00]	0.35	[0.02]	0.31	[0.02]	69.4	[0.03]

Table 6.2: For each subject, mean and standard deviations of: MR-EPT conductivity reconstructions performed using both the large kernel K_7^{2D} and the small kernel K_3^{2D}, after erosion of the WM masks to exclude boundary error regions; wEPT conductivity reconstructions performed using eq. [6.4], calibrated using respectively literature EPs values or, for the WM, the mean MR-EPT-σ_{WM} value after eroding boundary regions; tissue water content in the WM.

6.3.2 Second analysis

If the WM regions affected by boundary errors are excluded by performing erosion of the WM masks, the mean ± standard deviation of $\sigma^{\mathrm{MREPT}}_{\mathrm{WM-Eroded}}$ among subjects is: 0.31 ± 0.23 S/m for K^{2D}_7, and 0.31 ± 1.00 S/m for K^{2D}_3 (Tab. 6.2). These $\sigma^{\mathrm{MREPT}}_{\mathrm{WM-Eroded}}$ values are in good agreement with the literature-σ_{WM} value ($\Delta\sigma_{\%} \approx 10\%$). The observed ~10% underestimation in the $\sigma^{\mathrm{MREPT}}_{\mathrm{WM-Eroded}}$ values seems to arise from the use of 2D kernels, i.e. assuming negligible conductivity contributions from second order derivatives across slices (see third simulation in supporting information). Furthermore, the higher standard deviations for K^{2D}_3 reconstructions compared to K^{2D}_7 indicate that, as expected, small derivative kernels are less noise-robust. Still, even if K^{2D}_7 is used, the observed standard deviations, comparable to the mean conductivity values, indicate low precision. Thus, the observed variability can not be linked to inter-subject variations.

By using $\sigma^{\mathrm{MREPT}}_{\mathrm{WM-Eroded}}$ in the calibration of the parameters in eq. [6.4], the reconstructed mean wEPT-σ_{WM} values agree with the mean wEPT-σ_{WM} values reconstructed in the first analysis, where literature EPs values were used in the calibration procedure. The difference in the mean wEPT-σ_{WM} values between the two different wEPT reconstructions is very small (<10%). This difference is in the range of the observed wEPT-σ_{WM} standard deviations. Thus, the variability in the mean wEPT-σ_{WM} values can not be attributed to inter-subject variability.

6.4 Discussion

In-vivo MR-EPT reconstructions suffer from inaccuracies. wEPT reconstructions are based on fixed relations calibrated used literature data (assumed correct). In this study, we first characterized the accuracy of these two techniques with respect to literature data by means of *in-vivo* EPs reconstructions on eight healthy subjects. Then, we verified the employed empirical relation between water content and conductivity in wEPT (eq. [6.4]) for the WM region by using independent MR-EPT conductivity reconstructions.

The presented results from simulations (supporting information) and *in-vivo* MRI measurements show that MR-EPT conductivity reconstructions are not accurate on a voxel scale for the adopted setup, while permittivity reconstructions are not feasible. These results were obtained using a 3T scanner and a transmit/receive head coil, as this is most widely available.

A major source of error in MR-EPT reconstructions is the computation of spatial derivatives on measured data. To mitigate the noise amplification in MR-EPT reconstructions, relatively large FD kernels such as the adopted K^{2D}_7 or the Savitzky-Golay kernels (13,15) are used.

This inevitably leads to severe numerical boundary errors. However, as shown in this work and demonstrated in the supporting information, if sufficient erosion is performed to avoid regions affected by boundary errors, we can obtain accurate mean MR-EPT σ_{WM} values. Unfortunately for the GM and CSF, this erosion can not be applied due to their limited spatial extension. Smaller resolutions and small kernels should be adopted to correctly quantify EPs in these regions, but this would lead to EPs maps completely corrupted by noise.

As shown in this work, wEPT reconstructions show clear advantages compared to MR-EPT, i.e. higher image resolutions free from boundary artifacts. Using MR-EPT validations, we tried to answer our main research question, i.e. whether literature EPs values can be used to calibrate the water-content/EPs relation in wEPT reconstructions. This assumes that inter-subject variations only arise from water content variations. For this purpose, wEPT-σ_{WM} reconstructions were performed using eq. [6.4] calibrated with the independently computed $\sigma^{MREPT}_{WM-Eroded}$ value, which was the mean WM conductivity value after proper erosion of boundary regions. The wEPT-σ_{WM} values reconstructed using eq. [6.4] calibrated respectively with the literature-σ_{WM} value (analysis 1) and the $\sigma^{MREPT}_{WM-Eroded}$value (analysis 2) are in good agreement. We can therefore conclude that the error introduced by calibrating the wEPT model with the literature-σ_{WM} value is negligible, for the WM region in healthy subjects. Unfortunately, we could not perform this evaluation for the GM and CSF, since MR-EPT reconstructions in these regions are completely corrupted by boundary errors.

Additionally, from our second analysis, a minimal variability in the reconstructed wEPT-σ_{WM} values is observed (0.02 S/m). This can be related to the fact that the ionic homeostasis maintains constant cellular osmolarity in healthy tissues. Therefore, it can be expected that inter-subject variations are very small for healthy subjects. However, since the inter-subject variation in the mean wEPT-σ_{WM} values is in the range of the wEPT-σ_{WM} standard deviation, this variation can not be linked to inter-subject variability.

According to the wEPT framework, small variations in water contents, associated to an altered ionic homeostasis and therefore to pathological situations, would lead to clearly visible variations in permittivity (for low water content tissues) and conductivity (for high water content tissues). However, it is likely that these fixed relations might not be directly applicable for pathological situations, since the adopted parameters are calibrated for healthy human brain tissues.

In future works, it would be interesting to evaluate up to what extent MR-EPT and wEPT are similar and whether they could lead to useful complementary information in case of pathological situations.

Going to higher field strengths (7T) might be of help to improve the accuracy of MR-EPT reconstructions as the local field curvature, in which information on tissue EPs is imprinted, increases (14,15). Additionally, higher field strengths can allow higher SNR levels and higher spatial resolutions, resulting in less noise amplification in the reconstructed EPs maps and lower boundary error propagation (37,38).

Furthermore, correlations between ionic content (sodium) and conductivity reconstructions using MR-EPT have been already anticipated (39), as well as correlations between ionic content and water content (24,40). Since MRI can allow independent measurements of tissue EPs, water content and ionic (sodium) content, it would be a suitable candidate to further investigate these correlations both in normal and pathological situations.

6.5 Conclusions

EPs reconstructions using MR-EPT are not sufficiently accurate for highly spatially convoluted tissues such as the human brain. Still, after sufficient erosion, accurate mean MR-EPT-σ_{WM} values can be obtained. wEPT reconstructions calibrated using literature EPs values allow much higher image resolutions free from boundary artifacts. The employed relation in wEPT between water content and conductivity has been verified for the WM region. However, care has to be taken when applying the wEPT framework to pathological cases, since this framework has been calibrated for healthy brain tissues.

6.6 Supporting information

Three in-silica tests were performed by approximating the experimental conditions.

6.6.1 Methods

A FDTD simulation was performed on a head model (Duke, Virtual Family) using the software Sim4Life (ZMT AG, Zurich, CH). Since the adopted head model had piecewise constant EPs, errors introduced by enforcing the homogeneous Helmholtz equation were avoided inside large homogeneous regions. This head model was placed in the center of a birdcage body coil model resonant at 128 MHz and driven in quadrature mode (Fig. 6.S1). An isotropic grid size of 2x2x2 mm^3 was adopted. The simulated complex B_1^+ field was used for MR-EPT reconstructions. Since in simulation the B_1^+ phase was available, errors introduced by the transceive phase approximation could also be avoided. Furthermore, simulations allowed knowledge of the ground truth, i.e. the dielectric properties of tissues used in input.

Noise was included by independently adding Gaussian noise to the real and imaginary parts of the simulated complex B_1^+ field, mimicking the SNR obtained in the Spin-Echo maps used to compute the transceive phase (SNR ≈ 70). The obtained noisy-complex B_1^+ field was used as input for MR-EPT conductivity reconstructions: convolution of the simulated 3D complex B_1^+ field with 3D FD kernels.

In particular, the 3D kernels used in the simulations were:

- K_7^{3D}: 7x7x5 voxels, combination of "k_{large}" for in-plane derivatives (x/y-directions), and "k_{small}" for derivatives through planes (z-direction). These kernels are described in reference (13).
- K_3^{3D}: 3x3x3 voxels (del2 function in Matlab), adopted in the second simulation test.

In this way, also the conductivity contribution arising from the computation of spatial derivatives through slices ($\partial^2 B_1^+ / \partial z^2$) was included.

In the first simulation test, MR-EPT conductivity reconstructions were performed in the WM using K_7^{3D} to verify the accuracy of the reconstructed WM conductivity values. The mean conductivity value among the 50 simulation runs was computed after erosion by one voxel of the WM mask. This erosion was performed to mimic the exclusion of the voxels at the interface between WM and other tissue types in the first analysis in the manuscript (i.e. the voxels with P < 99%).

In the second simulation test, we verified whether the additional erosion by 2 voxels performed in the second analysis in the manuscript would be sufficient to exclude WM regions affected by numerical boundary errors. Conductivity reconstructions were performed using K_7^{3D} and K_3^{3D}.

Mean WM conductivity values among 50 simulation runs were therefore computed inside the eroded WM mask ($\sigma^{\mathrm{MREPT}}_{\mathrm{WM-Eroded}}$), and compared to the input WM conductivity value. Since K_3^{3D} allows less boundary error compared to K_7^{3D}, we expect that mean WM conductivity values reconstructed using K_7^{3D} and K_3^{3D} agree after sufficient erosion.

As mentioned in the manuscript, reconstructions from MR measurements had unfortunately to be performed in a 2D fashion, since the adopted Multi Slice sequence demonstrated random phase offsets between slices on our scanner, which prevent computing spatial derivative through slices correctly. Therefore, in the third simulation test we verified that neglecting the $\partial^2 B_1^+/\partial z^2$ contribution in conductivity reconstructions does not lead to substantial miscalculations, as suggested in (36). We verified this for the white matter after performing erosion of the boundary regions (as in the second simulation test). For this purpose, conductivity reconstructions were also performed using the 2D kernels employed in the manuscript for the *in-vivo* reconstructions.

In particular, the 2D kernels were:

- K_7^{2D}: 7x7x1 voxels, corresponding to the "$k_{large,2}$" reported in appendix B of reference (13) (for derivatives along the x/y-directions).
- K_3^{2D}: 3x3x1 voxels, (del2 function in Matlab), adopted in the second test in the manuscript.

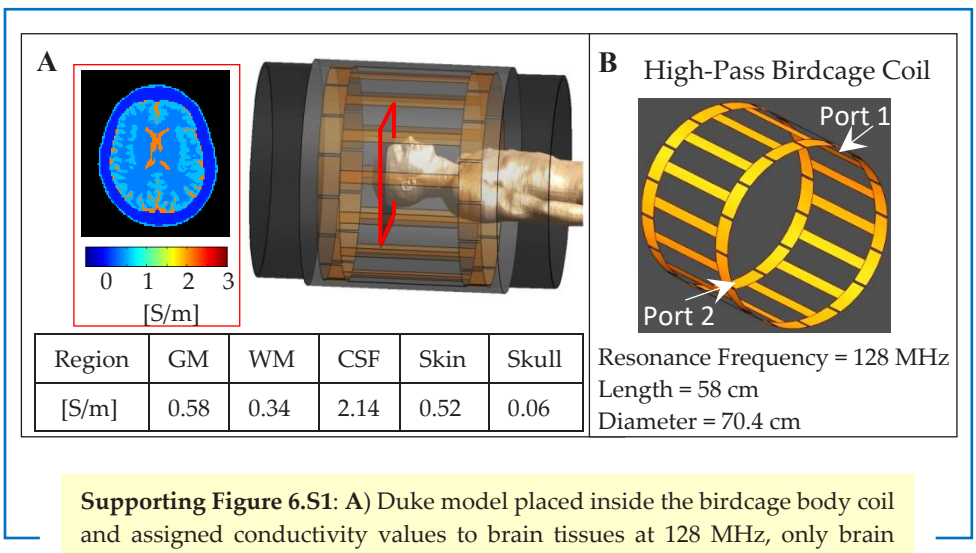

Region	GM	WM	CSF	Skin	Skull
[S/m]	0.58	0.34	2.14	0.52	0.06

Supporting Figure 6.S1: **A**) Duke model placed inside the birdcage body coil and assigned conductivity values to brain tissues at 128 MHz, only brain tissue values are reported. **B**) High-Pass Birdcage coil model.

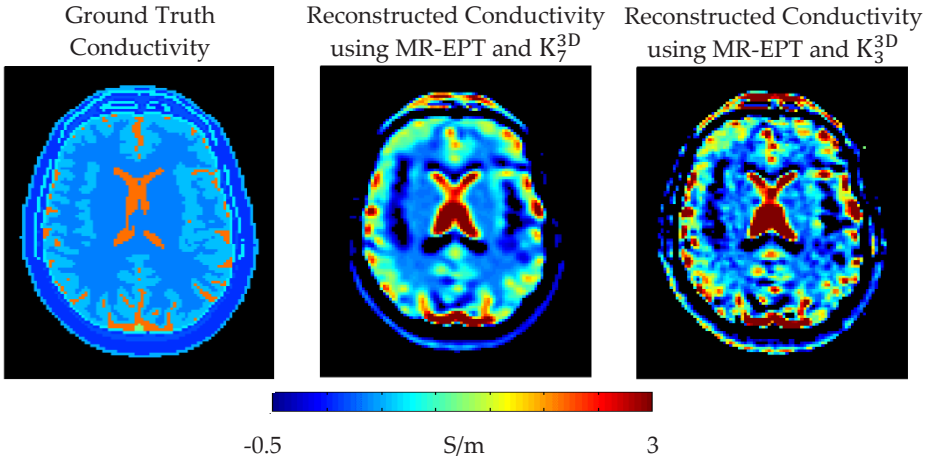

Supporting Figure 6.S2: Original and reconstructed conductivity maps using standard MR-EPT.

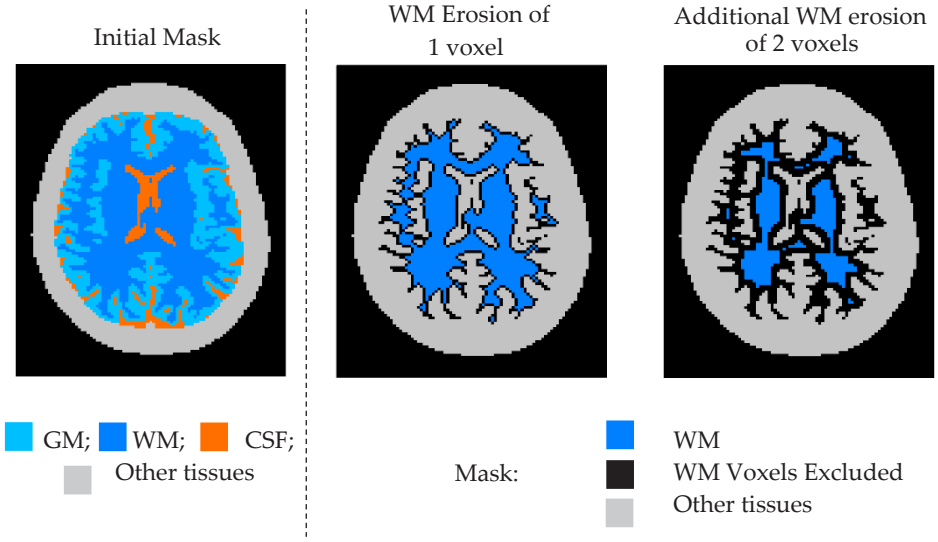

Supporting Figure 6.S3: Initial brain mask and the two masks used to compute the mean WM conductivity value in the two simulation tests.

6.6.2 Results

In Fig. 6.S2, the reconstructed conductivity maps using K_7^{3D} and K_3^{3D} are shown for one slice. The conductivity map reconstructed using the small derivative kernel (K_3^{3D}) shows a more speckled pattern than the conductivity map reconstructed using the large derivative kernel (K_7^{3D}). This is because the small derivative kernel K_3^{3D} is less noise-robust than large derivative kernel K_7^{3D}. However, the use of a small derivative kernel leads to less boundary errors (less blurring).

In Fig. 6.S3, one slice of the initial brain mask (left image) is shown, as well as the two corresponding masks used to compute the mean conductivity value in the WM region in the two simulation tests. The black voxels in the two white matter masks represent the eroded voxels inside the WM region. For the initial masks, the number of voxels in the WM is 49961. This number is reduced to 30619 and 13099, respectively after the first and the second erosion. These two eroded masks are similar to the ones obtained from the MR-measurements after segmentation and erosion (Fig. 6.1 in the manuscript).

In Fig. 6.S4, the result of the first simulation test is shown. The reconstructed mean σ_{WM} value among the 50 simulation runs is 0.41 S/m. This value is in line with the experimental mean σ_{WM} value among subjects obtained in the first analysis in the manuscript. By comparing the computed mean σ_{WM} value to the true input σ_{WM} value (0.34 S/m), an overestimation of ~ 20% is observed, as in the first analysis in the manuscript based on experimental data. This is mainly due to the severe boundary error introduced by the use of the large derivative kernel K_7^{3D}.

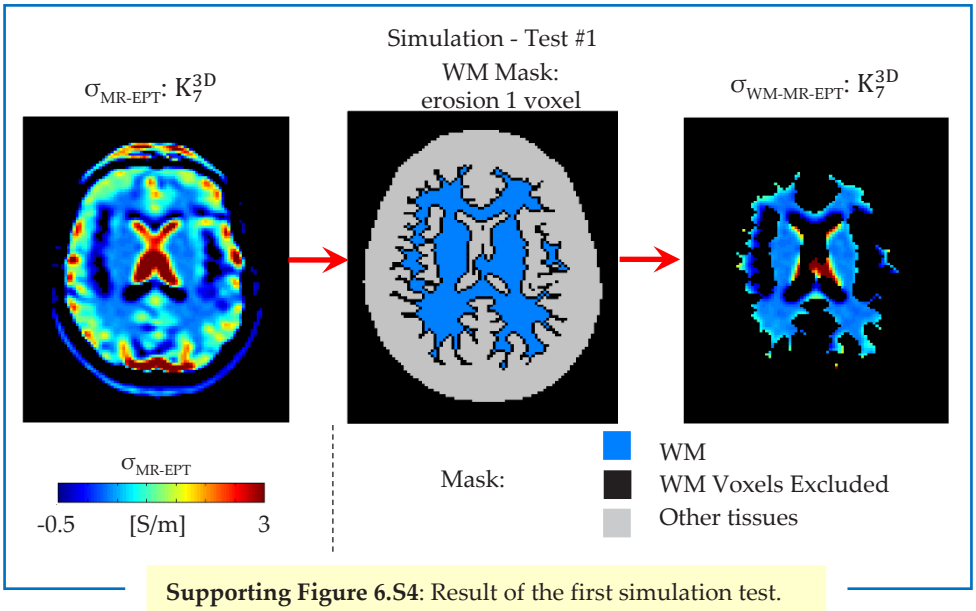

Supporting Figure 6.S4: Result of the first simulation test.

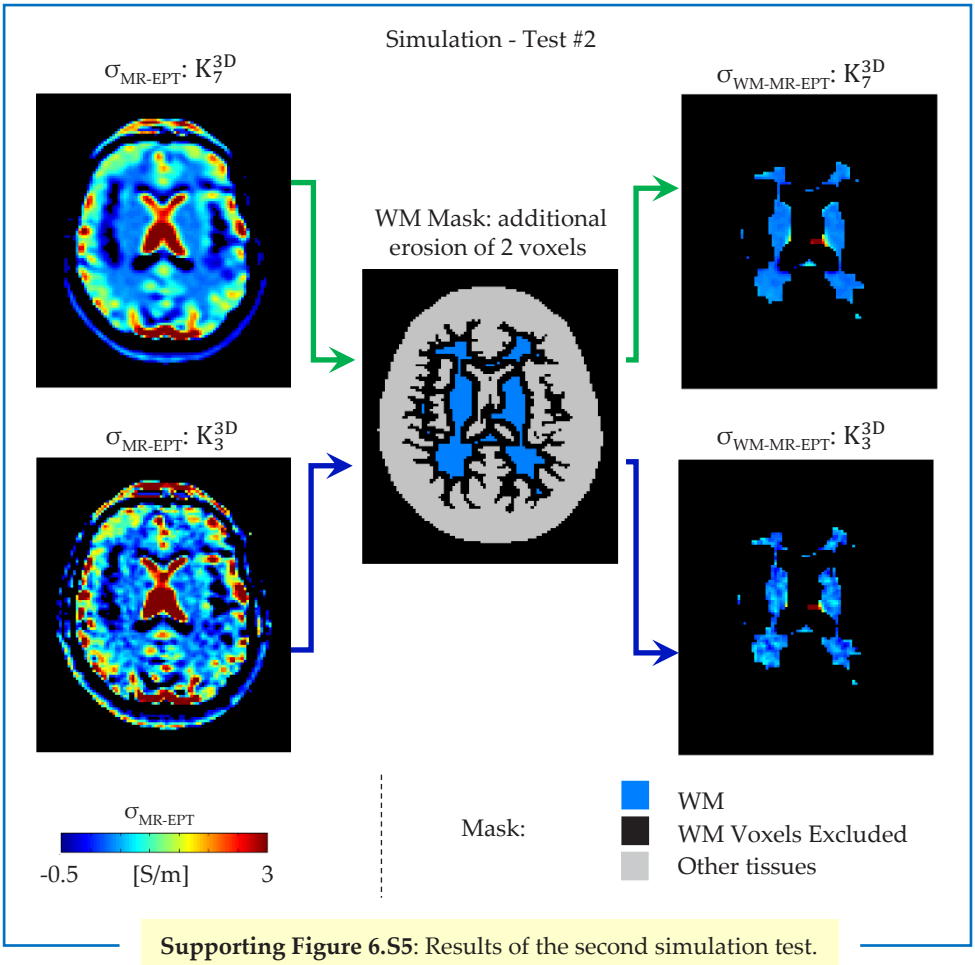

Supporting Figure 6.S5: Results of the second simulation test.

The result of the second simulation test is shown Fig. 6.S5. The reconstructed mean $\sigma_{WM-Eroded}^{MREPT}$ values among the 50 simulation runs are 0.33 S/m and 0.32 S/m for K_7^{3D} and K_3^{3D}, respectively. These values are in good agreement with the true input value (small underestimation $\Delta\sigma < 6\%$). Furthermore, we observe that these values also agree with the computed $\sigma_{WM-Eroded}^{MREPT}$ obtained in the second analysis in the manuscript, based on experimental data, after the same erosion by two voxels was performed.

Relatively to the third simulation test, we observed that if the conductivity contribution arising from the $\partial^2 B_1^+/\partial z^2$ term is neglected, i.e. the 2D kernels are used, an underestimation of about 10% in the mean WM conductivity value is observed. This might explain the underestimation of ~10% observed for the $\sigma_{WM-Eroded}^{MREPT}$ values reported in the second analysis in the manuscript.

6.6.3 Conclusions

These results suggest that the additional erosion of two voxels performed in the second analysis in the manuscript is sufficient to minimize the impact of the boundary error in the computation of the mean WM conductivity values. Additionally, neglecting the $\partial^2 B_1^+/\partial z^2$ term for the in-vivo MR-EPT reconstructions does not introduce substantial miscalculations (~10% underestimation compared to the literature value).

Provided negligible intra/inter-subject variations, the mean $\sigma_{\mathrm{WM-Eroded}}^{\mathrm{MREPT}}$ value is representative. Thus, this value can be used in the calibration procedure of the parameters $c_{1/2/3}$ for the wEPT conductivity reconstructions in the second analysis in the manuscript.

GM and CSF regions are severely affected by boundary errors, and tissue erosion can not be applied due to their limited spatial extension. Therefore, the performed verifications can not be done.

6.7 References

1. Katscher U, Voigt T, Findeklee C, Vernickel P, Nehrke K, Dössel O. Determination of Electric Conductivity and Local SAR Via B1 Mapping. IEEE Trans. Med. Imaging 2009;28: 1365–1374.
2. Bulumulla S, Yeo TB, Zhu Y. Direct calculation of tissue electrical parameters from B1 maps. Proc. 17th Sci. Meet. Int. Soc. Magn. Reson. Med. Honolulu, Hawaii, USA 2009; Honolulu:3043.
3. Voigt T, Katscher U, Doessel O. Quantitative conductivity and permittivity imaging of the human brain using electric properties tomography. Magn. Reson. Med. 2011;66:456–466. doi: 10.1002/mrm.22832.
4. Zhang X, Schmitter S, Moortele V de P, Liu J, He B. From Complex B1 Mapping to Local SAR Estimation for Human Brain MR Imaging Using Multi-Channel Transceiver Coil at 7T. IEEE Trans. Med. Imaging 2013;32:1058–1067. doi: 10.1109/TMI.2013.2251653.
5. Schepps JL, Foster KR. The Uhf and microwave dielectric properties of normal and tumor tissues variation in dielectric properties with tissue water content. Phys. Med. Biol. 1980;25:1149–1159.
6. Surowiec AJ, Stuchly SS, Barr JR, Swarup A. Dielectric Properties of Breast Carcinoma and the Surrounding Tissues. IEEE Trans. Biomed. Eng. 1988;35:257–263. doi: 10.1109/10.1374.
7. Shin J, Kim MJ, Lee J, Nam Y, Kim M, Choi N, Kim S, Kim D-H. Initial study on in vivo conductivity mapping of breast cancer using MRI. J. Magn. Reson. Imaging 2014:371–378. doi: 10.1002/jmri.24803.
8. Katscher U, Abe H, Ivancevic MK, Keupp J. Investigating breast tumor malignancy with electric conductivity measurements. Proc. 23nd Sci. Meet. Int. Soc. Magn. Reson. Med. Toronto, Canada 2015:3306.
9. Katscher U, Djamshidi K, Voigt T, Ivancevic M, Abe H, Newstead G, Keupp J. Estimation of breast tumor conductivity using parabolic phase fitting. Proc. 20th Sci. Meet. Int. Soc. Magn. Reson. Med. Melbourne, Victoria, Aust. 2012:2335.
10. van Lier ALHMW, Hoogduin JM, Polders DL, Boer VO, Hendrikse J, Robe PA, Woerdeman PA, Lagendijk JJW, Luijten PR, van den Berg CAT. Electrical conductivity imaging of brain tumours. Proc. 19th Annu. Meet. ISMRM. Montréal, Québec, Canada 2011;19:4464.
11. Katscher U, Kim DH, Seo JK. Recent progress and future challenges in MR electric properties tomography. Comput. Math. Methods Med. 2013:ID 546562. doi: 10.1155/2013/ 546562.
12. Katscher U, van den Berg C a. T. Electric properties tomography: Biochemical, physical and technical background, evaluation and clinical applications. NMR Biomed. 2017: early view. doi: 10.1002/nbm.3729.
13. van Lier ALHMW, Brunner DO, Pruessmann KP, Klomp DWJ, Luijten PR, Lagendijk JJW, Van Den Berg CAT. B1+ phase mapping at 7 T and its application for in vivo electrical conductivity mapping. Magn. Reson. Med. 2012;67:552–561. doi: 10.1002/mrm.22995.
14. van Lier ALHMW, Raaijmakers A, Voigt T, Lagendijk JJW, Katscher U, Van Den Berg CAT. Electric properties tomography in the human brain at 1.5, 3, and 7 T: a comparison study. Magn. Reson. Med. 2014;71:354–363. doi: 10.1002/mrm.24637.

15. Lee S, Bulumulla S, Hancu I. Theoretical Investigation of Random Noise-Limited Signal-to-Noise Ratio in MR-Based Electrical Properties Tomography. IEEE Trans. Med. Imaging 2015;34:2220–2232.

16. Shin J, Lee J, Kim M, Choi N, Seo JK, Kim D. Quantitative Conductivity Estimation Error due to Statistical Noise in Complex B + Map. Jksmrm 2014;18:303–313.

17. Mandija S, Sbrizzi A, van Lier ALHMW, Luijten PR, van den Berg CAT. Artifacts affecting derivatives of B1 maps for EPT reconstructions. Proc. 24th Sci. Meet. Int. Soc. Magn. Reson. Med. Singapore 2016:2989.

18. Michel E, Hernandez D, Lee SY. Electrical conductivity and permittivity maps of brain tissues derived from water content based on T 1 -weighted acquisition. Magn. Reson. Med. 2016; early view. doi: 10.1002/mrm.26193.

19. Schwan HP, Foster KR. Microwave dielectric properties of tissue. Some comments on the rotational mobility of tissue water. Biophys. J. 1977;17:193–197. doi: 10.1016/S0006-3495(77)85637-3.

20. Pethig R. Dielectric Properties of Biological Materials: Biophysical and Medical Applications. IEEE Trans. Electr. Insul. 1984;EI-19:453–474. doi: 10.1109/TEI.1984.298769.

21. Maxwell JC. Treatise of Electricity and Magnetism. 1954. doi: 10.1017/CBO9781107415324.004.

22. Fricke H. The Maxwell-Wagner dispersion in a suspension of ellipsoids. J. Phys. Chem. 1953;57:934–937. doi: 10.1021/j150510a018.

23. Foster KR, Schepps JL, Stoy RD, Schwan HP. Dielectric properties of brain tissue between 0.01 and 10 GHz. Phys. Med. Biol. 1979;24:1177–1187. doi: 10.1088/0031-9155/24/6/008.

24. Farace P, Pontalti R, Cristoforetti L, Antolini R, Scarpa M. An automated method for mapping human tissue permittivities by MRI in hyperthermia treatment planning. Phys. Med. Biol. 1997;2159:2159–2174. doi: 10.1088/0031-9155/42/11/011.

25. Neeb H, Zilles K, Shah NJ. A new method for fast quantitative mapping of absolute water content in vivo. Neuroimage 2006;31:1156–1168. doi: 10.1016/j.neuroimage.2005.12.063.

26. Abbas Z, Gras V, Möllenhoff K, Oros-Peusquens A-M, Shah NJ. Quantitative water content mapping at clinically relevant field strengths: A comparative study at 1.5T and 3T. Neuroimage 2015;106:404–413. doi: 10.1016/j.neuroimage.2014.11.017.

27. Fatouros PP, Marmarou a. Use of magnetic resonance imaging for in vivo measurements of water content in human brain: method and normal values. J. Neurosurg. 1999;90:109–15. doi: 10.3171/jns.1999.90.1.0109.

28. Andersen C. In vivo estimation of water content in cerebral white matter of brain tumour patients and normal individuals: Towards a quantitative brain oedema definition. Acta Neurochir. (Wien). 1997;139:249–256. doi: 10.1007/BF01844760.

29. Whittall KP, Mackay AL, Graeb D a., Nugent R a., Li DKB, Paty DW. In vivo measurement ofT2 distributions and water contents in normal human brain. Magn. Reson. Med. 1997;37:34–43. doi: 10.1002/mrm.1910370107.

30. Kiricuta I-CJ, Simplaceanu V. Tissue Water Content and Nuclear Magnetic Resonance in Normal and Tumor Tissues. Cancer Res. 1975;35:1164–1167.

31. Callaghan MF, Helms G, Lutti A, Mohammadi S, Weiskopf N. A general linear relaxometry model of R1 using imaging data. Magn. Reson. Med. 2015;73:1309–1314. doi: 10.1002/mrm.25210.

32. Yarnykh VL. Actual flip-angle imaging in the pulsed steady state: A method for rapid three-dimensional mapping of the transmitted radiofrequency field. Magn. Reson. Med. 2007;57:192–200. doi: 10.1002/mrm.21120.

33. Mandija S, van Lier ALHMW, Katscher U, Petrov PI, Neggers SFW, Luijten PR, van den Berg CAT. A geometrical shift results in erroneous appearance of low frequency tissue eddy current induced phase maps. Magn. Reson. Med. 2015. doi: 10.1002/mrm.25981.

34. Dietrich O, Raya JG, Reeder SB, Reiser MF, Schoenberg SO. Measurement of signal-to-noise ratios in MR images: Influence of multichannel coils, parallel imaging, and reconstruction filters. J. Magn. Reson. Imaging 2007;26:375–385. doi: 10.1002/jmri.20969.

35. Zhang X, Zhu S, He B. Imaging electric properties of biological tissues by RF field mapping in MRI. IEEE Trans. Med. Imaging 2010;29:474–481. doi: 10.1016/j.biotechadv.2011.08.021.

36. Gurler N, Ider YZ. Gradient-Based Electrical Conductivity Imaging Using MR Phase. Magn. Reson. Med. 2016;00:00–00. doi: 10.1002/mrm.26097.

37. Zhang X, De Moortele PF Van, Schmitter S, He B. Complex B1 mapping and electrical properties imaging of the human brain using a 16-channel transceiver coil at 7T. Magn. Reson. Med. 2013;69:1285–1296. doi: 10.1002/mrm.24358.

38. Liu J, Zhang X, Schmitter S, Van de Moortele P-F, He B. Gradient-based electrical properties tomography (gEPT): A robust method for mapping electrical properties of biological tissues in vivo using magnetic resonance imaging. Magn. Reson. Med. 2015;74:634–646. doi: 10.1002/mrm.25434.

39. van Lier ALHMW, de Bruin PW, Aussenhofer SA, Luijten PR, Lagendijk JJW, van den Berg CAT, Webb AG. 23Na-MRI and EPT: Are sodium concentration and electrical conductivity at 298 MHz (7T) related? Proc. 21st Sci. Meet. Int. Soc. Magn. Reson. Med. Salt Lake City, Utah, USA 2013:0115.

40. Madelin G, Kline R, Walvick R, Regatte RR. A method for estimating intracellular sodium concentration and extracellular volume fraction in brain in vivo using sodium magnetic resonance imaging. Sci. Rep. 2014;4:1–7. doi: 10.1038/srep04763.

Chapter 7

Summary and General Discussion

7.1 Low frequency EPs

In the past, preliminary studies suggested that a LF conductivity related contrast could be observed through LF-EPT using solely MRI hardware and imaging techniques (1–4). The results presented in these studies are however in sharp contrast with simulations.

Chapter 2 investigates this conflicting finding by means of MR measurements and simulations. In LF-EPT, subtractions of phase images acquired with opposite readout polarities are needed to decouple the RF phase (arising from the RF transmit field) and the gradient eddy current related phase (arising from the induced LF eddy currents). It has been found that, for this technique to work, it is necessary to perfectly decouple these two phase contributions. It was mathematically demonstrated that this operation is very sensitive with respect to even sub-millimeter geometrical distortions arising from imaging imperfections. Such small imperfections are very difficult to avoid in MRI experiments. It has been shown that even sub-voxel shifts in the order of 10% of the voxel size result in considerable (several milli-radians) RF phase leakage into the LF phase. This RF phase leakage explains the observed proportionality of conductivity with apparent LP phase pattern. In fact, this phase is not related to LF induced currents but to a leakage of RF phase, and thus related to RF conductivity. Additionally, it has been demonstrated by means of MR measurements and simulations that even if perfect decoupling between RF and LF phase is achieved, the expected LF phase is too small to be measured (micro-radians). In fact, after correcting for geometrical distortions, the LF phase is completely obscured by noise. To be able to measure LF phase contributions, either much higher SNR (at least three orders of magnitude) needs to be achieved, which is not realistic, or much stronger currents need to be induced in tissues, provided the perfect correction for geometrical distortions.

In chapter 4, a TMS device was used to augment the level of induced currents. By using a TMS device instead of MR gradients, much stronger incident time-varying magnetic fields can be obtained (5). In this way, the reported three orders of magnitude increase needed to measure the induced LF phase could theoretically be achieved (6). Furthermore, by using a TMS device, subtractions of phase maps acquired with opposite readout gradient polarities are not needed anymore. Therefore, RF phase leakage due to sub-millimeter geometrical distortions observed in LF-EPT is avoided. For such an inductive technique to work it is fundamental to disentangle the incident TMS magnetic field, which directly depends on the TMS coil current, from the induced magnetic field, in which information on LF EPs is imprinted. It was concluded that very strong, incident, time-varying TMS magnetic fields (20000 T/s) are needed in order to bring the induced LF phase above the MR noise level.

However as demonstrated in chapter 3 and 4, incident, non-homogeneous TMS magnetic fields of such strength would lead to strong gradients over a voxel, and subsequently considerable intra-voxel dephasing. This would result in severe signal loss in the reconstructed images right below the TMS coil, and thus, non-measurable LF phase.

Therefore from the results presented in chapters 2 and 4, it can be concluded that, although very appealing, LF phase measurements from which LF conductivity could be reconstructed can not be performed by inductively inducing current in tissues using time-varying incident magnetic fields with the applied techniques.

At the moment, LF conductivity reconstructions are only possible from MR measurements of the magnetic field created by LF tissue eddy currents directly injected using skin-surface electrodes (MR-EIT) (7–9). By directly injecting currents in tissues, there is no need anymore to discriminate between the incident (now absent) and the induced magnetic field. Interestingly, the strength of the induced magnetic field created by TMS induced LF eddy currents or directly injected currents in tissue with electrodes (as in MR-EIT) is the same. However, in MR-EIT longer current injection times (10 ms) with respect to LF-EPT (0.1 ms) allow for more phase accumulation, which makes the magnetic field induced by these tissue eddy currents measurable with clinical MRI scanners. Few *in-vivo* MR-EIT studies have been reported (10–14). However, in order to achieve enough SNR for *in-vivo* applications, strong injection currents and many measurements averaging resulting in long scan time are required. To reduce the scan time for *in-vivo* purposes, stronger currents should be injected. However, strong injection currents (10 mA) result in pain sensation. This is to the current main limitation of MR-EIT for *in-vivo* human studies. Based on the capability of MR-EIT to measure low frequency tissue conductivity, future research should be therefore focused on defining new injection protocols, which would permit feasible scan time and low levels of injected currents.

7.2 Can MRI provide guidance of TMS?

Currently, TMS dosimetry is performed in an empirical way, i.e. using the motor-threshold (MT) method over the motor cortex (see chapters 3 and 4). However, since tissue EPs and the brain cortex gyrification modulate the induced electric field in the brain, it is understandable that the TMS dose varies for different brain regions (15–18). Therefore, although widely used, the MT method can not be considered reliable for most TMS purposes (19–21).

MRI can provide important information to guide subject-specific TMS dosimetry. Firstly, as shown in chapter 3, it is possible to measure the z-component of the incident TMS magnetic field with MRI. These measurements can allow validation of electromagnetic (EM) models of TMS coils (22).

Subsequently, validated TMS coil models can be used in EM simulations in conjunction with subject-specific brain tissue geometry (obtained from MR images segmentations) and tissue EPs to accurately estimate the induced electric field in the brain (15,23,24). Finally, maps of the induced neuronal activity can be computed by combining the simulated electric fields with bio-electrical neuronal models. By adjusting the TMS machine output and the TMS coil position and orientation, different neuronal activation scenarios can be predicted. These pre-treatment predictions can therefore be used for subject-specific guidance of TMS treatments (25).

Furthermore, these simulations can allow validation of TMS induced neuronal activation. This validation can be performed by comparing subject-specific, simulated neuronal activation maps with neuronal activation maps reconstructed from concurrent TMS-fMRI experiments, provided that the same experimental conditions (coil placement and TMS dose) are reproduced in the simulations.

Currently, we are working on the development of such a framework. Preliminary fMRI results show that the same brain areas are activated in response to a voluntary thumb movement (as a reference) and in response to TMS stimulation on the motor cortex (after having observed TMS induced thumb movement). This agreement proves the feasibility of performing concurrent TMS-fMRI experiment. Future work will be focused on the validation of commonly adopted neuronal models by comparing TMS induced activation maps with simulated neuronal activation maps.

7.3 High frequency EPs

7.3.1 MR-EPT: Is it accurate enough?

The key point in MR-EPT reconstructions is the accurate computation of spatial derivatives on measured data (complex transmit B_1^+ field). This computation is performed by convolving the measured, complex B_1^+ field with finite difference schemes in the form of derivative kernels (26–28).

In chapter 5, the impact of this operation on conductivity reconstructions has been characterized. It has been mathematically demonstrated that the error introduced by the computation of second order derivatives on noisy data is in the range of the EPs values themselves. In particular, it has been shown that small derivative kernels are highly sensitive to noise, whereas large derivative kernels, more noise-robust, lead to severe boundary errors.

For spatially convoluted tissue structures such as the human brain, small derivative kernels (3×3×3 voxels) would be ideal, as they would lead to reduced boundary error propagation. However, small derivative kernels are highly sensitive to noise, and, in practice, large derivative kernels are adopted for *in-vivo* MR-EPT reconstructions.

This results in a much lower effective resolution in the reconstructed EPs maps: e.g. MR images acquired with a resolution of 2×2 mm^2 in-plane, combined with a large derivative kernel 7×7 voxels, would result in a 14x14 mm^2 in-plane resolution. As shown in chapters 5 and 6, this severely hampers the accuracy of EPs reconstructions for convoluted tissue structures such as the GM and CSF, as boundary errors would be dominant. As shown in chapter 6, if sufficient erosion is performed to avoid regions affected by boundary errors, accurate mean conductivity values can be obtained for the WM region.

Although the analysis presented in chapters 5 and 6 was based on conductivity reconstructions, these conclusions largely apply to permittivity reconstructions too. Permittivity reconstructions are even much more challenging than conductivity reconstructions, as precision of B_1^+ magnitude mapping techniques are typically lower. Furthermore, displacement currents related to permittivity are lower than conduction currents at field strengths smaller than 7T. In chapter 6, some *in-vivo* MR-EPT permittivity reconstructions at low field strength (3 T) are presented. Unfortunately, the presented results indicate that permittivity reconstructions are currently not feasible due to severe over/under-shootage of the reconstructed values.

On the reconstruction side, in chapter 5 it has been additionally investigated whether noise mitigation strategies such as Gaussian apodization, median filtering, and Gibbs ringing corrections could be of help. These strategies might help to reduce the impact of spatial fluctuations in the reconstructed EPs maps. However, these operations result in larger effective derivative kernels. Hence, they lead to even more extended boundary error propagations. Therefore, in chapter 5 it is concluded that these strategies would not substantially increase the accuracy of *in-vivo* MR-EPT reconstructions for convoluted tissues such as the human brain, as boundary errors are dominant.

From the results presented in chapters 5 and 6 it can be concluded that, at the current moment, MR-EPT does not allow EPs reconstructions on a voxel basis, but it can only provide qualitative and volumetric conductivity maps. In fact, MR-EPT can only provide accurate mean conductivity values in large homogeneous regions. As found in chapter 5, the major issue for *in-vivo* MR-EPT reconstructions in the brain is the computation of spatial derivatives on noisy data.

7.3.2 Water content EPT (wEPT): Is it a possible alternative to MR-EPT?

In chapter 6, a comparison between *in-vivo* MR-EPT and wEPT reconstructions has been presented. wEPT aims to reconstruct EPs maps from water content maps based on a fixed relation calibrated with literature data (29). Contrary to MR-EPT reconstructions, computations of spatial derivatives are avoided.

The results presented in chapter 6 show that *in-vivo* wEPT reconstructions have some advantages compared to MR-EPT reconstructions. Since wEPT is based on a pixel-wise reconstruction approach, a 1:1 correlation between the MR image resolution and the resolution of the reconstructed EPs is achieved. For this reason, EPs reconstructions are free from numerical boundary artifacts, which are instead the major cause of inaccuracy for MR-EPT reconstructions. There is of course a partial volume error at tissue interfaces but this can be mitigated by the relatively high spatial resolution. Since wEPT avoids derivative operations on measured data, the required SNR is lower. Therefore, much higher spatial resolutions in less scan time can be achieved in wEPT reconstructions (1×1 mm^2 in-plane) compared to standard MR-EPT reconstructions. Additionally, in chapter 6 it has been shown that wEPT allows reconstructions of permittivity maps at low field strengths (3 T), while this is not feasible with MR-EPT.

However, it is questionable whether the fixed relation employed in wEPT to convert water content maps into EPs maps still holds for a large population. This relation is calibrated using literature EPs values obtained from *ex-vivo* measurements. Thus, these values might differ from *in-vivo* values (30). In chapter 6, the validity of the relation employed in wEPT for conductivity reconstructions has been investigated for the WM region using independent MR-EPT reconstructions. It has been shown that the error introduced by calibrating the wEPT model using the literature WM conductivity value is negligible. Unfortunately, this validation could not be performed for other brain tissues such as the GM and CSF, since MR-EPT reconstructions in these regions are completely corrupted by numerical boundary errors.

wEPT exploits the fact that ionic homeostasis leads to a fixed cellular osmolarity (ionic concentrations) in healthy tissues, which, in turn, modulates free water content. Thus, tissue EPs can be correlated with the free water content (31–33). However, in pathological situations this equilibrium is altered, resulting in variations in the free water content. According to the wEPT framework, even small variations in the water content associated to pathological situations would clearly result into visible variations in conductivity (for high water content tissues) and permittivity (for low water content tissues). Future studies should evaluate to what extent this fixed framework is still valid, since the wEPT model is calibrated using healthy EPs values. For pathological situations where water content and EPs change (30,34–39), the model describing the correlation between water content and EPs might be different from the one employed by wEPT. Thus, wEPT reconstructions might not be quantitatively accurate anymore.

7.4 Future perspectives

7.4.1 New strategies for MR-EPT

From the MR-acquisition point of view, a possible way to improve the accuracy of Helmholtz-based MR-EPT reconstructions could be going to higher field strength (7T). This might particularly be beneficial for permittivity reconstructions. In fact, while the sensitivity of conductivity reconstructions scales linearly with the field strength, for permittivity reconstructions it scales quadratically (40,41). Furthermore, by going to higher field strengths, higher SNR levels can be achieved, allowing higher spatial resolutions in lower scan time. This would result in lower boundary error propagations in the reconstructed EPs maps, which is the major issue of *in-vivo* MR-EPT reconstructions, as shown in chapters 5 and 6. Based on these observations, further studies should therefore consider performing MR-EPT reconstructions at high field strengths in combination with multi-transmit array systems to circumvent the transceive phase assumption. Moreover, MR-EPT reconstructions based on the relative receive coil sensitivities (42,43) should be further explored, as much more input data can be acquired in less scan time.

In order to circumvent direct derivative operations on noisy measured B_1^+ field, different approaches have been recently proposed (44–47), such as Contrast Source Inversion (CSI)-EPT. These methods employ a forward model which relates the forward calculated, complex B_1^+ field to a model estimate of EPs. Defined as "inverse methods", these methods aim to solve an optimization problem where the model of the EPs distribution is fit to the measured B_1^+ field. This avoids direct derivatives of measured B_1^+ fields. For this reason, these methods are in principle more noise-robust. This fitting is based on an iterative minimization of a large system of non-linear equations. Among these approaches, CSI-EPT has shown good capability in reconstructing EPs maps free from boundary artifact from simulations in a human pelvis (44). Furthermore, it allows reconstructions of the electric field, which can be used in combination with the reconstructed conductivity for SAR estimations. However, CSI-EPT is currently based on a 2D model and EPs reconstructions are inaccurate where the electric field is small, as occurs for example in the center of a birdcage coil. Future research should therefore be focused on: extending the CSI-EPT model to 3D, finding new strategies to avoid reconstruction errors where the electric field is small and experimentally validating the presented *in-silico* simulations results.

7.4.2 Can we use MR-EPT for RF safety?

At low field strength and for volume coils RF safety assessment is based on global SAR. The global SAR limits are enforced for volume coils such as birdcage body coil for clinical MRI scanners.

However, since our body is electrically very heterogeneous, a complex EM scattering process takes place in our body. This can result in high peak local SAR values due to electric field foci (48–50). As demonstrated for 1.5 and 3T systems, this could lead to dangerous local temperature peaks although global SAR limits are respected. At high field strengths, because of the increasing use of multi-transmit phased arrays, even much higher local SAR values can be reached (51). To study this phenomenon properly, sufficient and reliable human EPs models are essential. While the tissue morphology can be obtained directly from segmentation of MRI images, assigning the correct, potentially subject-specific EPs is a challenge.

Unfortunately, as presented in chapter 6, *in-vivo* MR-EPT is not sufficiently accurate to address this challenge. The reconstructions are affected by high variability (low precision) in the reconstructed EPs values. This variability is in the range of the EPs themselves, and it is too high to justify intra-subject and inter-subjects EPs variations. As discussed in chapter 5, this variability is a direct consequence of the numerical errors introduced by the MR-EPT reconstruction approach. Even though the required accuracy and precision of EPs mapping for RF safety assessment is not clear, EPs reconstructions using MR-EPT in the current form are not yet suited as a direct input for RF safety assessment.

7.4.3 Can we use MR-EPT as a new biomarker for clinical applications?

Because of the aforementioned issues concerning boundary errors and effective resolution of reconstructed EPs maps, MR-EPT can only be used to characterize volumetric areas, instead of providing local information on EPs on a voxel-to-voxel basis (52). Therefore, MR-EPT seems to be suited for large regions (38), i.e. larger than typical sizes of derivative kernels: > 10 mm in diameter (38,53).

First studies on cancer are focused on brain (54), breast (37,38,55) and cervical cancer (56). For brain tumors, increased conductivity values up to 1.4 S/m (average value) were reported (51,57). For breast carcinoma, conductivity values of 0.9 S/m (average value) were observed (38). Additionally, a correlation between tumor conductivity and malignancy has also been suggested for large breast tumors (conductivity of 0.9-1.8 S/m for malignant tumors, and 0.4-0.6 S/m for benign tumors) (38,55). For cervical cancer, a mean conductivity value of 1 S/m was reported, showing an increase of 13% respect to literature data (56).

Based on these studies, MR-EPT seems to be suited to provide quantitative information on tumor conductivity, provided large tumor sizes (38,53). Still, before establishing MR-EPT as a new endogenous biomarker, further investigations are needed. In this sense, comparison between MR-EPT measurements with *ex-vivo* measurements performed immediately after tissue excision could give more confidence in the presented results.

Additionally, comparison between MR-EPT (conductivity being a proxy for sodium) and independent sodium and water content measurements could allow more insight into the processes underlying the conductivity increase in pathological situations.

7.4.4 The relation between HF tissue EPs and tissue structure and composition

To assess the potential value of tissue EPs as a new endogenous biomarker, it is fundamental to understand the physiological background of tissue EPs. This knowledge is largely lacking at the moment. Having this understanding would allow for a better diagnostic interpretation of the observed increase in conductivity values in tumor tissues (37,38,54,55). In addition to the relationship between water content and tissue conductivity, a relationship between conductivity and sodium content (^{23}Na) has already been shown (58–61).

At 7T, both tissue EPs and ^{23}Na can be independently measured. This makes 7T MRI systems a perfect candidate to further investigate the relationship between electrical conductivity and tissue sodium concentration. On this line of research, a recent collaboration has been started between the University Medical Center of Utrecht and Leiden. Since sodium appears in the human body in two states, i.e. bound and free sodium, it is important to understand whether RF conductivity is linked to total tissue sodium concentration (bound + free), or these two states of sodium have a different impact on tissue conductivity, given their different ionic mobility.

Although sodium imaging is a more direct biomarker than MR-EPT, performing *in-vivo* sodium imaging is quite challenging. In fact, sodium imaging requires dedicated hardware, particular MR sequences, and very high SNR levels. On the contrary, MR-EPT can be performed using standard hardware and sequences.

Preliminary results seem to suggest that conductivity and total sodium imaging are similar only to a leading order, but not identical (59–61). In presence of bound sodium, we have recently shown that conductivity values independently reconstructed from MR-EPT measurements and from total sodium measurements are not equal, and the differences increase with increasing concentrations of bound sodium (59). This suggests that free and bound sodium have a different impact on tissue conductivity, and that free sodium might be the most contributing electrolyte.

In presence of pathologies, the increase in tissue conductivity is a consequence of the increase in the intra-cellular sodium content, as the sodium-potassium pump, which regulates the ionic homeostasis, fails due to lack of nutrients and oxygen (62–67). Consequently, water molecules will enter the cells leading to abnormal cell swelling and finally cell membrane breakdown (35,68–72). This last stage will probably create a different ratio in free/bound sodium compared to initial pathological stages, resulting in different values of conductivity.

Being able to characterize different pathological stages using tissue conductivity as a surrogate of sodium imaging would be therefore important for diagnostic purposes.

7.5 Conclusions

In this thesis, various methodologies to measure tissue EPs both at low and high frequencies (kHz and MHz ranges) have been investigated, characterized and experimentally explored.

At low frequencies (kHz), fundamental and experimental problems hampering EPs reconstructions by means of MR compatible current induction methods have been characterized. Nevertheless, it has been shown that MRI measurements of the incident TMS magnetic field are feasible. These measurements are important to better guide TMS dosimetry. Future studies on low frequency EPs mapping should focus on direct current injection methods (MR-EIT, not directly investigated in this thesis), which allow for low frequency EPs reconstructions despite the need of long experimental time.

At high frequencies (Larmor frequencies), MR-EPT is widely used to reconstruct tissue EPs. However, several issues affect the accuracy of this technique. In this thesis, the impact of the computation of spatial derivatives on noisy data, required in the MR-EPT reconstruction framework, has been thoroughly analyzed. The results of the performed analysis suggest that the error introduced by this operation is the major cause of inaccuracy for MR-EPT reconstructions in the brain. Ultimately, for low fields (1.5 T and 3 T), MR-EPT is not able to provide detailed EPs measurements on a voxel level. Still, it can be used to investigate volumetric EPs changes, e.g. for better tumor characterization. Future MR-EPT studies should therefore be performed at high field strengths (7T), given the aforementioned advantages in section 7.4.1.

Finally, a newly proposed MR-based technique has been investigated: water content EPT. Although wEPT is built upon an empirical framework, it allows more detailed EPs reconstructions at RF frequencies for healthy brain tissues. The validity of the wEPT reconstruction model has been verified for conductivity reconstruction in the WM region. Future studies should focus on investigating the validity of this technique in pathological situations. Moreover, by correlating wEPT reconstructions with independent MR-EPT reconstructions and sodium imaging, better understanding of the relationships between electrical conduction and tissue structure and composition might be obtained. Ultimately, correct understanding of the physiological background of tissue EPs would be fundamental before EPs measurements could be used as a new endogenous biomarker for diagnostic purposes.

7.6 References

1. van Lier ALHMW, van den Berg CAT, Katscher U. Measuring electrical conductivity at low frequency using the eddy currents induced by the imaging gradients. Proc. 20th Sci. Meet. Int. Soc. Magn. Reson. Med. Melbourne, Victoria, Aust. 2012:3467.
2. Mandija S, van Lier ALHMW, Thielscher A, Antunes A, Neggers B, Luijten PR, Van Den Berg CAT. Characterizing electrical interactions of tissues with time varying gradient fields: Simulations and measurements. Proc. 22nd Sci. Meet. Int. Soc. Magn. Reson. Med. Milano, Italy 2014:639.
3. Liu C, Li W, Argyridis I. Imaging electric conductivity and conductivity anisotropy via eddy currents induced by pulsed field gradients. Proc. 22nd Sci. Meet. Int. Soc. Magn. Reson. Med. Milano, Italy 2014:638.
4. Oran OF, Hafalir FS, Gurler N, Ider YZ. Convection-Reaction Equation Based Low-Frequency Conductivity Imaging Using Readout Gradient Induced Eddy Currents. Proc. 21st Sci. Meet. Int. Soc. Magn. Reson. Med. Salt Lake City, Utah, USA 2013:4188.
5. Wood AW, Karipidis K. Non-ionizing Radiation Protection: Summary of Research and Policy Options. Wiley; 2017.
6. Oran OF, Ider YZ. Feasibility of Conductivity Imaging Using Subject Eddy Currents Induced by Switching of MRI Gradients. Magn. Reson. Med. 2016. doi: 10.1002/mrm.26283.
7. Ozparlak L, Ider YZ. Induced current magnetic resonance-electrical impedance tomography. Physiol. Meas. 2005;26:S289–S305. doi: 10.1088/0967-3334/26/2/027.
8. Woo EJ, Seo JK. Magnetic resonance electrical impedance tomography (MREIT) for high-resolution conductivity imaging. Physiol. Meas. 2008;29:R1–R26. doi: 10.1088/0967-3334/29/10/R01.
9. Oh SH, Lee B Il, Woo EJ, Lee SY, Kim T-S, Kwon O, Seo JK. Electrical conductivity images of biological tissue phantoms in MREIT. Physiol. Meas. 2005;26:S279–S288. doi: 10.1088/0967-3334/26/2/026.
10. Kim HJ, Kim YT, Minhas AS, Jeong WC, Woo EJ, Seo JK, Kwon OJ. In vivo high-resolution conductivity imaging of the human leg using MREIT: The first human experiment. IEEE Trans. Med. Imaging 2009;28:1681–1687. doi: 10.1109/TMI.2009.2018112.
11. Muftuler LT, Hamamura MJ, Birgul O, Nalcioglu O. In vivo MRI electrical impedance tomography (MREIT) of tumors. Proc. 14th Sci. Meet. Int. Soc. Magn. Reson. Med. Seattle, Washington, USA 2006:332.
12. Kim HJ, Oh TI, Kim YT, et al. In vivo electrical conductivity imaging of a canine brain using a 3 T MREIT system. Physiol. Meas. 2008;29:1145–1155. doi: 10.1088/0967-3334/29/10/001.
13. Jeong WC, Kim YT, Minhas a S, Lee TH, Kim HJ, Nam HS, Kwon O, Woo EJ. In vivo conductivity imaging of human knee using 3 mA injection current in MREIT. J. Phys. Conf. Ser. 2010;224:012148. doi: 10.1088/1742-6596/224/1/012148.
14. Kim YT, Meng Z, Minhas AS, Kim HJ, Woo EJ, Lim CY, Park HM. In vivo MREIT conductivity imaging of canine brain to evaluate ischemia and abscess. 8th Int. Conf. Bioelectromagn. NFSI ICBEM 2011:44–47. doi: 10.1109/NFSI.2011.5936817.
15. Janssen AM, Oostendorp TF, Stegeman DF. The effect of local anatomy on the electric field induced by TMS: evaluation at 14 different target sites. Med. Biol. Eng. Comput. 2014;52:873–883. doi: 10.1007/s11517-014-1190-6.

16. Komssi S, Kähkönen S, Ilmoniemi RJ. The Effect of Stimulus Intensity on Brain Responses Evoked by Transcranial Magnetic Stimulation. Hum. Brain Mapp. 2004;21:154–164. doi: 10.1002/hbm.10159.

17. Roth BJ, Saypol JM, Hallett M, Cohen LG. A theoretical calculation of the electric field induced in the cortex during magnetic stimulation. Electroencephalogr. Clin. Neurophysiol. Potentials Sect. 1991;81:47–56. doi: 10.1016/0168-5597(91)90103-5.

18. Tofts PS, Branston NM. The measurement of electric field, and the influence of surface charge, in magnetic stimulation. Electroencephalogr. Clin. Neurophysiol. 1991;81:238–239. doi: 10.1016/0168-5597(91)90077-B.

19. Neggers SFW, Petrov PI, Mandija S, Sommer IEC, van den Berg CAT. Understanding the biophysical effects of transcranial magnetic stimulation on brain tissue: The bridge between brain stimulation and cognition. Prog Brain Res, Comput. Neurostimulation 2015;222:229–259. doi: 10.1016/bs.pbr.2015.06.015.

20. Stokes MG, Chambers CD, Gould IC, Henderson TR, Janko NE, Allen NB, Mattingley JB. Simple Metric For Scaling Motor Threshold Based on Scalp-Cortex Distance: Application to Studies Using Transcranial Magnetic Stimulation. J. Neurophysiol. 2005;94:4520–4527. doi: 10.1152/jn.00067.2005.

21. Peterchev A V., Wagner TA, Miranda PC, Nitsche MA, Paulus W, Lisanby SH, Pascual-Leone A, Bikson M. Fundamentals of transcranial electric and magnetic stimulation dose: Definition, selection, and reporting practices. Brain Stimul. 2012;5:435–453. doi: 10.1016/j.brs.2011.10.001.

22. Petrov PI, Mandija S, van den Berg CAT, Neggers SFW. Impact of TMS coil modeling detail on FEM simulation accuracy of the induced electrical field. Proc. Int. Conf. Basic Clin. Multimodal Imaging 2015, Utrecht, Netherlands.

23. Opitz A, Windhoff M, Heidemann RM, Turner R, Thielscher A. How the brain tissue shapes the electric field induced by transcranial magnetic stimulation. Neuroimage 2011. doi: 10.1016/j.neuroimage.2011.06.069.

24. Thielscher A, Opitz A, Windhoff M. Impact of the gyral geometry on the electric field induced by transcranial magnetic stimulation. Neuroimage 2011;54:234–243. doi: 10.1016/j.neuroimage.2010.07.061.

25. Geeter N De, Dupré L, Crevecoeur G. Modeling transcranial magnetic stimulation from the induced electric fields to the membrane potentials along tractography-based white matter fiber tracts. J. Neural Eng. 2016;13:1–16. doi: 10.1088/1741-2560/13/2/026028.

26. van Lier ALHMW, Brunner DO, Pruessmann KP, Klomp DWJ, Luijten PR, Lagendijk JJW, Van Den Berg CAT. B1+ phase mapping at 7 T and its application for in vivo electrical conductivity mapping. Magn. Reson. Med. 2012;67:552–561. doi: 10.1002/mrm.22995.

27. Savitzky A, Golay MJE. Smoothing and Differentiation of Data by Simplified Least Squares Procedures. Anal. Chem. 1964;36:1627–1639.

28. Steinier J, Termonia Y, Deltour J. Comments on Smoothing and Differentiation of Data by Simplified Least Square Procedure. Anal. Chem. 1972;44:1906–1909. doi: 10.1021/ac6031 9a045.

29. Michel E, Hernandez D, Lee SY. Electrical conductivity and permittivity maps of brain tissues derived from water content based on T 1 -weighted acquisition. Magn. Reson. Med. 2016;early view. doi: 10.1002/mrm.26193.

30. Halter RJ, Zhou T, Meaney PM, et al. The correlation of in vivo and ex vivo tissue dielectric properties to validate electromagnetic breast imaging: initial clinical experience. Physiol. Meas. 2009;30:121–123. doi: 10.1088/0967-3334/30/6/S08.

31. Schwan HP, Foster KR. Microwave dielectric properties of tissue. Some comments on the rotational mobility of tissue water. Biophys. J. 1977;17:193–197. doi: 10.1016/S0006-3495(77)85637-3.

32. Foster KR, Schepps JL, Stoy RD, Schwan HP. Dielectric properties of brain tissue between 0.01 and 10 GHz. Phys. Med. Biol. 1979;24:1177–1187. doi: 10.1088/0031-9155/24/6/008.

33. Farace P, Pontalti R, Cristoforetti L, Antolini R, Scarpa M. An automated method for mapping human tissue permittivities by MRI in hyperthermia treatment planning. Phys. Med. Biol. 1997;2159:2159–2174. doi: 10.1088/0031-9155/42/11/011.

34. Surowiec AJ, Stuchly SS, Barr JR, Swarup A. Dielectric Properties of Breast Carcinoma and the Surrounding Tissues. IEEE Trans. Biomed. Eng. 1988;35:257–263. doi: 10.1109/10.1374.

35. Schepps JL, Foster KR. The Uhf and microwave dielectric properties of normal and tumor tissues variation in dielectric properties with tissue water content. Phys. Med. Biol. 1980; 25:1149–1159.

36. Joines WT, Zhang Y, Li C, Jirtle RL. The measured electrical properties of normal and malignant human tissues from 50 to 900 MHz. Med. Phys. 1994;21:547–550.

37. Katscher U, Djamshidi K, Voigt T, Ivancevic M, Abe H, Newstead G, Keupp J. Estimation of breast tumor conductivity using parabolic phase fitting. Proc. 20th Sci. Meet. Int. Soc. Magn. Reson. Med. Melbourne, Victoria, Aust. 2012:2335.

38. Shin J, Kim MJ, Lee J, Nam Y, Kim M, Choi N, Kim S, Kim D-H. Initial study on in vivo conductivity mapping of breast cancer using MRI. J. Magn. Reson. Imaging 2014:371–378. doi: 10.1002/jmri.24803.

39. Sabouni A, Hahn C, Noghanian S, Sauter E, Weiland T. Study of the Effects of Changing Physiological Conditions on Dielectric Properties of Breast Tissues. Hindawi Int. J. Biomed. Imaging 2013;2013:1–5.

40. van Lier ALHMW, Raaijmakers A, Voigt T, Lagendijk JJW, Katscher U, Van Den Berg CAT. Electric properties tomography in the human brain at 1.5, 3, and 7 T: a comparison study. Magn. Reson. Med. 2014;71:354–363. doi: 10.1002/mrm.24637.

41. Lee S, Bulumulla S, Hancu I. Theoretical Investigation of Random Noise-Limited Signal-to-Noise Ratio in MR-Based Electrical Properties Tomography. IEEE Trans. Med. Imaging 2015;34:2220–2232.

42. Marques JP, Sodickson DK, Ipek O, Collins CM, Gruetter R. Single acquisition electrical property mapping based on relative coil sensitivities: A proof-of-concept demonstration. Magn. Reson. Med. 2015;74:185–195. doi: 10.1002/mrm.25399.

43. Lee J, Shin J, Kim D. MR-Based Conductivity Imaging Using Multiple Receiver Coils. Magn. Reson. Med. 2015. doi: 10.1002/mrm.25891.

44. Balidemaj E, Trinks J, Van Den Berg CAT, Nederveen AJ, van Lier ALHMW, Stalpers LJ, Crezee J, Remis RF. CSI-EPT: A novel contrast source approach to MRI based electric properties tomography and patient-specific SAR. In: International Conference on Electromagnetics in Advanced Applications (ICEAA). IEEE; 2013. pp. 668–671. doi: 10.1109/ICEAA.2013.6632328.

45. Ropella KM, Noll DC. A regularized, model-based approach to phase-based conductivity mapping using MRI. Magn. Reson. Med. 2016;00:00:00. doi: 10.1002/mrm.26590.

46. Borsic A, Perreard I, Mahara A, Halter RJ. An inverse problems approach to MR-EPT image reconstruction. IEEE Trans. Med. Imaging 2016;35:244–256. doi: 10.1109/TMI.2015.2466082.

47. Serralles JE, Polimeridis A, Vaidya MV, Haemer G, White JK, Sodickson DK, Lattanzi R. Global Maxwell Tomography: A novel technique for electrical properties mapping without symmetry assumption or edge artifacts. Proc. 24th Sci. Meet. Int. Soc. Magn. Reson. Med. Singapore 2016:2993.

48. Neufeld E, Gosselin M-CM, Murbach M, Christ A, Cabot E, Kuster N. Analysis of the local worst-case SAR exposure caused by an MRI multi-transmit body coil in anatomical models of the human body. Phys. Med. 2011;4649:4649–4659. doi: 10.1088/0031-9155/56/15/002.

49. Murbach M, Cabot E, Neufeld E, Gosselin MC, Christ A, Pruessmann KP, Kuster N. Local SAR enhancements in anatomically correct children and adult models as a function of position within 1.5 T MR body coil. Prog. Biophys. Mol. Biol. 2011;107:428–433. doi: 10.1016/j.pbiomolbio.2011.09.017.

50. Murbach M, Neufeld E, Kainz W, Pruessmann KP, Kuster N. Whole-body and local RF absorption in human models as a function of anatomy and position within 1.5T MR body coil. Magn. Reson. Med. 2014;71:839–845. doi: 10.1002/mrm.24690.

51. Restivo MC, Van Den Berg C a. T, Van Lier ALHMW, Polders DL, Raaijmakers AJE, Luijten PR, Hoogduin H. Local specific absorption rate in brain tumors at 7 tesla. Magn. Reson. Med. 2016;75:381–389. doi: 10.1002/mrm.25653.

52. Zhang X, De Moortele PF Van, Schmitter S, He B. Complex B1 mapping and electrical properties imaging of the human brain using a 16-channel transceiver coil at 7T. Magn. Reson. Med. 2013;69:1285–1296. doi: 10.1002/mrm.24358.

53. Kim SY, Shin J, Kim DH, Kim MJ, Kim EK, Moon HJ, Yoon JH. Correlation between conductivity and prognostic factors in invasive breast cancer using magnetic resonance electric properties tomography (MREPT). Eur. Radiol. 2016;26:2317–2326. doi: 10.1007/s00330-015-4067-7.

54. van Lier ALHMW, Hoogduin JM, Polders DL, Boer VO, Hendrikse J, Robe PA, Woerdeman PA, Lagendijk JJW, Luijten PR, van den Berg CAT. Electrical conductivity imaging of brain tumours. Proc. 19th Annu. Meet. ISMRM. Montréal, Québec, Canada 2011;19:4464.

55. Katscher U, Abe H, Ivancevic MK, Keupp J. Investigating breast tumor malignancy with electric conductivity measurements. Proc. 23nd Sci. Meet. Int. Soc. Magn. Reson. Med. Toronto, Canada 2015:3306.

56. Balidemaj E, de Boer P, van Lier a LHMW, Remis RF, Stalpers LJ a, Westerveld GH, Nederveen a J, van den Berg C a T, Crezee J. *In vivo* electric conductivity of cervical cancer patients based on B1+ maps at 3T MRI. Phys. Med. Biol. 2016;61:1596–1607. doi: 10.1088/0031-9155/61/4/1596.

57. Tha KK, Stehning C, Suzuki Y, Katscher U, Keupp J, Kazumata K, Terasaka S, Cauteren M Van, Kudo K, Hiroki S. Noninvasive Evaluation of Electrical Conductivity of the Normal Brain and Brain Tumors. Proc. 22nd Sci. Meet. Int. Soc. Magn. Reson. Med. Milano, Italy 2014;3:1885.

58. van Lier ALHMW, de Bruin PW, Aussenhofer SA, Luijten PR, Lagendijk JJW, van den Berg CAT, Webb AG. 23Na-MRI and EPT: Are sodium concentration and electrical

conductivity at 298 MHz (7T) related? Proc. 21st Sci. Meet. Int. Soc. Magn. Reson. Med. Salt Lake City, Utah, USA 2013:0115.

59. Mandija S, Bruin P De, Webb A, Luijten PR, Berg C a. T Van Den. Investigating the relation between electrical conduction and tissue composition with proton and sodium MRI. Proc. 25th Sci. Meet. Int. Soc. Magn. Reson. Med. Honolulu 2017:3639.

60. Lechea N, Liao YP, Shah NJ. On the feasibility of synthetic sodium MRI based on tissue conductivity. Proc. 25th Sci. Meet. Int. Soc. Magn. Reson. Med. Honolulu 2017:1944.

61. Liao Y, Romanzetti S, Gras V, Huang DF, Shah NJ. The dielectric properties of brain tissues: variation in electrical conductivity with tissue sodium concentration and tissue water content at 3T/4T. Proc. 23nd Sci. Meet. Int. Soc. Magn. Reson. Med. Toronto, Canada 2015:3302.

62. Fraser SP, Diss JKJ, Chioni A-M, et al. Human Cancer Biology Voltage-Gated Sodium Channel Expression and Potentiation of Human Breast Cancer Metastasis. Am. Assoc. Cancer Res. 2005:5381–5389.

63. Camero IL, Smith NKR, Pool TB, Sparks RL. Intracellular Concentration of Sodium and Other Elements as Related to Mitogenesis and Oncogenesis in Vivo. Cancer Res. 1980;40: 1493–1500.

64. Ouwerkerk R, Bleich KB, Gillen JS, Pomper MG, Bottomley PA. Tissue sodium concentration in human brain tumors as measured with 23Na MR imaging. Radiology 2003;227:529–537. doi: 10.1148/radiol.2272020483.

65. Thulborn K, Lui E, Guntin J, Jamil S, Sun Z, Claiborne TC, Atkinson IC. Quantitative sodium MRI of the human brain at 9.4 T provides assessment of tissue sodium concentration and cell volume fraction during normal aging. NMR Biomed. 2015. doi: 10. 1002/nbm.3312.

66. Ouwerkerk R, Jacobs MA, Macura KJ, Wolff AC, Stearns V, Mezban SD, Khouri NF, Bluemke DA, Bottomley PA. Elevated tissue sodium concentration in malignant breast lesions detected with non-invasive 23Na MRI. Breast Cancer Res. Treat. 2007;106:151–160. doi: 10.1007/s10549-006-9485-4.

67. Boada FE, LaVerde G, Jungreis C, Nemoto E, Tanase C, Hancu I. Loss of cell ion homeostasis and cell viability in the brain: what sodium MRI can tell us. Curr. Top. Dev. Biol. 2005;70:77–101. doi: 10.1016/S0070-2153(05)70004-1.

68. Miklavcic D, Pavselj N, Hart FX. Electric properties of tissues. Wiley Encycl. Biomed. Eng. 2006;209:1–12. doi: 10.1.1.65.7364.

69. Kiricuta I-CJ, Simplaceanu V. Tissue Water Content and Nuclear Magnetic Resonance in Normal and Tumor Tissues. Cancer Res. 1975;35:1164–1167.

70. Ross KF a, Gordon RE. Water in malignant tissue, measured by cell refractometry and nuclear magnetic resonance. J. Microsc. 1982;128:7–21. doi: 10.1111/j.1365-2818.1982.tb 00433.x.

71. McIntyre GI. Increased cell hydration promotes both tumor growth and metastasis: A biochemical mechanism consistent with genetic signatures. Med. Hypotheses 2007;69: 1127–1130. doi: 10.1016/j.mehy.2007.01.080.

72. McIntyre GI. Cell hydration as the primary factor in carcinogenesis: A unifying concept. Med. Hypotheses 2006;66:518–526. doi: 10.1016/j.mehy.2005.09.022.

Chapter 8

Samenvatting

8.1 Samenvatting

Onderzoek naar de elektrische eigenschappen (EPs) van weefsel, d.w.z. conductiviteit en permittiviteit, is van fundamenteel belang voor het begrijpen van de biofysische interacties en het effect van tijds-oscillerende elektromagnetische velden, zoals die door MRI scanners en transcraniële magnetische stimulatoren (TMS) worden geproduceerd, op ons lichaam. Kennis van de EPs van weefsel zou waardevol zijn voor diagnostische doeleinden in oncologie, en kan een betere schatting van de weefselopwarming (gekwantificeerd middels de specifieke absorptie ratio (SAR)) geven voor RF patiëntveiligheid. Verder kunnen metingen van de EPs van weefsel betere therapieplanning , en dosimetrie voor TMS behandelingen bieden. In dit proefschrift zijn verschillende methodes om de EPs van weefsel, op lage en hoge frequenties (kHz en MHz bereik) , te meten onderzocht, gekarakteriseerd en experimenteel nagegaan.

Bij lage frequenties zijn fundamentele en experimentele problemen die de reconstructie van EPs doormiddel van inductieve stroomopwekking methodes belemmeren, gekarakteriseerd. In het bijzonder, in **Hoofdstuk 2** zijn elektrische stromen geïnduceerd door middel van het snel schakelen (< 0.1 ms) van de MR gradiënten. Om de sterkte van de geïnduceerde stromen te vergroten zijn in **Hoofdstuk 4** elektrische stromen inductief geïnduceerd met gebruik van een gecombineerde TMS-MRI opstelling. Deze opstelling, beschreven in **Hoofdstuk 3**, bestaat uit een 3T MRI systeem (Achieva, Philips, Best, Nederland) en een TMS stimulator(Magstim Rapid2, Whitland, VK). Middels een nieuw ontwikkelde, MRI gebaseerde TMS veld afbeeldingstechniek, kon het TMS magnetisch veld direct opgewekt door de TMS spoel, gemeten worden.

Zulke metingen leveren een nieuwe manier van kwantitatieve TMS dosimetrie op. Tevens, zoals gedemonstreerd in **Hoofdstuk 3** kunnen middels deze metingen gebruikt worden voor validatie van numerieke TMS spoel modellen die gebruikt worden voor planning van TMS geïnduceerde neuronale activering. Momenteel wordt deze opstelling gebruikt voor *in vivo* TMS-fMRI studies voor het onderzoeken van TMS geïnduceerde hersenactivering. In deze studies wordt subject data management en planning gedaan met HiX (ChipSoft, Amsterdam, Nederland).

Aangezien EPs variëren met de frequentie is in **Hoofdstuk 5** en **Hoofdstuk 6** de haalbaarheid van het accuraat meten van weefsel EPs bij RF frequenties onderzocht door middel van zogenaamde MR-Electrical Property Tomograpy (MR-EPT). Hiervoor zijn 3T Philips MRI systemen (Achieva en Ingenia) gebruikt.

Verschillende technische problemen beïnvloeden de nauwkeurigheid van deze techniek. In **Hoofdstuk 5** wordt het effect van de tweede orde, numerieke spatiële afgeleide op met ruis besmette data, welke nodig is in het MR-EPT reconstructie framewerk, grondig geanalyseerd. De resultaten van de analyse suggereren dat de

fout die door deze numerieke operatie geïntroduceerd wordt, de hoofdoorzaak is van de onnauwkeurigheid in de MR-EPT reconstructies van de hersenen. Uiteindelijk is gebleken dat voor lage veldsterktes (1.5 T en 3 T) MR-EPT niet in staat is om gedetailleerde, accurate EPs metingen te doen in weefsels waar op millimeter schaal weefselovergangen optreden.

De techniek kan nog wel gebruikt worden als functionele techniek in volumina welke homogeen zijn op een 7-15 mm schaal. Zo kan bijvoorbeeld de elektrische geleiding in grote brein- of borsttumoren betrouwbaar bemeten worden, zoals ook aangetoond in literatuur. Tenslotte wordt in **Hoofdstuk 6** een nieuwe voorgestelde MR gebaseerde techniek onderzocht: water gehalte EPT (wEPT). Hoewel wEPT gebaseerd is op een empirisch model, geeft het in tegenstelling tot MR-EPT wel gedetailleerde EPs reconstructies bij RF frequenties voor gezond hersenweefsel. Doormiddel van een *in vivo* studie is de validiteit van het wEPT reconstructie model geverifieerd voor elektrische geleiding bepaling voor witte stof.

Toekomstige onderzoeken zouden zich moeten focusseren op het onderzoeken van de validiteit van wEPT in pathologische situaties. Verder, zou door middel van correlatie van wEPT reconstructies met onafhankelijke MR-EPT reconstructies en MR gebaseerde natrium metingen, een beter begrip ontwikkeld worden voor de relatie tussen elektrische geleiding en weefselstructuur en samenstelling. Uiteindelijk zal volledig begrip van de biofysische achtergrond van weefsel EPs essentieel zijn eer EPs metingen gebruikt kunnen worden als nieuwe endogene biomarker voor diagnostische doeleinden.

Chapter 9

Publications

9.1 Publications in International Journals

Understanding the biophysical effects of Transcranial Magnetic Stimulation on brain tissue: the bridge between brain stimulation and cognition.
Neggers S.F.W., Petrov P.I., **Mandija S.**, Sommer I.E.C., van den Berg C.A.T., Progress in Brain Research 2015;222:229-59. doi: 10.1016/bs.pbr.2015.06.015.

A geometrical shift results in erroneous appearance of low frequency tissue eddy current induced phase maps.
Mandija S., van Lier A.L.H.M.W., Petrov P.I., Neggers S.F.W., Katscher U., Luijten P.R., van den Berg C.A.T., Magnetic Resonance in Medicine 2016;76(3):905-12. doi: 10.1002/mrm.25981.

MR-based measurements and simulations of the magnetic field created by a realistic TMS coil and stimulator.
Mandija S., Petrov P.I., Neggers S.F.W., Luijten P.R., van den Berg C.A.T., NMR in Biomedicine 2016;29(11):1590-1600. doi: 10.1002/nbm.3618.

Non-invasive electric current induction for low frequency tissue conductivity reconstruction: is it feasible with a TMS-MRI setup?
Mandija S., Petrov P.I., Neggers S.F.W., Luijten P.R., van den Berg C.A.T., Tomography 2016;2(3):203-214. doi: 10.18383/j.tom.2016.00232.

How much detail is needed in modeling a Transcranial Magnetic Stimulation figure-8 coil: Measurements and brain simulations.
Petrov P.I., **Mandija S.**, Sommer I.E.C., van den Berg C.A.T., Neggers S.F.W., PlosOne 2017;12(6):eD178952. doi:10.1371/journal.pone.0178952.

Error analysis of Helmholtz-based MR-Electrical Properties Tomography.
Mandija S., Sbrizzi A., Katscher U., Luijten P.R., van den Berg C.A.T., Magnetic Resonance in Medicine 2017; in press. doi: 10. 1002/mrm.27004.

Electrical Properties Tomography Using Contrast Source Inversion Techniques.
Remis R., Webb A.G., **Mandija S.**, Leijsen R., Fuchs P., Stijnman P., van den Berg C.A.T., IEEE-ICEAA 2017; 1025-1028. doi:10.1109/ICEAA.2017.8065434.

Helmholtz-based and water content MR-Electrical Properties Tomography: An in-vivo comparison study.
Mandija S., Petrov P.I., Vink J.T., Neggers S.F.W., Luijten P.R., van den Berg C.A.T., Magnetic Resonance in Medicine 2017; in submission.

9.2 Conference Proceedings

Characterizing electrical interactions of tissue with time-varying gradient fields: simulations and measurements.
Mandija S., van Lier A.L.H.M.W., Thielscher A., Antunes A., Neggers S.F.W., Luijten P.R., van den Berg C.A.T..
In: Proc. of the 9th Annual Meeting of ISMRM Benelux, Maastricht, The Netherlands, 2014 [Oral].
In: Proc. of the 22nd Annual Meeting of ISMRM, Milano, Italy, 2014: p. 639 [Power Pitch].

Predicting and validating TMS induced cortical currents using FEM and two non-invasive MR techniques.
Petrov P.I., Neggers S.F.W., van den Berg C.A.T., **Mandija S.**.
In: Proc. of the 20th Annual Meeting of OHBM, Hamburg, Germany, 2014: p. 3054 [Poster].

MR guidance of TMS for a patient specific treatment plan: MR-based TMS field measurements and electromagnetic simulations.
Mandija S., Petrov P.I., Neggers S.F.W., de Weijer A.D., Luijten P.R., van den Berg C.A.T..
In: Proc. of the 10th Annual Meeting of ISMRM Benelux, Gent, Belgium, 2015 [Poster].
In: Proc. of the 23rd Annual Meeting of ISMRM, Toronto, Canada, 2015: p. 931 [Oral].

Geometrical shift results in erroneous appearance of low-frequency tissue eddy current induced phase maps: theory, simulations and measurements.
Mandija S., van Lier A.L.H.M.W., Petrov P.I., Neggers S.F.W., Luijten P.R., van den Berg C.A.T..
In: Proc. of the 23rd Annual Meeting of ISMRM, Toronto, Canada, 2015: p. 3289 [Electronic Poster].

MR-based measurements of the TMS magnetic field.
Mandija S., Petrov P.I., Neggers S.F.W., Luijten P.R., van den Berg C.A.T..
In: Proc. of the 2nd Meeting of BaCI, Utrecht, The Netherlands, 2015 [Poster].

Impact of TMS coil modeling detail on FEM simulation accuracy of the induced electrical field.
Petrov P.I., **Mandija S.**, van den Berg C.A.T, Neggers S.F.W..
In: Proc. of the 45th Annual Meeting of SFN, Chicago, IL, USA The Netherlands, 2015 [Poster].
In: Proc. of the 2nd Meeting of BaCI, Utrecht, The Netherlands, 2015 [Poster].

Artifacts affecting derivative of B_1^+ maps for conductivity reconstructions.
Mandija S., Sbrizzi A., van Lier A.L.H.M.W., Petrov P.I., Neggers S.F.W., Luijten P.R., van den Berg C.A.T..
In: Proc. of the 11th Annual Meeting of ISMRM Benelux, Eindhoven, The Netherlands, 2016 [Poster].
In: Proc. of the 24th Annual Meeting of ISMRM, Singapore, SG, 2016: p. 2989 [Electronic Poster].

Physical limitations affecting non-invasive low-frequency tissue conductivity mapping using a TMS-MRI setup.
Mandija S., Petrov P.I., Neggers S.F.W., Luijten P.R., van den Berg C.A.T..
In: Proc. of the 33rd Annual Meeting of ESMRMB, Vienna, Austria, 2016: p. 40 [Electronic Poster].

Investigating the relation between electrical conduction and tissue composition with proton and sodium MRI.
Mandija S., de Bruin P.W., Webb A.G., Luijten P.R., van den Berg C.A.T..
In: Proc. of the 12th Annual Meeting of ISMRM Benelux, Tilburg, The Netherlands, 2017 [Oral].
In: Proc. of the 25th Annual Meeting of ISMRM, Honolulu, HI, USA, 2017: p. 3639 [Electronic Poster].

A novel MR-based framework for subject-specific guidance of TMS treatments.
Mandija S., Petrov P.I., Vink J.T., Schuite-Koops S., Luijten P.R., van den Berg C.A.T., Neggers S.F.W..
In: Proc. of the 25th Annual Meeting of ISMRM, Honolulu, HI, USA, 2017: p. 3798 [Electronic Poster].

Electrical Properties Tomography using Contrast Source Inversion techniques.
Remis R.F., Webb A., **Mandija S.**, Leijsen R.L., Fuchs P.S., Stijnman P.R.S., van den Berg C.A.T..
In: Proc. of the 19th Annual Meeting of ICEAA, Verona, Italy, 2017: p. 3639 [Oral].

9.3 Awards and Invited Talks

ISMRM - 1st prize EMTP Study Group Award:

Characterizing electrical interactions of tissue with time-varying gradient fields: simulations and measurements.
Mandija S., van Lier A.L.H.M.W., Thielscher A., Antunes A., Neggers S.F.W., Luijten P.R., van den Berg C.A.T..
In: Proc. of the 22nd Annual Meeting of ISMRM, Milano, Italy, 2014: p. 639.

ISMRM - Summa cum Laude Award:

Characterizing electrical interactions of tissue with time-varying gradient fields: simulations and measurements.
Mandija S., van Lier A.L.H.M.W., Thielscher A., Antunes A., Neggers S.F.W., Luijten P.R., van den Berg C.A.T..
In: Proc. of the 22nd Annual Meeting of ISMRM, Milano, Italy, 2014: p. 639.

Investigating the relation between electrical conduction and tissue composition with proton and sodium MRI.
Mandija S., de Bruin P.W., Webb A.G., Luijten P.R., van den Berg C.A.T..
In: Proc. of the 25th Annual Meeting of ISMRM, Honolulu, HI, USA, 2017: p. 3639.

ISMRM - Magna cum Laude Award:

MR guidance of TMS for a patient specific treatment plan: MR-based TMS field measurements and electromagnetic simulations.
Mandija S., Petrov P.I., Neggers S.F.W., de Weijer A.D., Luijten P.R., van den Berg C.A.T..
In: Proc. of the 23rd Annual Meeting of ISMRM, Toronto, Canada, 2015: p. 931.

ISMRM - Mention of honor EMTP Study Group Award:

Investigating the relation between electrical conduction and tissue composition with proton and sodium MRI.
Mandija S., de Bruin P.W., Webb A.G., Luijten P.R., van den Berg C.A.T..
In: Proc. of the 25th Annual Meeting of ISMRM, Honolulu, HI, USA, 2017: p. 3798 [Electronic Poster].

Invited talk – GECCI Workshop, Singapore, 2016:

Non-invasive MR-based measurements of low-frequency tissue conductivity: are they feasible?
Mandija S., van den Berg C.A.T..

Chapter 10

Dankwoord

"Iniziare un nuovo cammino spaventa. Ma dopo ogni passo ci rendiamo conto di quanto fosse pericoloso rimanere fermi."

Roberto Benigni

For me, these words ring true in many situations. This time, the first *"passo"* was the difficult decision to move to The Netherlands to start this PhD experience. Now, if I look back at the last four years, it surprises me how many things have changed. I am pleased and proud of being part of this amazing and successful working group.

Therefore, I first would like to thank my promotor, Prof. Peter Luijten, for having given me the opportunity to conduct my research in this group.

Next, an enormous thanks goes to my supervisors Nico van den Berg and Bas Neggers for having made all of this possible. Every day you guided me one step closer to this moment. Thank you for all your constructive advices and for teaching me how to look at my work also from a broader perspective and to not only be focused on little, although still important, details. It was a pleasure working with you! In particular, thank you Nico for your enthusiasm in our discussions and the great time spent together both at work and outside of work. You have been a constant point of reference for me over the past few years.

Thanks to my colleagues, Alberto, Alex, Alexander, Alessandro, Anja, Anita, Anna A., Anna D., Anna G., Anneloes, Arjan, Arjen, Bart, Bjorn, Carlo, Catalina, Cyril, Deji, Dennis, Ellis, Erwin, Frank, Freddy, Hans, Jaco, Jannie, Janot, Jeanine, Jeroen, Jill, Jolanda, Joep, Ingmar, Irene, Lara, Lennart, Lisa, Marielle, Markus, Mariska, Martijn, Matthew, Matteo, Mike, Natalia, Nikki, Oscar, Peter, Pim, Quincy, Rashid, Rob, Robin, Ronald, Sander, Soraya, Stefan, Sylvia, Tijl, Tim, Tina, Tom, Tristan, Vincent, Vitaly, Wieke, Wouter, Wybe, and Yulia. It was a pleasure meeting you all. Working with you is simply fun. Thanks for the nice discussions, coffee, BBQs, Basket beers, the great time during conferences, and for being always present with your never ending WhatsApp messages.

Thanks to my officemates Astrid, Matthew (actually wherever mate as we were sharing basically everything), Flavio, Tim, Edwin, Anna, and Niek for the good time spent together in these years.

Thanks to my TMS-mates. Petar, sharing this project with you in these years was great! Jord and Sanne, you gave me valuable support during the in-vivo study. Collaborating with you all was very nice. Thanks for the company and the help during all the scan sessions out of working hours.

Thanks to Ulrich, Astrid, Rob, Soraya and Peter for inspiring EPT discussions. With you, I never felt alone while working on this particular research topic.

Thanks to all the people in Leiden, in particular, Andrew and Paul. Experimenting sodium imaging with you was an exciting experience. Looking forward to future experiments. Paul, shall we also include some salty water fish next time?

Dank aan mijn andere collega's, de coil-boys, de studenten, de laboranted en de RaVoT-mates (de beste van Netherland) voor al de ontspannende momenten. Het was erg leuk om jullie te leren kennen.

I would also like to thank the reading committee members: Prof. Ramsey, Prof. Lagendijk, Prof. Dijkhuizen, Prof. Webb, Dr. Petridou for reviewing my thesis.

A particular thank goes to Little Italy in NL, Alessandro, Matteo, Soraya, Carlo, Flavio, Alberto, Anna, Davide, Leonardo e Gasta. Grazie a voi non mi sono ancora dimenticato l'italiano.

Thanks to my housemates and regular visitors of LN Aisha, Alex, Alessia, Ana, Anna, Anne, Anne, Anshu, Bart, Chantal, Carlo, Casper, Elena, Erik, Joana, Joao, Jurica, Lisa, Magda, Matteo, Matthew, Maxence, Natasha, Ouren, Pes, Roberto, Sara, Saskia, Soraya, Susana, Tessa, Tim, Tom, Tristan, and Wouter. Spending these years with you was amazing. I will bring memorable moments with me, and I am sure we will have many more! I could thank everyone singularly, each of you for certain different, particular things. But among all, there is one in particular which I believe is the most important. This regards you all. With you guys I did not share just a simple house, but you were my new home here in the Netherlands. Thanks!

Thanks to my paranymphs Alessandro and Matteo for the constant support in these years and for your enthusiasm (especially early in the mornings when we are the only people already at work). Alessandro, all these thanks wouldn't have been possible if I hadn't had met you. Thank you for that coffee in Valvasone and for all

the constructive discussions that followed. Matteo, thank you for always being there whenever I wanted to talk to somebody. We spent great moments together (lots of them food related), and I am sure we will have many more.

Grazie ai miei amici e compagni d'avventure sparsi in giro per l'Italia e l'Europa, Alessandro, Anna, Chiara B., Chiara C., Chiara G., Enrico, Fabio, Federico, Francesco, Gasta, Giulia, Giacomo, Jacopo, Laura, Leonardo, Lucia, Marco, Michela, Michele, Martina, Patrizia, Poldo, Riccardo, Serena. È sempre fantastico rivedervi quando sono in vacanza.

Dank Hester dat je er tijdens deze periode voor mij was en we dit samen hebben mee gemaakt. Je hebt me altijd gesteund met je enthousiasme. Je hielp mij tijdens moelijke momenten en als ik mijn doelen behaalde konden we dit samen vieren. Ondanks dat je in deze laaste periode neer een ander land bent verhuist, zijn we er altijd voor elkaar, en ik geloof dat we nog veel meer hebben om naar uit te kijken in de toekomst.

Infine, l'ultimo ringraziamento va alla mia famiglia. Grazie ai miei genitori Gioia e Sergio, alla mia sorellina Francesca, a mia zia Daniela ed a mio nonno Giovanni. Immagino che in cuor vostro foste tristi quando decisi di intraprendere questa esperienza. Comunque, nonostante tutto, mi avete sempre supportato e incoraggiato. Questo traguardo è in parte anche vostro grazie ai vostri insegnamenti e all'educazione che mi avete dato. Spero di rendervi orgogliosi.

And now?

"Avanti sempre".

Stefano Mandija

Chapter 11

Curriculum Vitae

Stefano Mandija was born on September 27th 1988 in Camposampiero (PD), Italy. He grew up in Padova where he received his diploma in 2007. After his diploma, he first entered the Italian Naval Academy. Then, he left the Academy to continue his studies at the University of Padova. He never regretted this choice. After a sportive student life, he graduated with a B.S. degree in Biomedical Engineering in 2010 and a M.S. in Bioengineering in 2013. In summer 2013, he left Italy to pursue a PhD at the University Medical Center Utrecht (Utrecht, The Netherlands). Under the supervision of Prof. P.R. Luijten, and Dr. Ir. C.A.T. van den Berg, Stefano worked towards the characterization of brain tissue electrical properties using MRI. Ad interim, he worked in collaboration with the Rudolf Magnitude Institute of Neuroscience (Utrecht, The Netherlands) under the supervision of S.F.W Neggers towards the realization of concurrent TMS-MRI studies. Upon completion of his PhD, Stefano decided to remain in the Netherlands and continue working at the same Research Institute.